COMBINED EFFECTS OF REYNOLDS NUMBER, TURBULENCE INTENSITY AND PERIODIC UNSTEADY WAKE FLOW CONDITIONS ON BOUNDARY LAYER DEVELOPMENT AND HEAT TRANSFER OF A LOW PRESSURE TURBINE BLADE

A Dissertation

by

BURAK ÖZTÜRK

Submitted to the Office of Graduate Studies of
Texas A&M University
in partial fulfillment of the requirements for the degree of

DOCTOR OF PHILOSOPHY

December 2006

Major Subject: Mechanical Engineering

COMBINED EFFECTS OF REYNOLDS NUMBER, TURBULENCE INTENSITY AND PERIODIC UNSTEADY WAKE FLOW CONDITIONS ON BOUNDARY LAYER DEVELOPMENT AND HEAT TRANSFER OF A LOW PRESSURE TURBINE BLADE

A Dissertation

by

BURAK ÖZTÜRK

Submitted to the Office of Graduate Studies of
Texas A&M University
in partial fulfillment of the requirements for the degree of

DOCTOR OF PHILOSOPHY

Approved by:

Chair of Committee,	Taher Schobeiri
Committee Members,	Je C. Han
	Sai Lau
	John C. Slattery
Head of Department,	Dennis O'Neal

December 2006

Major Subject: Mechanical Engineering

ABSTRACT

Combined Effects of Reynolds Number, Turbulence Intensity and Periodic Unsteady Wake Flow Conditions on Boundary Layer Development and Heat Transfer of a Low Pressure Turbine Blade. (December 2006)

Burak Öztürk, B.S., Middle East Technical University, Ankara, Turkey;
M.S.,Texas A&M University

Chair of Advisory Committee: Dr. M.T. Schobeiri

Detailed experimental investigation has been conducted to provide a detailed insight into the heat transfer and aerodynamic behavior of a separation zone that is generated as a result of boundary layer development along the suction surface of a highly loaded low pressure turbine (LPT) blade. The research experimentally investigates the individual and combined effects of periodic unsteady wake flows and freestream turbulence intensity (Tu) on heat transfer and aerodynamic behavior of the separation zone. Heat transfer experiments were carried out at Reynolds number of 110,000, 150,000, and 250,00 based on the suction surface length and the cascade exit velocity. Aerodynamic experiments were performed at Re = 110,000 and 150,000. For the above Re-numbers, the experimental matrix includes Tus of 1.9%, 3.0%, 8.0%,13.0% and three different unsteady wake frequencies with the steady inlet flow as the reference configuration. Detailed heat transfer and boundary layer measurements are performed with particular attention paid to the heat transfer and aerodynamic behavior of the separation zone at different Tus at steady and periodic unsteady flow conditions. The objectives of the research are (a) to quantify the effect of Tu on the aero-thermal behavior of the separation bubble at steady inlet flow condition, (b) to investigate the combined effects of Tu and the unsteady wake flow on the aero-thermal behavior of the separation bubble, and (c) to provide a complete set of heat transfer and aerodynamic data for numerical simulation that incorporates Navier-Stokes and energy equations.

The analysis of the experimental data reveals details of boundary layer separation dynamics which is essential for understanding the physics of the separation phenomenon under periodic unsteady wake flow and different Reynolds number and Tu. To provide a complete picture of the transition process and separation dynamics, extensive intermittency analysis was conducted. Ensemble averaged maximum and minimum intermittency functions were determined leading to the relative intermittency function. In addition, the detailed intermittency analysis reveals that the relative intermittency factor follows a Gaussian distribution confirming the universal character of the relative intermittency function.

DEDICATION

I would like to dedicate this work to my entire family: my father Nurettin Öztürk, my mother Nesrin Öztürk and my brother Ayberk Öztürk. Without their continuous support and motivation, this work would have not been possible.

ACKNOWLEDGMENTS

I would like to express my appreciation and thankfulness to Dr. Schobeiri for giving me an opportunity to work on this project. His guidance and support helped me reach my goals and broadened my knowledge of turbomachinery. I would also like to thank Dr. J.C. Han, Dr. S. Lau, and Dr. J. C. Slattery for being on my committee.

I would also like to thank Eddie Denk, the students and the staff at the Turbomachinery Laboratory for providing help and support. I would also like to thank my colleague Arun Suryanarayanan, who always made research interesting, for providing help and support.

Finally, I would like to acknowledge Dr. David Asphis of the NASA Lewis Research Center for his support and guidance on this research project.

TABLE OF CONTENTS

Page

Page

Page

LIST OF FIGURES

Page

Page

Page

Page

Page

Page

Page

Page

Page

Page

Page

Page

Page

LIST OF TABLES

Page

NOMENCLATURE

A_{foil}	total surface area of the Inconel-600 foil
b	intermittency wake width
c	blade chord [mm]
c_{ax}	axial chord [mm]
c_p	pressure coefficient, $C_p = \frac{(p_i - p_s)}{(p_t - p_s)_{inl}}$
C	threshold level
d_R	rod diameter [mm]
E	DC voltage signal of the hot film anemometer at test conditions [V]
E_o	DC voltage signal of the hot film anemometer at zero flow conditions [V]
E_{RMS}	AC voltage signal of the hot film anemometer at test conditions [V]
E_u	power density function of u'
FSTI	free stream turbulence intensity
G_{LE}	grid distance from the leading edge [mm]
G_O	grid bar opening [mm]
G_T	grid bar thickness [mm]
H	yaw calibration function
H^*	modified yaw calibration function
H_{12}	shape factor, $H_{12}=\delta_1/\delta_2$
h	heat transfer coefficient [$W/m^2.K$]
h_m	maximum separation bubble height [mm]
I	luminescent intensity of the paint at the test or wind-on condition
I_{ref}	luminescent intensity of the paint at a known reference or wind-off condition
$I(\mathbf{x},t)$	indicator function

L_{SS}	suction surface length [mm]
m	yaw correction parameter
M	number of samples
N	number of wake cycles
N_S	signal probe luminophor concentration
N_R	reference probe luminophor concentration
OHR	overheat ratio
p_i	static pressure taps i=1,..,48 [Pa]
p_s, p_t	static, total pressure on suction surface [Pa]
PSD	power spectral distribution of turbulence in x-directions
PSP	pressure sensitive paint
$Q"_{cond}$	conductive heat flux [W/m^2]
$Q"_{conv}$	convective heat flux [W/m^2]
$Q"_{rad}$	radiation heat flux [W/m^2]
Q(t)	fluctuating quantity, (e.g. a velocity component at a given point)
$\dot{Q}_w$	heat emitted by the sensor [W]
R	resistance of the sensor (wire or film) at the overheat temperature [Ω]
R_o	resistance of the sensor at the flow temperature [Ω]
Re_{LSS}	Reynolds number based $Re=L_{ss}V_{exit}/\nu$
s	streamwise distance from the leading edge of the blade [mm]
s_{md}	streamwise location of maximum separation bubble height
s_o	streamwise distance from the leading edge to the trailing edge of the blade [mm]
s_r	re-attachment point of the separation bubble from blade leading edge
s_s	start of the separation bubble at a streamwise distance from blade leading edge
S(**x**,t)	criterion function
S_B	blade spacing [mm]
S_{LE}	hot film sensor distance from the leading edge [mm]

S_R	rod spacing [mm]
t	time [s]
T	temperature from the liquid crystal or TSP [°C]
T_∞	free-stream air temperature [°C]
TG	turbulence generator grid
TSP	temperature sensitive paint
Tu	reference turbulence intensity
Tu_l	turbulence intensity level along the lower horizontal slot
Tu_m	turbulence intensity level along the middle horizontal slot
Tu_u	turbulence intensity level along the upper horizontal slot
<Tu>	ensemble-averaged turbulence intensity
U	belt translational velocity [m/s]
v	fluctuation velocity [m/s]
V	velocity [m/s]
V_{ax}	axial velocity [m/s]
V_{exit}	exit velocity [m/s]
V_{in}	inlet reverence velocity [m/s]
V_x	velocity component along x-direction of probe coordinate system [m/s]
V_y	velocity component along y-direction of probe coordinate system [m/s]
x	position vector
y	lateral distance from plate surface [mm]
α	angle between resultant velocity vector and x-axis
α_{id}	ideal flow angle
γ	cascade stagger angle
$\bar{\gamma}$	time-averaged intermittency
$<\gamma(t)>$	ensemble averaged intermittency
$<\gamma(t)>_{max}$	maximum ensemble-averaged intermittency
$<\gamma(t)>_{min}$	minimum ensemble-averaged intermittency
Γ	relative turbulence intermittency

δ	boundary layer thickness [mm]
δ_1	boundary layer displacement thickness [mm]
δ_2	boundary layer momentum thickness [mm]
δ_3	boundary layer energy thickness [mm]
ΔT	difference in temperature between the sensor and the flow [°C]
ϵ	emissivity of the liquid crystal sheet and temperature sensitive paint
Λ	integral length scale of turbulence [mm]
$\Lambda_{u,x}$	integral length scale of u' in streamwise direction [mm]
ζ	nondimensional coordinate, ξ_2/b
ν	kinematic viscosity of air [m^2/s]
ξ_2	transformed coordinate, $\xi_2=tS_R/\tau$
φ	flow coefficient, $\varphi = V_{ax}/U$
ρ	density of air [kg/m3]
σ	Stefan-Boltzmann constant [$\sigma=5.667\ 10^{-8}$ $W/m^2.K^4$]
σ	cascade solidity, $\sigma = c/S_B$
τ	one wake-passing period [s]
τ_w	wall shear stress [N/m^2]
ψ_A	Zweifel coefficient $\psi_A = 2\sin^2\alpha_2(\cot\alpha_2 - \cot\alpha_1)S_B / c_{ax}$
Ω	reduced frequency

1. INTRODUCTION

The continuous improvement of efficiency and performance of the low pressure turbine component (LPT) has motivated industry and research community to intensify the LPT aerodynamics research efforts. The efforts have been encompassing a wide variety of different research approaches such as steady and unsteady cascade aerodynamic research and rotating turbine research. The research has contributed to better understanding the LPT flow physics resulting in a state of the art LPT design with a reduced number of blades without substantially sacrificing the efficiency of the LPT blading. This reduction contributes to an increase in thrust/weight ratio, thus reducing the fuel consumption. Contrary to the high pressure turbine (HPT) stage group that operates in a relatively high Reynolds number environment, dependent on operation conditions, the LPT experiences a variation in Reynolds number ranging from 50,000 to 250,000. Since the major portion of the boundary layer, particularly along the suction surface is laminar, the low Reynolds number in conjunction with the local adverse pressure gradient makes it susceptible to flow separation, thus increasing the complexity of the LPT boundary layer aerodynamics. The periodic unsteady nature of the incoming flow associated with wakes that originate from upstream blades substantially influences the boundary layer development including the onset of the laminar separation, the extent of the separation bubble, and its turbulent re-attachment. While the phenomenon of the unsteady boundary layer development and transition in the absence of the separation bubbles has been the subject of intensive research, that has led to better understanding the transition phenomenon, comprehending the multiple effects of mutually interacting parameters on the LPT boundary layer separation and their physics still requires more research. This research addresses some of the fundamental problems of LPT-research, which have not been treated adequately in the existing literature. The issues, which warrant further investigation, are listed below:

The format of this dissertation follows the style of ASME Journal of Fluids Engineering.

- Quantifying the effects of unsteady wake flow frequency on the onset and the extent of the laminar separation and its turbulent re-attachment along the suction and pressure surfaces of a typical LPT-blade operating at low (cruise), medium, and high (takeoff) Reynolds numbers.
- Quantifying the effects of high turbulence intensity wake core on the extent of the separation zone along the suction and pressure surface, and on the flow field outside the boundary layer.
- Quantifying the boundary layer transition process with laminar separation along the suction and the pressure surfaces of typical LPT blades operating at low, medium and high Reynolds numbers.

To address the above-mentioned topics, a comprehensive experimental study was conducted. A large-scale high subsonic research facility was developed to research the influence of periodic unsteady and highly turbulent flow on turbine aerodynamics. Systematic experimental investigations involved the following tasks:

- varying the unsteady wake frequency parameter in the absence of high turbulence intensity, and Reynods number
- varying turbulence intensity parameter in the absence of unsteadiness, and Reynolds number
- Combining all parameters, namely, the unsteadiness and the turbulence at low, medium and high Reynolds numbers.

Measurements of turbulence distribution along with steady and unsteady boundary layer velocity profiles using hot wire anemometry documents the boundary layer development, separation and re-attachment. Further surface static pressure, surface temperature and heat transfer measurements were performed using pressure sensitive paint (PSP), temperature sensitive paint (TSP) and liquid crystal techniques respectively. This allows for an exhaustive set of data covering all the individual parameters affecting the flow across the LPT blade. The results help to understand better the physics of the flow separation phenomenon on the LPT blades under periodic unsteady wake flow conditions, and inlet turbulence distribution for different Reynolds numbers. The results indicate that

the location of the boundary layer separation was found to be dependent on the Reynolds number and also unsteady wake flow. It was observed that starting point of the flow separation and the re-attachment point moved further downstream with an increase in Reynolds number. Analysis of the experimental results provides insight into the nature of flow across the LPT blades, contributing to the improvement of blade design and overall turbine efficiency. Further, the collected data can be utilized to computationally model the turbulent unsteady flow along the LPT blades and reduce high experimental costs.

2. LITERATURE REVIEW

2.1 Flow Through a Multi-Stage Turbine

In turbomachinery aerodynamics the motion of neighboring blade rows generates the periodic unsteady wakes. Several factors such as wake interaction, endwall region, and secondary losses affect the flow behavior and thus the performance of the turbine blades and turbomachine. Therefore, wake induced unsteady flow has a profound affect upon the overall aerodynamic behavior of blade rows. This unsteady flow influences the individual boundary layer of each blade and is investigated in detail by Arndt [1] where he concluded that there are significant changes in the free stream turbulence levels and wake structures at each row location.

2.2 Boundary Layer Transition in Turbomachinery

Since the state of the boundary layer affects the loss production and the heat transfer characteristics, the turbine designer needs to know the information about the distribution of the laminar and turbulent flow regimes and where the transition starts and ends on the blade surfaces. While the transition to turbulent state has been extensively investigated, transition in highly disturbed environments such as turbomachinery flows are adequately documented. Boundary layer transition from laminar state to the turbulent state is a stochastical, three-dimensional, and unsteady process which occurs in a region where the flow is intermittently laminar and turbulent. In general, there are three significant modes of transition. The first is called “natural” transition, and this mode of transition starts with a weak instability in the laminar boundary layer and proceeds through a various stages of amplified perturbance to fully turbulent flow. Since this transition mode occurs only in low free-stream turbulence environments, it is of little importance in gas turbine flow fields. The second one is called “bypass” transition and is caused by a large disturbances in the external flow that directly produces a turbulent spot in the boundary layer. It has been the general perception that the presence of wakes causes the Tollmien-Schlichting waves to be bypassed (Mayle [2]). Extensive unsteady boundary layer investigations at Texas A&M

University Turbomachinery Performance and Research Laboratory (Schobeiri and Radke [3], Schobeiri et al. [4]) showed that despite the presence of wakes Tollmien-Schlichting waves are present. The third one is called “separated-flow” transition and it occurs in a separated laminar boundary layer. When a laminar boundary layer separates, transition may occur in the free shear layer near the surface and separation bubble length strongly depends on the transition process in the shear layer. This mode of transition occurs in gas turbine engines, particularly in the compressors and low-pressure turbines.

A review of boundary layer development and the periodic unsteady flow studies are presented.

2.3 Periodic Unsteady Boundary Layer Research

One of the major effects of unsteady wake flow is on the boundary layer development and the transition from laminar to turbulent state. Realizing the importance of unsteady flow, there has been an extensive research on unsteady aerodynamics of turbomachines in the past two decades. Initial studies utilized simplified models to simulate the turbomachinery flow conditions. Precise knowledge on how the unsteady flow affects the distribution of the laminar boundary layer development is of great importance for the turbine designer and also to develop better transition correlations for use in computational fluid dynamic codes.

An extensive unsteady boundary layer research program was initiated mid sixties at the Technical University Darmstadt, Germany. Fundamental studies by Pfeil and Pache [5], Pfeil and Herbst [6], Schröder [7] studied and quantified the effect of unsteady wake flow on the boundary layer transition along flat plates. They used squirrel cage type of wake creator, with a series of cylindrical rods, which is connected on two parallel rotating disks. Their studies show that the unsteady wakes generated by the cylindrical rods caused the boundary layer to become turbulent during their impingement on the plate and affect the length of the boundary layer transition region. They also pointed out that, wake-induced transition zones, which propagated downstream of the plate at velocity less than the wake passing velocity.

Orth [8] studied and quantified the effect of unsteady wake flow on the boundary layer transition along a flat plate. First, he observed an early onset of transition when the high turbulence level of the wake disturbs the boundary layer and leads to the formation of turbulent patches. Second, laminar becalmed regions are formed behind the turbulent patches so that brief periods of laminar flow are still observed beyond the location at which the steady flow boundary layer is fully turbulent.

The effects of passing wakes have also been investigated by Dullenkopf et al. [9], Liu and Rodi [10]. Their results showed that an increase in wake passing frequency caused the transition region to shift towards the leading edge for the suction surface. Higher frequencies were noted by all the investigators to significantly enhance the heat transfer on both surfaces due to the increased turbulence intensity. Also, Liu and Rodi [10] carried out the boundary layer and heat transfer measurements on a turbine cascade, which was installed downstream of a squirrel cage type wake generator mentioned previously.

Schobeiri and his co-workers [3], [11], [12], [13] experimentally investigated the effects of the periodic unsteady wake flow and pressure gradient on the boundary layer transition and heat transfer along the concave surface of a constant curvature plate. The measurements were systematically performed under different pressure gradients and unsteady wake frequencies using a squirrel cage type wake generator positioned upstream of the curved plate.

Halstead et al. [14], performed an experimental studies of boundary layer development on the suction surface of the low pressure turbine blade. They found a region of laminar and transitional flow on the suction surface without flow separation. They also showed that becalmed regions generated by the turbulent spots produced in the wake path, were effective in suppressing the flow separation.

Lou and Hourmouziadis [15] investigated the mechanism of separation, transition, and re-attachment, and the effect of oscillating inlet flow conditions on laminar boundary layer separation along a flat plate under a strong negative pressure gradient which was similar to the LPT pressure gradient. This was simulated by contouring the top wall. They studied the Reynolds number effect on the transition region. Their results showed that the higher

Reynolds numbers cause an earlier transition and reduction of the transition length, while the separation point does not change its location. Kaszeta, Simon and Ashpis [16] experimentally investigated the laminar-turbulent transition aspect within a channel with the side walls resembling the suction and pressure surfaces of a LPT blade. Using the top wall contouring as in [15], Volino and Hultgren [17] performed an experimental study and measured the detailed velocity along a flat plate which was subjected to a similar pressure gradient as the suction side of a low pressure turbine blade. They also stated that the location of the boundary layer separation does not strongly depend on the Reynolds number or free-stream turbulence level, as long as the boundary layer remains non-turbulent before separation occurs. Furthermore, they showed that the extent of the transition is strongly dependent on the Reynolds number and turbulence intensity.

Using the surface mounted hot film measurement technique, Fottner and his coworkers [18] and [19] , Schröder [20], and Haueisen, Hennecke, and Schröder [21] documented strong interaction between the wakes and the suction surface separation bubble on the LPT blades, both in wind tunnel cascade tests and in a turbine rig. Furthermore, they investigated the boundary layer transition under the influence of the periodic wakes along the LPT surface and found that the interaction of the wake with the boundary layer greatly affects the loss generation. Shyne et al. [22] performed an experimental study on a simulated low pressure turbine. The experiments were carried out at Reynolds numbers of 100,000 and 250,000 with three levels of free-stream turbulence. They indicated that the transition onset and the length are strongly dependent on the free-stream turbulence. As the free-stream turbulence increases, the onset location and the length of the transition are decreased. Treuren et al. [23] performed an experimental study along a LPT surface at the very low Reynolds number of 25,000 and 50,000 with different free-stream turbulence levels. They showed that a massive separation at the very low Reynolds number of 25,000 is persistent, in spite of an elevated free stream turbulence intensity. However, at the higher Reynolds number of 50,000, there was a strong separation on the suction side for the low free-stream turbulence level. The separation bubble was eliminated for the higher free-stream turbulence level of 8-9%. The investigations by Halstead et al. [14] on a large scale LP

turbine uses surface mounted hot films to acquire detailed information about the quasi-shear stress directly on the blade surface. Investigations by Cardamone et al. [19] and Schröder [21] indicate that the benefit of the wake-boundary layer interaction can be used for the design procedure of modern gas turbine engines with a reduced LPT blade number without altering the stage efficiency.

Most of the studies mentioned above on LP turbine cascade aerodynamics have largely concentrated on the measurement of the signals stemming from hot films mounted on the suction and pressure surfaces of the blades under investigation. Although this technique is qualitatively reflecting the interaction of the unsteady wake with the boundary layer, because of the lack of an appropriate calibration method, it is not capable of quantifying the surface properties such as the wall shear stress. The few boundary layer measurements are not comprehensive enough to provide any conclusive evidence for interpretation of the boundary layer transition and separation processes and their direct impact on profile loss, which is a critical parameter for blade design. Furthermore, the numerical simulation of the unsteady LPT blade aerodynamics using conventional turbulence and transition models fails if it is applied to low Reynolds number cases. Recent work presented by Cardamone et al. [19] shows that in the steady state case at Re= 60,000, the separation is captured, however, for the unsteady case, the separation bubble is not reproduced.

A recent LPT-aerodynamic research at *TPFL* has been focused on stability of the suction surface laminar flow, laminar-turbulent transition, onset and extent of the separation zone and turbulent re-attachment. Particular attention has been paid to kinematics and dynamics of the separation zone and its control and suppression under periodic unsteady condition as is present in a turbine operation environment. Recent comprehensive experimental studies by Schobeiri and Öztürk [24] and [25] investigated the physics of the inception, onset and extent of the separation bubble along a low pressure turbine blade periodic under unsteady inlet flow condition. A detailed experimental study on the behavior of the separation bubble on the suction surface of a highly loaded LPT blade under a periodic unsteady wake flow was presented in [24]. Surface pressure measurements were performed at Re= 50,000, 75,000, 100,000, 125,000. Increasing the Reynolds number has

resulted in no major changes to the surface pressure distribution. They concluded that the unsteady wake flow with its highly turbulent vortical core over the separation region caused a periodic contraction and expansion of the separation bubble. It was proposed that, in conjunction with the pressure gradient and periodic wakes, the temporal gradient of the turbulence fluctuation, or more precisely the fluctuation acceleration $\partial v_{rms}/\partial t$ provides a higher momentum and energy transfer into the boundary layer, energizing the separation bubble and causing it to partially or entirely disappear. They found that for $\partial v_{rms}/\partial t>0$, the separation bubble starts to contract whereas for $\partial v_{rms}/\partial t<0$, it gradually assumes the shape before the contraction. They argued that not only the existence of higher turbulence fluctuations expressed in terms of higher turbulence intensity influences the flow separation, but also its gradient is of crucial importance in suppressing or preventing the onset and the extent of the separation bubble. They stated that the fluctuation gradient is an inherent feature of the incoming periodic wake flow and does not exist in a statistically steady flow that might have a high turbulence intensity. They also stated that, unsteady wake flow with its highly turbulent vortical core over the separation region, caused a periodic contraction and extension of the separation bubble and a reduction of the separation bubble height. Increasing the passing frequency associated with a higher turbulence intensity further reduced the separation bubble height [25]. Continuing the LPT-research, Öztürk and Schobeiri [26] investigated the effect of Reynolds number and periodic unsteady wake flow condition on boundary layer development, separation, and re-attachment along the suction surface of a low pressure turbine blade. They also provided an insight into intermittent behavior of the separated boundary layer along the suction surface of a low pressure turbine blade under periodic unsteady flow conditions [27]. The results of this investigations confirmed the unsteady universal intermittency model developed by Schobeiri and his co-workers [3], [11] , [12] and [13]. The model also was applied to high pressure turbine boundary layer under unsteady flow conditions at a high Reynolds number [28], [29] and its subsequent analysis [30] and [31] verified the universal character of the relative intermittency function. Ongoing LPT research, Öztürk and Schobeiri [32] investigated the effect of turbulence intensity and and periodic unsteady wake flow condition on boundary

layer development, separation, and re-attachment over the separation bubble along the suction surface of a low pressure turbine blade. The objective of their research is (a) to quantify the effect of Tu_{in} on the dynamics of the separation bubble at steady inlet flow condition, and (b) to investigate the combined effects of Tu_{in} and the unsteady wake flow on the behavior of the separation bubble. They found that the periodic unsteady wake flow definitely determines the separation dynamics as long as the level of the time averaged turbulence fluctuations is below the maximum level of the wake fluctuation v_{max}. They stated that increasing the inlet turbulence level above v_{max} caused the wake periodicity totally submerge in turbulence. They also stated that the separation dynamics of the separation bubble is governed by the flow turbulence that is responsible for complete suppression of the separation bubble. One of the striking features of their study reveals is that the separation bubble has not disappeared completely despite the high turbulence intensity and the significant reduction of its size which is reduced to a tiny bubble.

Coton and Arts [33], [34] investigated a high lift LPT blade submitted to passing wakes in two parts. In part 1 of their research, they discussed the blade performance. However in part 2 they investigated the boundary layer transition and its interaction with the incoming wakes. They showed that the beneficial effects of the wakes in suppressing the separation bubble with a loss reduction of 36%.

Opoka et al. [35] presented the results of an experimental study of the interaction between the suction surface boundary layer of a cascade of LP turbine blades and a fluctuating downstream potential field. Their measurements revealed that the magnitudes of the suction surface pressure variations induced by the oscillating downstream pressure field, just downstream of the suction peak, were approximately equal to those measured in earlier studies involving upstream wakes. They showed that the transition on the suction surface responds to the freestream velocity changes driven by the downstream pressure field. They also showed that the oscillatory influence upon the pressure distribution forces the flow to accelerate and decelerate with a period equal to the bar passing period. They concluded that during the decelerating phase, transition was promoted further upstream than in steady flow.

An intensive efforts have been reported by several researchers to control the separation zone using active and passive control procedures. Rivir et al. [36] investigated passive and active control of separation in gas turbines using embedded flow control devices. They used a wide variety of flow control devices including passive surface protrusions (delta wings) and recesses (dimples), MEMs actuators, heated wires, electro-static discharge devices, and vortex generating jets. The pulsed vortex generator jets method, suggested to control or prevent the separation. This method produce no important adverse effects at higher Reynolds number. Recently Bons et al. [37] applied this method to low pressure turbine. He showed that the separation region was almost eliminated and there is a significant reduction in momentum loss downstream of the blade. Vortex generators has been applied to wind turbines. While energizing the boundary layer and preventing the separation at low Reynolds numbers, there is a penalty at high Reynolds number which is considered unacceptable. On the other hand, Lin [38] showed that micro-vortex generators are effective reducing the separation zone with a little drag penalty.

Very recently, Bons et al. [39] successfully used pulsed vortex generators to actively control the flow separation along the suction surface of a Pratt&Whitney PakB"-blade which is a Mach number scaled version of a typical highly loaded LPT blade. The research has been continued by Sondergaard et al. [40] and Bons et al. [41]. The measurement were performed in a rectilinear cascade at steady inlet flow condition. Active and passive control methods reported by Volino [42] used synthetic vortex generator jets for active separation control. Volino performed the experiments in a test section consisting of two PakB-type blade contours that formed the flow passage. Further investigations by Auliffe and Sjolander [43] report an active flow separation control by blowing along the suction surface of Pak-B blade mentioned earlier. Huang et al. [44] and Hultgren and Ashpis [45] employed high voltage electrodes to produce glow discharge plasma in a boundary layer to control separation. Continuing the active control of the flow separation, Bons et al. [46] investigated separated flow transition on an LP turbine blade with pulsed flow control. They concluded that the pulsed jets play a critical role in creating premature transition on the blade, thus bringing momentum into the separation zone and reducing its size dramatically.

While active flow control provides a means for adjusting to change flow conditions, passive flow control holds the advantage of simplicity. Lake et al. [47] suggested to use dimples on the suction surface of a turbine blade to control separation for the low Reynolds number. Their research showed a decrease in loss coefficient at low Reynolds number with an aerodynamic penalty at higher Reynold number.

Volino [48] rectangular bars for passive separation control. Volino found that the optimal bars were not large enough to immediately trip the boundary layer to turbulent, but instead allowed a small separation bubble to form. The bars introduced small disturbances that grew and caused transition and reattachment to move upstream of their location in the uncontrolled case. He defined that the optimal bar height depended on the flow conditions. He concluded that *as* Reynolds number or freestream turbulence is lowered, the separation bubble becomes larger, so a larger bar is needed to produce enough of a disturbance to move transition sufficiently far upstream. He also showed that a flow control device producing too small a disturbance will allow a larger separation bubble than desired, resulting in a thicker boundary layer downstream of reattachment and higher losses. Similarly, too large a disturbance will move transition farther upstream than necessary, resulting in a longer turbulent region and higher losses. Further, Bohl and Volino [49] used a small vertical cylinders with two different heights and a wide range of spacings for the passive separation control. A row of cylinders was placed at the pressure minimum on the suction side of a typical airfoil. They showed that reattachment moved upstream as the cylinder height was increased or the spacing was decreased. They also showed that the cylinders were not as effective for maintaining low losses over a range of Reynolds numbers as the bars.

Zhang and Hodson [50] investigated the combined effects of surface trips and unsteady wakes on the boundary layer development along the suction surface of a different type of LPT-blade (T106C). They reported that the incoming wakes were not strong enough to periodically suppress the large separation bubble on the smooth suction surface of the T106C- blade. Therefore, they argued, that the profile loss is not reduced as much as one might expect. However, they found that the combined effects of the surface trip and

unsteady wakes further reduce the profile losses. Zhang et al. [51] continued the above investigations with the emphasize on separation and transition control on an aft-loaded turbine blade at low Reynolds numbers. Further, Van Treuren et al. [52], Murawski and Vafai [53], Byerlet et al. [54], Sieverding et al. [55] and Vera et al. [56] used various passive devices under LPT conditions to control separation and reduce losses. Most of the investigations conducted using a small trip wire or bar, on the suction surface of a low pressure turbine blade.

Parameters that substantially affect the stability of the suction surface laminar flow, laminar-turbulent transition, onset and extent of the separation zone and turbulent re-attachment can be summarized as unsteady wakes, Re-number, turbulence intensity and surface roughness. Studies in [24] through [27] showed that the impingement of unsteady wakes on separation zone triggers a periodic process of contraction, suppression and recovery of the separation zone. However, it does not completely prevent its generation. This finding was confirmed by the very recent work by Zhang and Hodson [50]. Increasing the Re-number to prevent the generation of separation zones, though effective, is not an option, since in a cruise operation condition the LPT is always subjected to a low-Reynolds number which is responsible for laminar boundary layer separation. As extensively discussed in [24], the dynamic process of contraction and suppression of the separation zone is caused by an intensive exchange of momentum and energy from the main flow outside the boundary layer into the separation zone, thus periodically energizing the boundary layer. Once the wake has passed over the separation zone the bubble begins to recover and the process repeats periodically. This indicates that the combination of wake impingement and higher turbulence intensity may result in a complete suppression of the separation bubbles.

Even though, the published studies helped in better understanding the wake development, unsteady transition and the boundary layer development including the onset and extent of the laminar separation and its turbulent reattachment, they are neither complete to be applicable to turbomachinery flow nor to develop a theoretical framework.

2.4 Intermittent Behavior in Turbomachinery

To better understanding of the transition phenomenon, grasping the multiple effects of mutually interacting parameters on the LPT boundary layer separation and their physics still requires more research To fully understand the basics involving the separation bubble phenomenon, an intermittency analysis has been performed.

Studies by Abu-Ghannam and Shaw [57], Gostelow and Blunden [58], and Dullenkopf and Mayle [59], were conducted to determine the effect of free-stream turbulence and pressure gradient on the spot production rate and the intermittency factor. Significant contributions to steady and unsteady boundary layer research was made by Pfeil and his co-researchers ([60], [61], [62], [7], [8]). Pfeil and Herbst [6], utilizing the squirrel cage-type wake generator and a flat plate, developed a wake-induced transition model that is now generally accepted as correct. They also showed that the boundary layer grew naturally in between the induced transition regions by wakes. Comprehensive investigations on the effect of periodic unsteady flow on a curved plate were performed by Schobeiri and Radke [3], and Schobeiri et al. [11]. They showed that an increase in wake passing frequency as a result of reducing the wake spacing results in changing the wake turbulence structure, and also a shift of transition region towards the leading edge. Experiments for the effect of unsteady wake flow on the boundary layer transition were also conducted by Walker [63], Paxson and Mayle [64], and Orth [8]. Paxson and Mayle investigated the effect of unsteady passing wakes on the laminar boundary layer near the stagnation region. Dullenkopf and Mayle [65] proposed a time averaged transition model. Few of these researchers have addressed the effect of wake frequency and the structure on the boundary layer transition.

The transition process was investigated by Emmons [66] through the turbulent spot production theory. This theory was later promoted by Dhawan and Narasimha [67], who found the intermittency factor for natural transition. Unlike the steady boundary layer transition case, the calculation of intermittency function under the unsteady flow situation exhibits a difficult task because of the free-stream turbulence distribution, which is periodically changing from almost non-turbulent to high turbulent intensity values. The process of turbulent/non-turbulent decisions from the instantaneous signals measured under

these unsteady conditions is reviewed by Hedley and Keffer [68]. They proposed derivatives of velocity signals as the detector function to identify the turbulent and non-turbulent parts in the signals. This method was also used by Antonia and Bradshaw [69], Kovasznay, et al. [70], and Bradshaw and Murlis [71]. Mayle and Paxson [64] and Mayle [2] used a similar method for unsteady flows.

Developing an unsteady transition model is essential to accurately predict the unsteady boundary layer characteristics such as skin friction and heat transfer coefficients. With an appropriate transition model, it is possible to numerically solve the boundary layer equations using different methods such as those proposed by Launder and Spalding [72], Crawford and Kays [73], and Schmidt and Patankar [74]. Implementing such a model in an unsteady Navier-Stokes code enables reliably predicting the turbomachinery profile loss coefficients and thus, the efficiency.

Based on the fundamental investigations of the velocity and the turbulence structure of the impinging wakes and their interaction with the boundary layer, Chakka and Schobeiri [13] developed an intermittency based unsteady boundary layer transition model. The analysis revealed a universal pattern for the relative intermittency function for all the frequencies and pressure gradients investigated. However, the above investigations were not sufficient to draw any conclusion with regard to an eventual universal character of the relative intermittency function. Further detailed investigations of the unsteady boundary layer on a high Reynolds number turbine cascade by Schobeiri et al. [28], [29] and its subsequent analysis [30] and [31] verified the universal character of the relative intermittency function.

The current investigation attempts to extend the intermittency unsteady boundary layer transition model developed by Schobeiri and his coworkers ([13], [30], [31]) to the LPT cases, where a massive separation occurs on the suction surface at a low Reynolds number at the design and off-design points. Furthermore, the experimental results are intended to serve as benchmark data for a comparison with numerical computation using DNS or RANS-codes.

2.5. Cascade Blade Heat Transfer Research

2.5.1 LPT Heat Transfer Research

LPT-aerodynamics and heat transfer aspects of separated flow along the pressure was treated in [75]. Here as in [76], the separation was triggered by varying the incidence angle that caused moderate to massive separation zones on the pressure surface of a highly loaded LPT-blade T106-300. The research provides a detailed velocity, heat transfer, and pressure measurement along the pressure surface. Another interesting study that incorporates both, the aerodynamics and film cooling aspects of a separated flow along a flat plate is presented in [77]. Unlike the periodic unsteady wake flow that is inherent to turbomachinery aerodynamics, the periodic unsteady flow in [75] is established by a rotating valve that provides a periodic mass flow along the surface. The LPT-pressure distribution is emulated by contouring the upper channel wall.

Butler et al. [78] studied the effect of turbulence intensity and length scale on LPT blade aerodynamics. Heat transfer distribution on a Langston turbine blade shape was measured in a linear cascade for free-stream turbulence intensity levels of 0.8% and 10% for Reynolds numbers of 40-80k. They used uniform heat flux (UHF) liquid crystal technique for the heat transfer measurement. They observed that as the turbulence increased, stagnation heat transfer increased and the location of the suction side boundary layer transition moved upstream toward the blade leading edge. They also observed that, for this turbine blade shape of transition location did not depend on turbulence length scale, the location is more dependent on pressure distribution, Reynolds numbers and turbulence intensity levels. They also observed separation for all of the low turbulence cases while transition locations corresponded to local minimums in heat transfer. Reattachment points did not correspond to local maximums in heat transfer, however, the heat transfer coefficient continued to rise downstream of the reattachment point.

Choi et al. [79] investigated the effect of free-stream turbulence on heat transfer and pressure coefficient distributions of a turbine blade in low Reynolds number flows. This study documented the effect of increasing Reynolds number and free-stream turbulence in suppressing separation, promoting boundary layer transition, and enhancing heat transfer

on blade surfaces. They observed that flow separation in the leading edge region of the blade is enhanced by decreasing Reynolds number but suppressed as the turbulence intensity increases. They showed that local Nusselt number increases with increasing Reynolds number and increasing turbulence intensity. They also showed that the local Nusselt number in the separation region near the leading edge decreases with decreasing Reynolds number, but increases as the turbulence intensity increases. Finally, they concluded that increasing Reynolds number and turbulence intensity tend to promote boundary layer transition and enhance local heat transfer coefficient.

Cotton and Arts [33] investigated a high lift LPT blade submitted to passing wakes in two parts. In part 1 of their research, they discussed in details the profile losses and heat transfer. They showed that increasing the Reynolds number and turbulence intensity promote the transition and the bubble reattachment. They also confirmed their results with heat transfer coefficient distributions. They also showed that the change of dominant mode of transition, from separation to bypass, with the upstream shift of the transition onset when Reynolds numbers and inlet free-stream turbulence intensity levels are increased.

Further intensive literature search and the subsequent communications with heat transfer experts [80] and [81] did not result in finding more papers that cover this topic.

2.5.2 HPT Heat Transfer Research

HPT-heat transfer aspects of gas turbine blades are reported in many papers. Detailed heat transfer measurements along the surfaces of a HPT-blade under periodic unsteady wake flow condition, Reynolds numbers and free-stream turbulence levels is reported in many studies, where the experiments were focused on obtaining the surface heat transfer information and pressure distribution without unsteady boundary layer measurements.

Effects of Unsteady Wake Flow Conditions on Heat Transfer Experiments: There have been many studies that analyze the effects of unsteady wakes by the upstream blade row on the surface heat transfer coefficients of the downstream blade row. Wake simulation experiments typically used either a rotating spoked-wheel wake generator or a rotating squirrel wake generator.

Dullenkopf et al. [9] conducted time-averaged heat transfer measurements using spoked-wheel wake generator. They used an oil fired combustion chamber for simulating high temperature fluid flow through the turbomachine. Experimentally evaluated mean heat transfer coefficients obtained under different unsteady initial conditions are reported. The results show the strong effect of unsteady wakes to the suction side boundary layer and heat transfer. Temporary laminar and turbulent conditions in the boundary layer lead to an elongated transitional zone where the wake frequency is a dominant factor for the mean heat transfer.

Liu and Rodi [10] conducted a detailed experimental study on the wake-induced unsteady flow and heat transfer in a linear turbine cascade. The unsteady wakes with passing frequencies in the range zero to 240 Hz were generated by moving cylinders on a squirrel cage device to see its effect on the surface heat transfer coefficients. Their investigations showed that the boundary layer remained laminar on the pressure side of the turbine blade under all the wake flow conditions and in the case of suction surface the boundary layer was observed to be laminar under steady flow conditions. Under unsteady flow conditions on the suction surface the boundary layer was transitional and the boundary layer transition was seen to start earlier as the wake frequency is increased.

Han et al. [82] studied the effects of wake Strouhal number and concluded that both Reynolds number and Strouhal number are important for calculation of unsteady flow heat transfer coefficients. They studied the effect of rod speed, rod number, rod diameter and mainstream velocity on the blade heat transfer coefficient distribution. Their studies showed that the unsteady passing wake promotes earlier and broader boundary layer transition and causes much higher heat transfer coefficients on the suction surface, whereas the passing wake also significantly enhances heat transfer coefficients on the pressure surface.

Schobeiri and Chakka [31] investigated experimentally and theoretically the effects of periodic unsteady flow on heat transfer and aerodynamic characteristics, particularly on the boundary layer transition along the suction and pressure surfaces of a typical gas turbine blade. Comprehensive aerodynamic and heat transfer experimental data were collected for different unsteady passing frequencies that are typical of gas turbines. They developed a

new unsteady boundary layer transition model to predict the effect of the impinging periodic unsteady wake flow on the heat transfer and the aerodynamics of turbine blades. They also observed the enhancement of the heat transfer coefficient with increase in the passing wake frequency. The transition point moved toward the leasing edge as wake frequency increased. However, there is no apparent transition phenomena occurring on the pressure surface of the turbine blade, which is also evident from the aerodynamic measurements presented in the paper.

While above investigators collected time-averaged heat transfer coefficients, some investigators (Dunn et al. [83], Doorly [84], [85] and Abhari et al. [86]) used fast response sensors and collected real time variation on the blade surface heat transfer data under unsteady wake flow conditions. Doorly et. al measured large unsteady increases in the surface heat flux at the wake cutting frequency and traced the propagation and growth of turbulent regions along the suction surface. All these investigations showed that increasing the wake frequency causes increased stagnation region heat transfer and an early laminar-turbulent boundary layer transition.

Mayle and Dullenkopf [87] developed their model based on Emmons [66] original idea of natural transition where he considered the propagation and growth of turbulent spots along a surface within a laminar boundary layer. Assuming the turbulent spots produced normally or wake induced are independent of each other, Mayle and Dullenkopf defined the time-averaged intermittency factor. They showed that the time-averaged heat transfer distribution on the airfoil surface can be obtained from the predicted time-averaged intermittency factor. They also compared the theory with the measurement of the time-averaged heat transfer coefficient on the suction surface of a turbine blade in a spoked wheel generated wake flow condition.

Effects of Free-Stream Turbulence Intensity on Heat Transfer Experiments: There have been many studies that analyze the effects of free-stream turbulence intensity on gas turbine airfoils. Brown and Burton [88] and Brown and Martin [89], [90] investigated the effects of free-stream turbulence intensity on local heat transfer for a range of Reynolds numbers. Brown and Burton concluded that increasing the free-stream turbulence intensity increases

the local heat transfer in the laminar boundary layer regions. They also showed that the position of start of transition from laminar to turbulent boundary layer is affected by turbulence intensity, velocity distribution, and Reynolds number. Brown and Martin reported that at gas turbine conditions, the scale and frequency of free-stream turbulence may be as important as its intensity in determining local heat transfer coefficients around the blade.

Blair [91] investigated the influence of free-stream turbulence on boundary layer transition on a heated wall with a favorable pressure gradients. Their results showed a forward movement of transition with increasing turbulence levels. Blair [92], [93] conducted an experimental research program to determine the influence of free-stream turbulence on zero pressure gradient. He showed that for fully turbulent boundary layer flow, both the skin friction and heat transfer increased substantially for the higher levels of free-stream of turbulence. Simonich and Bradshaw [94] and Hancock and Bradshaw [95] reported similar results.

Simon et. al. [96], [97] studied hydrodynamic and thermal development of flat plate and convex-curved surfaces respectively on boundary layers undergoing natural transition. They observed that increased turbulence intensity decreases the transition onset Reynolds number and the length of transition. Cases with both curvature and higher free-stream turbulence intensity showed a pronounced dominance of the latter. They also concluded that free-stream turbulence effects dominate, but the curvature effect is still observable in the flow. Further, Kestoras and Simon [98] conducted experiments in the turbulent boundary layer over a concave wall under different free-stream turbulence intensity levels. Their results showed that turbulent intensities in the outer region of the boundary layer increase profoundly above values found in the flat plate boundary layer residing in low free-stream intensity level. They also showed that Stanton numbers showed very little increase on the upstream part of the concave wall when turbulence intensity is elevated. On the latter part of the concave wall, however, Stanton numbers rise 5% over values in low-turbulence concave-curved case.

Dullenkopf and Mayle [59] investigated the effect of free-stream turbulence length scale on laminar heat transfer. First, they re-examined the effect of free-stream turbulence in terms of the Nusselt number and turbulence parameter which correctly account for the free-stream acceleration. They also obtained a correlation for both turbulence level and length scale. Their results indicated that the heat transfer for these flows is linearly dependent on the "effective" free-stream turbulence intensity.

Zhang and Han [99] studied the influence of mainstream turbulence on surface heat transfer coefficients of a gas turbine blade. A five-blade linear cascade in a low-speed wind tunnel facility was used in the experiments. The mainstream Reynolds numbers were 100,000, 200,000, and 300,000 based on the cascade inlet velocity and blade chord length. The grid-generated turbulence intensities at the cascade inlet were varied between 2.8 and 17 percent. Their results showed that the mainstream turbulence promotes earlier and broader boundary layer transition, causes higher heat transfer coefficients on the suction surface, and significantly enhances the heat transfer coefficient on the pressure surface. They also concluded that the heat transfer coefficient augmentations and peak values on the suction and pressure surfaces are affected by the mainstream turbulence and Reynolds number.

Combined Effects of Free-Stream Turbulence on Heat Transfer Experiments: Zhang and Han [82], [99] individually studied the effects of unsteady wakes flow conditions generated using the spoke-wheel wake generator and free-stream turbulence intensity respectively. Then, Zhang and Han [100] combined both unsteady wake effects and free-stream turbulence effects and compared that to the primary effects. They indicated that the upstream wake-shedding frequency does not have any effect when free-stream is highly turbulent.

Dullenkopf and Mayle [101] investigated the effects of free-stream turbulence and moving wakes on augmenting heat transfer in accelerating laminar boundary layers. First, the effect of free-stream turbulence is re-examined in terms of the Nusselt number and turbulence parameter which correctly account for the free-stream acceleration. They also obtained a correlation for both cylinders in cross flow and airfoils with regions of constant

acceleration. This correlation is then used in a simple quasi-steady model to predict the effect of periodically passing wakes on airfoil laminar heat transfer. A comparison of the predictions with measurements showed good agreement.

2.6. PSP and TSP Research in Turbomachinery

While the phenomenon of the unsteady boundary layer development and transition with or without the separation bubbles has been the subject of intensive research, that has led to better understanding the transition phenomenon, comprehending the multiple effects of mutually interacting parameters on the LPT boundary layer separation. All the previous investigations were carried out using the hot wire probes, surface mounted hot films, thermocouples and surface static pressure taps. However, to the knowledge of the researcher, there is no investigation reported in the literature that has taken a close look not only at the flow separation, pressure and temperature distributions, but also the Nusselt number distributions associated with flow separation in turbine blade cascade at low Reynolds number conditions using PSP and TPS measurement techniques. However, film cooling effectiveness measurements on the turbine cascade or wind tunnel model pressure distribution measurements have already been carried out immensely using PSP and TSP measurement techniques.

Measurements using PSP [102] and TSP have been demonstrated in several challenging flow fields such as on the suction surface of an advanced compressor blade [103] and an aircraft wing [104] in flight. The advantages of PSP and TSP include non-intrusive pressure and temperature measurements and high spatial resolution when compared to conventional measurement techniques.

3. OBJECTIVES

The objective of this study is to investigate the individual and combined effects of Reynolds number, periodic unsteady flow and free-stream turbulence intensity (FSTI) on aerodynamics of a highly loaded turbine blade. Detailed boundary layer measurements are performed along the suction and pressure surface of a highly loaded turbine blade with a separation zone. Measurements were performed in a single row cascade representative of LP turbine designs. A large-scale, high subsonic research facility has been used for the investigation. The wake passing frequency is varied from 0 to 120 Hz to simulate various turbomachinery-operating conditions.

3.1 Experimental Study

Careful documentation was made of (1) the development of the boundary layer which approaches the separated flow region, (2) the free shear layer over the separation region and (3) the reattached flow downstream of the separation bubble. Particular attention is paid to the aerodynamic of the separation zone at different Reynolds numbers and FSTIs at steady and periodic unsteady flow condition. Systematic experimental investigations involve the following tasks: (a) Variation of the unsteady wake frequency parameter in the absence of high turbulence intensity and Reynolds number, (b) Variation of Reynolds number and turbulence intensity parameter in the absence of unsteadiness, and (c) Combination of all parameters, namely, the Reynolds number, the unsteadiness and the turbulence.

Detailed steady and unsteady boundary layer velocity, turbulence intensity, static pressure and heat transfer measurements have been performed along the suction and pressure surface of the LPT blade. A single hot wire probe has been used for the velocity measurements.

In addition to unsteady boundary layer measurements, blade surface measurements are investigated at Re=110,000, 150,000, and 250,000 with a free-stream turbulence intensities of 1.9%, 3.0%, 8.0%,13.0%. For each Reynolds number and turbulence intensity level, surface pressure and heat transfer measurements are carried out at one steady and two

different unsteady inlet conditions. Surface static pressure, surface temperature and heat transfer measurements were performed using static pressure blade, temperature sensitive paint (TSP) and liquid crystal techniques respectively. In addition, surface mounted hot-film measurements were performed at Re=110,000 with a turbulence intensity level of 1.9% at one steady and two different unsteady inlet conditions. Surface mounted hot-films provided detailed aerodynamic information along the suction surface of the LPT blade. This allows for an exhaustive set of data covering all the individual parameters affecting the flow across the LPT blade. The results help to understand better the physics of the flow separation phenomenon on the LPT blades under periodic unsteady wake flow conditions, and inlet turbulence distribution for different Reynolds numbers.

3.2 Data Analysis

The aerodynamic experimental data collected have been analyzed for intermittency calculations. For intermittency calculations, the square of the second order derivative of the random instantaneous velocity from hot-wire measurements is used as the criterion function and the results, after applying threshold level, are time-averaged for steady case and ensemble-averaged for unsteady flow conditions. The boundary layer behavior under unsteady flow conditions has been explained in detail through the presentation of intermittency. Based on the wake theory of Schobeiri et al [11], the distribution of intermittency inside the wake region is analyzed through introduction of relative intermittency factor. The effect of wake frequency on ensemble-averaged intermittency factor at the wake core and outside the wake core are analyzed.

The current investigation attempts to extend the intermittency unsteady boundary layer transition model developed by Schobeiri and his coworkers ([13], [30], [31]) to the LPT cases, where a massive separation occurs on the suction surface at a low Reynolds number at the design and off-design points. Furthermore, the experimental results are intended to serve as benchmark data for a comparison with numerical computation using DNS or RANS-codes.

4. EXPERIMENTAL TEST FACILITY

In order to perform a detailed investigations on two-dimensional periodic unsteady wake aerodynamics, a large scale, high-subsonic research facility has been used. The facility in its original configuration, shown in Figure 4.1, is described by Schobeiri et al. [4] and [29]. The unique capability of this facility lies in its capability to sequentially generate up to four different unsteady inlet flow conditions that lead to four different unsteady wake structures, passing frequencies, and free-stream turbulence intensities. A detailed description of various components of the test facility is given below.

4.1 Air Supplier

Air, with a maximum volumetric flow rate of 15 m^3, is supplied from a large centrifugal fan, which is driven by 93 kW (125 hp), 3-phase AC electric motor running at a rated speed of 1760 rpm, which is reduced to the fan speed of 1035 rpm by a belt-pulley transmission. The fan is capable of generating a maximum mean velocity of 100 m/s at the test section inlet. It corresponds to a Mach number of M=0.6 for a turbine cascade with an acceleration ratio of $V_2/V_1=2$. Variation of inlet velocity and hence Reynolds number can be obtained by changing the fan speed or by operating a throttle located at the fan exit. For the present investigation, the throttle is adjusted to give a maximum Reynolds number 110,000 at the inlet of the test section. To protect the hot-wire system, a fiber-glass filter with a thickness of 50 mm and a pore size of 5μm is attached at the inlet of the fan.

Since the fan exit has a higher elevation than the test facility, a set of transition ducts followed by a straight pipe with a diameter of 600 mm are used for the smooth channeling of the flow from the fan exit to the diffuser inlet. A hot wire probe is located at the inlet of the diffuser to get the variations in the mean velocity resulting from the voltage difference, fluctuations of the fan speed, or change of environmental temperature and pressure.

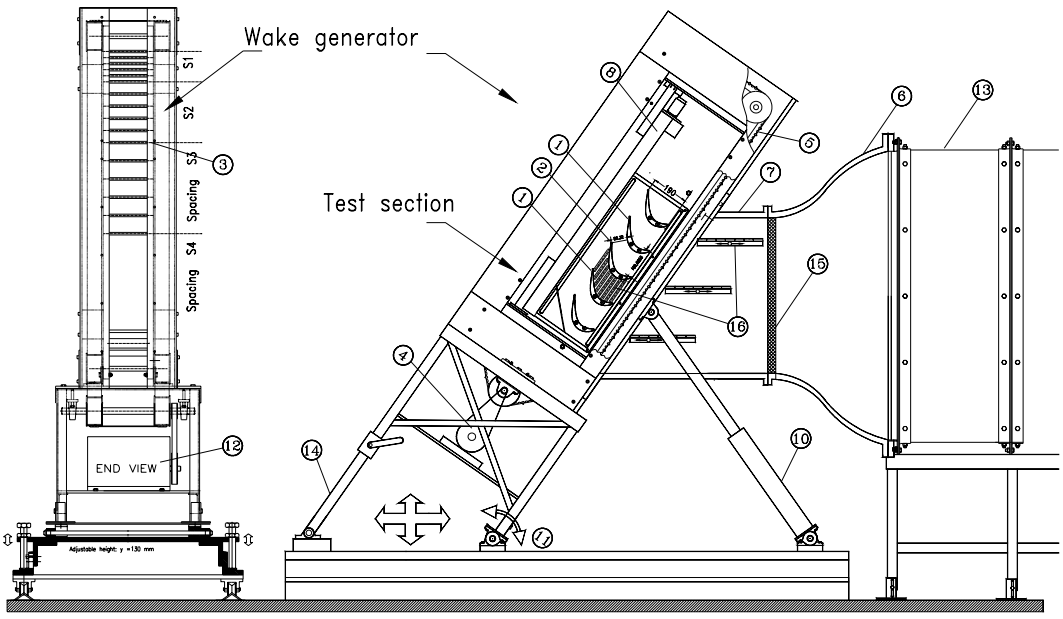

① Static pressure blade
② Blade with hot film sensors
③ Wake generating rods
④ Wake generator
⑤ Timing belts. rod attachments
⑥ Transition duct
⑦ Straight duct
⑧ Traversing system
⑨ Inlet nozzle
⑩ Hydraulic cylinders
⑪ Pivot point
⑫ Wake generator e-motor
⑬ Large silence chamber with honeycom and five screens
⑭ Telescope supprt
⑮ Honeycomb flow straightener
⑯ Traversing slots

Figure 4.1. Turbine cascade research facility with the components and the adjustable test section

4.2 Diffuser, Settling Chamber, and Nozzle Assembly

A diffuser of length 1500 mm and an area ratio of 1:4.75 is located downstream of the straight pipe that connects the diffuser with the fan. The diffuser decelerates the flow before entering the settling chamber. The settling chamber is made of four sections each of length 900 mm and cross section 1500mm×900mm. Five screens and one honeycomb flow straightener are used in the settling chamber to control the flow uniformity and turbulence intensity level. The screens are made of stainless steel and have different mesh sizes and wire diameters. The first screen is placed at the diffuser exit to reduce the scale of vortices generated by the diffuser vanes. The honeycomb flow straightener with a cell size of 6 mm is placed between the first two settling chamber. The second screen is located directly downstream of the honeycomb. The honeycomb and screen combination results in a much lower turbulence intensity than a honeycomb alone because the large eddies exiting from

the honeycomb cells are broken into smaller eddies. The other screens are placed downstream of the second, third and fourth sections of the settling chamber. The nozzle is located downstream of the settling chamber with an area ratio of 6.75:1. The flow accelerates before entering the wake generator and the nozzle provides a smooth transition of flow from the settling chamber to the wake generator. A straight channel transition piece is attached to the nozzle to accommodate the test section inclination.

4.3 Periodic Unsteady Inlet Wake Flow Generator

Two-dimensional periodic unsteady inlet wake flow is simulated by the translational motion of the wake generator shown in Figure 4.2. A series of cylindrical rods are attached on both side of the timing belt driven by an electric motor. The timing belts with a length of 4.96 m span over 5 shaft-pulleys arranged around the cascade test section. The drive pulleys also control the belt tension. The use of cylinder to simulate rotor blade wake is appropriate, as shown in several studies, since the turbulence characteristics of cylinder wake flows, in terms of Reynolds stress components, are similar to those of rotor blade wakes. To simulate the wake width and spacing that stem from the trailing edge of rotor blades, the diameter and number of rods can be varied. The rod diameter can be varied from 2-10 mm. For the present investigation, a constant rod diameter of D_R=2 mm is used. The rod spacing, $S_{R,}$ can be changed by attaching or detaching the rods to or from the belts. The wake flow generator system is driven by an electric motor with a maximum power of 7.5 kW (10hp) and a maximum rotational speed of 1745 rpm. The controller allows the belt translational speed up to 25 m/s. For the present investigation, a belt speed of U=5 m/s is chosen. And also, a fiber optic system is used to monitor the wake passing frequency and it also serves as a trigger for the data acquisition.

4.4 Sequential Generation of Unsteady Wakes

With the special design of the test facility, it is possible to measure the velocities for different wake passing frequencies in one data set, when performing the boundary layer experiments. The wake passing frequency can be varied by changing the speed of the belt

or the spacing of the rods on the belt, S_R, shown in the Figure 4.2. For the present study, the belt is subdivided into three different clusters of the same length. The first one with the spacing $S_R=\infty$, which is steady flow case with no rods. The second and the third part have the rod spacing of S_R=160mm and 80 mm respectively. Within each cluster the rods have the same spacings. The clusters are all arranged with a certain distance from each other. By using the triggering system, a continuous data set is acquired and the buffer zones between the data clusters are visible. The data analysis program is able to cut the buffer zone and evaluates the data for each cluster. Comprehensive preliminary measurements were carried out to make sure that the data were exactly identical to those, when the entire belt length was attached with rods of constant spacing, which corresponded to each individual cluster spacing. In order to account for the unsteadiness caused by the frequency of each individual wake generating cluster and its spacing, the flow velocity and the cascade parameters the

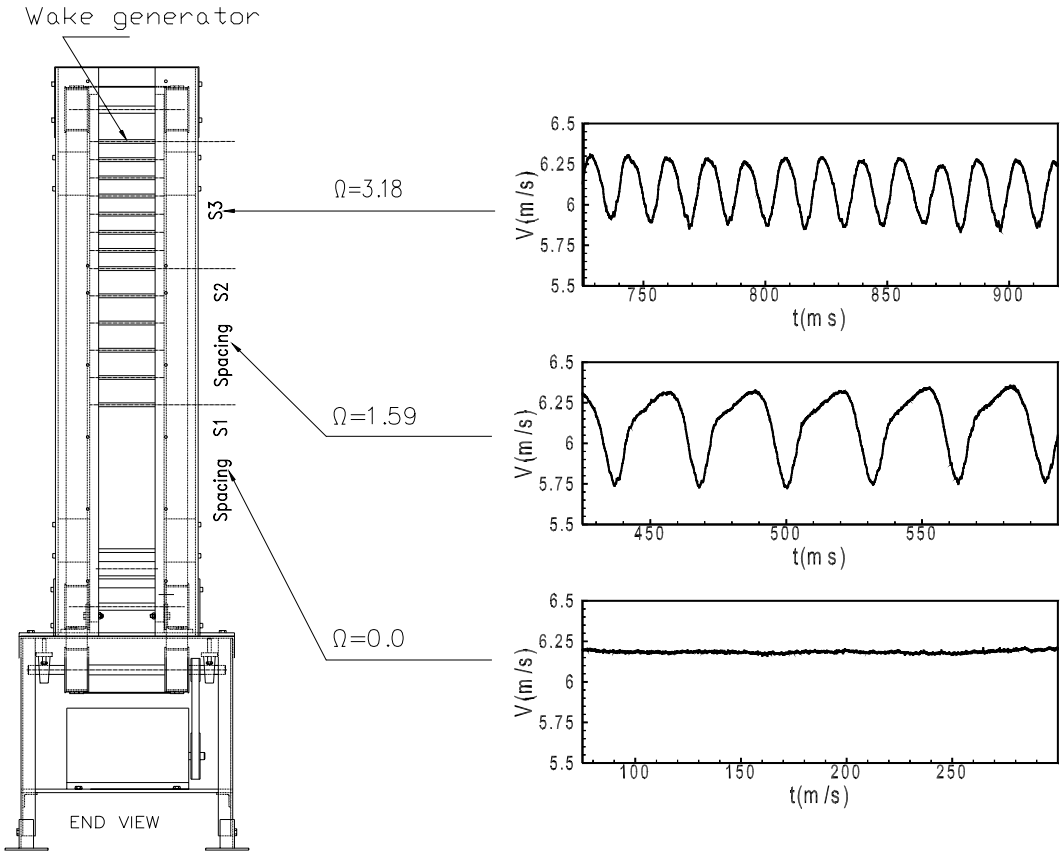

Figure 4.2 Wake generator

unsteady flow parameter Ω is defined:

$$\Omega = \frac{c}{S_R}\frac{U}{V_{ax}} = \frac{\sigma}{\varphi}\frac{S_B}{S_R} \tag{4.1}$$

Table 4.1. Parameters of turbine cascade test section

Parameters	Values	Parameters	Values
Inlet velocity	V_{in} = 4 m/s	Inlet turbulence intensity	Tu_{in} = 1.9 %
Rod translational speed	U = 5.0 m/s	Blade Re-number	Re = 110,000
Nozzle width	W = 200.0 mm	Blade height	h_B = 200 mm
Blade chord	c = 203.44 mm	Cascade solidity	σ = 1.248
Blade axial chord	c_{ax} = 182.85mm	Zweifel coefficient	ψ_A = 1.254
Blade suction surface length	L_{SS} = 270.32 mm	Cascade angle	φ = 55°
Cascade flow coefficient	Φ = 0.80	Cascade spacing	S_B = 163 mm
Inlet air angle to the cascade	α_1 = 0°	Exit air angle from the cascade	α_2 = 90°
Rod diameter	D_R = 2.0 mm	Rod distance to lead. edge	L_R = 122 mm
Cluster 1 (no rod, steady)	S_R = ∞ mm	Ω - parameter steady case	Ω = 0.0
Cluster 2 rod spacing	S_R = 160.0 mm	Ω - parameter for cluster 1	Ω = 1.59
Cluster 3 rod spacing	S_R = 80.0 mm	Ω - parameter for cluster 2	Ω = 3.18
Turbulence grid TG1	GT = 6.35 mm	Grid Opening GO = 77 %	Tuin = 3.0%
Turbulence grid TG2	GT = 9.52 mm	Grid Opening GO = 55 %	Tuin = 8.0%
Turbulence grid TG3	GT = 12.7 mm	Grid Opening GO = 18 %	Tuin = 13.0%
Length scale at Tu_{in} = 1.9 %	$\Lambda_{u,x}$ = 41.3 mm	Length scale at Tu_{in} = 3 %	$\Lambda_{u,x}$ = 32.5 mm
Length scale at Tu_{in} = 8 %	$\Lambda_{u,x}$ = 30.1 mm	Length scale at Tu_{in} = 13 %	$\Lambda_{u,x}$ = 23.4 mm
Grid distance from L.E.	$G_{T.E.}$ = 160 mm	Tu measurements from L.E.	$S_{T.E.}$=30 mm

Many researchers have used Strouhal number as an unsteady flow parameter which includes the wake generator speed and the inlet flow velocity. However the unsteady flow parameter which is defined above and includes the cascade solidity, the flow coefficient,

the blade spacing and the rod spacing, is an extension of Strouhal number in the sense that it additionally includes the rod spacing S_B and blade spacing S_R. The individual cluster configurations with the corresponding Ω parameter are specified in Table 4.1.

4.5 Cascade Test Section

The cascade test section shown in Figure 4.3 is located downstream of the wake generator and it has an inlet cross section of 1000 mm×200 mm. The test section can incorporate to 5 blades with a blade height of 200 mm and a chord of 203.44 mm. For boundary layer investigations, five identical blades designed by Pratt&Whitley were implemented whose cascade geometry is given in Table 4.1. The blade resembles the essential feature such as the laminar boundary layer separation that is inherent to typical LPT-blades. This blade number is necessary and sufficient to secure a spatial periodicity for the cascade flow. It also consists of two plexiglas side walls. One of the side walls includes inlet, exit traversing slots and the slots for the boundary layer measurements which are placed between the second and the third blade from the bottom as shown in Figure 4.1 item 16.

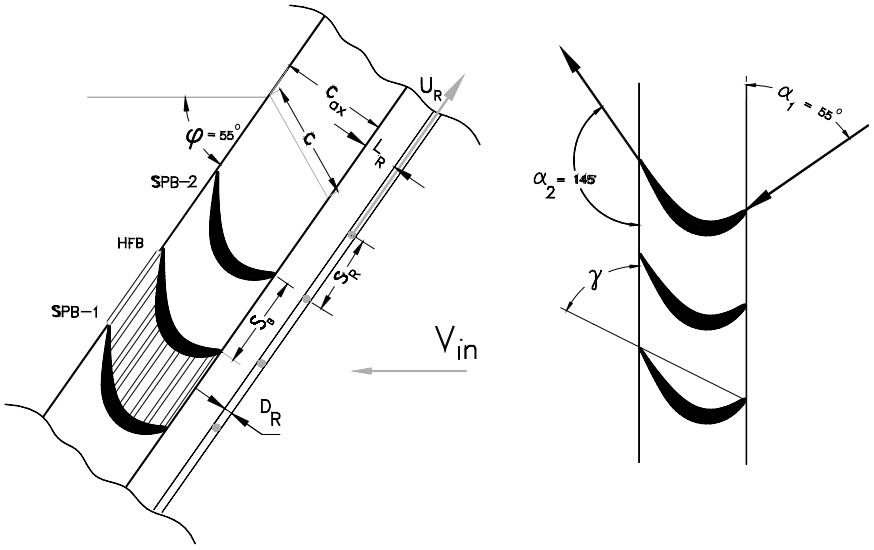

Figure 4.3. Cascade geometry with flow, and stagger angle

4.6 Turbulence Grids

Three different turbulence grids were manufactured for producing inlet turbulence intensities of 3.0%, 8.0%, and 13.0%. The grids consist of square shaped aluminum rods with the thickness G_T and opening G_O given in Table 4.1. The Turbulence intensity values were measured at the cascade inlet with the location from the cascade leading edge listed in Table 4.1. The grids were subsequently installed upstream of the wake generator with the distance form cascade leading edge G_{LE} defined in Table 4.1.

4.7 Hydraulic Platform

To account for a high flow deflection of LPT-cascade, the entire wake generator and test section unit including the traversing system was modified to allow a precise angle adjustment of the cascade relative to the incoming flow. This is done by a hydraulic platform, which simultaneously lifts and rotates the wake generator and test section unit. The unit is then attached to the tunnel exit nozzle with an angular accuracy better than 0.05^{o}, which is measured electronically.

4.8 Inlet and Exit Flow Traversing System

A computer controlled traversing system is used to measure velocities and turbulence intensities at the inlet and exit of the cascade test section. The traversing system is mounted vertically on one of the plexiglas side walls. It consists of a power screw with a maximum traversing length of 1200 mm which is connected to a stepper motor to provide the drive. It receives a signal from the LABVIEW program and turns the power screw by an exact number of pulses required. An optical encoder with 400 radial slots connected to the stepper motor provides a feedback to the stepper motor for accurate movement along the traversing system and the traversing system is capable to move in a small steps of 2.5 μm. The traversing system also includes a switch to prevent the probes movements beyond the desired limit.

4.9 Probe Traversing System

A computer controlled traversing system is used to measure the inlet velocities and turbulence intensities, as well as the boundary layers on suction and pressure surfaces. The traversing system as shown in Figure 4.4, was modified to allow the probe to reach all streamwise positions along the suction and pressure surfaces. The three axis traversing system is vertically mounted on the plexiglass side wall. Each axis is connected to a DC-stepper motor with an encoder and decoder. The optical encoder provides a continuous feedback to the stepper motor for accurate positioning of the probes. The system is capable of traversing along the suction and pressure surfaces in small steps up to 1 μm, and the third axis is capable of rotating with an angular accuracy less then 0.05°, which is specifically required for boundary layer investigations where the measurement of the laminar sublayer is of particular interest.

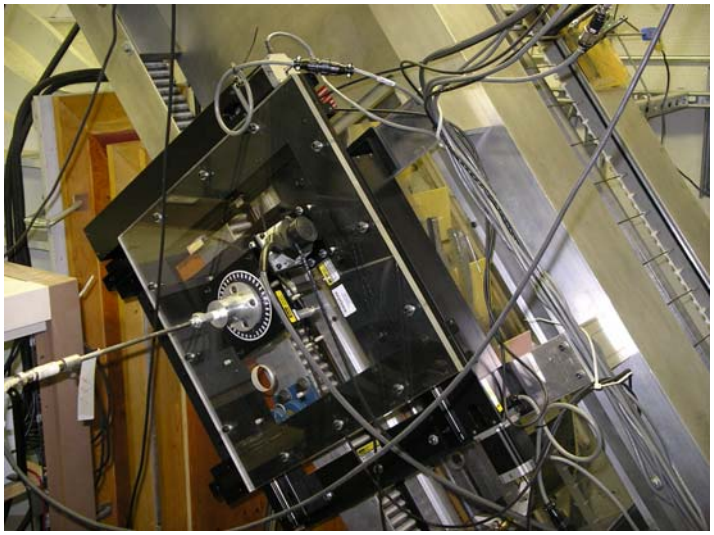

Figure 4.4. Turbine cascade research facility with 3-axis traversing system

5. INSTRUMENTATION AND DATA ACQUISITION

The test facility is instrumented for fully automated digital data acquisition. The details about the instrumentation and data acquisition procedure follow in the next sections.

5.1 Instrumentation of the Test Facility

The schematic layout of the test facility instrumentation is shown in Figure 5.1. For the aerodynamic investigations, the data acquisition and reduction system is controlled by a computer. For the data acquisition and analysis, a 16 channel 12-bit analog-digital (A/D) board (NI PCI-MIO 16-E1) is installed in the computer. The outputs from instruments are connected to the channels of the NI extension board from where the data are sampled by the computer. The NI board also has a separate DAC channel through which an analog voltage can be sent out. This DAC channel is used to control and acquire data from a 48-port scanivalve system for the static pressure measurement.

Mean velocities and turbulent fluctuations are obtained using a 3-channel (TSI, IFA-100), constant temperature hot-wire anemometer system. The system has signal conditioner with an adjustable low pass filter, DC-offset, and adjustable gain. The offset and the gain can be adjusted to get the maximum resolution and signal noise ratio. The low pass filter of the signal conditioner has been set to the half of the sampling frequency of 20 kHz to avoid the aliasing effects. The hot wire is operated at 1.8 overheat ratio and 250° C sensor operating temperature. All the hot wire sensors used are made of tungsten with a diameter of 4 μm. The first channel of the first anemometer is connected to a single hot-film probe for measuring the time-dependent velocity distributions within the blade channel. The second channel is used for calibration of the single hot-wire probe connected the second channel of the Ni extension board.

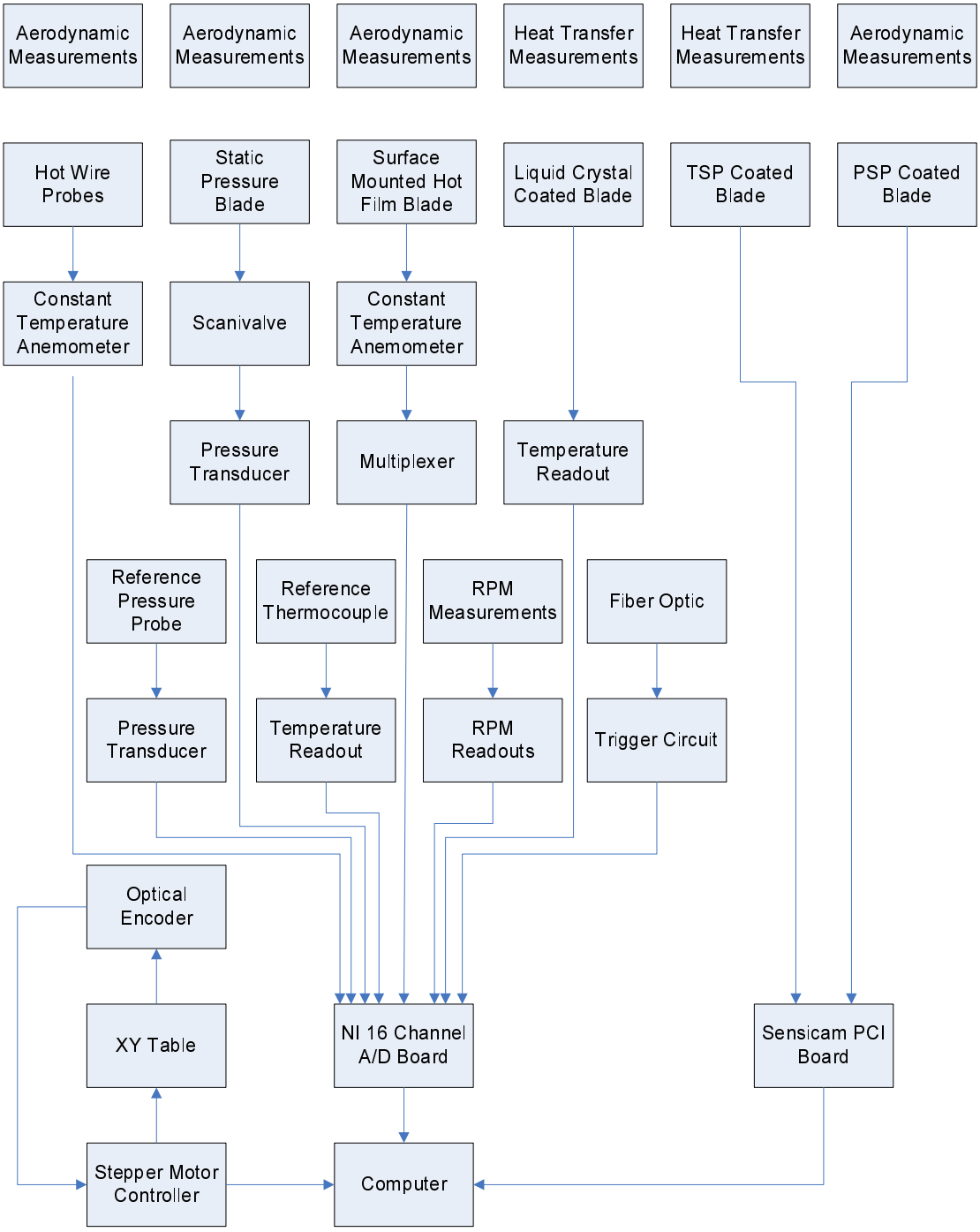

Figure 5.1. Schematic layout of the test facility instrumentation

To measure the free-stream temperature, an OMEGA T-type thermocouple mounted at the top of the Plexiglas wall is connected to the third channel of the NI-board. Fourth

channel of the NI-board is connected to a high precision capacitance type 0-10 mmHg differential pressure transducer (MKS) with a 0-10 Volt analog output. A Prandtl probe, placed upstream of the diffuser, monitors the reference velocity at a fixed location.

For the unsteady investigations, a mechanism to externally trigger the A/D board is required for phase-averaging the instantaneous data. A high response, reflective type, fiber optic proximity sensor placed close to the pulley of the wake generator, produces a signal once every revolution. The passage signals of the rods are detected by the sensor using a silver-coated reflective paint on one side of the wake generating timing belts. This signal is converted to 0-5 V level and is transferred to zeroth channel of the A/D board for rpm measurement. The rpm of the wake generator can be calculated from the sampled voltage from the zeroth channel of A/D board and calculating the elapsed time between successive high pulses. This method gives an accurate readout of the speed of the wake generator and the passing frequency of the rods and requires no calibration.

5.1.1 Blade Instrumentation for Surface Mounted Hot Film Probes

A specially manufactured surface mounted hot film blade is used to investigate the time dependent boundary layer transition and the local wall shear stresses. The blade shown in Figure 5.2 is instrumented with 160 hot-film sensors on the suction and the pressure surface of the LPT blade. The hot-film sensors are of Langley design and manufacture. All sensors are Nickel on polyimide, and their resistance is 0.5 Ohms/square. Hot film sensor are glued on the thin Kapton sheet with a thickness of 2 mils to obtain very similar resistances. The leads which are onnected to the hot-film probe are copper plated to reduce resistance. Hot-film sensors is operated at overheat ratio of 1.1 to 1.2. They are connected to 4-channel constant temperature hot-film anemometer system which is been developed at NASA Dryden. The anemometer has a DC output of the low-pass filtered bridge voltage with an option of output of a zero shifted to DC output for increased dynamic range. It also has an AC-output which is amplified to the desired level and low-pass filtered at 72 kHz. For each hot-film anemometer channel, 32 hot-film sensors connected to a constant temperature anemometer board, an adjust resistor was soldered onto another board that

connects into the main hot-film anemometer board. As hot film resistances tend to shift under temperature, fixed resistances had to be utilized. Thus, for a change in the overheat temperature ΔT of a hot-film sensor, its adjust resistor had to be exchanged. Due to individual adjust resistors the overheat temperature could be set to the same ΔT for very sensor, even tough the wall temperature and the resistance vs. temperature calibrations may have been different. The sensors and their respective adjust resistors are successively switched into the actual Wheatstone bridge using a 160 -relay Cytec JX-series multiplexer.

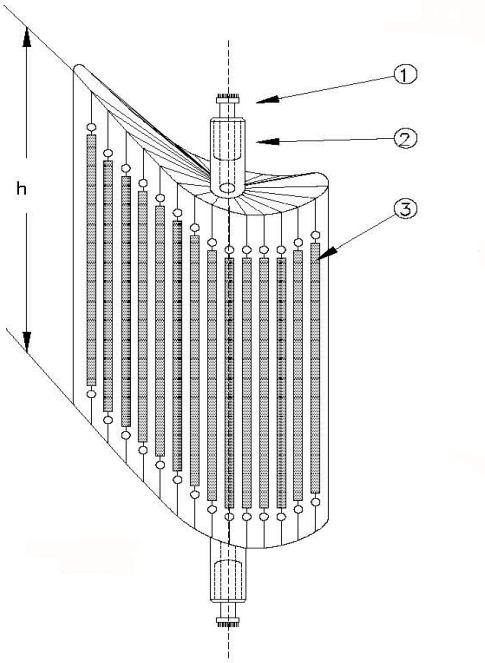

Figure 5.2. Surface mounted hot-film blade

5.1.2 Blade Instrumentation for Surface Pressure Measurements

Static Pressure Blade: One of the blades of the turbine cascade as seen in Figure 5.3, is manufactured with 48 static pressure taps to obtain the surface pressure distribution. For static pressure measurement around the blade surface and also to make measurements with

the five hole probe, it is necessary to consequently read pressures from several ports. A 48-port scanivalve system is used for this purpose. The output of the scanivalve system is connected to the MKS pressure transducer. By using the scanivalve system, it is possible to measure 48 pressures using the same pressure transducer. This is done by sequentially connecting the pressure transducer to each of the 48 ports. The 48 taps on the blade are connected with the 48 ports of the scanivalve.

PSP (Pressure Sensitive Paint) Coated Blade: The test blade as shown in Figure 5.3 was coated with a Binary FIB pressure sensitive paint (PSP) developed by Innovative Scientific Solutions, Inc. The time response of the paint is 0.3s and the pressure sensitivity is greater than 5% per psi. A water-cooled INNOVA 70C5 argon ion laser system with a power output of 5W is used as an illumination source. It operates at a wavelength of 488 nm to excite the luminescent molecules during measurements. The blade is imaged through a 2 filters, a 645-nm long pass filter for the signal probe and a 550 ± 40-nm band-pass filter for the reference probe. The camera generates 12 bit (4096 grey levels) images with 640(horizontal) x 480 (vertical) pixels. The pictures are saved on a PC using a PCI interface board.

Figure 5.3 Blade for surface pressure measurements with 48 static pressure taps and a binary pressure sensitive paint (PSP)

5.1.3 Blade Instrumentation for Heat Transfer Measurements

Liquid Crystal Blade: For the heat transfer measurements a specially designed heat transfer blade is used. The blade consists of a polyurethane core, two copper connection pieces and is covered with an adhesive sheet, an inconel 600 foil and a liquid crystal sheet. The structure of the blade and its mounting in the cascade test section is shown in Figure 5.4 and Figure 5.5. The inconel 600 foil is attached to the surface of the blade with a double sided adhesive sheet and is connected electrically conductive to the copper pieces. The Inconel foil is covered with a self adhesive liquid crystal sheet that is used to measure the surface temperature. The liquid crystals have a yellow color (yellow band) within a very small temperature range, thus allowing a very precise temperature measurement of the blade surface. The power required for heating the heat transfer blade is supplied by a Sytron 10V-200A (maximum) DC power supply. For the measurements a scale and gridlines of 10 mm increments are attached on each side of the blade starting at the leading edge. The actual blade is as shown in Figure 5.6.

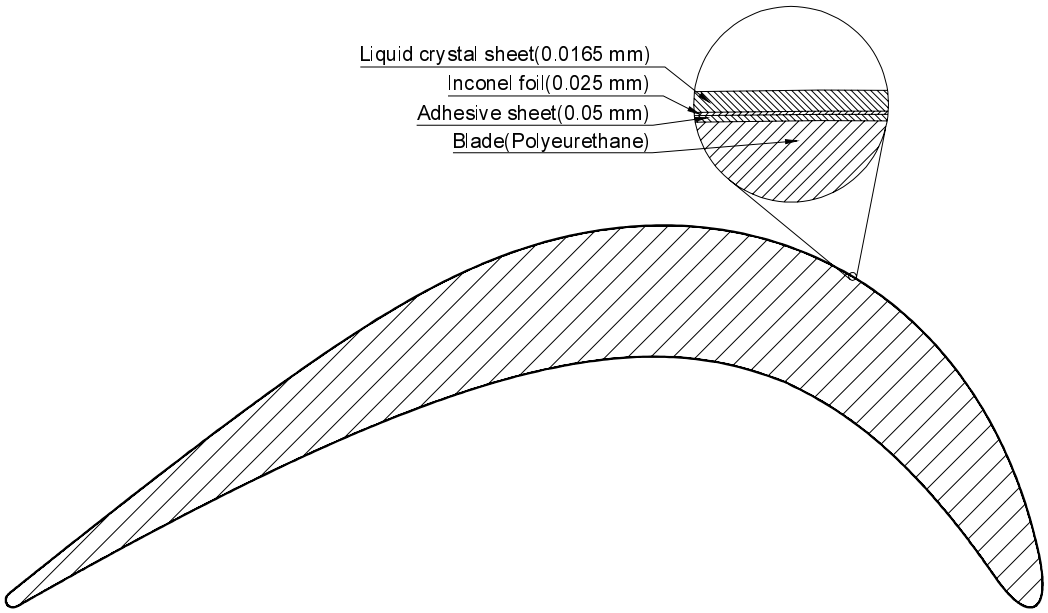

Figure 5.4. Cross-section of the heat transfer blade

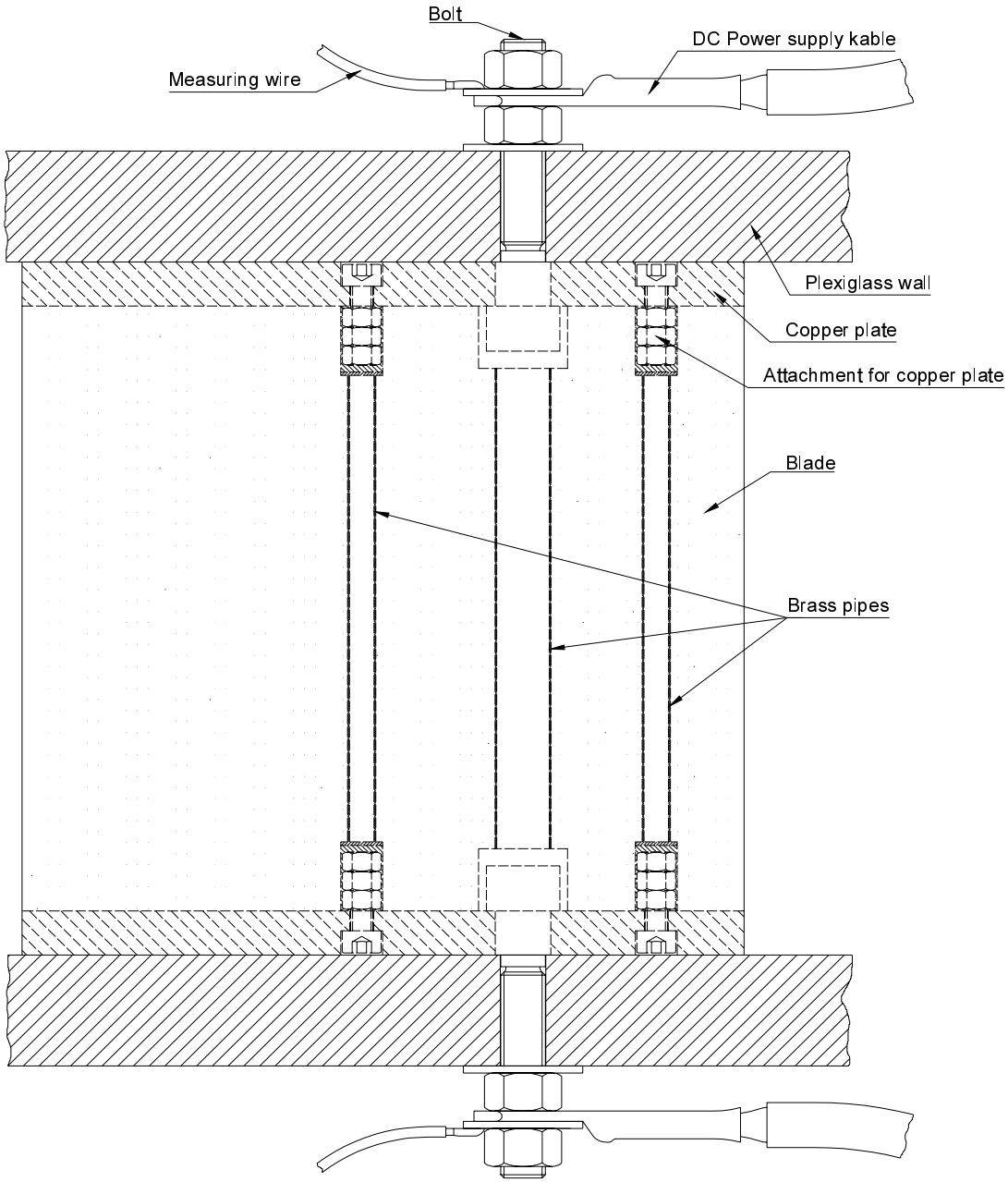

Figure 5.5. Mounting of the heat transfer blade

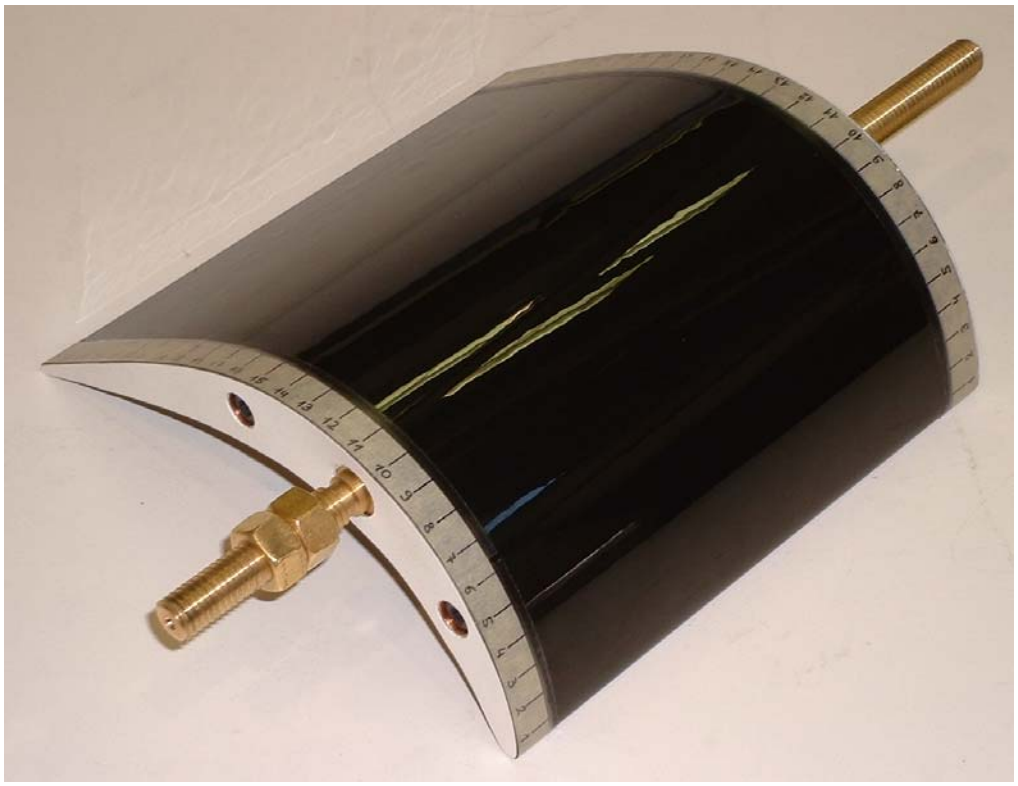

Figure 5.6. Liquid crystal coated heat transfer blade

TSP (Temperature Sensitive Paint) Coated Blade: The blade as shown in Figure 5.7 was coated with a UniCoat temperature sensitive paint (TSP) developed by Innovative Scientific Solutions, Inc. The time response of the paint is 0.3s with no pressure sensitivity. The instrumentation of the TSP measurement is exactly the same as for PSP except for the long pass filter. The blade is imaged through a 570-nm long pass filter. For the heat transfer measurement, the blade is heated by a Sytron 10V-200A (maximum) DC power supply.

5.2 Data Acquisition Procedure

The data acquisition system is computer controlled. The required code is written with LABVIEW. The computer acquires the data as a voltage from the differential pressure transducer, thermocouple, trigger circuit, Sytron power supply and from TSI IFA-100 flow analyzer.

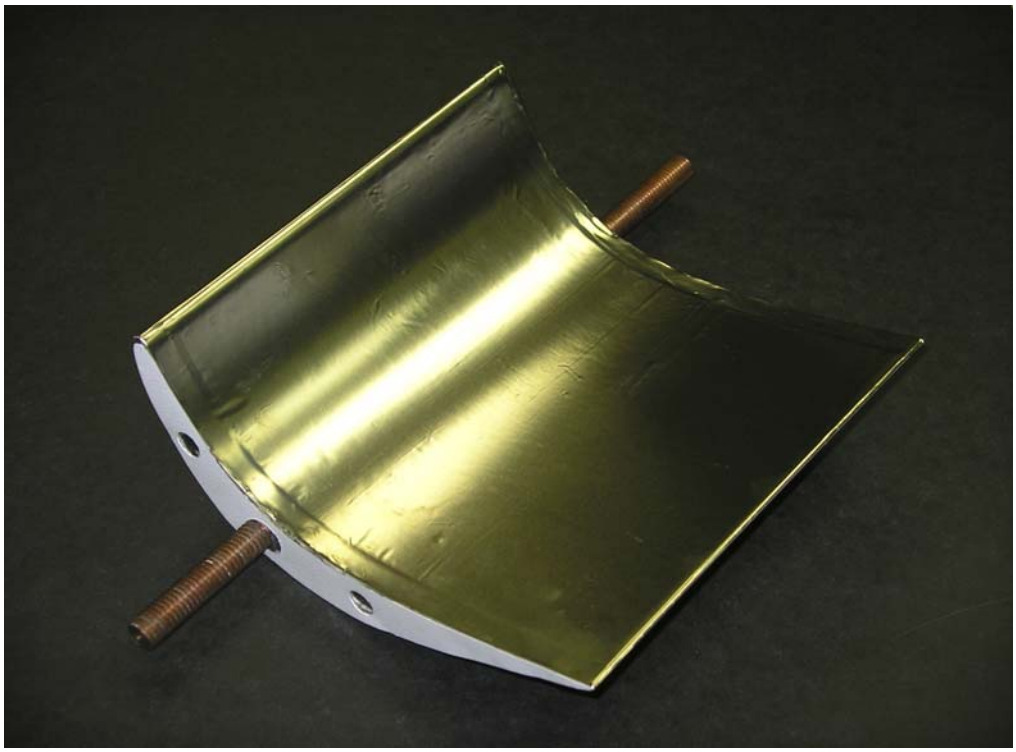

Figure 5.7. TSP/liquid crystal blade (uncoated)

5.2.1 Data Acquisition for Unsteady Boundary Layer Investigations

A single-wire probe is used for boundary layer study under the effect of periodic unsteady wake flow. For steady flow investigations, 20,000 samples is taken at a rate of 20 kHz. For unsteady boundary layer investigations, 20,000 samples is taken at a rate of 20 kHz for each of the 100 revolutions of the wake generator. The low pass filter of the hot wire anemometer is set to 10 kHz to prevent the aliasing effect. The data are phase-averaged with respect to the rotational period of the wake generator. The above number of samples and revolutions is chosen after a preliminary study where the number of samples and revolutions is varied and optimum values is found.

5.2.2 Data Acquisition for Surface Mounted Hot Film Probes

Surface mounted hot-film probes is used to determine the transition location, characteristics and wall shear stresses. For steady flow and zero-flow investigations, 10,000 samples is taken at a rate of 10 kHz for Ac and DC-components. For unsteady flow

investigations, 10,000 samples is taken at a rate of 10 kHz for each of the 50 revolutions of the wake generator for AC and DC-components. The 160 hot-film sensors on the blade and their respective adjust resistors are connected to the 5-channel Dryden anemometer with the 160 relays of the Cytec multiplexer. When the data acquisition program is executed, the computer acquires 10,000 samples at a rate of 10 kHz starting from the first relay. The data acquisition process is repeated until all the relays are closed.

5.2.3 Data Acquisition for Surface Pressure Measurements

Static Pressure Blade: One of the blades was produced with 48 static pressure taps to obtain pressure distribution on the suction and the pressure surface of the blade. The 48 taps on the blade are connected with the 48 ports of the scanivalve and the output is connected to a high precision differential pressure transducer. When the data acquisition program is executed, the computer acquires 4096 samples at a rate of 4096 Hz from the first port and stores the mean pressure. Then the program sends out a voltage pulse through DAC port and steps the scanivalve to the next port. The system waits until steady state is reached before sampling the data of the next port. The process is repeated until all the ports are scanned.

PSP (Pressure Sensitive Paint) Coated Blade: Images are taken for one steady and two unsteady inlet flow conditions for different Reynolds numbers and turbulence intensity levels on the suction and the pressure surface at 50 streamwise positions. The borescope which is connected to the CCD-camera traverse for PSP measurements from leading edge to the trailing edge by a stepper motor driven traversing system with micro motion capability and optical encoder feedback. Images obtained from the camera at different 50 streamwise positions is saved as TIF images. 300 images is captured for each case and the average pixel intensity is calculated from these images. To present the data over the whole area a Matlab program is developed which is able to correlate the data recorded by the PSP System.

5.2.4 Data Acquisition for Heat Transfer Measurements

Liquid Crystal Blade: For the determination of the temperature on the liquid crystal sheet, the blade is heated. As described in the previous section, the inconel foil is connected to the power supply. Dependent on the surface temperature, the Liquid Crystals changes its color from black to red, yellow, blue and then black again with rising temperature. In this particular liquid crystal sheet the yellow color has the smallest temperature range (~44.6 $^{\circ}$C). The circuit diagram of the blade is shown in Figure 5.8.

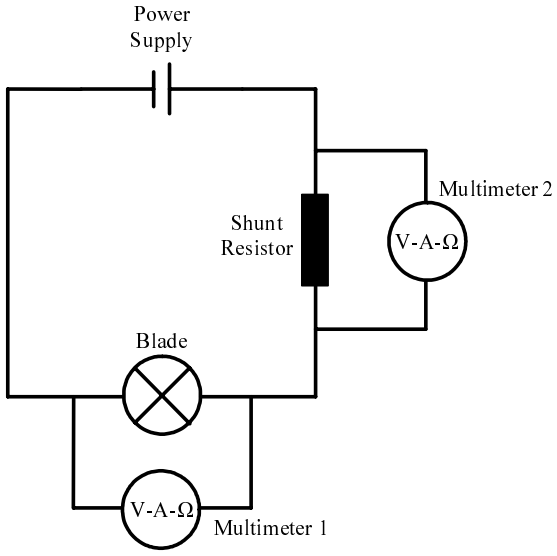

Figure 5.8. Circuit diagram for heat transfer blade

The blade voltage is measured by the Multimeter 1. The current cannot be measured directly because of the high magnitude (up to 150 A). Therefore a shunt resistor, with a resistance of 1 mΩ, is installed. Thus, the current can be evaluated via the voltage drop at the Multimeter 2. The values for the voltage and the current used for heating the blade is used to calculate the power. The free stream air temperature is measured by a thermocouple thermometer at the exit of the test section. With these values a calculation of the heat transfer coefficient is performed.

The blade voltage is set to a constant value to preheat it. The system waits until steady state is reached before sampling the data. Then the blade voltage is raised in small steps

until the yellow band is visible. Between the changing of the voltage and acquiring the data a time from 10 to 15 minutes is allowed. After the acquisition a constant waiting time is kept. The voltage steps, in a range between 0.012 V and 0.1 V, are chosen after the desired resolution of the heat transfer coefficient distribution.

TSP (Temperature Sensitive Paint) Coated Blade: As described in the previous section, for the determination of temperature using liquid crystal technique the blade has to be heated. First, the blade voltage is set to a constant value. Then, the system waits until steady state is reached before sampling the data. After it reaches steady state, the data acquisition for TSP measurements is the same as in described for PSP measurements.

6. CALIBRATION PROCEDURE

Calibration of sensors is of great importance for accurate measurement of any physical quantity. The data acquisition procedures involve sampling of voltage signals from the NI board channels. These voltage signals have to be converted into real physical quantities by means of calibration. These quantities are temperature, pressure, flow velocity, flow angle etc. The pressure transducer is calibrated using a dead weight tester while the thermocouple is connected to the thermocouple calibrator. Least square polynomial fits are used to fit the averaged output voltages with the actual readings obtained from the dead weight tester and thermocouple calibrator. These coefficients are stored in separate data files. However, the calibration of five-hole probes and hot wire probes are more extensive and is performed in uniform flow open jet calibrating facility.

6.1 Description of the Calibration Facility for Hot-Wire Probes

A schematic of the calibration facility is shown in Figure 6.1. This facility has been used to calibrate the hot wire as in [105] and five-hole probes. Compressed air is drawn from a reservoir passes through a pressure regulator, filter and flow control valve before entering the calibration facility. It consists of settling chamber followed by a pipe with three axis-symmetric sections, each having a diameter of 150 mm. Screens are placed between flanges of the sections to reduce the turbulence level. The turbulence intensity level at the jet exit is approximately 0.35%. A nozzle with an exit diameter of 38.1 mm is attached at the end of the pipe. The inlet and outlet of the nozzle are parallel to the axis of the facility. A thermocouple is placed in the first section of the calibration facility to measure the air temperature. And a pressure tap is placed in the last section of the pipe to measure the pressure difference between static pressure inside the pipe and the atmospheric pressure with a differential pressure transducer. Two lynx stepper motor controllers are used to automatically change the pitch and yaw angle. The tip of the probes were placed about

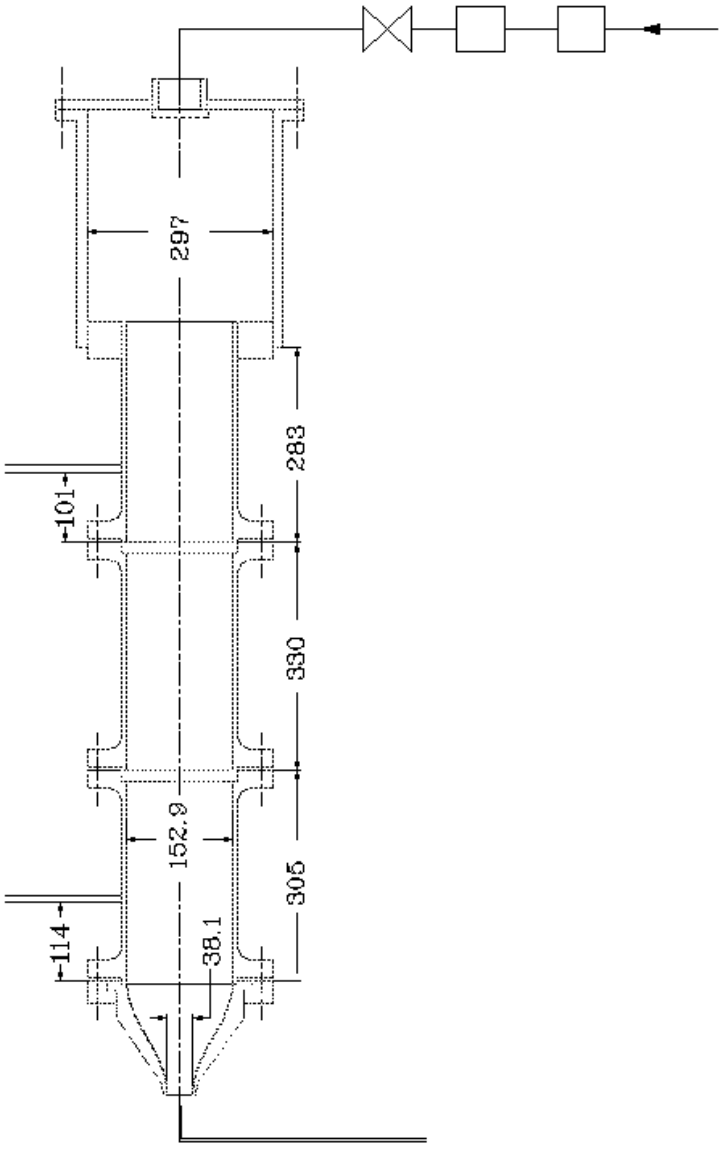

Figure 6.1. Test facility for calibrating hot-wire and the five-hole probes

0.4 diameters downstream of the nozzle exit plane and within the potential core of the jet. The analog signal from the differential pressure transducer, thermocouple, stepper motor control and hot wire anemometer are transferred to the A/D board from where they are sampled.

6.2 Description of Calibration Technique for Hot-Wire Probes

To measure the unsteady velocity in the boundary layer, a single sensor hot wire probe is used which is shown in Figure 6.2. The wire is made of tungsten with a diameter of 4 μm. The wire temperature is constant, and the sensor temperature of the T_{probe}=250° C. The amount of electrical energy dissipated in the sensors is a measure of the cooling effect of the fluid past the heated sensor. The actual velocity is a function of the dissipated energy and the fluid temperature, assuming constant pressure and fluid properties.

A constant temperature anemometer is used to vary the electrical current through the hot wire in order to maintain a constant wire temperature T_{probe}. This is done by controlling the hot wire's resistance, which is a linear function of the temperature.

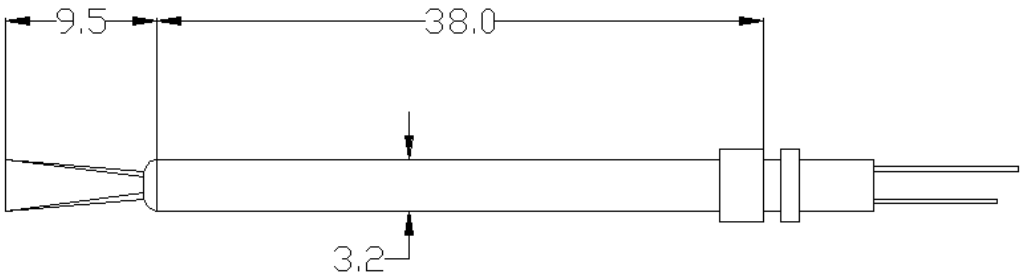

Figure 6.2. Single sensor hot-wire probe

6.3 Calibration Procedure for Hot-Wire Probes

During the velocity calibration, single hot wire probe is kept normal to flow and the flow velocity is varied. The exit velocity is calculated by the differences between the static pressure at the inlet p_1 and the static pressure at the outlet of the nozzle p_2. From the Bernoulli-equation:

$$p_1 - p_2 = \frac{\rho}{2}(v_2^2 - v_1^2) \tag{6.1}$$

and the continuity equation for incompressible flow:

$$v_1 d_1^2 = v_2 d_2^2 \tag{6.2}$$

the formula for the exit velocity is:

$$v_2 = \sqrt{\frac{2\Delta p}{\rho}\frac{d_1^4}{d_1^4 - d_2^4}} \tag{6.3}$$

the density is calculated by the ideal gas equation:

$$\rho = \frac{p_1}{RT_1} \tag{6.4}$$

The temperature is measured by a thermocouple inside of the facility. All variables are displayed in Figure 6.3.

The exit velocity of the nozzle was varied from 0 to 12 m/s. For each velocity, a set of data from constant temperature anemometry, thermocouple, pressure voltage signals were taken. The data are averaged for each channel. The correlation between the hot wire voltage (E) and the velocity (V) by a fourth-order polynomial:

$$V = a_0 + a_1 E + a_2 E^2 + a_3 E^3 + a_4 E^4 \tag{6.5}$$

The coefficients are calculated using the least-square method. The results of the calibration is shown in Figure 6.4.

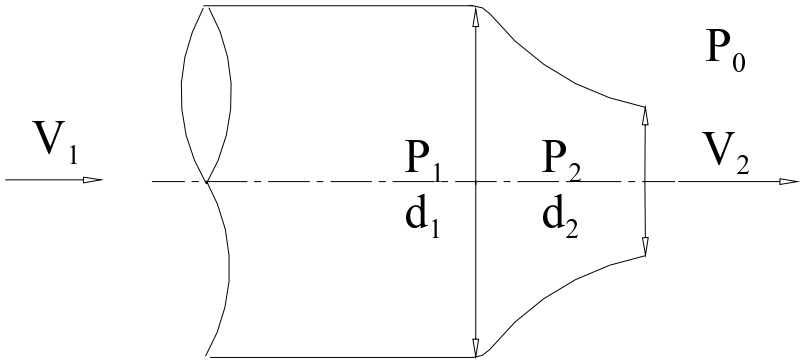

Figure 6.3. Nozzle of calibration facility

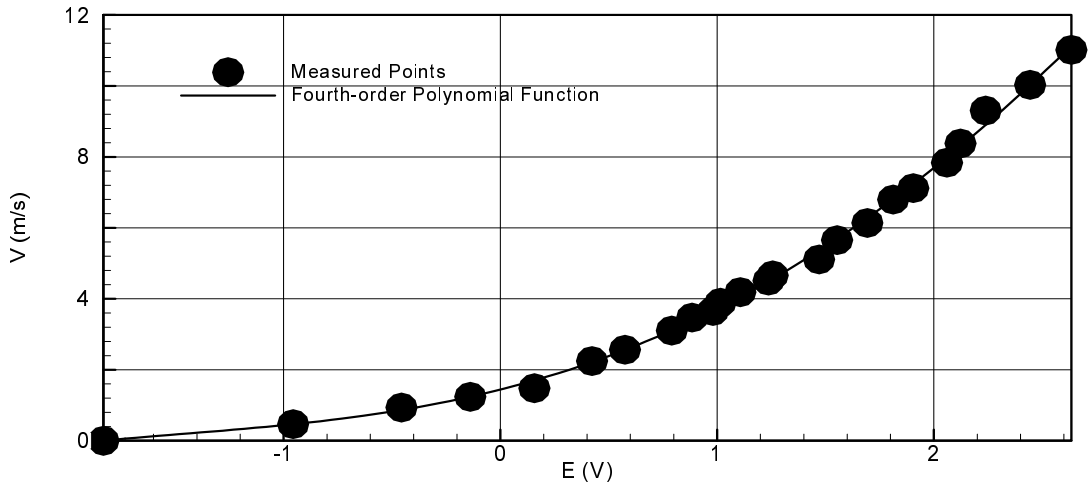

Figure 6.4. Calibration curve of single hot-wire probe

The temperature compensation of the velocity is made later, adjusting the anemometer output voltage according to the formula.

$$E_{adj} = E\frac{T_{probe} - T_{cal}}{T_{probe} - T} \tag{6.6}$$

where E is the sampled anemometer voltage, T is the actual temperature and T_{probe} is the operating temperature of the hot wire.

6.4 Description of Calibration Technique for X-Wire Probes

A simple and accurate method by John and Schobeiri [106] has been used for calibrating X-wire probe. The calibration is required to determine the relation between the effective cooling velocity of each sensor and the anemometer output voltage and also the yaw response at different flow angles. The above described calibration facility is used for this purpose. initially, theoretical background on calibrating at a single free-stream velocity is given. This is followed by description of the calibration procedure, uncertainty analysis, and finally the yaw angle correction at low velocities.

The X-wire probe geometry, in mm, and the flow coordinates are shown in Figure 6.5. Each sensor makes an angle of α_s=45° with respect to x-axis. The components of flow velocity C along and perpendicular to the probe axis are denoted by V_x and V_y, respectively.

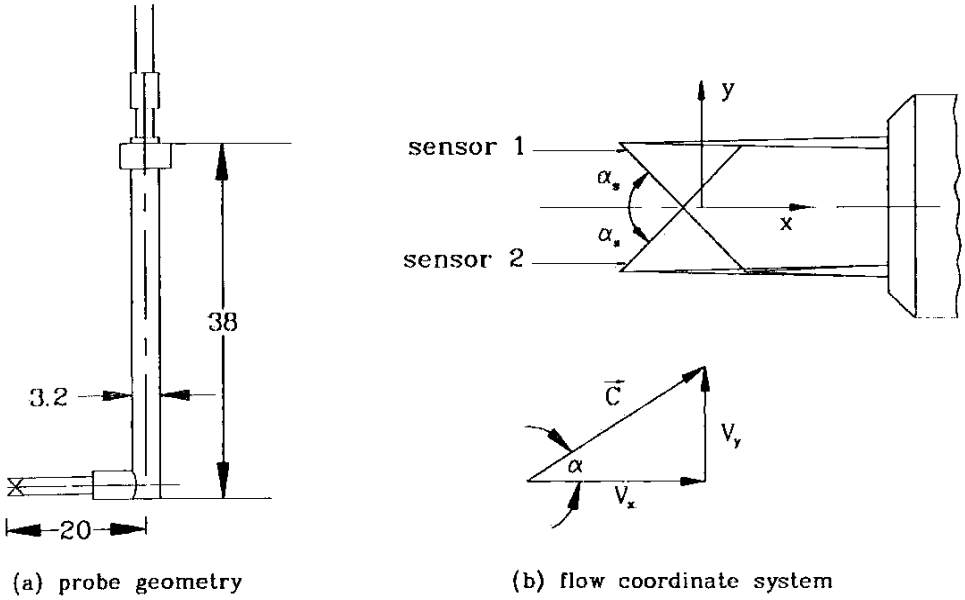

Figure 6.5. X-wire probe geometry and flow coordinate system (Pappu [105])

6.4.1 Theory for X-Wire Calibration

The velocity calibration evaluates the coefficients in Eq. (6.5) for each sensor. The next step in the calibration is to obtain the directional response of hot wire probe. The most

accurate representation of the directional response of hot wire or hot film probes is given by:

$$V_e^2 = V_N^2 + k^2 V_T^2 \tag{6.7}$$

The above representation has been introduced by Hinze [107] and Champagne et al. [108]. A review of existing calibration methods is thoroughly described in John [106]. Using Eq. (6.7), the angle response equations for sensors 1 and 2 can be derived from Eq. (6.5) as:

$$V_{e1}^2 = C^2[\sin^2(\alpha_s + \alpha) + k_1^2 \cos^2(\alpha_s + \alpha)] \tag{6.8}$$

$$V_{e2}^2 = C^2[\sin^2(\alpha_s - \alpha) + k_2^2 \cos^2(\alpha_s - \alpha)] \tag{6.9}$$

Here, C is the flow velocity, V_{e1} and V_{e2} and are the effective cooling velocities, and k_1 and k_2 are the yaw coefficients for sensors 1 and 2. initial calibrating techniques evaluated the values of k at different velocities. However, these techniques resulted in significant errors especially at higher yaw angles. So, Schröder [109] introduced a simplified method by introducing an ideal flow angle α_{id} for which k_j are equal to zero. Compared to constant k-factor methods, the method by Schröder was more accurate to a wide range of flow angles ($-40° < \alpha < 40°$).

Applying the ideal flow angle α_{id} defined by Schröder for which k_j are equal to zero, Eqs. (6.8) and (6.9) lead to:

$$\alpha_{id} = \tan^{-1}\left(\frac{V_{e1} - V_{e2}}{V_{e1} + V_{e2}} \tan\alpha_s\right) \tag{6.10}$$

The geometry of the sensors, refer to Figure 6.5, is such that $\alpha_s = 45°$. Therefore Eq. (6.5) can be written as:

$$\alpha_{id} = \tan^{-1}\left(\frac{V_{e1}}{V_{e2}}\right) - 45 \tag{6.11}$$

Schröder also introduced a nondimensional parameter H that relates the effective cooling velocities ton the actual flow velocity as:

$$H = \frac{C^2}{V_{e1}^2 + V_{e2}^2} \tag{6.12}$$

The yaw calibration involves determining the values of α_{id} and H for various α. Once the values are determined, α and H are represented by fifth-order, least-squares polynomial fits as:

$$H = b_o + b_1\alpha_{id} + b_2\alpha_{id}^2 + b_3\alpha_{id}^3 + b_4\alpha_{id}^4 + b_5\alpha_{id}^5 \tag{6.13}$$

$$\alpha = c_0 + c_1\alpha_{id} + c_2\alpha_{id}^2 + c_3\alpha_{id}^3 + c_4\alpha_{id}^4 + c_5\alpha_{id}^5 \tag{6.14}$$

In order to increase the curve fit accuracy, John and Schobeiri [106] introduced a new function H^* defined as:

$$H^* = \frac{C\cos\alpha}{\sqrt{V_{e1}^2 + V_{e2}^2}} \tag{6.15}$$

Again the new function H^* is represented by fifth-order, least-squares polynomial function of α_{id} as:

$$H^* = d_0 + d_1\alpha_{id} + d_2\alpha_{id}^2 + d_3\alpha_{id}^3 + d_4\alpha_{id}^4 + d_5\alpha_{id}^5 \tag{6.16}$$

The yaw angle calibration determines the coefficients c_i and d_i in Eqs. (6.14) and (6.16), respectively. The details of calibration procedure is the focus of next section.

6.4.2 Calibration Procedure for X-Wire Probes

The calibration procedure has two steps, velocity calibration and yaw angle calibration. During the velocity calibration to obtain the coefficients of Eq. (6.5), each of the sensors is kept normal to the flow and the flow velocity C is varied. Since the sensors are kept normal to the flow, the effective cooling velocity V_{ej} is equal to the flow velocity C. The velocity calibration is done for about 30 different velocity values in a preselected range. The flow velocity is calculated from the pressure drop across the nozzle which is given by:

$$C = \sqrt{\frac{2\Delta P}{\rho}} \sqrt{\frac{1}{1-\left(\frac{d_2}{d_1}\right)^4}} \tag{6.17}$$

Here, ΔP is the pressure drop across the nozzle, ρ is the density of air, and d_2/d_1 is the diameter ratio of the nozzle exit to the inlet. Equation (6.17) has been derived by applying Bernoulli's equation for an incompressible flow through the nozzle.

Once the velocity calibration is complete, next step is the yaw angle calibration. The yaw angle calibration is done for α ranging from -40° to 40° in 2° increments while keeping the flow velocity C constant. The values of α_{id} and H^* are tyhen calculated from Eqs. (6.11) and (6.15). The coefficients c_i in Eq. (6.14) and (6.16) are obtained from least-squares fit of α and H^* against α_{id}. The values α_{id} and H^* are found to have good reproducibility. However, the velocity calibration in Eq. (6.5) is found to drift with time and hence requires frequent calibration.

The results of velocity and yaw angle calibration are presented in Figures 6.6 through 6.8. Figure 6.6 shows variation of the ideal flow angle α_{id} with the actual flow angle α. The variation of α_{id} with α is almost the same for all the velocities α ranging from -20° to 20°. Beyond this range of α, the variation is very pronounced and becomes a strong function of flow velocity. The variation appears to be quite strong at lower flow velocities ($C < 15$ m/s). Thus, for velocities greater than 10 m/s, the yaw response is considered to be independent of flow velocity C and the coefficients c_i in Eq. (6.14) are obtained by least-squares of fit of data corresponding to C=30 m/s. However, when using these coefficients for $C < 15$ m/s, significant errors are introduced unless some correction is applied. This dependence of yaw response on velocity at low velocities is accounted for by an yaw angle correction which is discussed in a later section. Figure 6.7 shows the variation of H^* with α_{id}. The same tendencies discussed with reference to Figure 6.6 can also be observed here. Figure 6.8 shows the velocity calibration curves obtained by keeping each sensor normal to the flow, i.e., α=+45° when sensor 1 is normal to the flow α=-45° when sensor 2 is normal to the

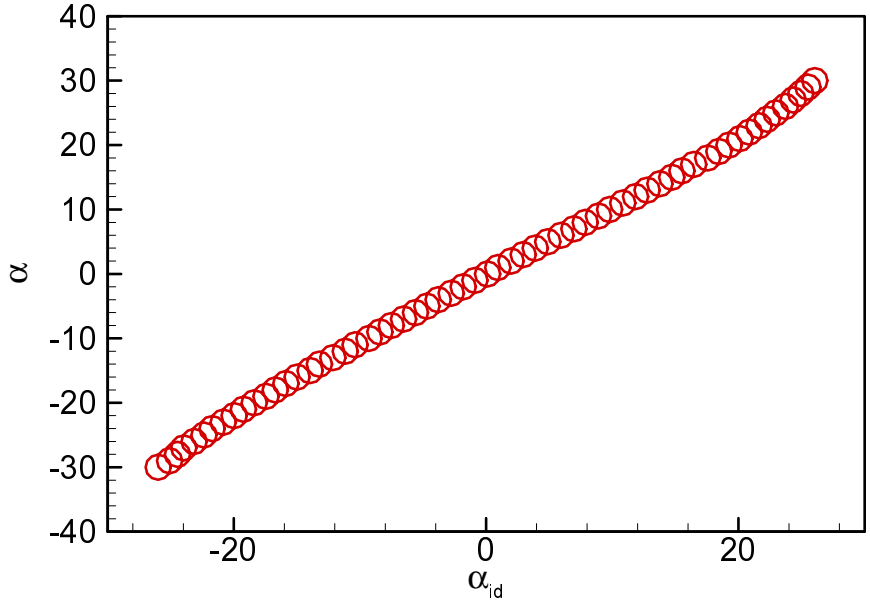

Figure 6.6. Variation of α and α_{id} at C=10 m/s

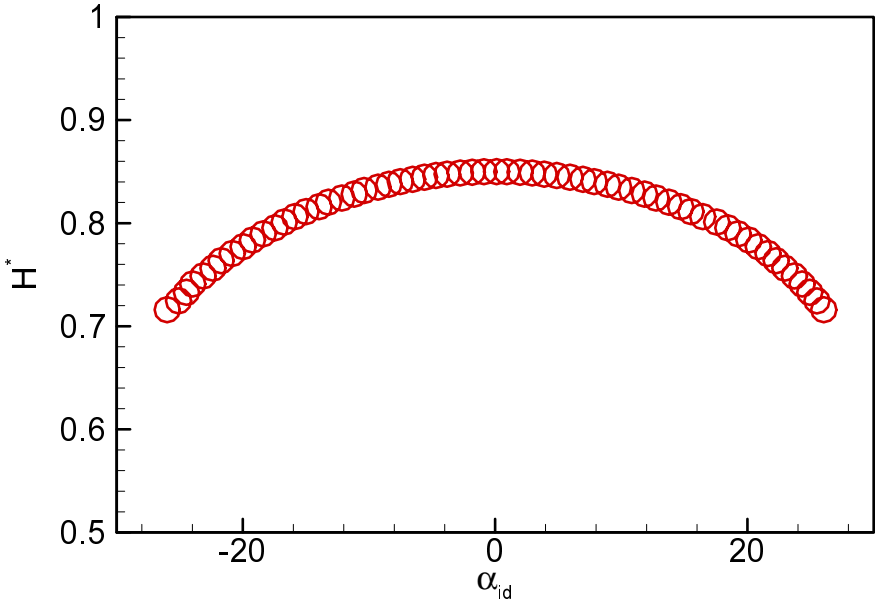

Figure 6.7. Variation of H^* with α_{id} at C=10 m/s

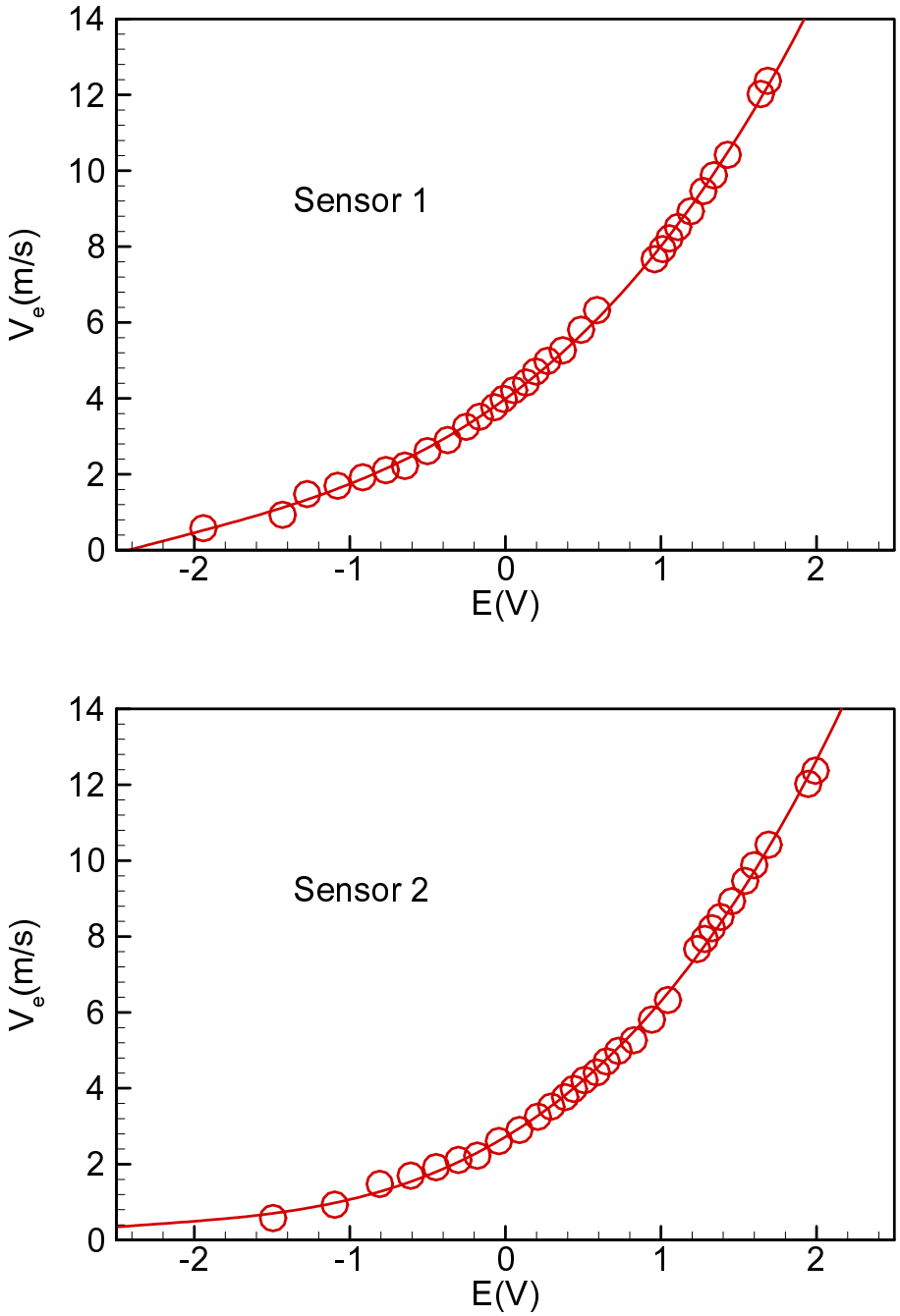

Figure 6.8. Effective velocities of sensor 1 (top) and sensor 2 (bottom)

flow. Since velocity calibration needs to be performed frequently to account for the drift with time, keeping each sensor normal to the flow and varying the velocity is time consuming. The calibration time could be reduced by half if both the sensors could be calibrated simultaneously at any flow angle α. John and Schobeiri [105] discussed one such method that can be implemented once the yaw angle response is obtained and the coefficents c_i and d_i are determined. For a known angle α and α_{id} is obtained from Eq. (6.14) by using Newton-Raphson method. Then, the corresponding H^* is calculated from Eq. (6.16). Finally, the effective cooling velocities are calculated from the following relations obtained from Eq. (6.11) and (6.15):

$$V_{e1} = \frac{C\cos\alpha\tan(\alpha_{id} + 45)}{H^*\sqrt{1+\tan^2(\alpha_{id} + 45)}} \tag{6.18}$$

$$V_{e2} = \frac{C\cos\alpha}{H^*\sqrt{1+\tan^2(\alpha_{id} + 45)}} \tag{6.19}$$

As shown in Figure 6.8, the curves obtained by simultaneously calibrating both the sensors using the above technique with α=0° fell very close to those when the sensors were kept normal to the flow. This verifies the validity of the calibration method.

6.4.3 Yaw Calibration at Different Velocities and Yaw Angle Correction

As discussed in section 6.4.2, the yaw response is dependent only on the flow angle but also on the flow velocity. The dependence appears to be quite stronger at very low flow velocities as can be seen from Figure 6.6. For a given α, the variation α_{id} increases with decreasing flow velocity C. The yaw angle calibration can be considered independent of velocity when C is greater than 10 m/s. However, when using this calibration for flow velocities less than 10 m/s, a correction needs to be applied. Based on power law relationship, John and Schobeiri [105] derived the following relationship for yaw angle correction.

$$\frac{\tan(\alpha_{id\,ref} + 45)}{\tan(\alpha_{id} + 45)} = \left(\frac{C_{ref}}{C}\right)^{m} \tag{6.20}$$

In Eq. (6.20), the subscript ref denotes the quantities at a reference velocity at which the yaw angle calibration is done. The power m is a function of α and can be approximated by a third-order, least-squares polynomial fit as shown in Figure 6.9, i.e.,

$$m = e_o + e_1\alpha + e_2\alpha^2 + e_3\alpha^3 \tag{6.21}$$

Figure 6.9 is obtained by using the yaw angle calibration at a reference velocity of 30 m/s and three other yaw angle calibrations at 5 m/s, 10 m/s, and 15 m/s.

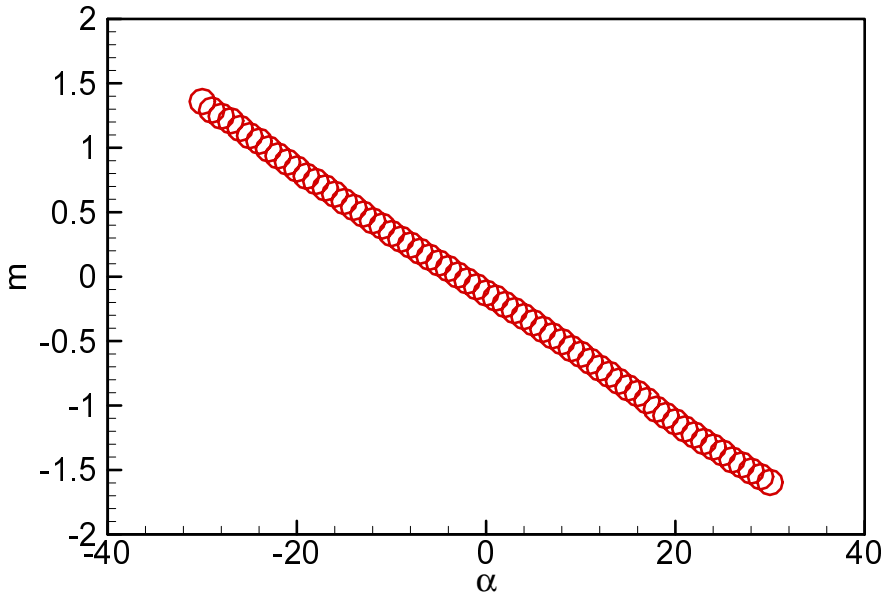

Figure 6.9. Variation of yaw correction m with α at C=10 m/s

6.5 Description of Calibration Technique for Hot-Film Sensors

Before the instrumented surface mounted hot film sensor blade is installed in the cascade test section, a resistance versus temperature calibration is carried out for each hot-film sensor. Resistance versus temperature calibration can be performed in two different methods for every sensor:

Current calibration- The first test of the sensor is generally heating with a constant current source at room temperature. The relationship between the current through the film and the resistance is determined in this manner. Both the absolute value and the differences between the sensors is examined, since this would reveal both differences occurring due to differences in etching and small substrate imperfections.

Oven calibration- In this calibration method, the oven is stepped to different temperature levels and the resistance of the films are recorded. Roughly 1 hour is allowed for the heating of the sensor at each point. Since a calibration takes one day or more, an automatic calibration system has to be developed that does the entire calibration sequence.

One problem with the current calibration is that the highest heating points often can be affected by thermal convection caused by the heating of the film. It is not possible to avoid it entirely. That's why oven calibration method is carried out for each hot-film sensor. For this purpose, surface mounted hot-film blade is subjected to ten different temperatures and the resistances of the actual sensors (without wires and connecting flags) is measured and tabulated. Example of typical hot-film sensor calibration curves is shown in Figure 6.10. The temperatures of the wires and the connecting flags are assumed to remain constant during the tests.

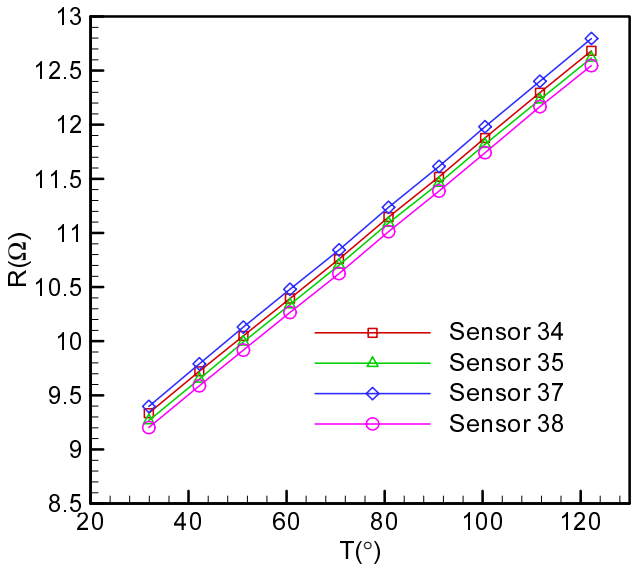

Figure 6.10. Resistance vs temperature calibration curves for different hot-film sensors

6.6 Description of Calibration Technique for UNI-FIB Pressure Sensitive Paint

The functional relationship between luminescent intensity from a paint and the pressure and temperature experienced is determined using the PSP calibration chamber as shown in Figure 6.11. A small copper test sample is painted with the Uni-Fib PSP to be calibrated and this test sample is mounted inside the calibration chamber. The pressure inside the calibration chamber is monitored using a PSI pressure transducer while the temperature of the sample is controlled using an Omega temperature controller. The sample is illuminated using a water-cooled INNOVA 70C5 argon ion laser system. It operates at a wavelength of 488 nm to excite the luminescent molecules during measurements. The luminescence from the sample is collected through a 610nm long-pass filter onto a PCI Series SensiCam CCD camera. The calibration is begun by recording the luminescence of the sample at 298 K and 1 atm, this serves as the reference condition. The temperature and pressure within the chamber are then varied over a range of temperatures and pressures. The luminescence from the sample is recorded at each condition and the ratio I(Tref, Pref) over I(T, P) is computed and plotted versus pressure. Figure 6.12 shows the calibration curve of intensity ratio vs. pressure ratio, which is found to be linear except the high vacuum range.

6.7 Description of Calibration Technique for Binary Pressure Sensitive Paint

The equipment and procedure for calibration of a binary pressure sensitive paint is similar to that used for single component paint systems. Once again, the same pressure sensitive paint calibration chamber (Figure 6.11) is used to control the temperature and pressures to which the paint is exposed. A copper test sample is painted with the binary pressure sensitive paint and this test sample is mounted inside the calibration chamber. The pressure inside the calibration chamber is controlled using a PSI pressure controller while the temperature of the sample is controlled using an Omega temperature controller. The sample is illuminated using a water-cooled INNOVA 70C5 argon ion laser system. It operates at a wavelength of 488 nm to excite the luminescent molecules during measurements. The sample is imaged through a filter wheel onto a PCI Series SensiCam CCD camera. The test sample is imaged through a 2 filters, a 645-nm long pass filter for the

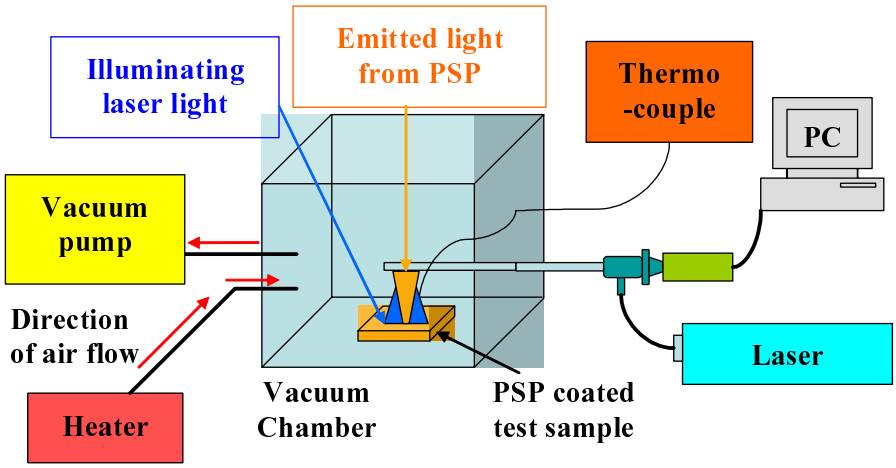

Figure 6.11. Test facility for calibrating TSP and PSP

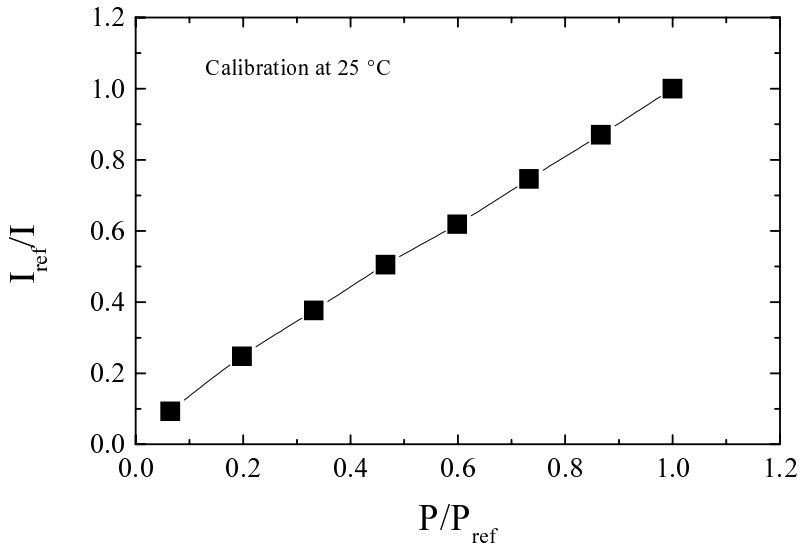

Figure 6.12. Calibration curve of Uni-Fib PSP

signal probe and a 550 ± 40-nm band-pass filter for the reference probe. The calibration is begun by recording the luminescence of the signal (FS) and reference (FR) probes at 298 K and 1atm, this serves as the reference condition. The temperature and pressure within the chamber are then varied over a range of temperatures and pressures. The luminescence from each probe is recorded at each condition and the ratio of ratios is computed and plotted

versus pressure. A calibrations for binary this binary paint is shown in Figure 6.13, this paint exhibits good pressure sensitivity (4.5% per psi) with very little temperature sensitivity (less than 0.03 % per K).

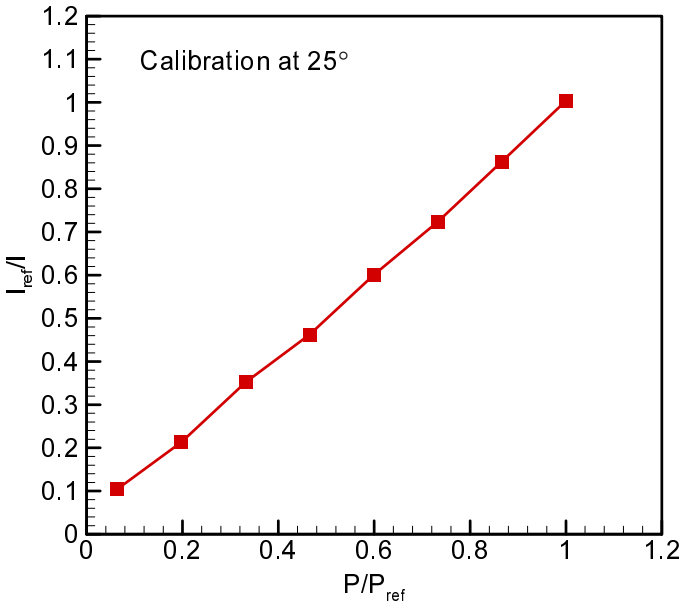

Figure 6.13. Calibration curve of binary pressure sensitive paint

6.8 Description of Calibration Technique for TSP

This is identical to the procedure utilized for pressure sensitive paints. The experimental setup for temperature sensitive paints is similar to that for pressure sensitive paints and is shown in Figure 6.6. A small copper test sample is painted with the TSP to be calibrated and this test sample is mounted inside the calibration chamber. The temperature inside the calibration chamber is monitored using an Omega temperature controller. The sample is illuminated using a water-cooled INNOVA 70C5 argon ion laser system. It operates at a wavelength of 488 nm to excite the luminescent molecules during measurements. The luminescence from the sample is collected through a 570nm long-pass filter onto a PCI Series SensiCam CCD camera. The calibration is begun by recording the luminescence of the sample at 298 K and 1 atm, this serves as the reference condition. The

temperature within the chamber are then varied over a range of temperatures. During the calibration procedure, only the temperature is varied. Because TSP is not sensitive to pressure changes. The luminescence from the sample is recorded at each condition and the ratio $I(T_{ref}, P_{ref})$ over $I(T, P)$ is computed and plotted versus temperature. Figure 6.14 shows the calibration curve of intensity ratio vs. temperature.

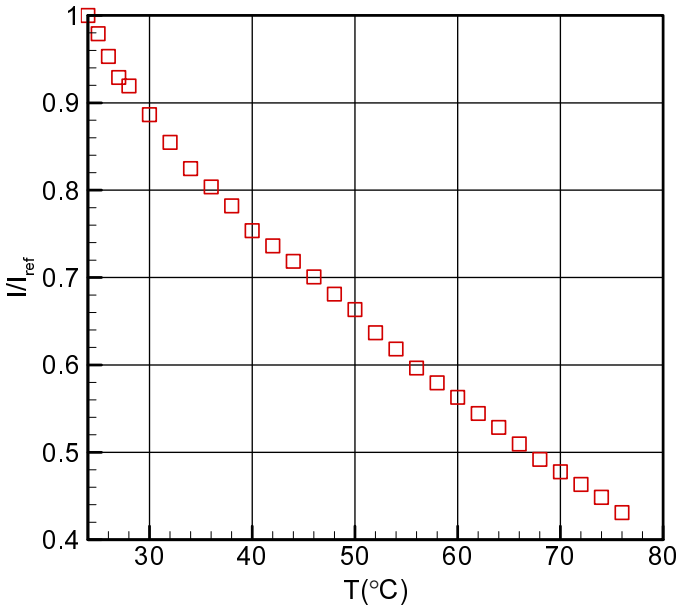

Figure 6.14. Calibration curve of TSP

7. PSP AND TSP MEASUREMENT THEORY

Traditional measurement techniques for acquiring surface pressure and temperature distributions on models have utilized embedded arrays of pressure taps and thermocouples. This requires extensive construction time while producing data with limited spatial resolution. An alternative approach is to use Pressure Sensitive Paint (PSP) and Temperature Sensitive Paint (TSP) to measure surface pressure and temperature. Measurements using PSP [102] and TSP have been demonstrated in several challenging flow fields such as on the suction surface of an advanced compressor blade [103] and an aircraft wing [104] in flight. The advantages of PSP and TSP include non-intrusive pressure and temperature measurements and high spatial resolution when compared to conventional measurement techniques.

7.1 Uni-Fib Pressure Sensitive Paint Measurement

The PSP method is based on the sensitivity of certain luminescent molecules to the presence of oxygen. A typical PSP is comprised of two main parts, (Figure 7.1) an oxygen-sensitive fluorescent molecule, and an oxygen-permeable binder. When a luminescent molecule absorbs a photon, it is excited to an upper singlet energy state. The molecule then typically recovers to the ground state by the emission of a photon of a longer wavelength. Pressure sensitivity of the luminescent molecules results when an excited luminophor interacts with an oxygen molecule and transfers some of the excited state energy to a vibrational mode of the oxygen molecule. The resulting transition to the ground state is radiationless, this process is known as oxygen quenching. The rate at which the quenching process competes with the radiation process is dependent on the partial pressure of oxygen present, with a higher oxygen pressure quenching the molecule more, thus reducing fluorescence.

Conceptually a PSP system (Figure 7.1) is composed of a test component painted with PSP, an illumination source, a detector, and a long-pass filter. The PSP is distributed over the model surface and the surface is then illuminated by the excitation source causing the PSP to luminesce. The luminescent intensity from the PSP is recorded by the detector and

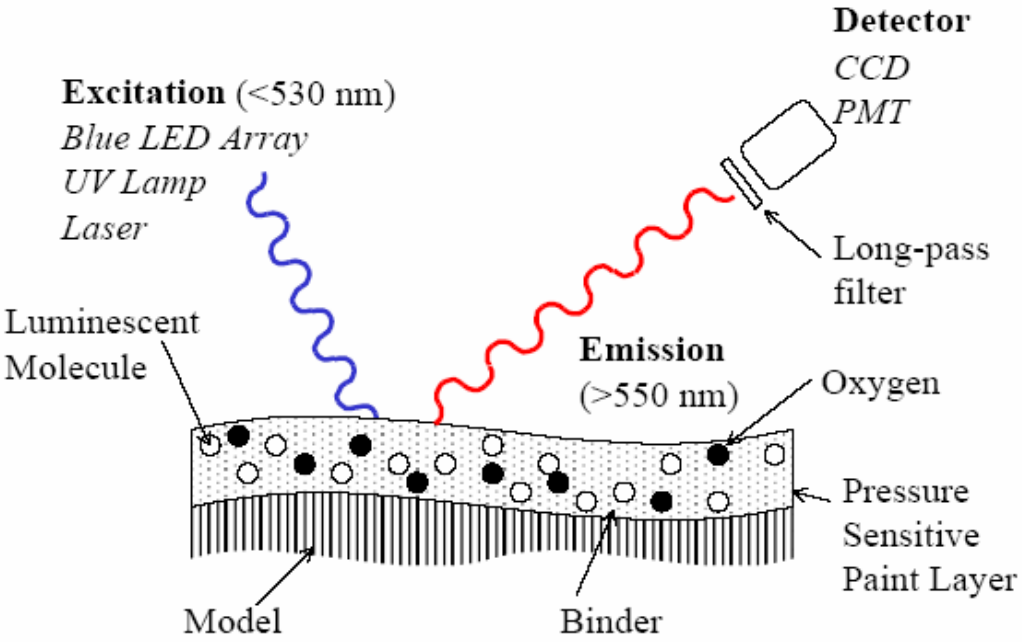

Figure 7.1. Basic Uni-Fib pressure sensitive paint system

converted to pressure using a previously determined calibration. Unfortunately, the luminescent intensity from a pressure-sensitive coating can be a function of several parameters such as; spatial variations in excitation illumination, pressure-sensitive luminophor concentration, paint layer thickness, and camera sensitivity. These spatial variations are minimized by ratioing the luminescent intensity of the paint at the test or wind-on condition (I_T, T_T) with the luminescent intensity of the paint at a known reference or wind-off condition (I_{ref}, T_{ref}). The oxygen partial pressure information is obtained from the following equation as in [110].

$$\frac{I_{ref} - I_{blc}}{I_{air} - I_{blc}} = f\left(\frac{(P_{o_2})_{air}}{(P_{o_2})_{ref}}\right) \tag{7.1}$$

A final issue of concern for PSP is the dependence of luminescence on temperature. Temperature sensitivity of a PSP is generated by two mechanisms, thermal quenching of the luminescent probe and temperature dependent oxygen permeability within the polymer matrix that holds the pressure-sensitive probe. Regardless of the mechanism, temperature

sensitivity must be considered a major source of error [111], particularly for low-speed measurements. Generally a pressure sensitive paint is calibrated at a series of temperatures and the appropriate calibration is applied in the data reduction process. The topic of minimizing errors in pressure sensitive paint measurements caused by variations in temperature and illumination is discussed in more detail in Binary Pressure Sensitive Paint.

7.2 Binary Pressure Sensitive Paint Measurement

It is well documented in the literature that pressure sensitive paints exhibit undesirable sensitivity to variations in temperature and illumination. In fact, these variations in temperature and illumination are identified as the major sources of error in pressure sensitive paint measurements [111]. Several techniques for minimizing errors due to variations in temperature and illumination have been demonstrated, among the most promising is the concept of using a reference luminophor that simultaneously compensates for illumination and temperature. This concept is the basis of the Binary Pressure Sensitive Paint.

7.2.1 Compensation for Variations in Illumination

The luminescent intensity F, of a temperature- or pressure-sensitive paint as a function of pressure (P), temperature (T), luminophor concentration (N), and illumination (I) can be represented as

$$F = f(P, T, N, I) \tag{7.2}$$

The common approach to eliminating variations in illumination, as well as variations in luminophor concentration or paint layer thickness, involves taking the ratio of a wind off image to that of a wind on image. This approach however assumes that the illumination at any point on the model surface is constant. The assumption of constant illumination is easily violated by slight variations in illumination intensity from the lamps, or more commonly, by slight movement or deformation of the model within the illumination field due to aerodynamic loads. The errors that result from these slight variations in illumination are more pronounced at low speeds where small changes in pressure (less than 1 psi) yield

small changes in pressure sensitive paint luminescence (less than 1%). Therefore small variations in illumination significantly degrade the quality of the pressure data in low speeds.

One means of dealing with this issue is to employ a reference luminophor as shown in Figure 7.2. The goal is to use the luminescence of the reference probe ($_R$) to correct for variations in the luminescence of the signal probe ($_S$, the pressure sensitive probe) that are caused by variations in paint illumination. This is accomplished by taking a ratio of the luminescence of the signal probe,

$$F_S = f_S(P,T,N_S,I) \tag{7.3}$$

to the luminescence of the reference probe,

$$F_R = f_R(P,T,N_R,I) \tag{7.4}$$

Assuming that both the reference and signal probes response is linearly proportional to the local illumination and luminophor number density the resulting function r is

$$r(P,T) = \frac{F_S(P,T)N_S * I}{F_R(P,T)N_R * I} = \frac{F_S(P,T)N_S}{F_R(P,T)N_R} \tag{7.5}$$

The dependence of r(P,T) on illumination has been removed, however the system is still a function of temperature, pressure, and relative luminophor concentration. Theoretically, the paint components are homogeneous and the ratio of signal probe to reference probe (N_S/N_R) is constant, experience has shown that this is not the case. To remove the variations in the relative number density of the two probes, a wind on and wind off ratio (a ratio of ratios) is used.

$$L(P,T) = \frac{r_o(P_o,T_o)^{N_S/N_R}}{r(P,T)^{N_S/N_R}} = \frac{r_o(P_o,T_o)}{r(P,T)} \tag{7.6}$$

The noise caused by the non-uniform probe concentration has been significantly reduced and the system response is now a function of pressure and temperature only. At first

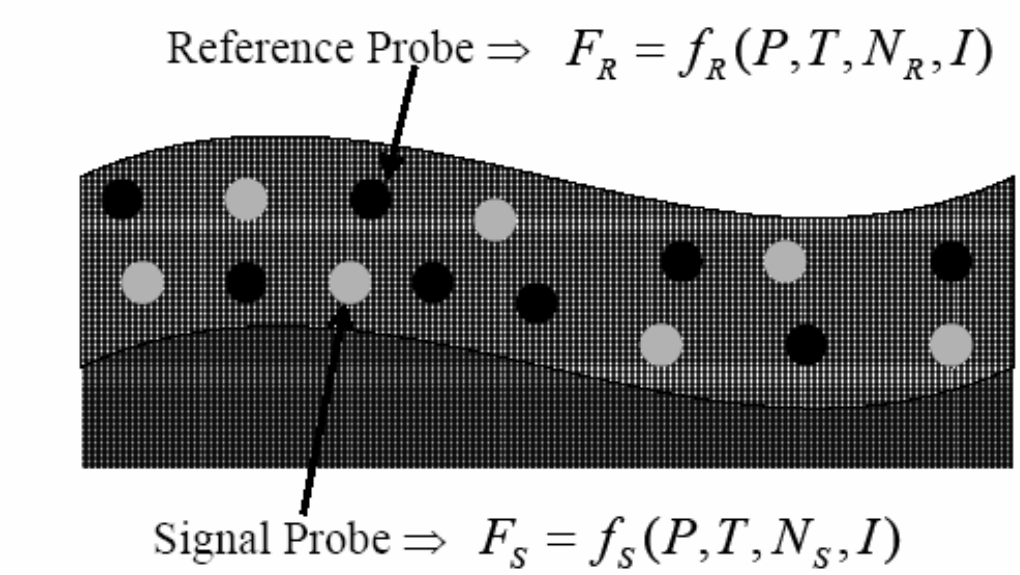

Figure 7.2. Binary pressure sensitive paint showing signal and reference probes

it may appear that little has been gained by the system described in Equation (7.6). It is still required to acquire a wind off image, in fact two images are now required at each condition rather than one. To demonstrate the power of the binary paint technique the user must also incorporate the process of image alignment or image mapping. The data reduction process described by Equation (7.6) is carried out in two steps. First the ratio of the signal probe to the reference probe is computed for both the wind off and wind on conditions. This ratio eliminates illumination from the system. Now to remove probe concentration, the wind on ratio image is mapped onto the wind off ratio image and the ratio of ratio is computed to remove the effects of probe concentration. Note that since all wind on images can be mapped back onto a single wind off image only a single wind off image is required. Used in this mode, the binary paint effectively eliminates half of the model configurations because only a single wind off condition is necessary. At the same time the errors in the pressure measurements caused by illumination have also been minimized therefore, the binary paint system provides several significant improvements over a traditional pressure sensitive paint system.

Selection of the reference probe is by no means trivial. The reference probe must be excited by the same illumination source that is used to excite the signal probe and the luminescence of the reference probe must be spectrally separated from the luminescence of the signal probe. Finally to maximize the pressure sensitivity of the system, the reference probe should exhibit as little sensitivity to pressure as possible.

7.2.2 Compensation for Temperature

With illumination removed from equation (7.6) the goal becomes minimizing the sensitivity of the system to temperature. The approach utilized involves allowing the reference probe, which is eliminating sensitivity to illumination, to compensate for the temperature sensitivity as well. While any degree of temperature-sensitivity in the reference probe will yield a reduction in the temperature sensitivity of the final pressure sensitive paint calibration, effective temperature compensation over a wide range of pressures is most easily attained by using an ideal paint.

All pressure sensitive paints exhibit some temperature sensitivity. Temperature sensitivity of pressure sensitive paint is caused by several physical processes such as temperature dependent oxygen permeability in the paint binder and thermal quenching of the luminescent probe. For most pressure sensitive paints the temperature sensitivity of the paint is a function of pressure and the pressure sensitivity of the paint is a function of temperature. This coupling of temperature and pressure sensitivity was recognized as an undesirable feature by Gouterman [112]who outlined the concept of the ideal paint. In an ideal paint the pressure dependence is not a function of temperature and the temperature dependence is not a function of pressure.

Eliminating sensitivity to temperature sensitivity is accomplished by adding two constraints to the selection criteria already outlined for a the binary paint. 1) The combination of the signal probe and paint binder must form an ideal paint. 2) The temperature sensitivity of the reference probe must match the temperature sensitivity of the ideal paint.

7.3 Temperature Sensitive Paint Measurement

High resolution non-intrusive measurements of temperature and heat transfer using temperature sensitive paint have been demonstrated by several researchers. A typical TSP consists of the luminescent molecule and an oxygen impermeable binder as seen in Figure 7.3. The basis of the temperature sensitive paint method is the sensitivity of the luminescent molecules to their thermal environment. The luminescent molecule is placed in an excited state by absorption of a photon. The excited molecule deactivates through the emission of a photon. A rise in temperature of the luminescent molecule will increase the probability that the molecule will return to the ground state by a radiationless process, this is known as thermal quenching. The temperature of the painted surface can be measured by detecting the fluorescence intensity of the luminescent paint.

The luminescent intensity of the temperature sensitive paint at a given point is not only a function of temperature. For practical applications of TSP spatial variations in illumination, probe concentration, paint layer thickness, and camera sensitivity will result

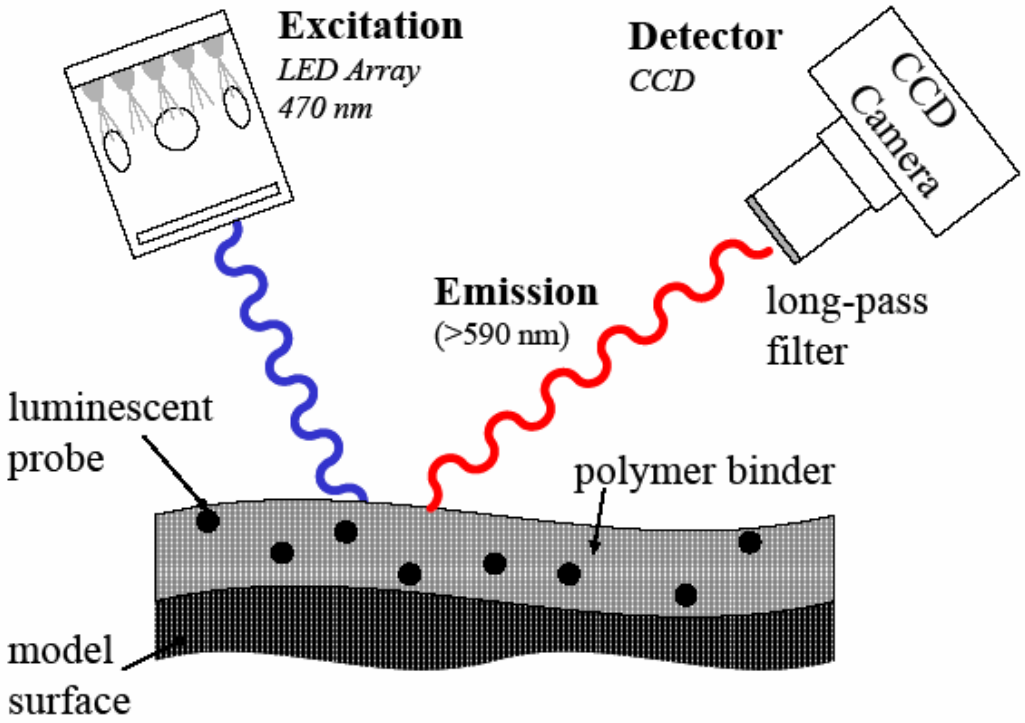

Figure 7.3. Basic temperature sensitive paint system

in a variation in the detected luminescent intensity from the test surface. These spatial variations are eliminated by taking the ratio of the luminescent intensity of the paint at the unknown test condition (wind-off) with the luminescent intensity of the paint at a known reference condition (wind-on). This is identical to the procedure utilized for pressure sensitive paints. The experimental setup for temperature sensitive paints is similar to that for pressure-sensitive paints.

7.4 Image Processing

Optical mapping methods are now widely used in turbomachinery for measurements on the blade. They require applying a data reduction method that includes image processing. From this point of view, Pressure Sensitive Paint (PSP) and Temperature Sensitive Paint (TSP) methods are an extremely demanding techniques. PSP and TSP techniques use images that have to be processed to calculate the pressure and temperature field on the model. The image processing procedure utilized in this study for the pressure and temperature images consists of three steps including:

- image averaging
- alignment and ratio of wind-off and wind-on images,
  - using cross correlation method
  - using the markers
- conversion to temperature and pressure .

7.4.1 Image Averaging

Images are taken for one steady and two unsteady inlet flow conditions for different Reynolds numbers and turbulence intensity levels on the suction and the pressure surface of a LPT blade at 39 streamwise positions for suction surface and 50 streamwise positions for pressure surface. The borescope which is connected to the CCD-camera traverses for PSP measurements from leading edge to the trailing edge by a stepper motor driven traversing system with micro motion capability and optical encoder feedback. Images obtained from the camera at different streamwise positions is saved as TIF images. To

increase the signal-to-noise of the experimental data, 250 images were averaged for each experimental configuration (wind-on and wind-off). The average pixel intensity is calculated from these images.

7.4.2 Image Alignment

Test image alignment is needed, firstly for image averaging, when the borescope experiences vibration, secondly it can be used to relate pixels in wind-off and wind-on images before rationing, and thirdly it can be used to combine the overlapping images. This alignment must be done with high accuracy because the final quality of the pressure mapping depends greatly on it. For the real measurements images are either mapped using markers or aligned using the same markers. There are two main methods developed for the image alignment; (1) cross-correlation method, (2) geometrical positioning using markers.

Image Alignment Using Cross-Correlation Method: In this example as described in detail in [113], the data to be processed is the film cooling effectiveness results obtained using PSP technique from the film cooling blade. Images are taken along the leading edge of a turbine blade at 16 positions. The program using the cross-correlation approach is used to create a single image by combining and aligning the overlapping images.

This is a basic statistical approach for measuring similarity between the two overlapping images. For these two overlapping images, the two dimensional normalized cross-correlation measuring the similarity for each translation (Δx, Δy) can be obtained by equation (7.7).

$$r(\Delta x, \Delta y) = \frac{\sum_{x=1}^{N_x}\sum_{x=1}^{N_y} I_m(x,y).I_{ma}(x+\Delta x, y+\Delta y)}{\sqrt{\sum_{x=1}^{N_x}\sum_{x=1}^{N_y} {I_m}^2(x,y)}.\sqrt{\sum_{x=1}^{N_x}\sum_{x=1}^{N_y} {I_{ma}}^2(x+\Delta x, y+\Delta y)}} \qquad (7.7)$$

In (7.7) r is the cross correlation factor with 0's representing the minimum match and 1's indicating the maximum match of the overlapping images. I_{im} is the intensity of the main picture at the coordinates of x and y, while I_{ma} is the intensity of the mask picture as shown in Figures 7.4 and 7.5. The result of the correlation is the percentage of the match of the mask and the main picture as seen in Figure 7.6. In the following example a part of the left image is the mask, and the right image is the main image. The unusable data from pixel 1 to 20 in the x-direction in the left image is due to the inhomogeneous laser light, and this data will be eliminated during image processing. At the location of the maximum cross-correlation factor the program merges both images as seen in Figure 7.7.

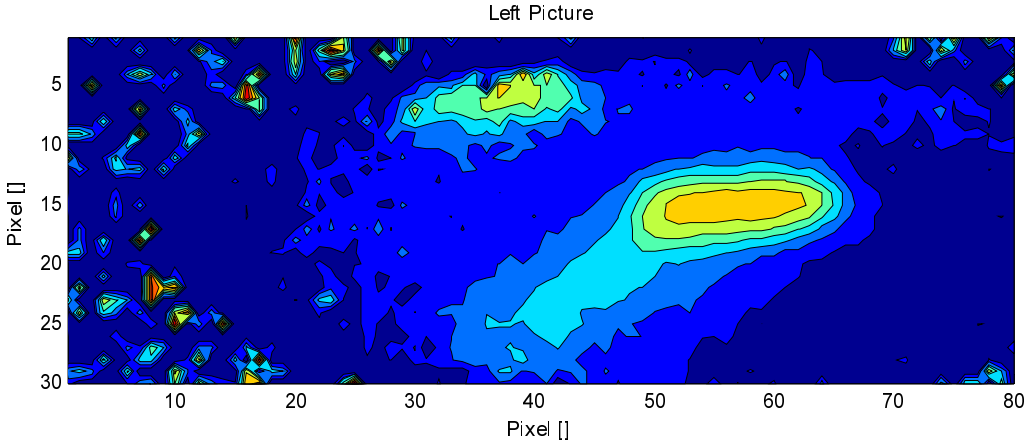

Figure 7.4. Left picture

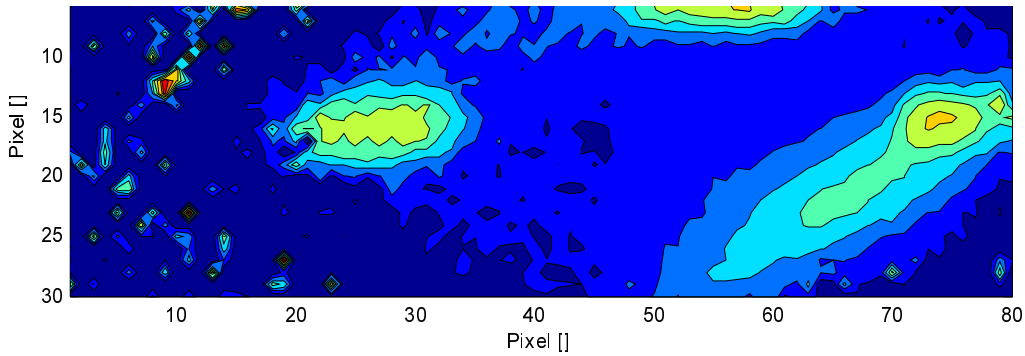

Figure 7.5. Right picture

The correlation r is shown in the following figure:

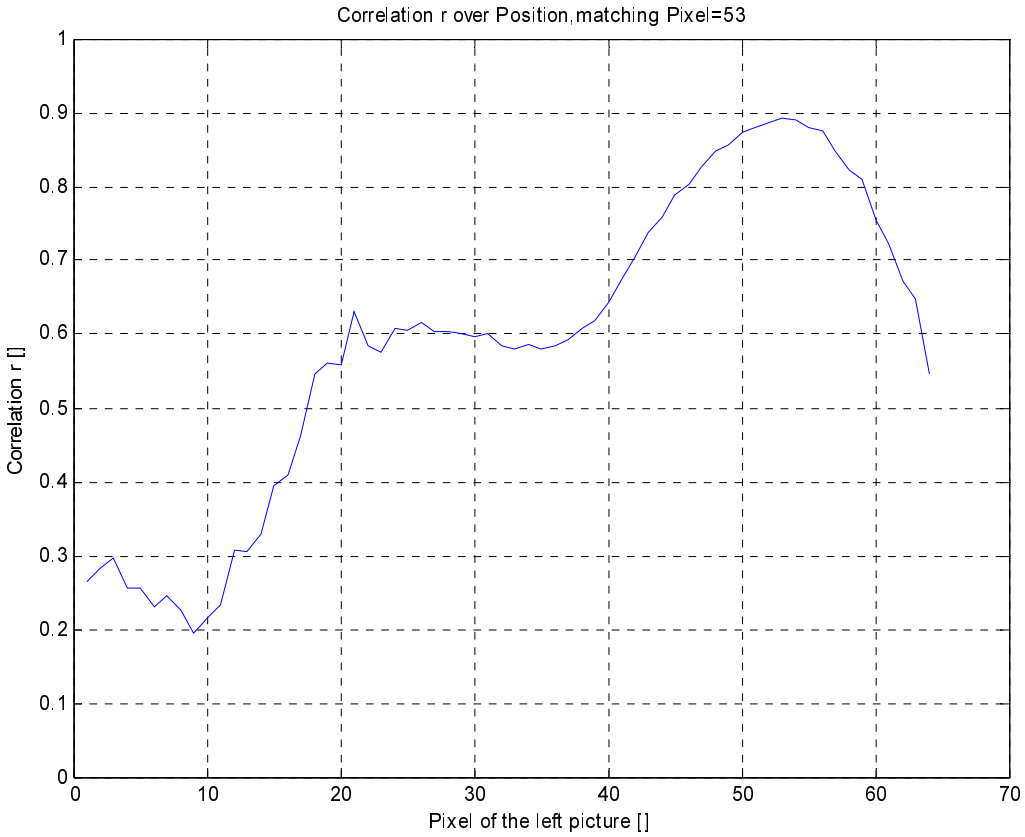

Figure 7.6. Cross-correlation factor of r

The resulting picture is:

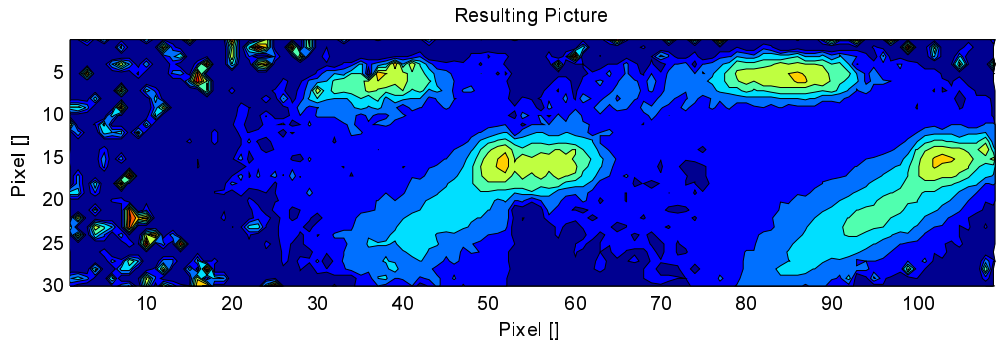

Figure 7.7. Merged picture

Due to the inhomogeneous data quality, the resulting picture shows a non-continuous part at pixel 53. To solve this problem, an averaging operation was performed. At the left edge of the overlapping area, the weighting function of the left picture is 90 % and the weighting function of the right picture is 10 %. At the right edge it is the other way around. This averaging function is shown in the following Figure 7.8.

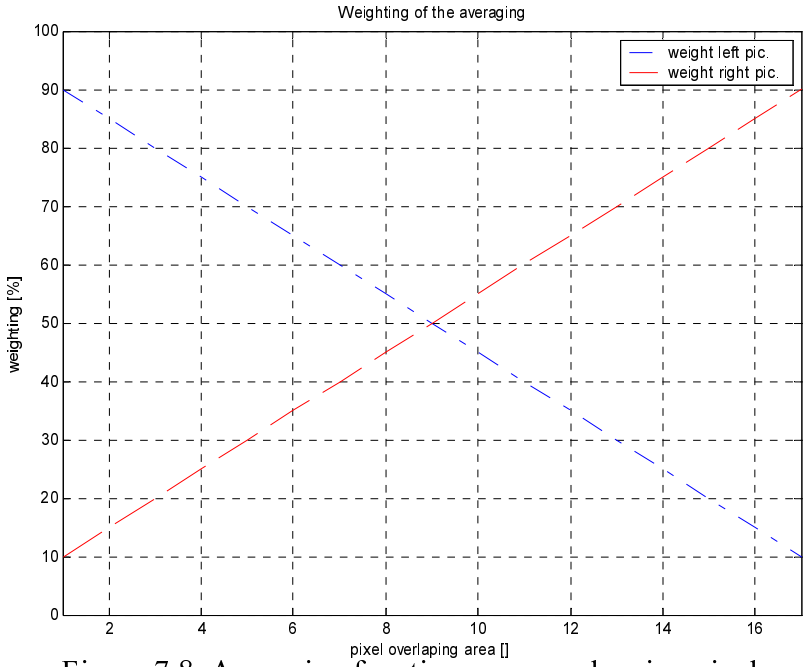

Figure 7.8. Averaging function over overlapping pixels

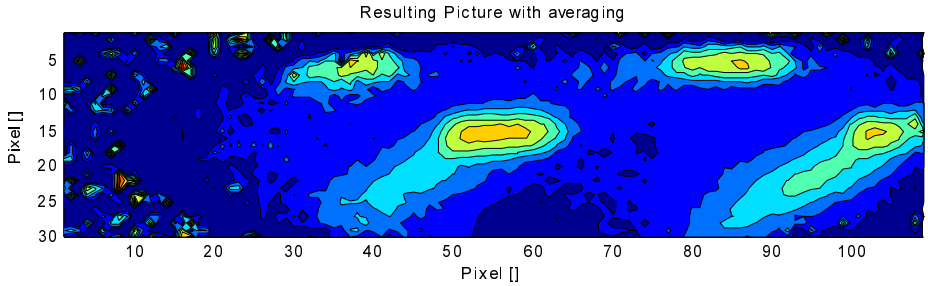

Figure 7.9. Resulting picture with weighting function

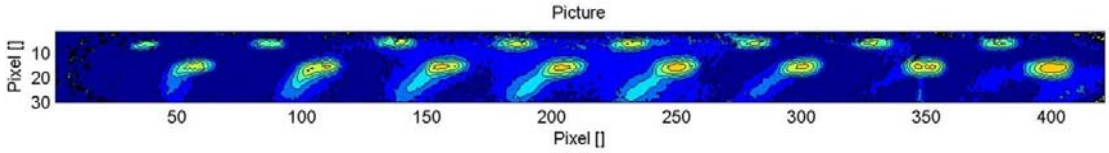

Figure 7.10. Complete merged picture

The result of the averaging is shown in the following picture as in Figures 7.9 and 7.10.

To verify the averaged data set, the "search" mode of the correlation program is used. This mode is able to locate the position of a picture fragment over the main picture. This operation was performed for original data of the third hole from the left. Third hole was identified correctly with a match of 99.35 % as shown in Figures 7.11 and 7.12.

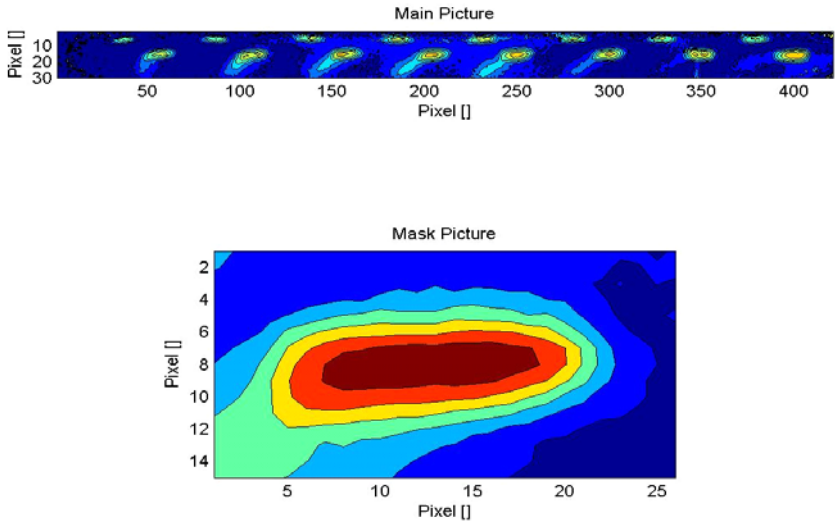

Figure 7.11. Main and the mask picture

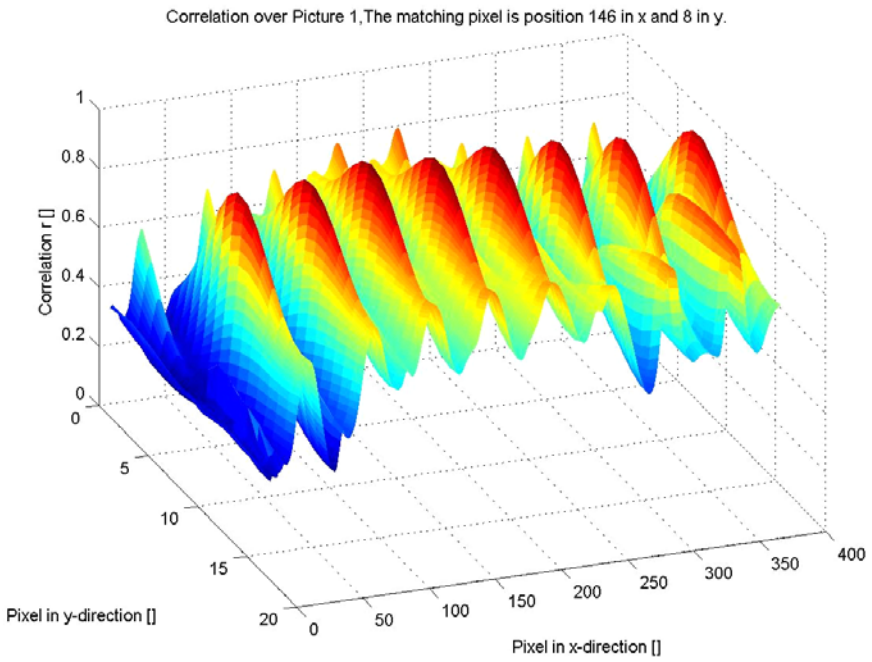

Figure 7.12. Cross-correlation factor for matching the cropped data

Image Alignment Using the Markers: Markers are placed (painted marks, holes...) for providing a geometric reference on the test object during data acquisition and processing. They can be any visible features on the model such as static pressure taps and film cooling holes. The contours of the model are not suitable markers as they are often not clearly distinguishable, even with advanced image processing tools, this is due to blurring effect and lightning conditions. The method with markers relies on the ability to find centers of markers with sub-pixel precision. Thus, the markers to be recognized with sub-pixel accuracy are generally made to be a few pixels in size. This method has several limitations: the models have to have markers themselves which is not possible sometimes, the markers should be distributed evenly on the surface of the model, because the error in determining relation between pixels increases in the outer areas.

In this example, the data to be processed is the pressure and temperature results obtained using PSP and TSP measurement techniques from LPT blade. Images of the marker are taken along the suction and pressure surface of a turbine blade at 50 different streamwise positions. The program using the geometrical positions of the markers is used to create a single image by combining and aligning the overlapping images.

This is the basic geometrical approach for measuring similarity between the two overlapping images and aligning the wind-on and wind-off images. For these two overlapping images, the centers of markers is found with sub-pixel precision. Images are taken for one steady and two unsteady inlet flow conditions for different Reynolds numbers and turbulence intensity levels on the suction and the pressure surface. The borescope which is connected to the CCD-camera traverse for PSP and TSP measurements from leading edge to the trailing edge. The third axis is capable of rotating with an angular accuracy of less than 0.05^{o}, which is specifically required for TSP and PSP investigations where the borescope has to be perpendicular to the blade surface. Images obtained from the camera at different 50 streamwise positions is saved as TIF images. 300 images are captured for each case and the average pixel intensity is calculated from these images. Unprocessed images with markers from the first four streamwise position is shown in Figure 7.13. Each single images are rotated and cropped for the required size before combining the

overlapping images as shown in Figure 7.14. To increase the quality of the combined image, the overlapping pixels are averaged and presented in Figure 7.15.

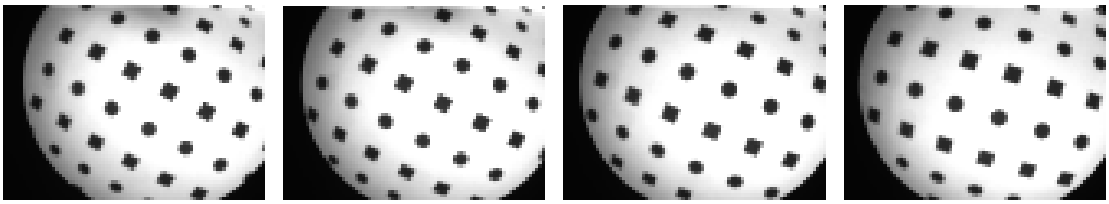

Figure 7.13. Unprocessed images from the first four streamwise position

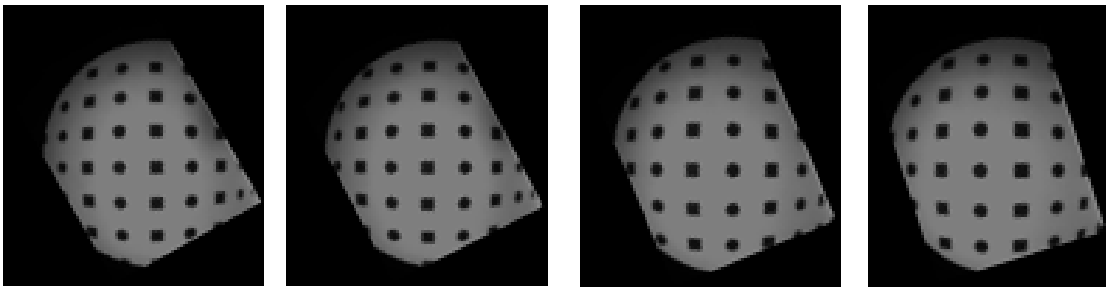

Figure 7.14. Rotated images before merging the overlapped areas of the first four streamwise position

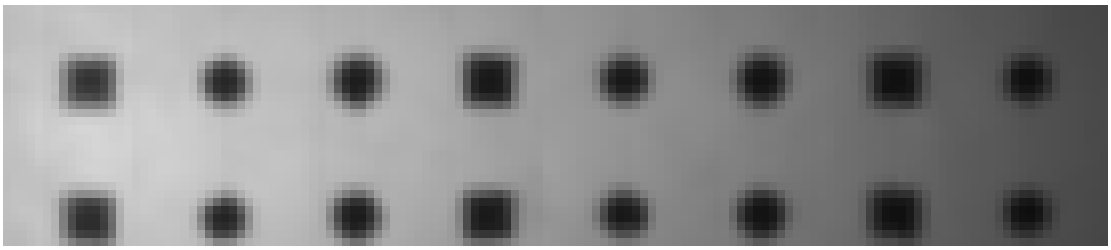

Figure 7.15. Combined image of the first four streamwise position

7.4.3 Conversion to Pressure and Temperature Fields

The temperature and pressure fields are calculated from the relative intensity distributions by using the calibration coefficients. The calibration data sets are obtained in a vacuum chamber capable of precise control of temperature and pressure. The calibration data for the pressure sensitive paint is fitted with the following equation:

$$P = a_o + a_1 I_r + a_2 I_r^2 \tag{7.8}$$

where I_r is the relative intensity in the pressure sensitive data and a_i is the pressure calibration coefficient. The calibration data for the temperature paint are fitted with the following equation:

$$T = b_0 + b_1 I_r + b_2 I_r^2 \tag{7.9}$$

where I_r is the relative intensity in the temperature sensitive data, and b_i is the temperature calibration coefficient.

8. DATA REDUCTION AND ANALYSIS FOR HOT WIRE AND SURFACE MOUNTED HOT-FILM SENSORS

As explained in the earlier sections, digital data acquisition is used for automating the data acquisition procedure. This section deals with the methods used to reduce and analyze the digitized data obtained from single hot-wire and surface mounted hot-film sensors..

8.1. Data Reduction and Analysis for Hot Wire Sensors

8.1.1 Data Reduction for Boundary Layer Measurement

A single hot-wire probe is used for boundary layer development study. The response of boundary layer to one steady and two periodic unsteady flow conditions have been investigated.

Steady Flow: For data reduction and analysis, the characteristic response of the hot wire probe is stored in form of calibration constants. The instantaneous velocity component is calculated from the temperature compensated instantaneous voltages by using the calibration coefficients. The instantaneous velocity is represented in the following form:

$$V = \overline{V} + v \tag{8.1}$$

where $\overline{V}$ is the mean (time-averaged) velocity and v is the turbulent fluctuation component. The mean velocity, also known as the time-average, is given by:

$$\overline{V} = \frac{1}{N}\sum_{j=1}^{N} V_j \tag{8.2}$$

where N is the total number of samples taken at one boundary layer location. A sampling rate of 20kHz was used for investigating the steady flow (no wakes). The root mean square value of the turbulent velocity fluctuation is obtained from the instantaneous and mean velocities by:

$$v = \sqrt{\frac{1}{N}\sum_{j=1}^{N} (V_j - \overline{V})^2} \tag{8.3}$$

and the local turbulence intensity is defined as:

$$Tu_{loc} = \frac{v}{\overline{V}} \times 100 = \frac{1}{\overline{V}} \sqrt{\frac{1}{N} \sum_{j=1}^{N} (V_j - \overline{V})^2} \times 100 \tag{8.4}$$

Periodic Unsteady Flow: The unsteady data are reduced by ensemble-averaging method with respect to the rotation of the wake generator. At each boundary location, 20,000 samples are taken at a sampling rate of 20 kHz. The ensemble-averaged results are calculated for 100 rotation of the wake generator. For unsteady cases, the ensemble-averaged velocity, fluctuation velocity, and the turbulence intensity are calculated from the instantaneous velocity samples by:

$$V_i(t_i) \equiv < V_i(t_i) > \equiv \frac{1}{N} \sum_{j=1}^{N} V_{ij}(t_i) \tag{8.5}$$

$$v_i(t_i) \equiv < v_i(t_i) > = \sqrt{\frac{1}{N} \sum_{j=1}^{N} [V_{ij}(t_i) - < V_i(t_i) >]^2} \tag{8.6}$$

$$Tu_i(t_i) \equiv < Tu_i(t_i) > = \frac{< v_i(t_i) >}{< V_i(t_i) >} \times 100 \tag{8.7}$$

where N= 100 is the total number of wake generator cycles. $<V_i\ (t_i)>$ is the ensemble averaged velocity for a particular spatial location.

The ensemble-averaged boundary layer parameters such as displacement thickness $<\delta_1>$, momentum thickness $<\delta_2>$, and shape factor $<H_{12}>$ are calculated from:

$$\delta_1 \equiv < \delta_1 > = \int_0^{<\delta>} \left(1 - \frac{< V >}{< V >_e}\right) dy \tag{8.8}$$

$$\delta_2 \equiv < \delta_2 > = \int_0^{<\delta>} \frac{< V >}{< V >_e} \left(1 - \frac{< V >}{< V >_e}\right) \tag{8.9}$$

$$H_{12} \equiv < H_{12} > = \frac{< \delta_1 >}{< \delta_2 >} \tag{8.10}$$

8.1.2 Accurate Estimation of Boundary Layer Thickness

The accuracy of the boundary layer parameters such as displacement, momentum, and energy thickness depends primarily on an accurate estimation of the boundary layer thickness δ. Since in a turbine or compressor blade channel the velocity distribution outside the boundary layer is not constant as shown in Figure 8.1 (a). The estimation method used in conventional flat plate boundary layer calculation leads to incorrect results. In the following, a simple iterative method, developed by Schobeiri [114], is presented that accurately determines the boundary layer thickness and thus the boundary layer parameters.

In Figure 8.1 the experimental velocity distribution on the pressure and suction surfaces are shown. To determine the boundary layer thickness, first a least square fit (LSQ) is performed and the velocity profile outside the boundary layer and its intersection with the u-axis is found. Starting from a first guessed value δ^1, the area F^1 is found using the relation:

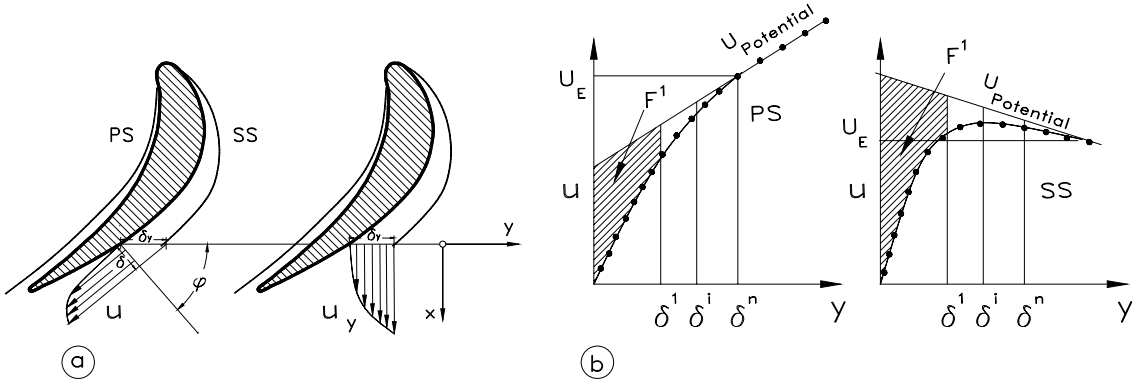

Figure 8.1. (a) Boundary layer velocity traverse, (b) boundary layer edge velocity on pressure and suction side from Schobeiri [114]

$$F^1 = \int_0^{\delta^1} (U_{pot} - u)dy \tag{8.11}$$

In the next iteration step with δ^i the boundary of the integral in (8.11) is increased by a very small increment (for example 0.001mm) and the area F^i is calculated:

$$F^i = \int_0^{\delta^i} (U_{pot} - u)dy \tag{8.12}$$

We define the following ratio with the accuracy ϵ:

$$R = \frac{\left|F^i - F^{i+1}\right|}{F^i} \leq \varepsilon = 10^{-6} \tag{8.13}$$

and check if the ϵ has been reached. If the next iteration step with δ^{i+1} fulfils the above criterion, then the desired boundary layer thickness is δ^n , which can be used or the boundary layer thickness to be implemented into equations (8.8) to (8.10).

8.2. Data Reduction and Analysis for Surface Mounted Hot-Film Sensors

The surface hot-film technique is very similar to hot wire anemometry. A thin nickel film form one resistor of a Wheatstone bridge and an adjust resistor in the opposite bridge arm unbalances the bridge. Due to individual adjust resistors the overheat temperature could be set to the same ΔT for very sensor, even tough the wall temperature and the resistance vs. temperature calibrations may have been different.

The hot-film resistance is a function of temperature, which depends on the current through the film. A feedback amplifier varies the bridge voltage and thereby the current, which changes the gauge resistance until the bridge is balanced again. The resulting constant hot-film resistance leads to a constant hot-film temperature. The power required to keep the film temperature constant depends on its heat loss towards the fluid. Thus, the constant temperature hot-film anemometer output power is proportional to the heat transfer from the sensor to the flow. For this reason, the sensors must be heated to enable constant temperature hot-film anemometer output signals. The bridge is adjusted to attain a sensor

temperature 60 K higher than the flow temperature. Experience made by several other authors shows that this is the best trade-off between the quality of the signals and the life time of the sensors.

8.2.1 Overheat Ratios and Frequency Response

The over heat ratio is defined as

$$OverHeatRatio = \frac{R}{R_o} \tag{8.14}$$

where R is the resistance of the sensor (wire or film) at the overheat temperature, and R_o is the resistance of the sensor at the flow temperature. Using the highest possible overheat ratio ensures the highest frequency response from the system. The frequency response of the films and wires are further optimized with a square wave test signal that was available from the anemometer bridges. For hot wires, an overheat ratio of 1.8 is used, while this value is 1.2 for the surface mounted hot-film sensors. The temperature of a sensor can be calculated with knowledge of its thermal coefficient of resistivity, α from (8.15).

$$T = T_o + \left(\frac{R}{R_o} - 1 \right) \frac{1}{\alpha} \tag{8.15}$$

8.2.2 Evaluation of Surface Hot-Film Sensors

The output signal of the hot film anemometry can be related to the wall shear stress τ_w. The measurement of wall shear stress using hot film sensors was developed by Bellhouse and Schultz [115]. The operation of hot film sensors relies on the similarity between the velocity boundary layer and the thermal boundary layer generated by a hot film sensor. The heat transfer from the hot film sensor is related to the bridge output voltage as shown below:

$$Q_w \propto E^2 \propto \Delta T$$

The relation between the wall shear stress and the heat transfer by convection to the fluid is given by (8.16).

$$a\tau_w^{1/3} = \frac{\dot{Q}_w}{\Delta T} \tag{8.16}$$

where $\dot{Q}_w$ is the heat emitted by the sensor and ΔT the difference in temperature between the sensor and the flow. The overall heat dissipated by a hot-film sensor, $\dot{Q}_w$ can be expressed in terms of electrical power with the voltage on the sensor and its resistance;

$$\dot{Q}_w = \frac{E^2}{R} - \frac{E_0^2}{R_o} \tag{8.17}$$

The constant *a* can be determined by calibration, but this is a difficult and time-consuming process. Also, errors of 20-30% or more can arise when hot films are calibrated in a laminar flow are used in a turbulent flow. Thus, a calibration of the hot film sensors is not feasible here. However, according to Schröder [116] the qualitative relation between the cube root of the wall shear stress and the hot film signal, provides already sufficient information on the state of boundary layers. Haueisen [117], Tiedemann [118] came to the same conclusion during his research, the surface mounted hot film technique can be successfully applied in a qualitative manner. The effects of possible manufacturing differences of the hot film sensors can be eliminated by normalizing the signals with E_o (Schröder [110]). Thus the parameter $(E-E_o)/E_o$, which is used throughout this investigation, is proportional to $\tau_w^{1/3}$ and enables the comparison of signals from different sensors.

The unsteady data from surface mounted hot film sensors are reduced by ensemble-averaging method with respect to the rotation of the wake generator. At each boundary location, 10,000 samples were taken at a sampling rate of 10 kHz. The ensemble-averaged results were calculated for 50 rotation of the wake generator. For unsteady cases, the ensemble-averaged of the output voltage, RMS value of the voltage E_{RMS}, and the turbulence intensity were calculated from the instantaneous velocity samples by:

$$E_i(t_i) \equiv < E_i(t_i) > \equiv \frac{1}{N}\sum_{j=1}^{N} E_{ij}(t_i) \tag{8.18}$$

$$E_{RMS}(t_i) \equiv < E_{rms}(t_i) > = \sqrt{\frac{1}{N}\sum_{j=1}^{N} [V_{ij}(t_i) - < V_i(t_i) >]^2} \tag{8.19}$$

where N= 50 is the total number of wake generator cycles and M the number of samples taken per cycle. $<E_i (t_i)>$ is the ensemble averaged voltage value for a particular spatial location.

Dimensionless parameter of $f(s/s_o)$ as shown below, is proportional to the cube root of the wall shear stress

$$f(s/s_o) = \frac{E - E_o}{E_o} \tag{8.20}$$

Dimensionless RMS voltage distribution is represented in the following for,

$$f'(s/s_o) = \frac{E_{RMS}}{E_o} \tag{8.21}$$

9.UNCERTAINTY ANALYSIS

Uncertainty analysis is performed on the single hot-wire measurements after calibration and data reduction utilizing the methods of Kline-McClintock [119] and Yavuzkurt [120]. Kline and McClintock presented a technique to calculate how the uncertainty in individually measured values add together to result in an uncertainty for a quantity calculated from those values. However, it should be noted that the determined uncertainty may not be the actual uncertainty of the results because the Kline and McClintock method calculates the worst possible uncertainty. The main difference between these two uncertainty analysis method is coming from the way in which the actual uncertainty is calculated. The uncertainty for the Kline and McClintock method is a equivalent to the 95% confidence band that surrounds the single hot-wire curve fit. Since each point may have a different confidence interval, the uncertainty for each data point may be different. On the other hand, Yavuzkurt calculates the uncertainty by taking the square root sum of the squared errors divided by the number of data points. The results of the uncertainty analysis and the most significant equations used to determine the uncertainty for each case is presented below with the actual calculations documented in Appendix B.

9.1 Uncertainty Analysis for Single Hot-Wire Measurements

The uncertainty in velocity for the single hot-wire probe after calibration and data reduction is given in Table 9.1 for the Kline and McClintock and Table 9.2 for the Yavuzkurt method. In addition, the uncertainty in velocity for the X-wire probe after calibration and data reduction is given in Table 9.3. The uncertainty in velocity during calibration increases when the flow velocity decreases. It is primarily due to large uncertainty in the pressure transducer that is used for calibration. As for the uncertainty in velocity after data reduction, the trend continues due to the fact that the calibration uncertainty is incorporated into the final velocity. For this case, the pneumatic velocity uncertainty and the total calibration uncertainty was determined using Equations (9.1) and (9.3.)

The uncertainty in the pneumatic velocity was found with the following equation;

$$\omega_v = \sqrt{\left[\left(\frac{\partial V}{\partial P}\right)\omega_p\right]^2 + \left[\left(\frac{\partial V}{\partial \rho}\right)\omega_\rho\right]^2 + \left[\left(\frac{\partial V}{\partial D_{ni}}\right)\omega_{D_{ni}}\right]^2 + \left[\left(\frac{\partial V}{\partial D_{no}}\right)\omega_{D_{no}}\right]^2} \qquad (9.1)$$

In the above equation, ω_p is the uncertainty of pressure readings from pressure transducer, ω_ρ is the uncertainty during the calculation of density, $\omega_{Dno,}$ ω_{Dni} are respectively the uncertainty of the outer and inner diameter of calibration nozzle. The pneumatic velocity is calculated:

$$V = \sqrt{\frac{2P}{\rho\left[1 - \left(\frac{D_{no}}{D_{ni}}\right)^4\right]}} \qquad (9.2)$$

In the above equation, P is the transducer pressure, D_{no} is the outside diameter of the calibration nozzle, D_{ni} is the inside diameter of the nozzle, ρ is the air density. The uncertainty in the effective velocity after the calibration for the Kline and McClintock method is:

$$\omega_{Ve_j} = \sqrt{\left(\frac{\partial Ve_j}{\partial e_j}\omega_{e_j}\right)^2 + \omega_{cf}{}^2 + \omega_V{}^2} \qquad (9.3)$$

where ω_{Ve} is the effective velocity, ω_e is the uncertainty of the constant hot wire anemometry voltage readings, ω_V is the velocity and ω_{cf} is the uncertainty of the least square fit and equivalent to the 95% confidence interval which surrounds the curve fit. The effective velocity for any particular wire is represented by the following equation:

$$Ve_j = a_{0j} + a_{1j}E_j + a_{2j}E_j{}^2 + a_{3j}E_j{}^3 + a_{4j}E_j{}^4 \qquad (9.4)$$

where a_{ij} are the coefficients determined by the least square fit.

As for the uncertainty in velocity after data reduction, it is given by the following equation;

$$\omega_{V_r} = \sqrt{\left(\frac{\partial V_r}{\partial e}\omega_e\right)^2 + \omega_{calib}{}^2} \tag{9.5}$$

where ω_{calib} is the uncertainty in the calibration.

The uncertainty in the curve fit from S. Yavuzkurt method is given by;

$$C_s = \frac{\sum_{i=1}^{n}\left[\left(\frac{\Delta V}{Ve}\right)^2 * i\right]^{\frac{1}{2}}}{n} \tag{9.6}$$

where n is the number of data points, and ΔV is the residual. This value is squared and added to the square of $\Delta V/V$, and raised to the one half power. This calculated value is the uncertainty of effective velocity.

The curve fit uncertainty for the Yavuzkurt method is much larger than the uncertainty determined from the 95% confidence interval.

Table 9.1. Uncertainty in velocity after calibration and data reduction for single wire (Kline and McClintock Method)

V (m/s)	$\omega V/V$ (%)	$\omega V_e/V_e$ $(\%)_{calib}$	$\omega V/V$ $(\%)_{red}$
3	5.59	5.92	6.07
5	2.06	2.36	2.44
10	0.54	0.76	0.83

Table 9.2. Uncertainty in velocity after calibration and data reduction for single wire (Yavuzkurt Method)

V (m/s)	$\omega V/V$ (%)	$\omega V_e/V_e$ (%)$_{calib}$	$\omega V/V$ (%)$_{red}$
3	5.59	5.71	5.72
5	2.06	2.30	2.35
10	0.54	1.28	1.37

Table 9.3. Uncertainty in velocity after calibration and data reduction for X- wire (Kline and McClintock Method)

C (m/s)	$\omega C/C$ (%)	$\omega V_e/V_e$ (%)	$\omega\alpha_{id}/\alpha_{id}$(%)	$\omega H^*/H^*$ (%)
5	1.96	2.19	3.85	2.97
10	0.49	1.12	1.85	1.42
15	0.23	1.03	1.63	1.28

9.2 Uncertainty Analysis for Liquid Crystal Measurements

Using Kline-McKlintock uncertainty analysis, the uncertainty in heat transfer coefficient given by Equation (13.1):

$$\frac{w_h}{h} = \sqrt{\left(\frac{w_{Q_{conv}}}{Q_{conv}}\right)^2 + \left(\frac{w_{T_{yl}-T_\infty}}{T_{yl}-T_\infty}\right)^2} \tag{9.7}$$

Similarly, from Equation (13.2), the uncertainty in Q_{conv}, Q_{foil} and Q_{rad} is given by:

$$\frac{w_{Q_{conv}}}{Q_{conv}} = \sqrt{\left(w_{Q_{foil}}\frac{Q_{foil}}{Q_{foil}-Q_{rad}}\right)^2 + \left(w_{Q_{rad}}\frac{Q_{rad}}{Q_{rad}-Q_{foil}}\right)^2} \tag{9.8}$$

and

$$w_{Q_{foil}} = \sqrt{\left(\frac{w_v}{V}\right)^2 + \left(\frac{w_I}{I}\right)^2} \tag{9.9}$$

$$w_{Q_{rad}} = \sqrt{\left(\frac{\partial Q_{rad}}{\partial T_{yl}} w_{T_{yl}}\right)^2 + \left(\frac{\partial Q_{rad}}{\partial T_{\infty}} w_{T_{\infty}}\right)^2} \tag{9.10}$$

Uncertainties in heat transfer coefficients are calculated using the above expressions and are tabulated in Table 9.4 for suction surface measurements. The uncertainties in heat transfer coefficients are 4.5% approximately. These uncertainties arise mainly due to the higher uncertainty in radiation heat loss form the blade surface. Also, uncertainties in radiation heat losses are sensitive to individual uncertainties in the measurement of yellow line temperature and the temperature of the free stream air. These values are taken to be 0.5 K which is the uncertainty with the thermocouples used in the measurement of the free stream air. Uncertainties in the heat inputs to the blade are of the order of 0.4% and are relatively low when compared to the radiation losses. Also, uncertainties increase with decreasing energy input. This is acceptable because higher heat transfer coefficients will be more accurate and this is important for the prediction purposes near the leading edge of the turbine blade. The uncertainties calculations are given in detail in Appendix B.

Table 9.4. Uncertainties on suction surface of the turbine blade
for Ω=0 and Tu=1.9, 3, 8 and 13% at Re=110,000

s/s_0	w_h/h(%) at Tu_{in}=1.9%	w_h/h(%) at Tu_{in}=3%	w_h/h(%) at Tu_{in}=8%	w_h/h(%) at Tu_{in}=13%
0.1	3.7845	3.3319	6.4702	5.5869
0.3	3.7263	3.3751	6.1126	5.9434
0.5	3.6045	3.6984	5.9884	5.8282
0.7	3.7845	3.2722	6.7059	5.7276
0.9	3.7506	3.1788	6.822	5.4456

9.3 Uncertainty Analysis for PSP Measurements

The error in the pressure measurement can have contributions from several factors including detector thermal noise, temperature measurement uncertainty, system contamination (fog, oil, dust), and many other effects that can influence intensity based measurements. These error sources can be categorized into three separate error contributions, namely, calibration error, intensity measurement error and temperature measurement error. Both contribute to the error in the derived pressure field, but with different weighting factors. To understand these errors, an analysis of the measurement uncertainty is in order.

The pressure images are converted to absolute pressure through fitted calibration curves. The error in the measured pressure is given by

$$w_p = \left[\left(\sum_{i=1}^{3} \left(\frac{\partial P}{\partial a_i} \right)^2 w_{a_i}{}^2 \right) + w_{cal}{}^2 + \left(\frac{\partial P}{\partial I_r} \right)^2 w_{I_r}{}^2 + \left(\frac{\partial P}{\partial T} \right)^2 w_T{}^2 \right]^{1/2} \tag{9.11}$$

where the first term represents the error in the calibration coefficients, the second term represents the error during the calibration, the third term represents the error in the intensity measurement, and the fourth term represents the error in the temperature measurement. Making the simplifying assumption that the maximum errors are due to the calibration, the intensity and temperature measurements, Equation (9.11) reduces to

$$w_p = \left[w_{cal}{}^2 + \left(\frac{\partial P}{\partial I_r} \right)^2 w_{I_r}{}^2 + \left(\frac{\partial P}{\partial T} \right)^2 w_T{}^2 \right]^{1/2} \tag{9.12}$$

Utilizing the calibration parameters, the measurement error predicted by Equation (9.12) can be evaluated for the PSP used in this study. For Uni-PSP, the uncertainty increased dramatically with elevated temperature. Again this is due to the high sensitivity of the PSP to temperature changes at elevated temperatures. This indicates that highly accurate temperature measurements are needed for accurate determination of the pressure

field. This is the case even in static wind tunnel tests where the change in the surface temperature is expected to be only a few degrees. Making the simplifying assumption for the binary-PSP ,the maximum errors are due to the calibration and the intensity measurements, Equation (9.13) reduces to

$$w_p = \left[{w_{cal}}^2 + \left(\frac{\partial P}{\partial I_r} \right)^2 {w_{I_r}}^2 \right]^{1/2} \tag{9.13}$$

The uncertainty for PSP measurements is estimated to be ≈5%. This uncertainty is contributed by the uncertainties in calibration (4%) and image capturing (1%). Also, the level of the shot noise was estimated to be 0.4% [111], [121].

9.4 Uncertainty Analysis for TSP Measurements

As described in the previous section, for the determination of uncertainties for PSP measurements, the error in the temperature measurement can have contributions from several factors including detector thermal noise, system contamination (fog, oil, dust), and many other effects that can influence intensity based measurements. These error sources can be categorized into two separate error contributions, namely, intensity measurement error and calibration error. Both contribute to the error in the derived temperature field, but with different weighting factors. To understand these errors, an analysis of the measurement uncertainty is in order.

The temperature images are converted to absolute temperature through fitted calibration curves. The error in the measured temperature is given by

$$w_T = \left[\left(\sum_{i=1}^{3} \left(\frac{\partial T}{\partial b_i} \right)^2 {w_{b_i}}^2 \right) + {w_{cal}}^2 + \left(\frac{\partial T}{\partial I_r} \right)^2 {w_{I_r}}^2 \right]^{1/2} \tag{9.14}$$

where the first term represents the error in the calibration coefficients, the second term represents the error during the calibration, the third term represents the error in the intensity

measurement. Making the simplifying assumption that the maximum errors are due to the calibration and the intensity, Equation (9.14) reduces to

$$w_T = \left[{w_{cal}}^2 + \left(\frac{\partial T}{\partial I_r} \right)^2 {w_{I_r}}^2 \right]^{1/2} \tag{9.15}$$

Utilizing the calibration parameters, the measurement error predicted by Equation (9.15) can be evaluated for TSP used in this study. For this study, the uncertainty for TSP measurements is estimated to be ≈5%. This uncertainty is contributed by the uncertainties in calibration (4%) and image capturing (1%). Also, the level of the shot noise was estimated to be 0.4% [111], [121].

10. INLET FLOW CONDITIONS

To investigate the influence of the unsteady wake flow, and freestream turbulence intensity levels on the boundary layer development along the suction and pressure surfaces of the LPT blade and, particularly, its impact on the inception and onset of the separation bubble, the detailed inlet velocity, turbulence measurements, length scale, and angle distributions were performed at a Reynolds number of 110,000.

10.1 Inlet Velocity and Turbulence Measurements Along the Horizontal Slots

The freestream uniformity of the approach velocity and turbulence level measurements have been performed upstream of the leading edge along the three different horizontal slots as shown in Figure 4.1 by using the X-wire probe as shown in Figure 10.1. The probe traverse covered the full extent of the straight duct length of x=580 mm, 420 mm, 260 mm that corresponds the upper, middle, and lower section of the horizontal slots.

For the inlet flow measurements, the calibration of hot wire and five-hole probe is very important and is performed in a low turbulence, uniform flow, open jet calibrating test facility. A simple and accurate method by John and Schobeiri [105] has been used for calibrating the X-wire probe.

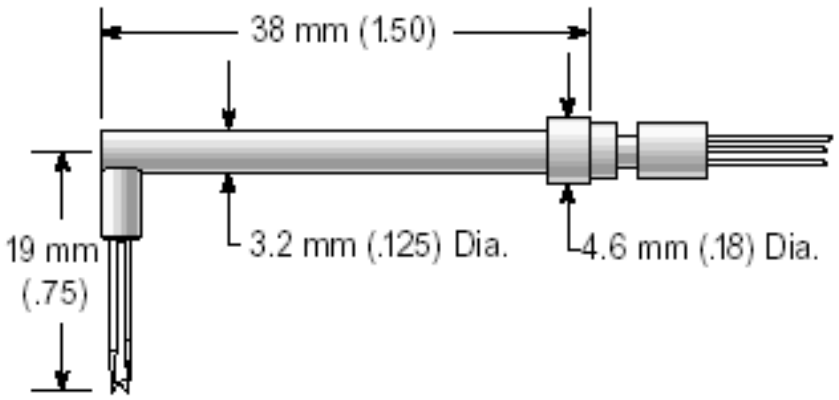

Figure 10.1. Cross flow X-wire probe

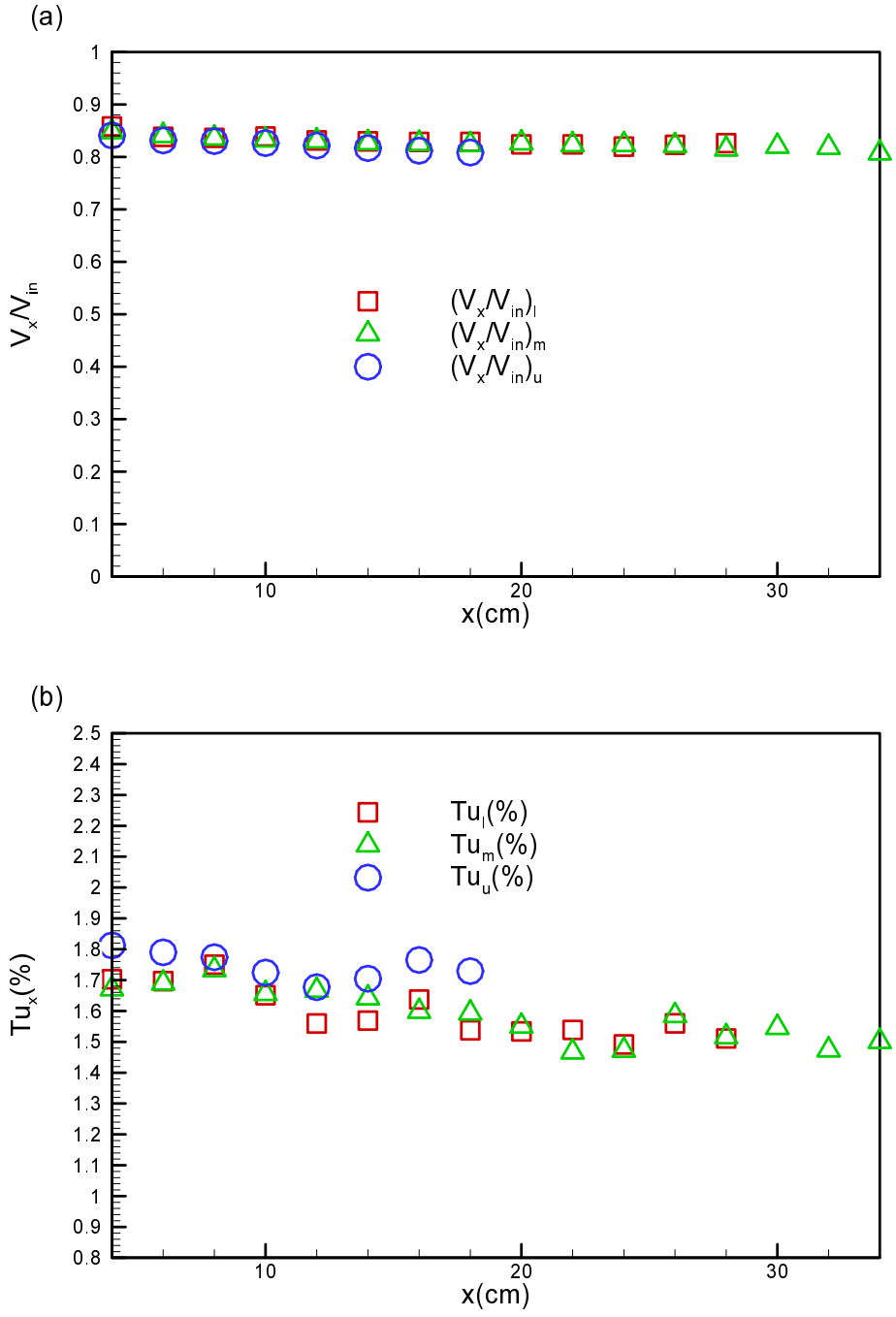

Figure 10.2. (a) Velocity and (b) turbulence intensity distributions along the upper, middle, and lower horizontal slots at Re=110,000

The time-averaged velocity profiles, and turbulence intensity distributions are presented for the corresponding slot positions along the straight duct section at different longitudinal locations in Figure 10.2 (a) and (b). Figure 10.2 (a) shows the time-averaged normalized velocity distribution (V_x/V_{in}) along the straight duct section at the upstream of the cascade section. Inlet velocity distributions show that the flow is uniform and constant inside the straight duct section. In addition to velocity distributions, turbulence intensity level show the decay along the straight duct section ahead of the test case section.

10.2 Inlet Velocity and Turbulence Measurements Along the Inlet Vertical Slot

The freestream uniformity of the approach velocity and turbulence level measurements have been performed in the leading edge plane of the linear turbine cascade and at the using both the X-wire and five-hole probes. The traverse covered three full blade spacings that corresponds to y=400 mm. The probe traverse is done using the vertical slot present at the inlet of the leading edge as shown in Figure 4.1. The tip of the X-wire was at a distance of 19 mm from probe shaft as shown in Figure 10.1. For X-wire probe measurements, the probe tip was about 50 mm from the leading edge.

The effect of the wake frequency on the time-averaged velocity profiles, turbulence intensity and flow direction distributions are presented for three different reduced frequencies, namely Ω = 0.0, 1.59, and 3.18 with corresponding rod spacings of $S_R=\infty$ mm, 80 mm, and 160 mm at the inlet test section at different lateral locations are shown in Figures 10.3 to 10.5. The inlet velocity distribution shows the effect of curved plate on the flow upstream of the leading edge. As shown in Figures 10.2 (a) to 10.5(a), toward the leading edge , the velocity is reduced due to the effect of the stagnation region. It is worth noting that the velocity and turbulence intensity distributions give good information about the uniformity and periodicity of the flow. Figures 10.2 (e) to 10.5(e) display the turbulence intensity distributions at the inlet test section for one steady and unsteady flow conditions. As seen, increase in reduced frequency, Ω, from 0 to 3.18 has increased the turbulence level due to their high turbulence intensity vortical cores.

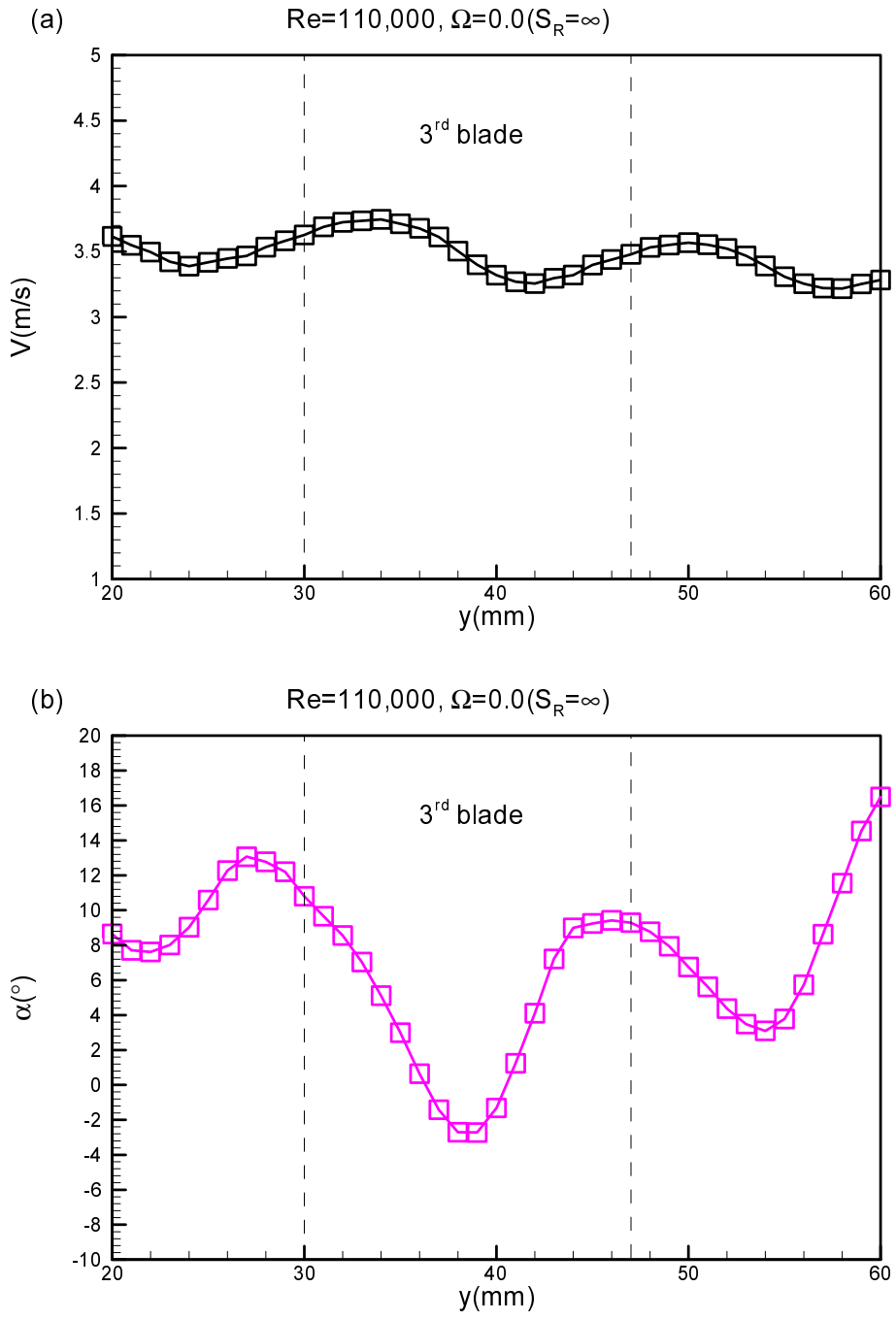

Figure 10.3. Inlet flow conditions for Ω=0.0 (S_R=∞). (a) velocity vector and (b) angle distribution at the inlet section using X-wire probe at Re=110,000

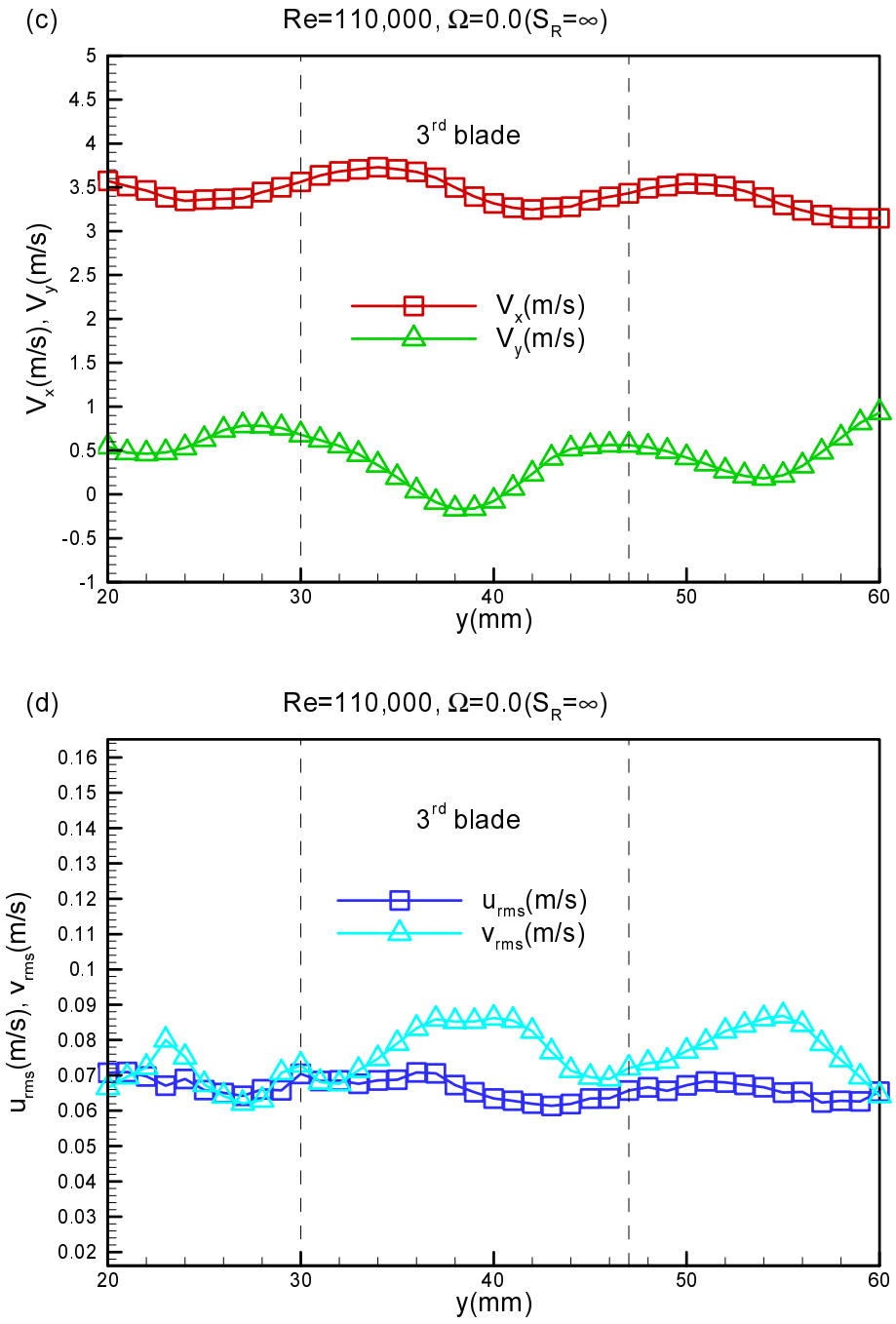

Figure 10.3. Continued. (c) x and y-component of velocity and (d) x and y-component of the fluctuation velocity distribution using X-wire probe at Re=110,000

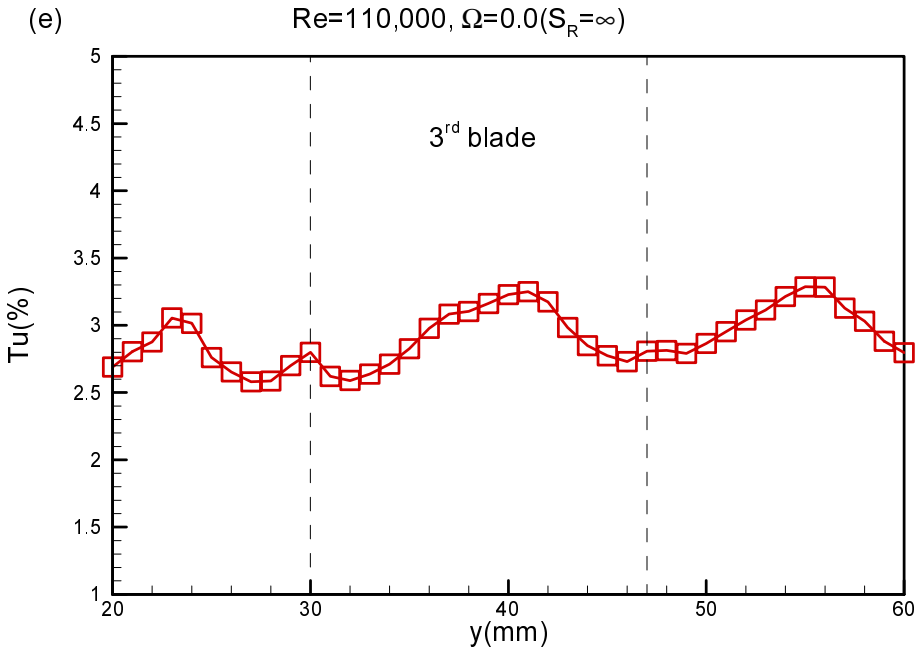

Figure 10.3. Continued. (e) Turbulence intensity distribution at the inlet section using X-wire probe at Re=110,000

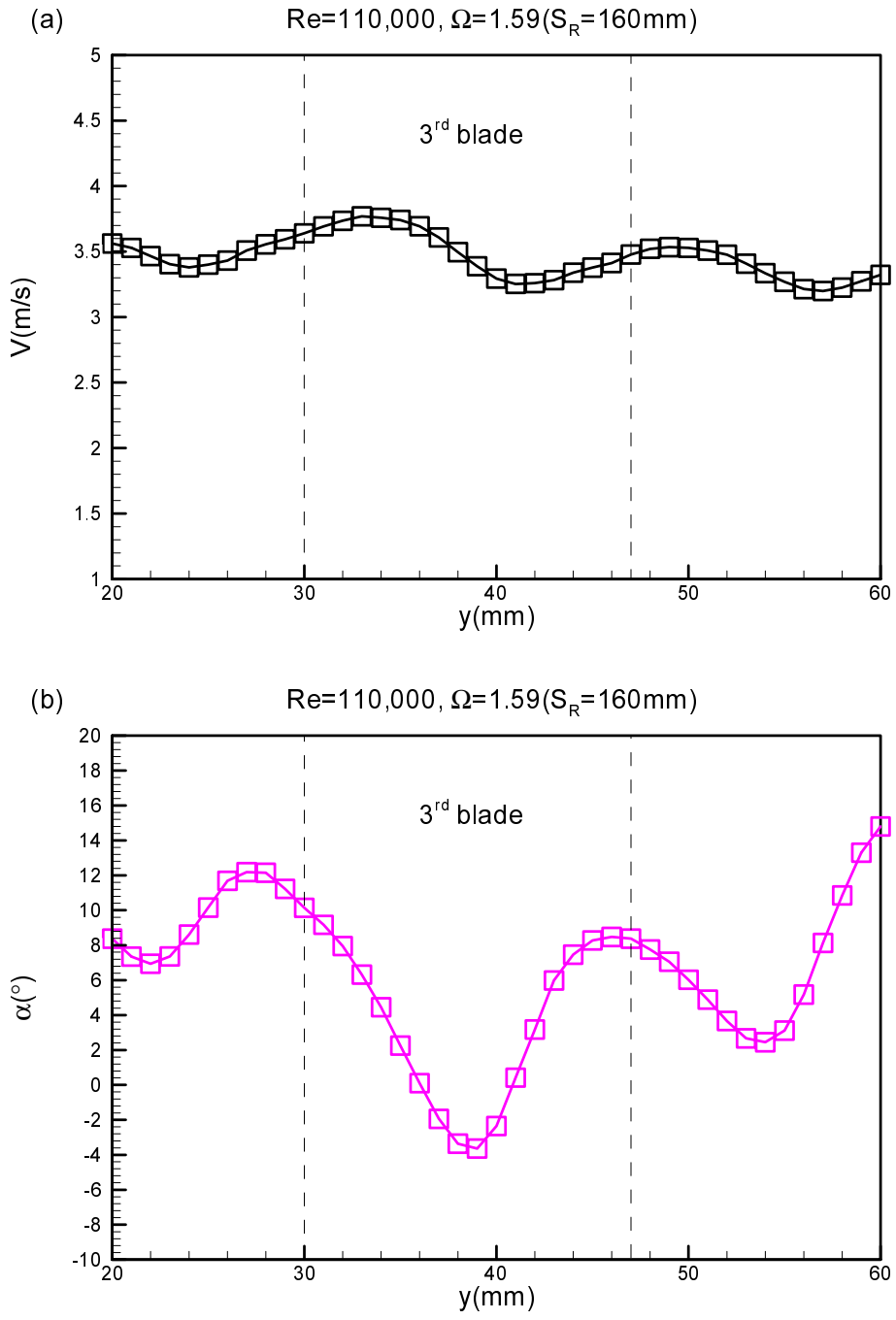

Figure 10.4. Inlet flow conditions for Ω=1.59 (S_R=160 mm). (a) Velocity vector and (b) angle distribution at the inlet section using X-wire probe at Re=110,000

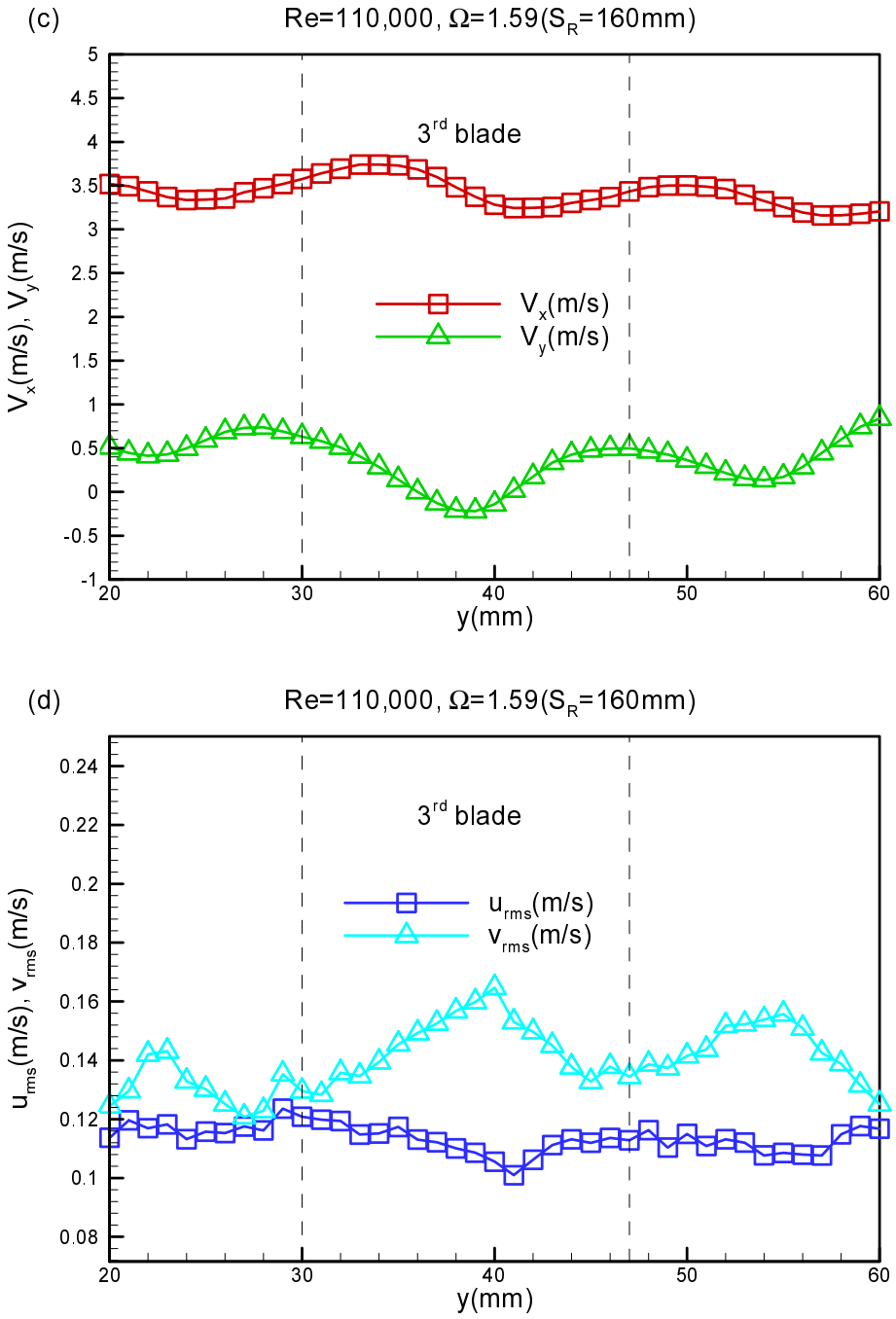

Figure 10.4. Continued. (c) x and y-component of velocity and (d) x and y-component of the fluctuation velocity distribution using X-wire probe at Re=110,000

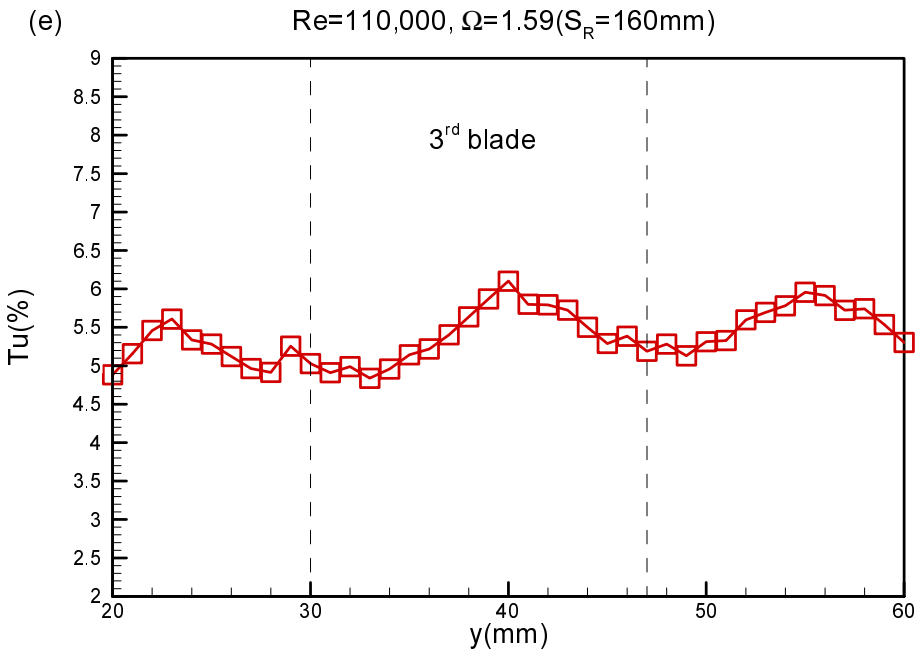

Figure 10.4. Continued. (e) Turbulence intensity distribution at the inlet section using X-wire probe at Re=110,000

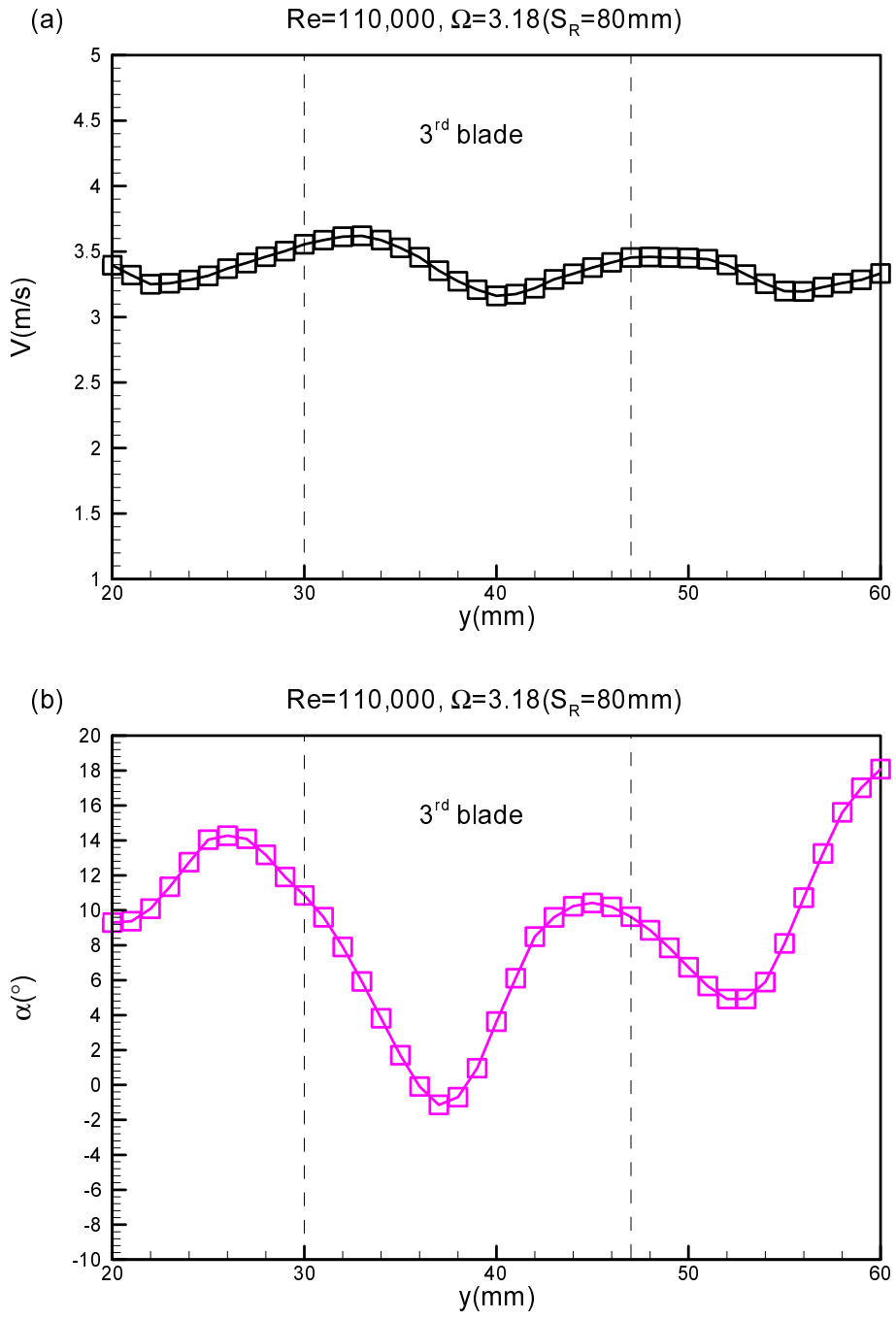

Figure 10.5. Inlet flow conditions for Ω=3.18 (S_R=80 mm). (a) Velocity vector and (b) angle distribution at the inlet section using X-wire probe at Re=110,000

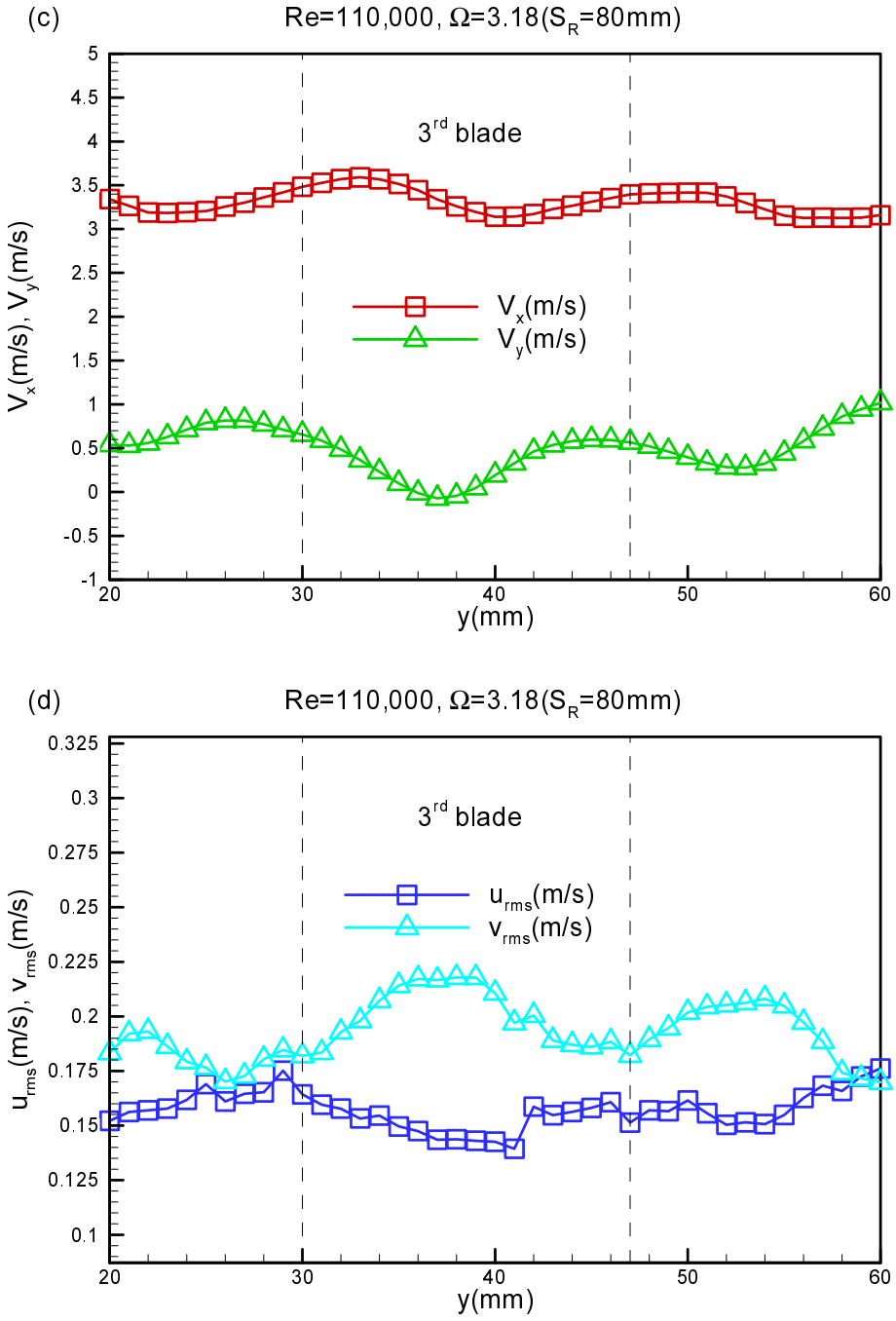

Figure 10.5. Continued. (c) x and y-component of velocity and (d) x and y-component of the fluctuation velocity distribution using X-wire probe at Re=110,000

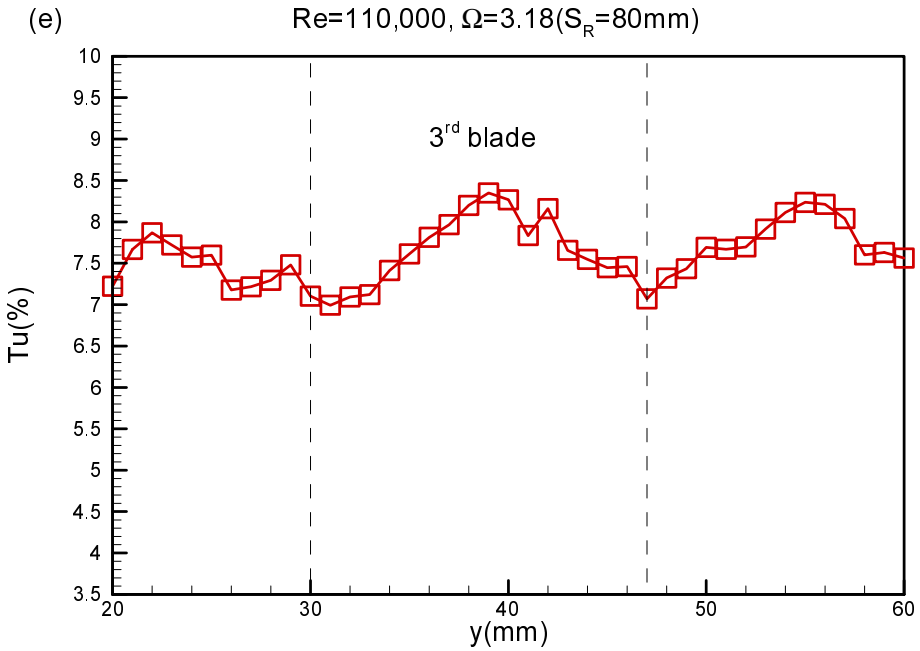

Figure 10.5. Continued. (e) Turbulence intensity distribution at the inlet section using X-wire probe at Re=110,000

10.3 Turbulence Length Scale Measurements

Three different turbulence grids were manufactured for producing inlet turbulence intensities of 3.0%, 8.0%, and 13.0%. The grids were subsequently installed upstream of the wake generator, parallel to the plane of the cascade blade row with the distance form cascade leading edge G_{LE} defined in Table 4.1. The turbulence intensity values were measured at the cascade inlet with the location from the cascade leading edge listed in Table 1. An adequate description of the inlet flow condition requires, in addition to the time dependent velocity distribution and freestream turbulence intensity, the information about the turbulence length scale. To document the turbulence length scales, one dimensional power spectra of the velocity fluctuations were measured using a single-wire probe. The spectral measurements used 20,000 data points at 20 kHz (low-pass filtered at 10 kHz). From these data, the integral length scale Λ was calculated for each turbulence grid using the relations developed by Hinze [107] and the power density values were extrapolated to the frequency f = 0. The results of these calculations presented in Table 4.1 indicate a decrease in length scale with increasing the freestream turbulence intensity .

$$\Lambda_{u,x} = \frac{\bar{u}E_u(f = 0)}{4u'^2_{rms}} \tag{10.1}$$

11. BOUNDARY LAYER MEASUREMENTS

In this section, the experimental results from the steady and unsteady boundary layer development, periodic unsteady wake development, surface pressure measurements and the velocity distributions will be presented at Reynolds number of 110,000.

Detailed surface pressure and boundary layer measurements were performed at a Reynolds number of 110,000. This Reynolds number, which pertains to a typical cruise operation, exhibits a representative value within LPT operating range between 75,000 and 400,000 as discussed by Hourmouziadis [122]. Furthermore, it produces separation bubbles that can be accurately measured by miniature hot wire probes. Surface pressure measurements at Reynolds numbers of 75,000, 110,000, 125,000, and 150,000 presented in [24] shows that pressure distribution for these Reynolds numbers do not differ substantially from each other. Therefore, for the boundary layer investigations, a representative Reynolds number of 110,000 was chosen. For generation of the unsteady wakes, cylindrical rods with the diameter d_R = 2mm were chosen to fulfill the criterion that requires the generation of a drag coefficient C_D that is approximately equal to the C_D of the turbine blade with the chord and spacing given in Table 4.1 (details are reported in [4] and [123]).

To accurately account for the unsteadiness caused by the frequency of the individual wakes and their spacings, the flow velocity, and the cascade parameters, a reduced frequency Ω is defined that includes the cascade solidity σ, the flow coefficient φ, the blade spacing S_B, and the rod spacing S_R. Many researchers have used Strouhal number as the unsteady flow parameter, which only includes the speed of the wake generator and the inlet velocity. However, the currently defined reduced frequency Ω is an extension of Strouhal number in the sense that it incorporates the rod spacing S_R and the blade spacing S_B in addition to the inlet velocity and wake generator speed. For surface pressure measurement rods with uniform spacings as specified in Table 4.1 were attached over the entire belt length. For boundary layer measurement, however, clusters of rods were attached, as mentioned previously.

$$\Omega = \frac{c}{S_R}\frac{U}{V_{ax}} = \frac{\sigma}{\varphi}\frac{S_B}{S_R} \tag{11.1}$$

with $\sigma = \frac{c}{S_B}$ and $\varphi = \frac{V_{ax}}{U}$

Experimental investigations were performed for three different reduced frequencies Ω=0.0, 1.59, and 3.18 that correspond to the rod spacings S_R=∞ mm, 80 mm, and 160 mm.

11.1 Surface Pressure Distributions

For the Reynolds number of 110,000 with freestream turbulence intensity of 1.9%, three different reduced frequencies, namely Ω = 0.0, 1.59, and 3.18, are applied that correspond to the rod spacings S_R = ∞, 160mm, and 80 mm. The pressure distributions in Figure 11.1 show the results of the steady case and two unsteady cases. The pressure signals inherently signify the time-averaged pressure because of the internal pneumatic damping effect of the connecting pipes to the transducer. It is worth noting that the pressure distribution gives reasonably good information about the extent of the flow separation. However, it does not provide the information about the exact begin and end of the separation bubble. This is due to the longitudinal spacing between the pressure taps. Furthermore, the static pressure distribution does not provide the necessary information about the lateral extent of the separation bubble. This deficiency is eliminated by traversing the boundary layer from leading edge to trailing edge, where detailed timed dependent flow velocity information are extracted.

The time-averaged pressure coefficients along the pressure and suction surfaces are plotted in Figure 11.1. The suction surface (upper portion) exhibits a strong negative pressure gradient. On the pressure surface, the flow decelerates at a very slow rate, reaches a minimum pressure coefficient at s/s_o= 0.42 and accelerates until the trailing edge has been reached. Passing through the minimum pressure, the fluid particles within the boundary layer encounter a positive pressure gradient that causes a sharp deceleration until s/s_o = 0.55

has been reached. This point signifies the beginning of the laminar boundary layer separation and the onset of a separation bubble. As seen in the subsequent boundary layer discussion, the separation bubble characterized by a constant C_p-plateau extends up to s/s_o = 0.74, thus, occupying more than 19% of the suction surface and constituting a massive separation. Passing the plateau, the flow first experiences a second sharp deceleration indicative of a process of re-attachment followed by a further deceleration at a moderate rate. On the pressure surface, the flow accelerates at a very slow rate, reaches a minimum pressure coefficient at $s/s_o = 0.42$ and continues to accelerate until the trailing edge has been reached. Unlike the suction surface, the pressure surface boundary layer does not encounter any adverse positive pressure gradient that triggers separation. However, close to the leading edge, a small plateau extending from s/s_o= 0.08 to 0.16 indicates the existence of a small size separation bubble that might be attributed to a minor inlet flow incident angle.

Considering the unsteady case with the reduced frequency Ω = 1.59 (S_R =160 mm), Figure 11.1 exhibits a slight difference in the pressure distribution between the steady and unsteady cases. This deviation is attributed to the momentum deficiency of the main flow due to the drag forces caused by the moving rods. This momentum deficiency leads to a reduction of the total and static pressure.

For Re = 110,000, the wakes have a reducing impact on the streamwise extent of the separation plateau. As seen in Figure 11.1, the trailing edge of the plateau has shifted from $s/s_o = 0.74$ to $s/s_o = 0.702$. This shift reduced the streamwise extent of the separation plateau from 19% to 15% of the suction surface length which is in this particular case, 21% of .reduction in streamwise extent of the separation. Increasing the reduced frequency to Ω = 3.18 by reducing the rod spacing to S_R = 80 mm causes a slight shift of C_p-distribution compared with $\Omega = 1.59$ case. One should bear in mind that pneumatically measured surface pressure distribution represents a time integral of the pressure events only.

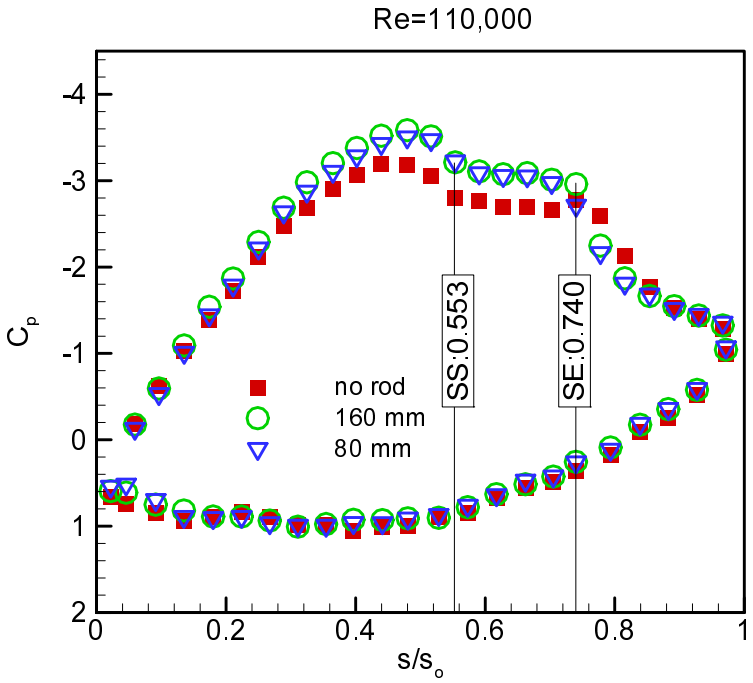

Figure 11.1. Static pressure distributions at Re=110,000 and reduced frequencies Ω=0, 1.59, 3.18 (no rod, 160 mm, 80 mm), SS=Separation start, SE= Separation end

11.2 Surface Mounted Hot-Film Distributions

Following the surface pressure investigations that mainly addressed the onset and extent of the separation zone discussed previously, comprehensive surface mounted hot-film measurements were performed to identify the streamwise and normal extent as well as the deformation of the separation zone under unsteady wake flow. The steady state case serves as the reference configuration.

Detailed hot-film measurements were taken at Re = 110,000 with freestream turbulence intensity of 1.9% on the suction surface along 32 streamwise locations parallel to the cascade front. For Reynolds number of 110,000 three different reduced frequencies, namely $\Omega = 0.0$, 1.59, and 3.18 are applied that correspond to the rod spacings S_R = 80 mm, 160 mm, and ∞ mm. The hot-film distributions in Figures 11.2 (a) and (b) show the results of the steady case and two unsteady cases. Figure 11.2 (a) shows the time-averaged normalized heat dissipation due to forced convection $((E-E_o)/E_o)$ along the suction surface

of a low pressure turbine blade. As described in section 8.2.2, this parameter is proportional to the cube root of the wall shear stress. However the second plot Figure 11.2 (b) displays the time-averaged random fluctuations of the hot-film signals, which is proportional to the fluctuating heat transfer. Both figures are made dimensionless by dividing by the sensor voltage at zero flow conditions E_o and are plotted versus the relative sensor position in streamwise distance from blade leading edge s/s_o. E_o corresponds to the heat flow due to free convection and heat conduction in the turbine blade.

Length and position of separation bubbles can be determined with high accuracy by the hot-film signals. The averaged voltage E of the anemometer output signal is proportional to the shear stress. As shown in Figure 11.2 (a) dimensionless $((E-E_o)/E_o)$ ratio drops in the laminar boundary layer with increasing boundary layer thickness as seen in Figure 11.24. However, $((E-E_o)/E_o)$ rises steeply in the transition area and slopes again in the turbulent boundary layer area. Minimum in the hot-film signal occurred inside the separation bubble. In the RMS voltage distribution shown in Figure 11.2 (b), first and second pick can be attributed to separation bubble location. The reattachment point of the turbulent boundary layer is located at the end of the higher fluctuation peak at $s/s_o = 0.69$. Hourmouziadis et al. [124] observed the same pattern on an annular low pressure turbine stator vane, indicating that the pure motion of the bubble edges can cause the two observed fluctuation peaks. In their case, the connection between the fluctuation pattern and the bubble was confirmed by flow visualization and numerical prediction. Thus, the peaks in the fluctuation data indicate the existence of a separation bubble.

11.3 Ensemble-Averaged Boundary Layer Velocity Distributions

Figure 11.3 displays two representative temporal ensemble-averaged velocity distributions for (a) steady and (b) unsteady flow condition with their characteristic features. Both figures show the boundary layer development from the freestream to the blade surface at a streamwise position of $s/s_o = 0.0208$. Approaching the wall surface, both velocities experience a continuous deceleration. The velocity gradient in both cases causes generation

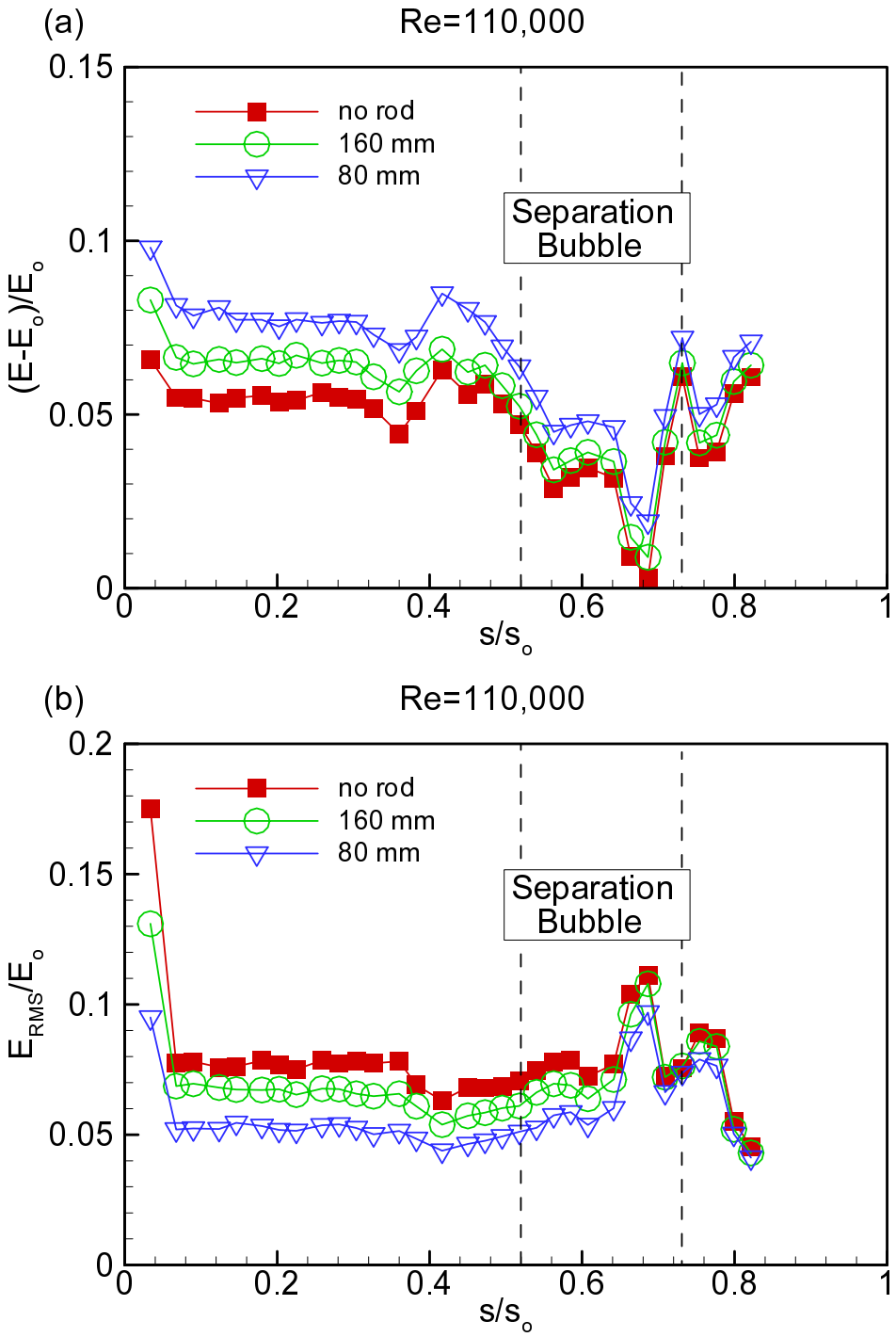

Figure 11.2. Time-averaged hot-film distributions at Re=110,000 and reduced frequencies Ω=0, 1.59, 3.18 (no rod, 160 mm, 80 mm)

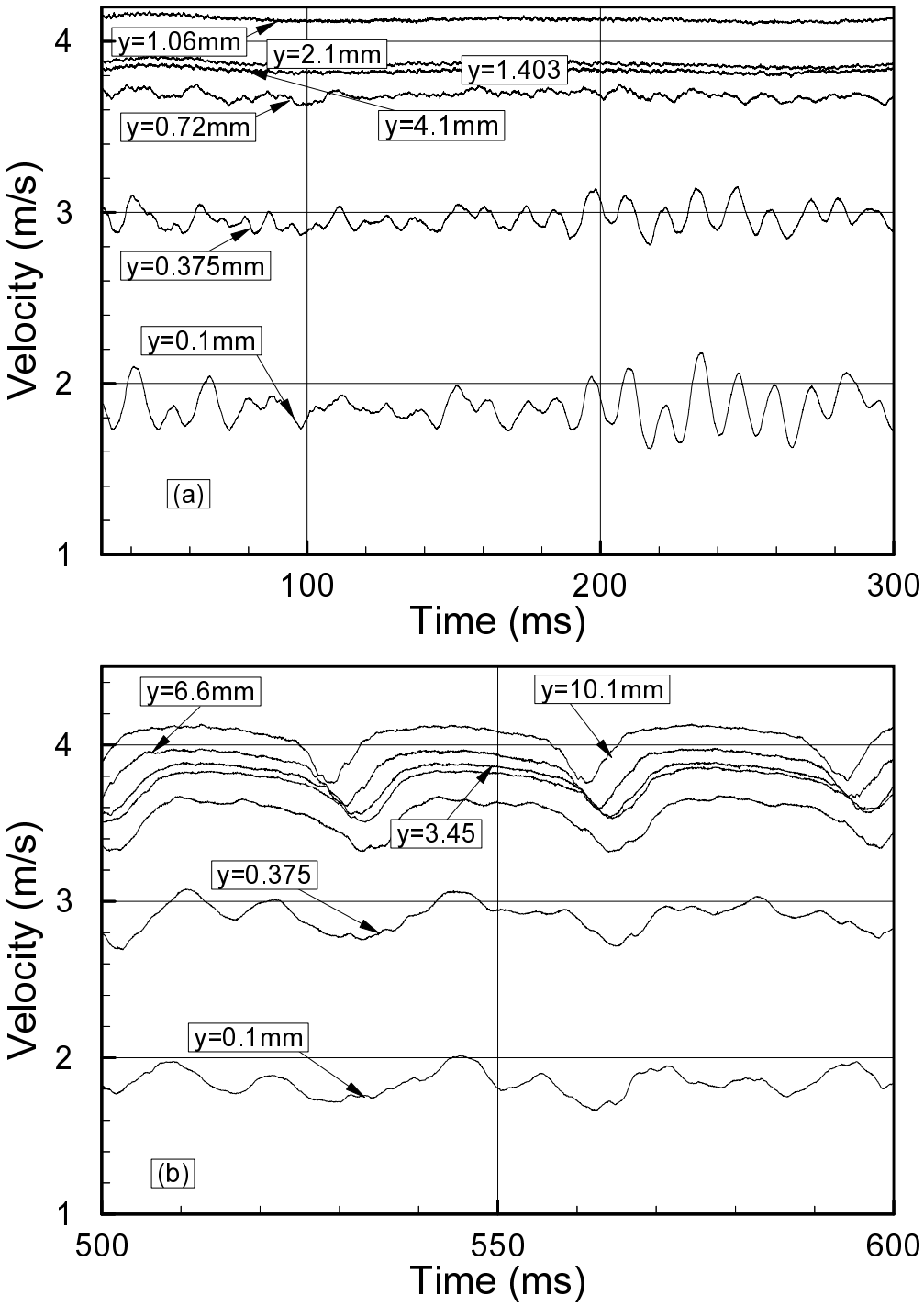

Figure 11.3. Ensemble averaged velocity as a function for (a) steady flow case Ω=0 (S_R=∞) and (b) unsteady case Ω=1.59 (S_R=160 mm) at s/s_0=0.0208 and Re=110,000

and formation of vortices that transform the steady nature of case (a) into an unsteady one as clearly demonstrated in Figure 11.3(a). The unsteady case displayed in Figure 11.3(b) is characterized by its deterministic temporal periodicity. Approaching the wall surface from y=10.1mm to 3.45mm, the traveling periodic wake experiences a phase shift, while maintaining its deterministic nature. However, by penetrating into the boundary layer, the interaction between wake and boundary layer causes the deterministic nature to degenerate into a stochastic one. The results presented in Figure 11.3 are in full agreement with those discussed in [13] and [21].

11.4 Time Averaged Velocity Distributions

Consistent with the surface pressure distributions which is discussed above, the effect of the wake frequency on the time-averaged velocity profiles and turbulence intensity distribution are presented for the corresponding rod spacings of $S_R=\infty$ mm, 80 mm, and 160 mm at different longitudinal locations in Figures 11.4 to 11.11. In the upstream region of the separation bubble, the flow is attached. Upstream of the separation bubble at $s/s_o= 0.52$ and also at its immediate proximity $s/s_o=0.588$, the velocity distributions inside the boundary layer experience a slight decrease with increasing the reduced frequency. Inside the separation bubble at $s/s_0=0.705$, a substantial influence of the wake frequency is observed. The higher wake frequency introduces a fluctuation kinetic energy into the boundary layer trying to reverse the separation tendency. As it can be seen from the velocity distribution profiles, the onset and the length of the separation bubble are not changed. However, there is a slight change of the bubble height. This shows that the flow does not have the capability to suppress the separation bubble. It only reduces the separation bubble height. In the downstream of the separation bubble, where the flow is fully reattached, $s/s_o=0.951$, the impact of the wake on the boundary layer is reduced. This effect is clearly shown in the velocity distribution at $s/s_o=0.951$. According to the previous investigations by Schobeiri et al. [29] on a HP-turbine cascade, an increased wake frequency causes turbulence fluctuations to rise inside and outside the boundary layer. However, in the LPT

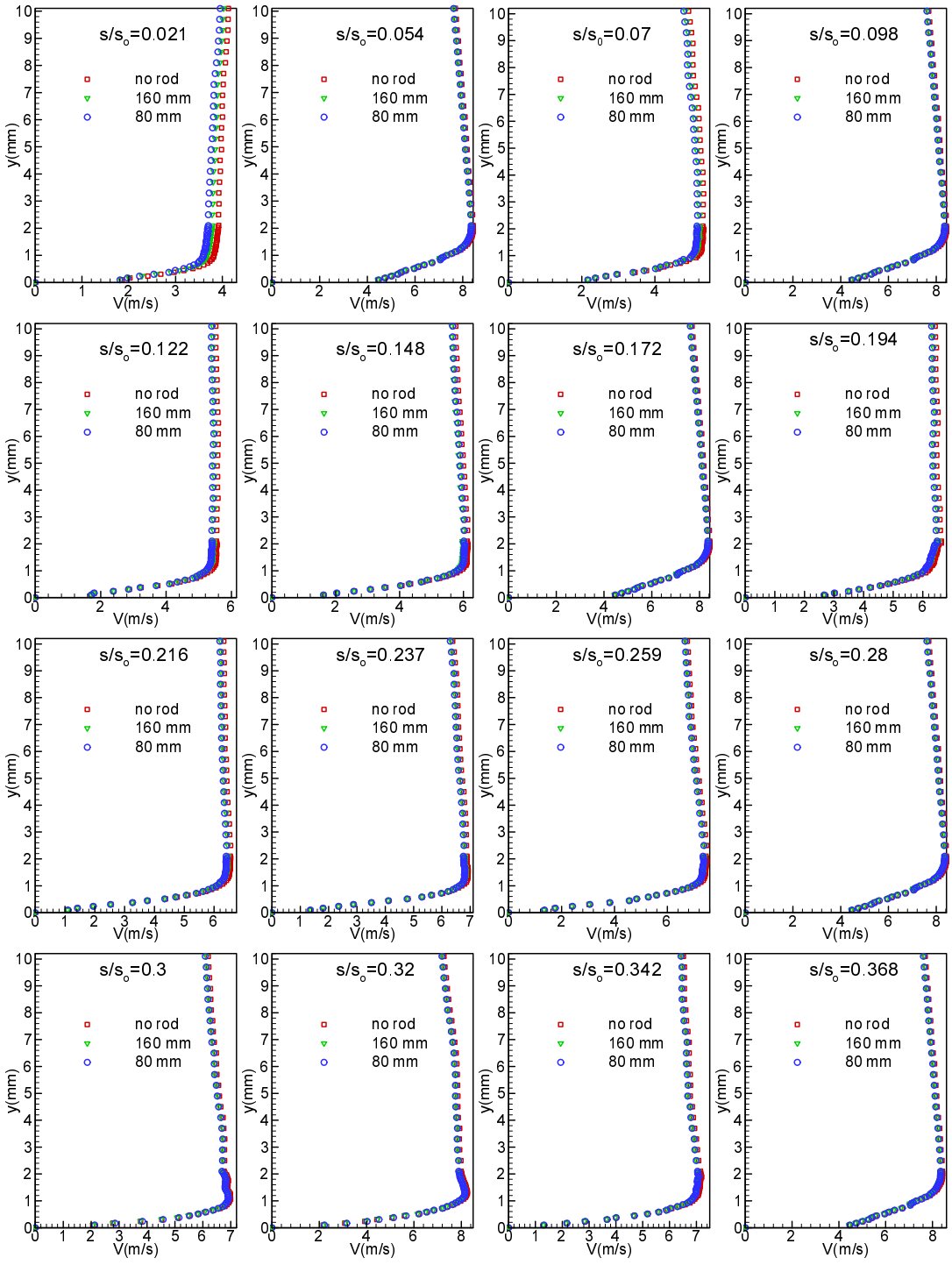

Figure 11.4. Distribution of the time-averaged velocity along the suction surface for three different reduced frequencies of Ω=0 (S_R=∞), Ω=1.59 (S_R=160 mm), Ω=3.18 (S_R=80 mm) atRe=110,000

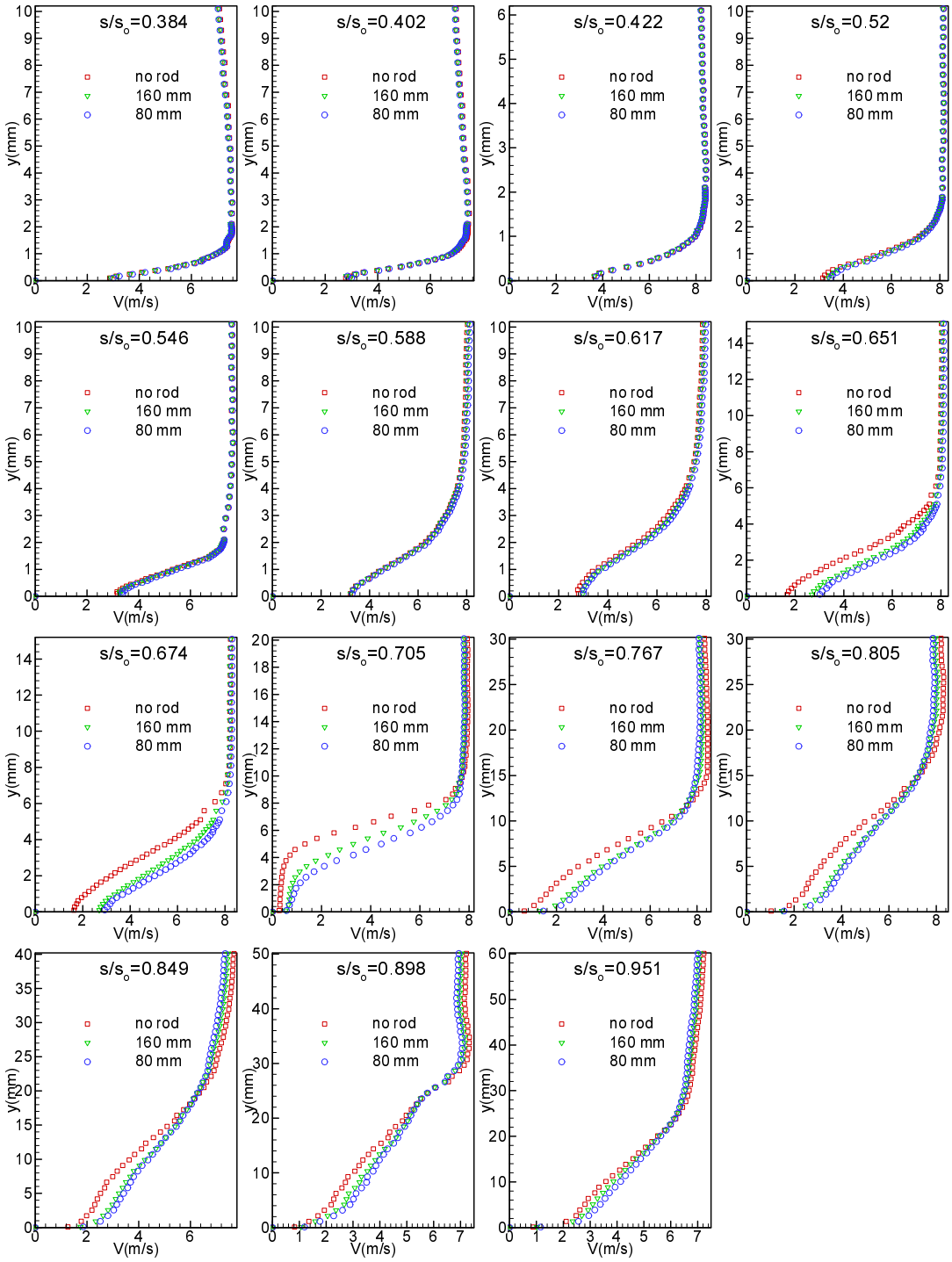

Figure 11.4. Continued

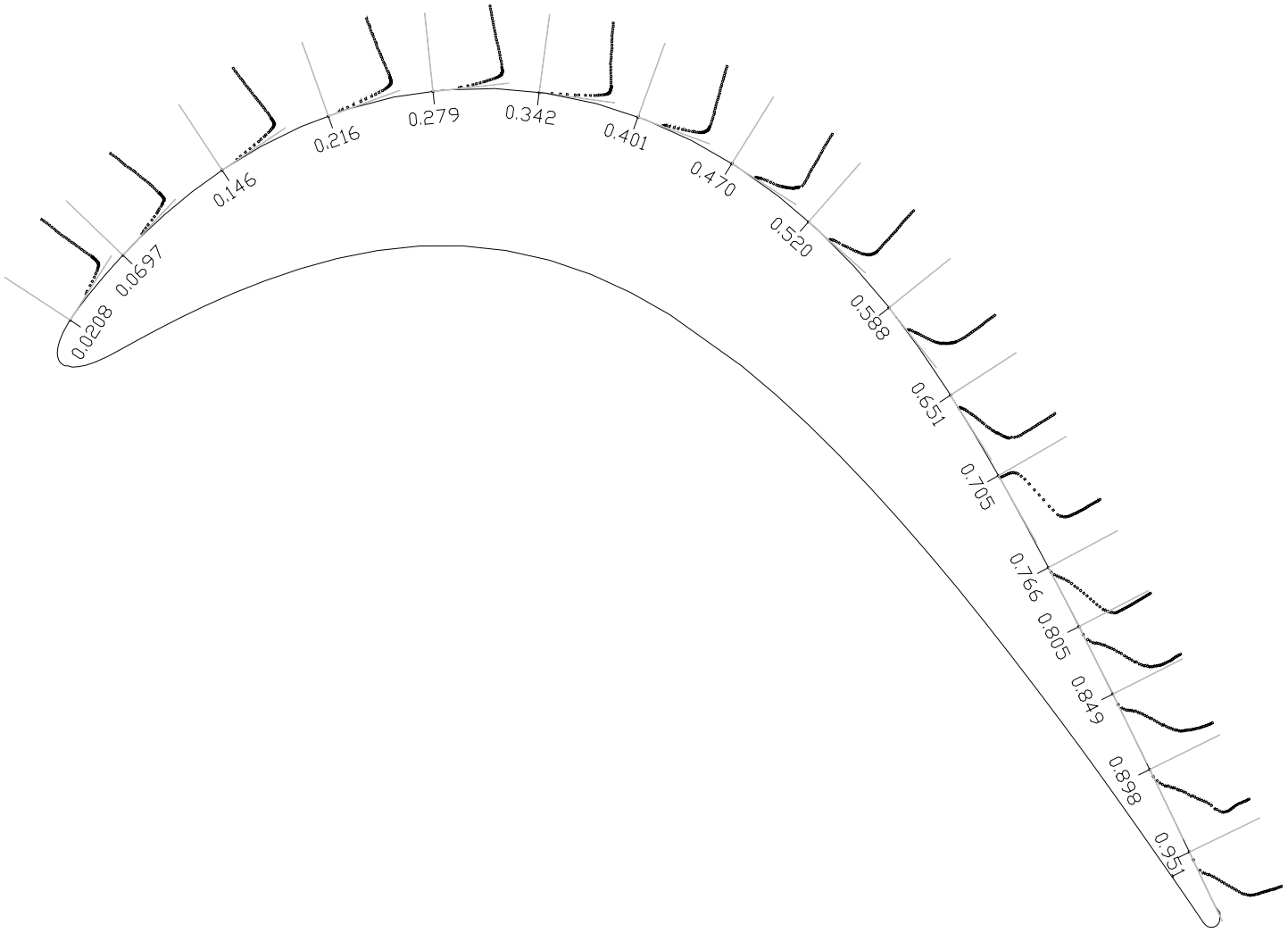

Figure 11.5. Time-averaged velocity profiles along the suction surface of the blade at Ω=0.0, Re=110,000

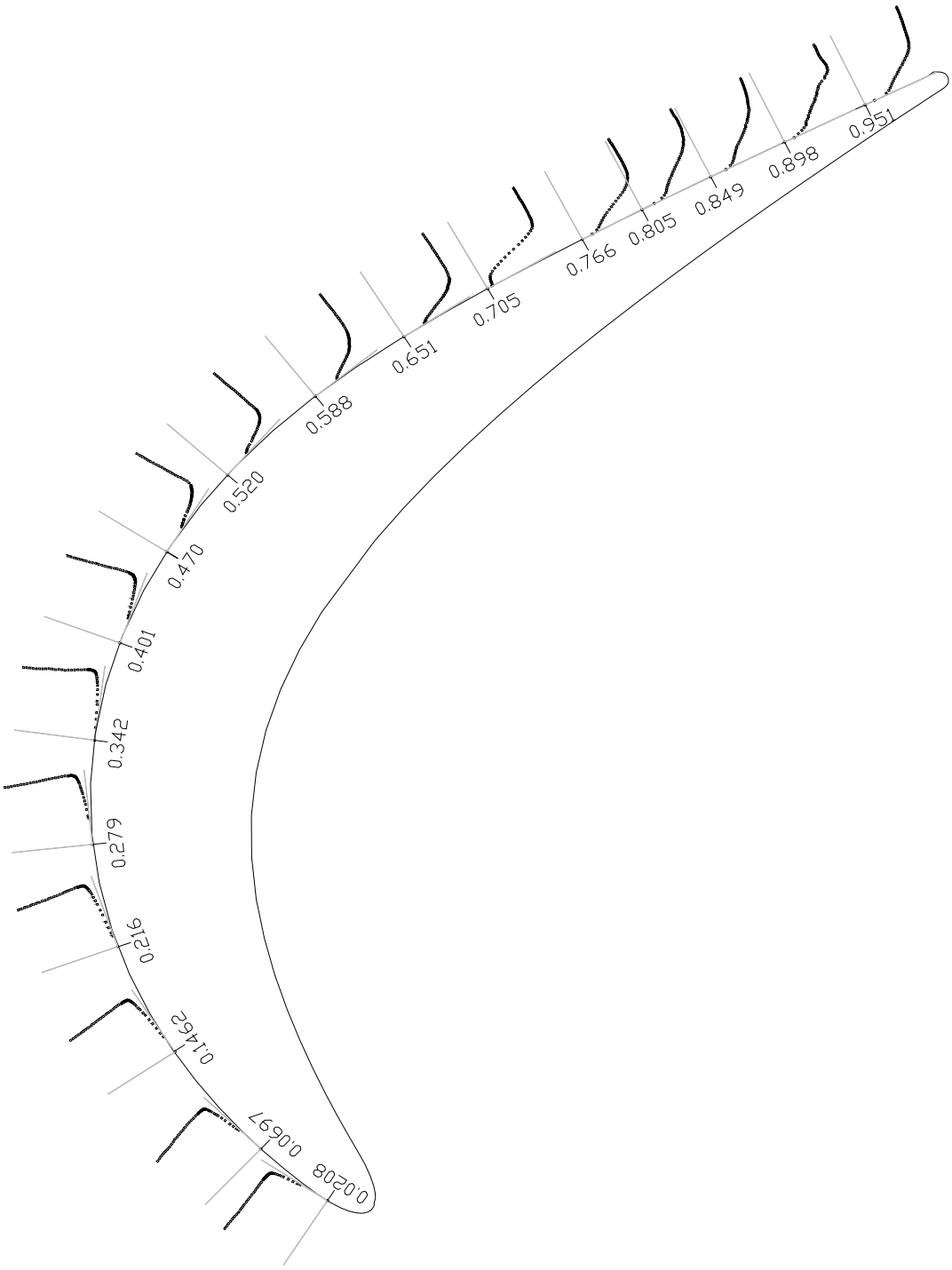

Figure 11.6. Time-averaged velocity profiles along the suction surface of the blade at Ω=1.59, Re=110,000

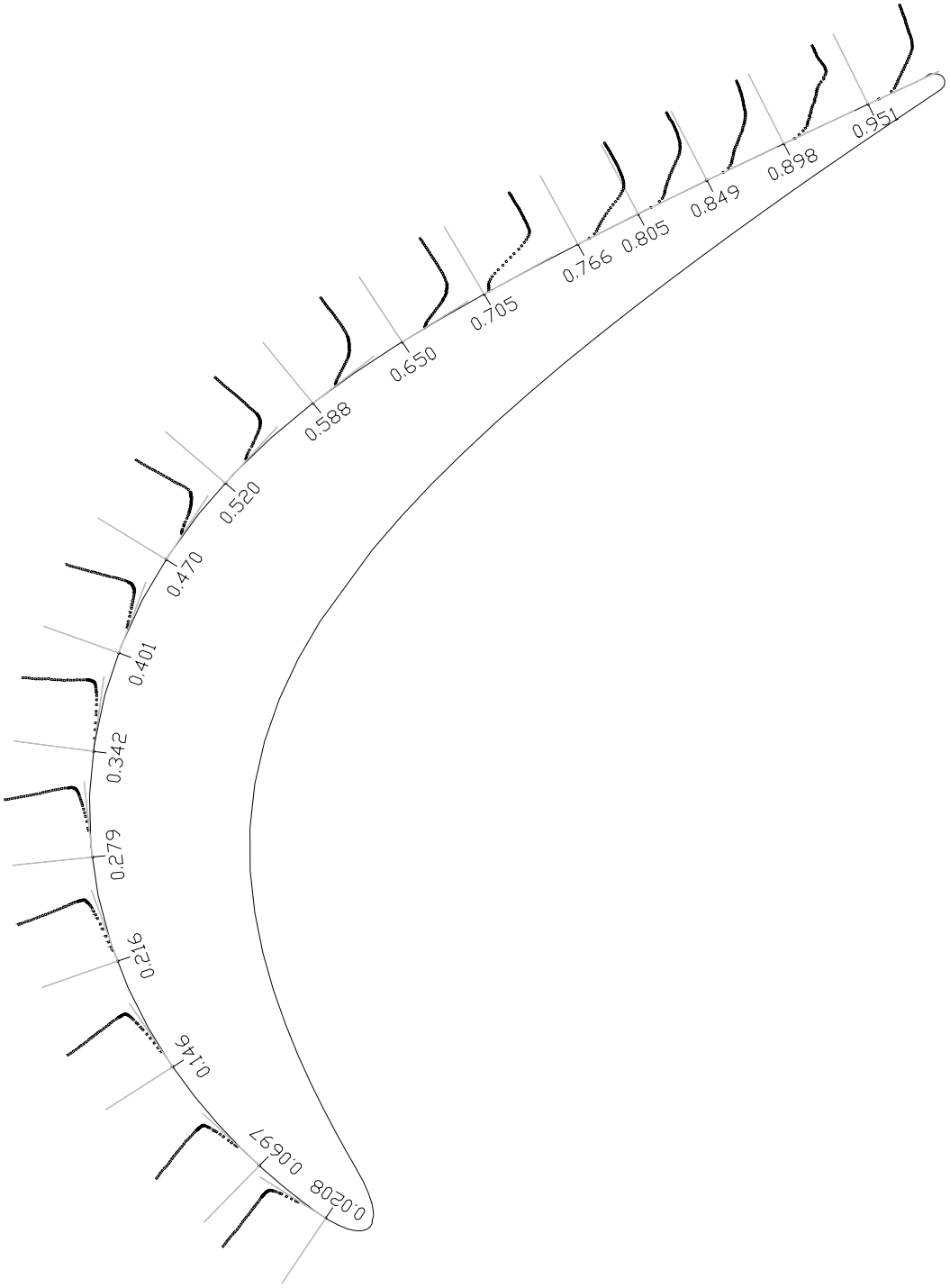

Figure 11.7. Time-averaged velocity profiles along the suction surface of the blade at Ω=3.18, Re=110,000

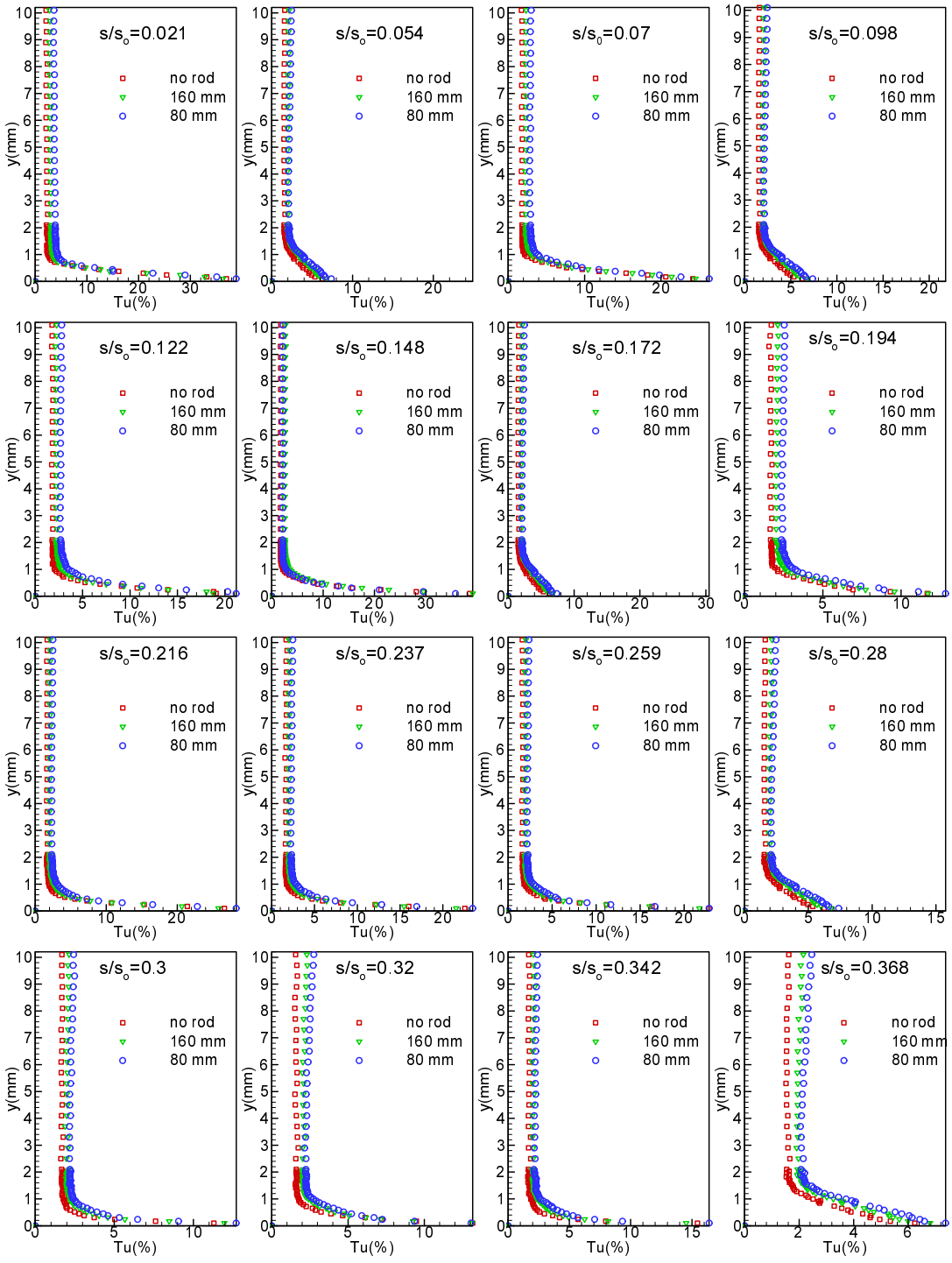

Figure 11.8. Distribution of the time-averaged turbulence intensity along the suction surface for three different reduced frequencies of Ω=0 (S_R=∞), Ω=1.59 (S_R=160 mm), Ω=3.18 (S_R=80 mm) at Re=110,000

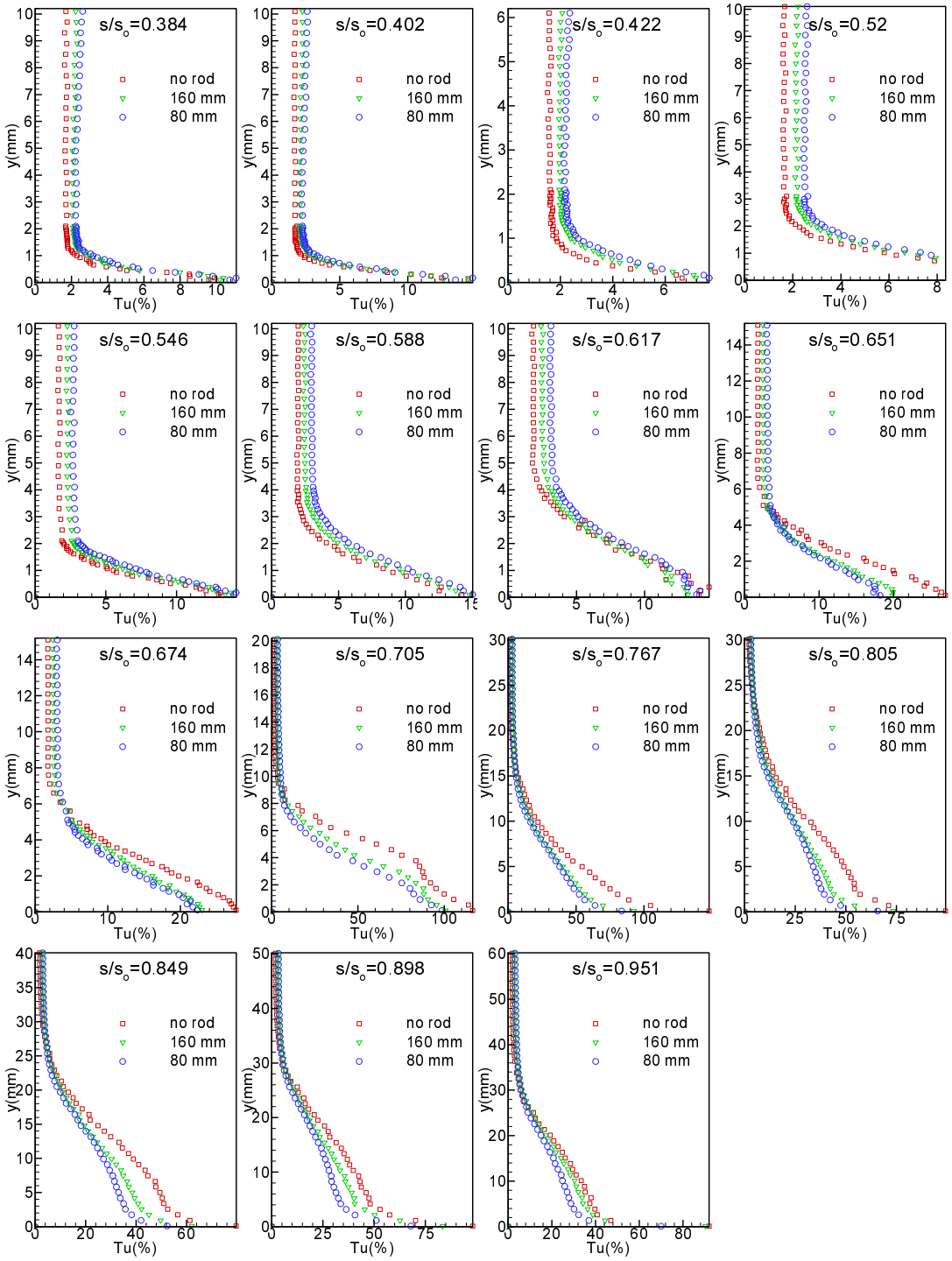

Figure 11.8. Continued

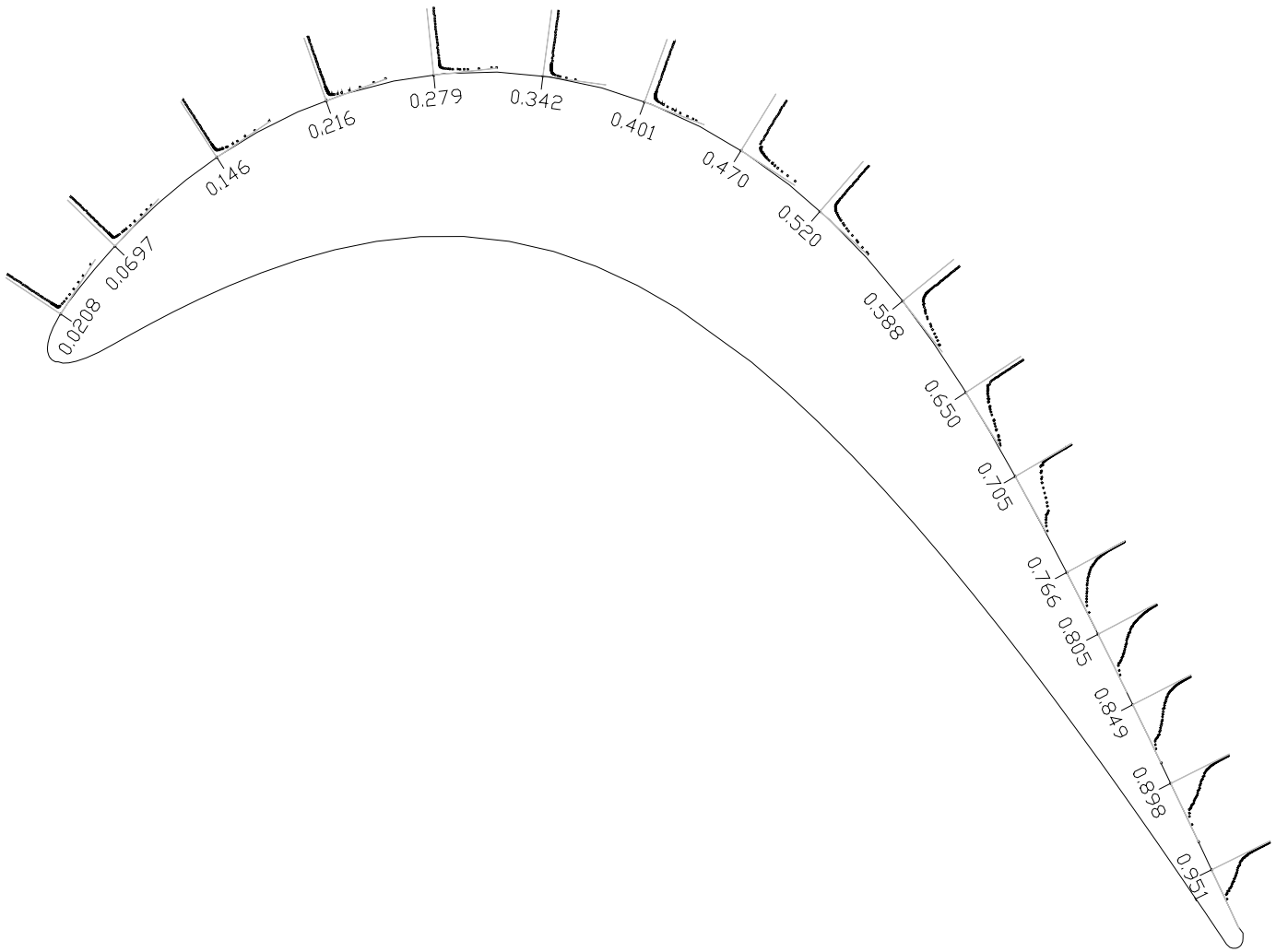

Figure 11.9. Time-averaged turbulence intensity profiles along the suction surface of the blade at Ω=0.0, Re=110,000

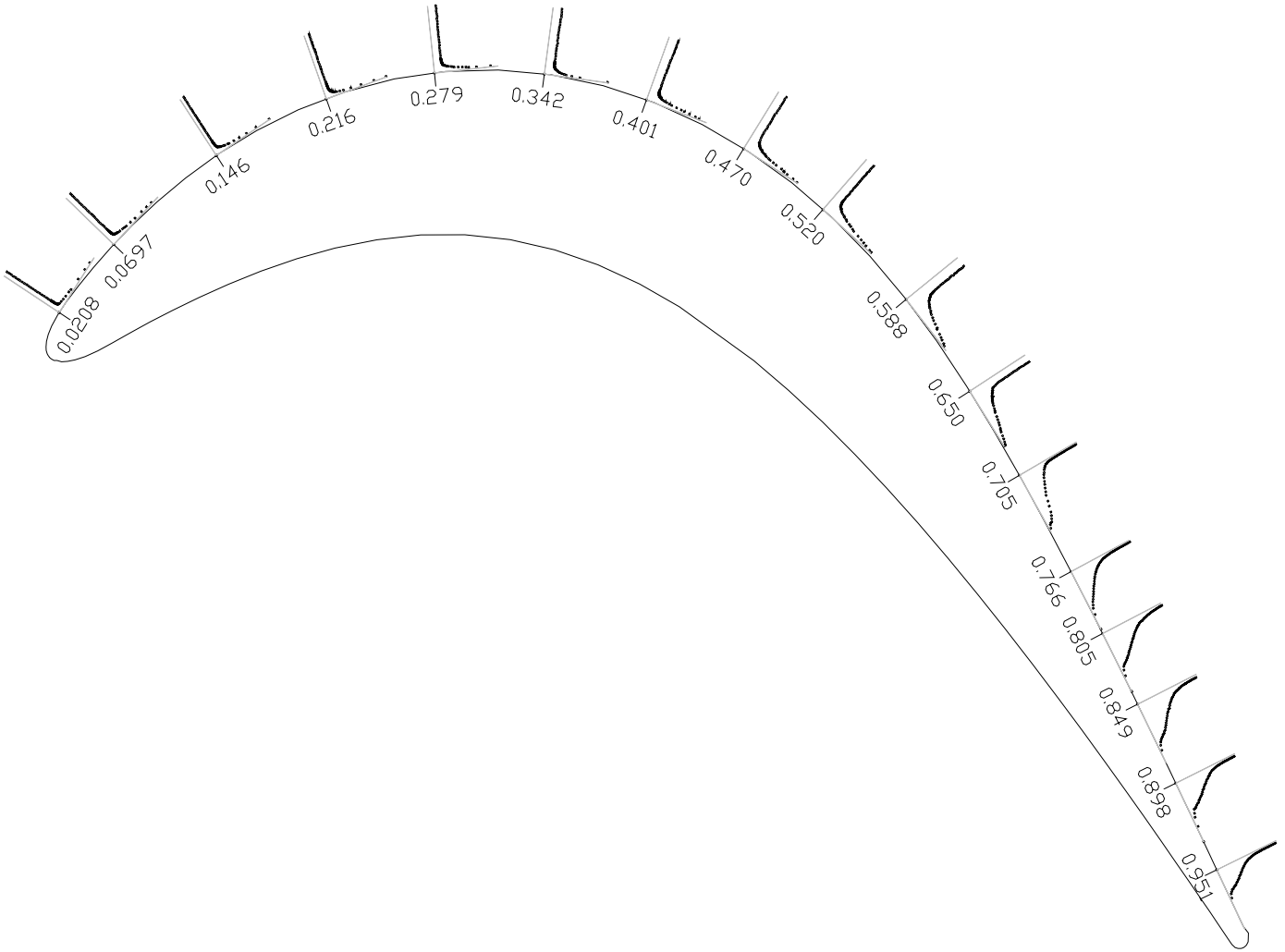

Figure 11.10. Time-averaged turbulence intensity profiles along the suction surface of the blade at Ω=1.59, Re=110,000

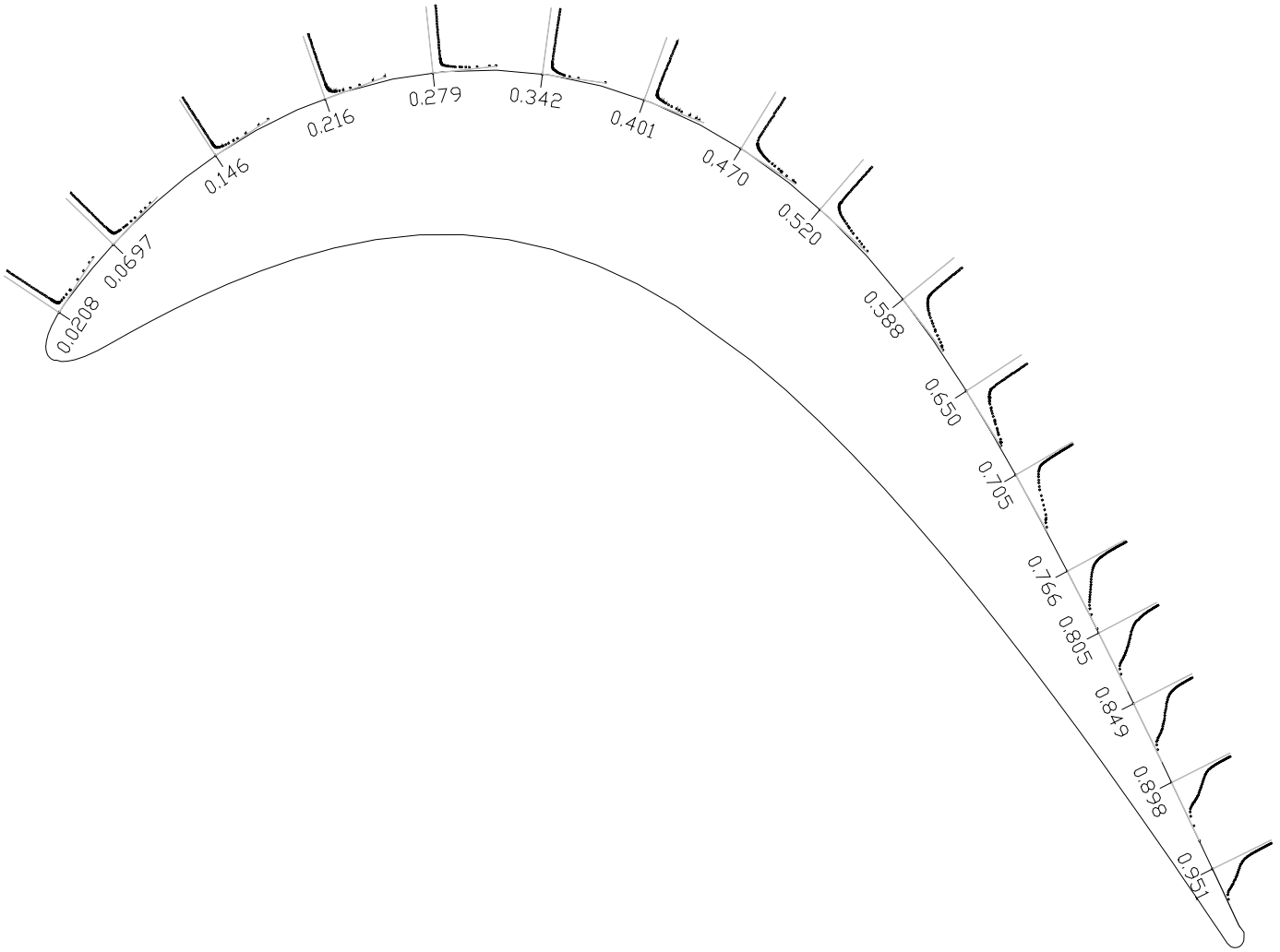

Figure 11.11. Time-averaged turbulence intensity profiles along the suction surface of the blade at Ω=3.18, Re=110,000

case with the boundary layer separation once the boundary layer is re-attached and the velocity distribution assumes a fully turbulent profile, no major changes are observed neither in the velocity nor in the turbulence intensity distribution.

11.5 Temporal Behavior of the Separation Zone Under Unsteady Wake Flow

Velocity distributions on the suction surface with time as parameter are plotted in Figure 11.12 and 11.13. The non-dimensional time (t/τ) values are chosen so that they represent the temporal states within one full period of wake passing. As Figures 11.12 (a) to (h) shows, the velocity distributions inside and outside the boundary layer at fixed s/s_0-locations experience moderate to pronounced changes at Ω=1.59. Starting with the initial state of flow being under the influence of free-stream turbulence to the final state where the flow is totally under the influence of wake the boundary layer undergoes a sequence of changes. Figure 11.12 (a) represents the instantaneous velocity distribution upstream of the separation zone followed by Figure 11.12 (b,c,d,e) which represent the velocity distributions inside the separation zone. Figure 11.12 (f) exhibits the instantaneous velocity distribution downstream of the separation zone. Figure 11.12 (g,h) represent the instantaneous velocity distributions, where the flow is fully reattached. In discussing the following results, we simultaneously resort to the wake distribution as well as the turbulence fluctuation results.

Figure 11.12 (a) exhibits the velocity distribution on the suction surface at $s/s_0 = 0.402$. At this streamwise position, the laminar boundary layer is subjected to a strong negative pressure gradient. The boundary layer distributions at different (t/τ) experience changes in magnitude that reflect the corresponding changes of the impinging periodic wake velocity. It is worth noting, that despite the injection of turbulence kinetic energy by the vortical core of the impinging wakes, no local instantaneous boundary layer transition occurs. This is because of the strong negative pressure gradient that prevents the boundary layer from becoming instantaneously transitional.

Representative for the instantaneous velocity distribution inside the separation zone, shown in Figure 11.12 (b,c,d,e,f), we discuss the results plotted in Figure 11.12 (e) at s/s_0 = 0.674. During the time interval from t/τ close to 0.5 (1.5, 2.5, etc) to about t/τ = 0.75

(1.75, 2.75 etc) the separation zone is exposed to the wake external flow being under the influence of relatively lower turbulence does not have the capability to suppress the separation zone. Thus, the separation region is clearly shown by the velocity distributions at $t/\tau = 0.5$ and $t/\tau = 0.75$. As the wake passes over the blade at $s/s_0 = 0.674$ introducing high turbulence kinetic energy into the boundary layer, the boundary layer is energized causing the separation zone to partially reduce or disappear. This leads to an instantaneous re-attachment. This time interval corresponds to the case where the flow is completely under the influence of wake and correspondingly the re-attached velocity distribution assumes a turbulent profile characterized by the curves at $t/\tau = 1.0$, $t/\tau = 0.05$, and $t/\tau = 0.25$ shown in Figure 11.12(e). To underline this statement, the steady state velocity distribution at the same streamwise position is also plotted in Figure 11.12 (e) using full circles. It shows clearly the separated nature of the boundary layer which coincides with the instantaneous velocity profile at $t/\tau = 0.5$. Intermediate times reflect the gradual change between the separation and re-attachment as the flow is undergoing the influence of the oncoming wake. Moving to the trailing edge of the separation zone, at $s/s_0 = 0.705$, when the flow is completely under the influence of the wake corresponding to the curves at $t/\tau = 1.0$, $t/\tau = 0.05$, and $t/\tau = 0.25$ shown in Figure 11.12 (f), a partial reduction in boundary layer thickness as a result of wake impingement is visible, however, the separation zone does not seem to disappear. But, the compression of the bubble height is very clear.

Figure 11.12 (g,h) exhibits the velocity distributions on the suction surface respectively at $s/s_0 = 0.849$ and $s/s_0 = 0.898$ where the flow is fully reattached. At this streamwise position, the boundary layer distributions at different (t/τ) experience changes in magnitude that reflect the corresponding changes of the impinging periodic wake velocity. Once, the boundary layer is reattached and the velocity distribution assumes a fully turbulent profile, no major changes are observed.

Figures 11.13 (a) to (h) show, the velocity distributions inside and outside the boundary layer at fixed s/s_0-locations experience moderate to pronounced changes at Ω=3.18. Similar instantaneous velocity distribution is observed when operating at a reduced frequency of Ω=3.18. Compared with Ω=1.59, a stronger suppression of the separation zone

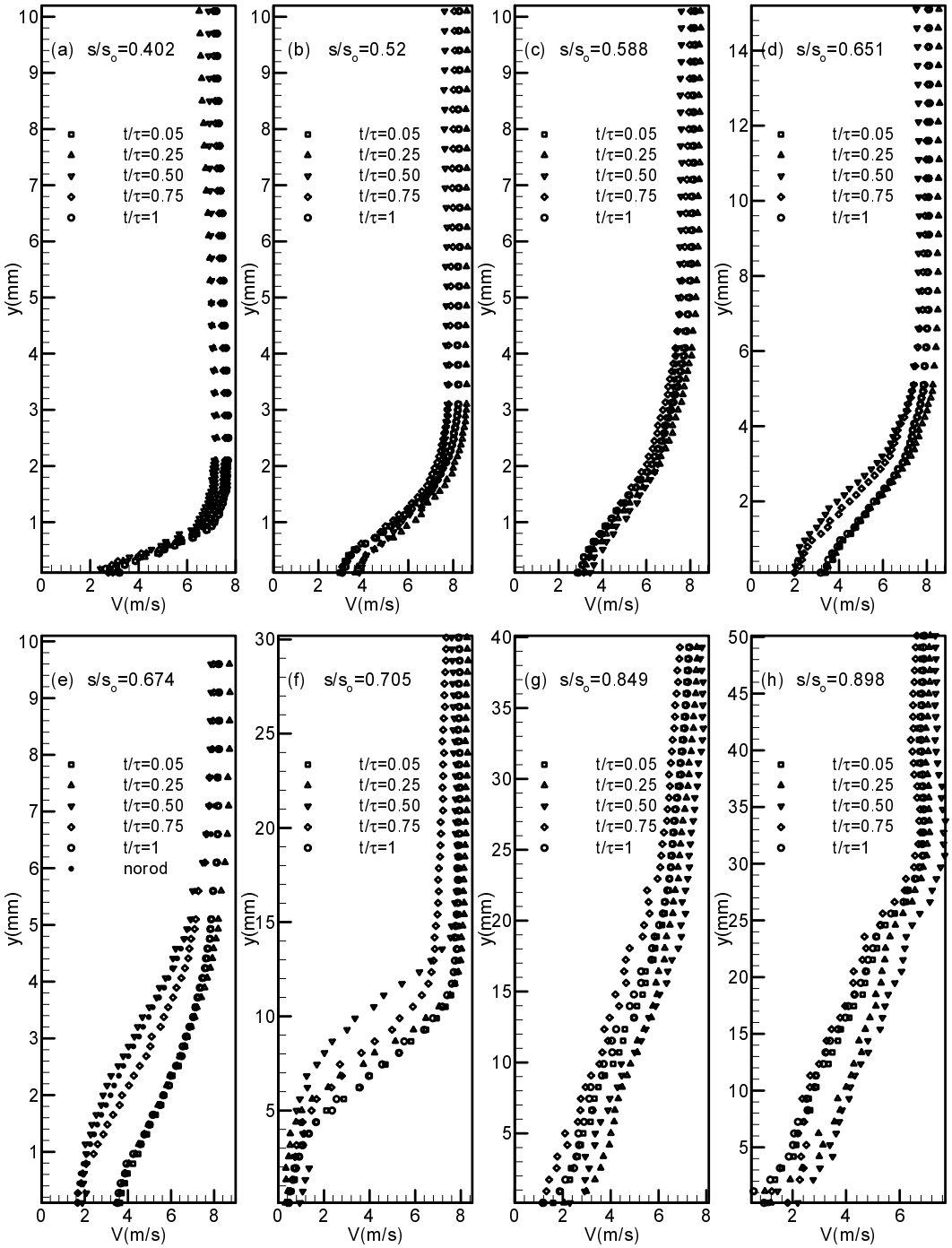

Figure 11.12. Distribution of the ensemble-averaged velocity development along the suction surface for different s/s_o with time t/τ as parameter for Ω=1.59 (S_R=160 mm), Re=110,000

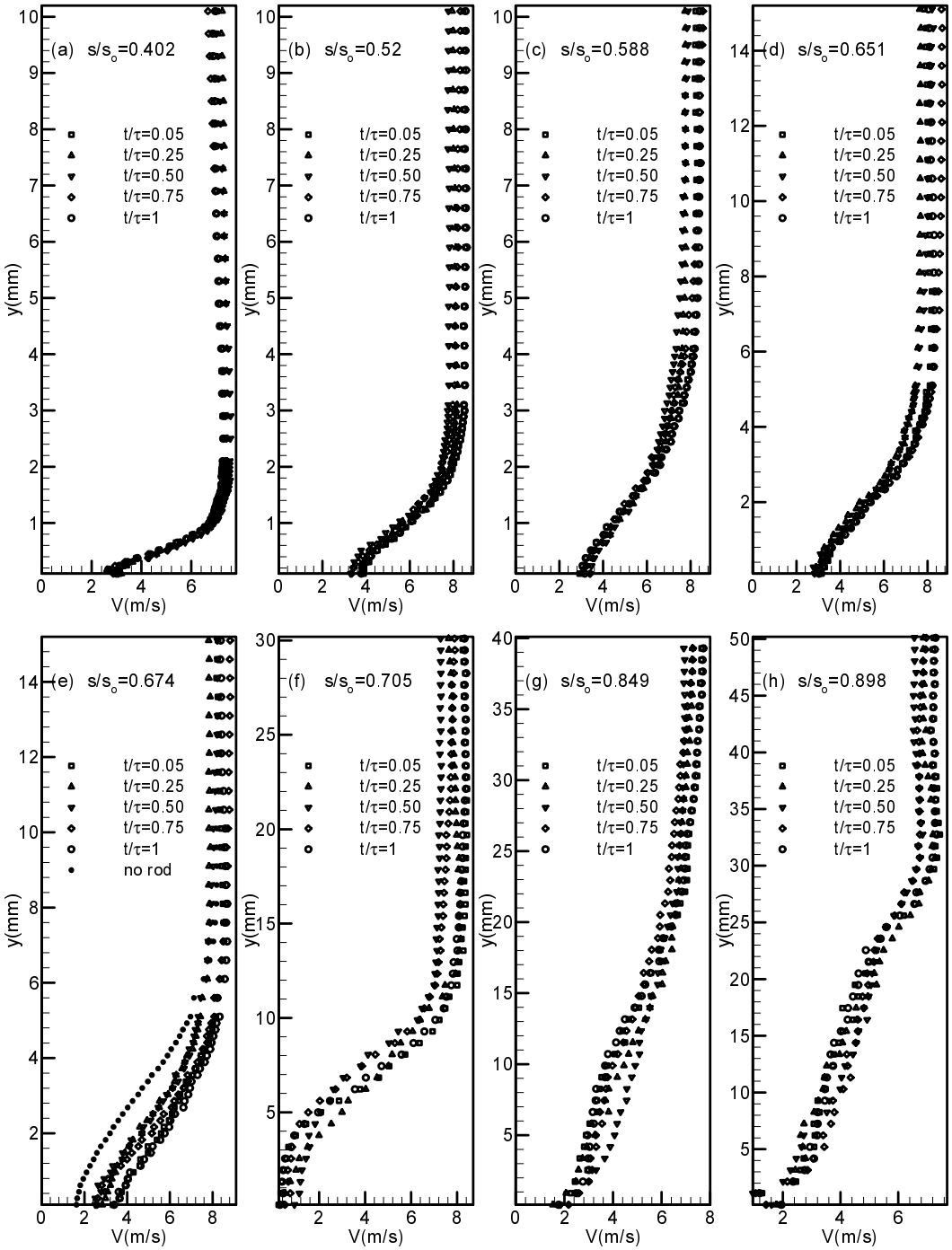

Figure 11.13. Distribution of the ensemble-averaged velocity development along the suction surface for different s/s_o with time t/τ as parameter for Ω=3.18 (S_R= 80 mm), Re=110,000

is noticed at Ω=3.18. When the wake passing frequency is increased over the blade, it is also increasing high turbulence kinetic energy. Therefore, boundary layer is energized comparatively more than the reduced frequency of Ω=1.59 and it causes the separation zone to partially reduce more.

11.6 Temporal-Spatial Resolution of the Separation Zone

The separation zone can be thought of as a curve that connects the velocity inflection points along the suction surface. Starting with a reduced frequency of Ω = 1.59 (S_R = 160 mm) at s/s_o=0.520, Figure 11.14 (a) exhibits the start of the separation zone with a lateral extension of about 0.2 mm. The impingement of the periodic wake vortical core with the high turbulence intensity causes a local periodic contraction of the zone in lateral direction. Convecting downstream, the lateral extension increases, thus the contraction appears more pronounced, Figure 11.14 (b,c,d). Substantial contraction occurs toward the trailing edge of the separation zone as shown in Figure 11.14 (e,f). At this streamwise position, the separation zone starts to contract at t/τ=1.25 and 2.25. This points coincides with the streamwise position of the velocity maximum, which exactly correspond to the position of the minimum fluctuation. Similar results are observed when operating at a reduced frequency of Ω=3.18 which is shown in Figure 11.15 (a,b,c,d,e,f). As we discussed earlier from the other results, increasing the reduced frequency help to reduce more separation boundary layer. As a result, it helps to decrease the losses coming from the large bubble.

Increased passing frequency causes an increase in turbulence kinetic energy. This in turn energizes the boundary layer. This is seen by comparing the velocity distribution for Ω=3.18 and Ω=1.59.

11.7 Change of Separation Bubble Height Under Unsteady Wake Flow

The shape of the bubble configuration can be identified from the time-averaged velocity distributions. The dividing streamline and the line of inflection points is found by taking second derivative and equating to zero. A similar bubble formation is found for three

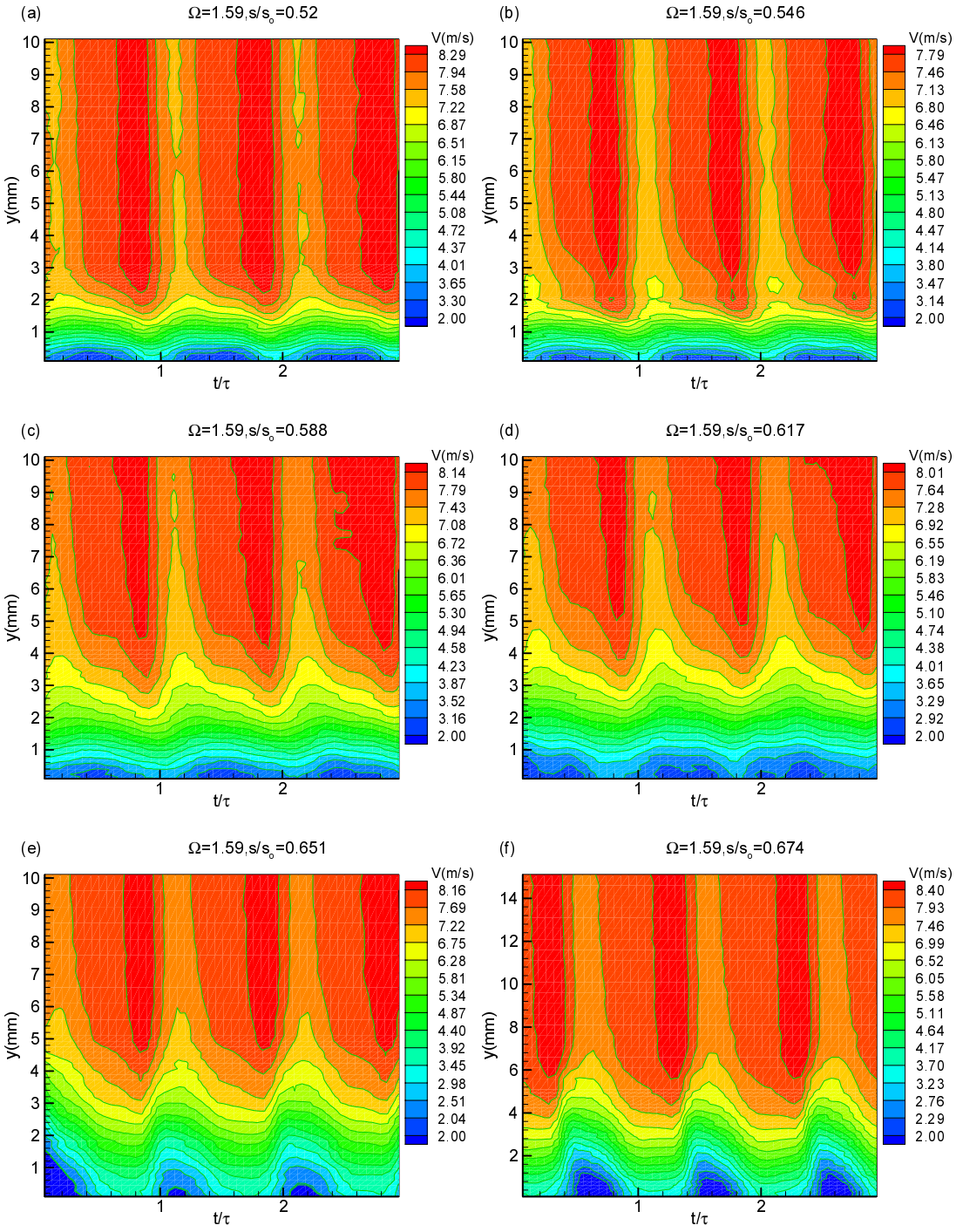

Figure 11.14. Contour plot of the ensemble averaged velocity distribution showing the effect of periodic wakes on the separation zone at at Ω=1.59 (S_R=160 mm) at Re = 110,000

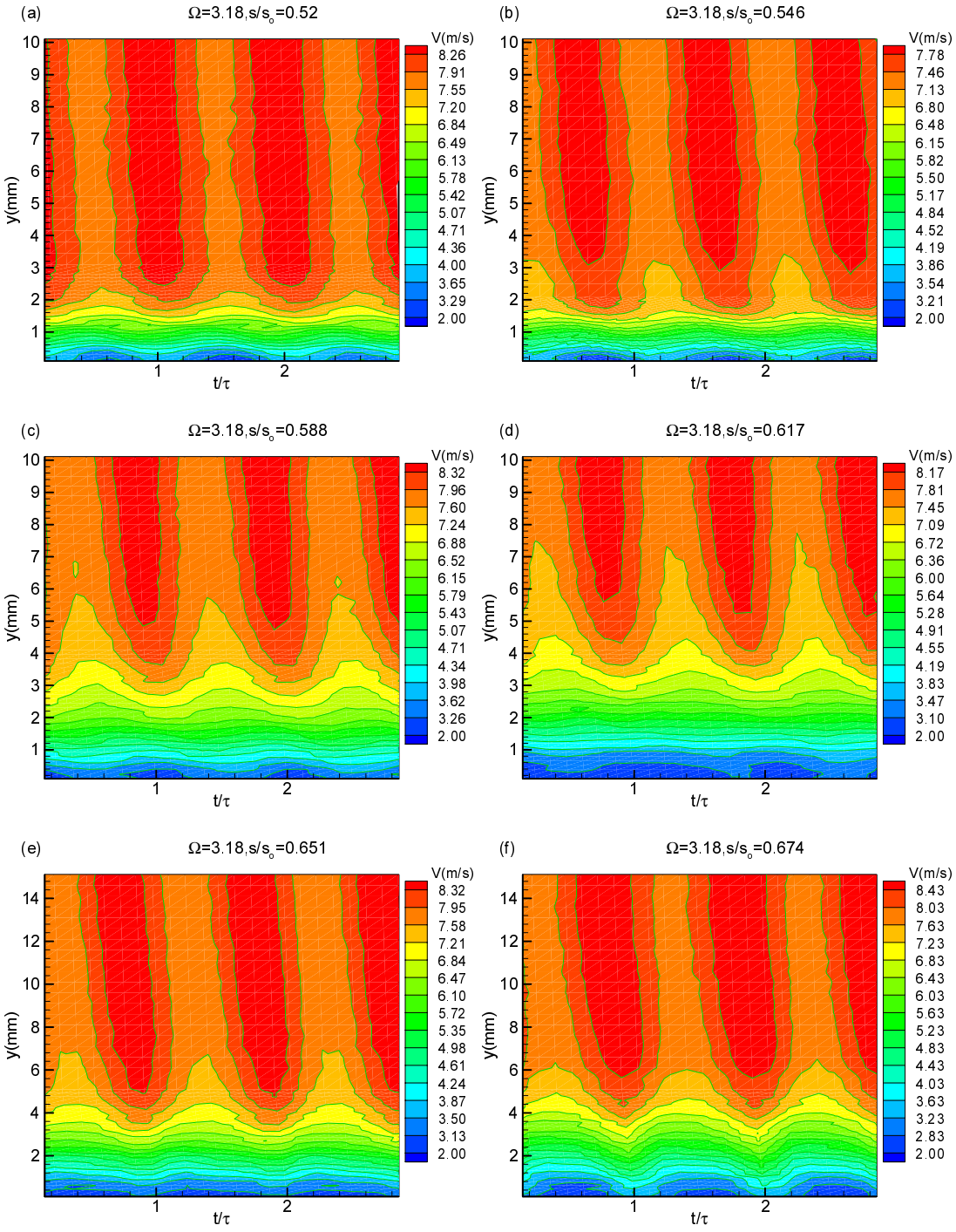

Figure 11.15. Contour plot of the ensemble averaged velocity distribution showing the effect of periodic wakes on the separation zone at at Ω=3.18 (S_R=80 mm) at Re = 110,000

different frequencies as shown in Figure 11.16. The separation points, where the separation starts and ends, remain the same for the three different frequencies. The separation bubble height decreases with the increase of the reduced frequency. The separation zone is exposed to wake external flow being under the influence of relatively lower turbulence followed by a periodic sequence of wake impingements. When the wake passes over the blade introducing high turbulence kinetic energy into the boundary layer, the boundary layer is energized causing the separation zone to partially reduce. Thus, this flow does not have the capability to completely suppress the separation zone. The main parameters describing the separation bubble for the three test frequencies are presented in Table 11.1.

Table 11.1. Parameters describing separation bubble for three different frequencies

Parameters	**Ω=0.0**	**Ω=1.59**	**Ω=3.18**
s_s/s_o	0.5	0.5	0.5
s_m/s_o	0.705	0.705	0.705
s_r/s_o	0.746	0.746	0.746
h_m(mm)	6.123	5.818	5.358

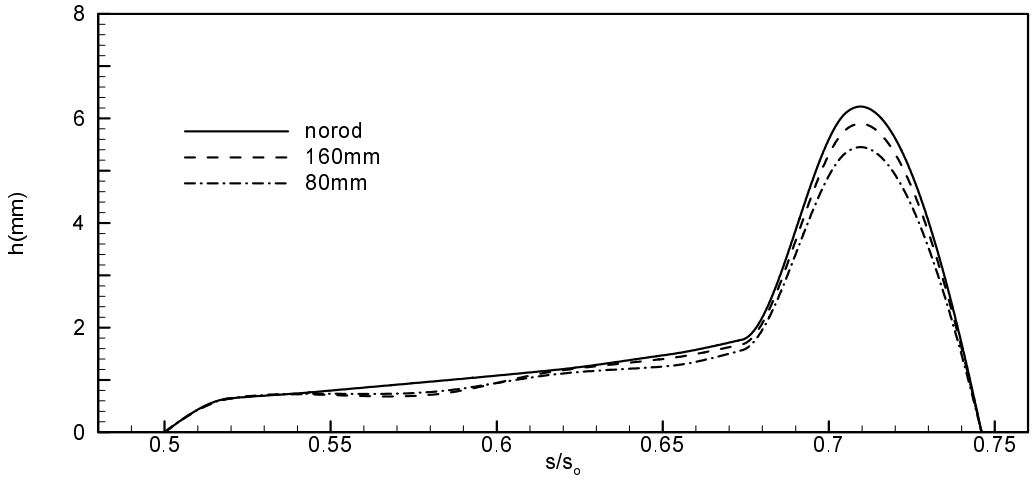

Figure 11.16. Change of separation bubble height under the influence of different reduced frequencies of Ω=0, 1.59, 3.18 (S_R=∞, 160 mm, 80 mm), Re=110,000

11.8 Separation Bubble Behavior Under Wake Propagation

The effect of the periodic unsteady wakes on the onset and extent of the separation bubble is shown in Figure 11.17 and 11.18 for two different frequencies, namely Ω=1.59 and Ω=3.18. These figures display the full extent of the separation bubble and its behavior under a periodic wake flow impingement at different t/τ. The wake propagation for Ω=1.59 and Ω=3.18 is analyzed, and the value of t/τ corresponds to the point in the cycle at which the data acquisition system is triggered. During a rod passing period, the wake flow and the separation bubble undergo a sequence of flow states which are not noticeably different when the unsteady data are time-averaged. To compare the temporal changes of the spatial position of the separation bubble, the time-averaged separation bubble is marked red. Starting with a reduced frequency of Ω=1.59 at t/τ=0.25, the separation bubble is under a full influence of the wake. The wake passing over the blade introduces a high turbulence kinetic energy into the boundary layer. The energized boundary layer bubble is partially reduced or disappeared compared to the time-averaged separation bubble size shown red in Figure 11.17(a). As the wake passes, t/τ=0.50, the height of the separation bubble reaches its maximum size at s/s_o=0.705. The contraction starts again that reduces the size of the separation bubble at t/τ=0.75. At s/s_o=0.705 the core region has slightly moved towards to the leading edge. At t/τ=1, the full effect of the wake on the boundary layer can be seen before another wake appears and the bubble moves back to the original position. Once the wake starts to penetrate into the separation bubble, the turbulent spot produced in the wake paths causes a total suppression at some streamwise positions. Similar results are observed when operating at a reduced frequency of Ω=3.18. The wake frequency exerts no influence on the position of the separation bubble. However, doubling the reduced frequency is associated with the higher turbulence intensity that leads to stronger suppression of the separation bubble as shown in Figure 11.18.

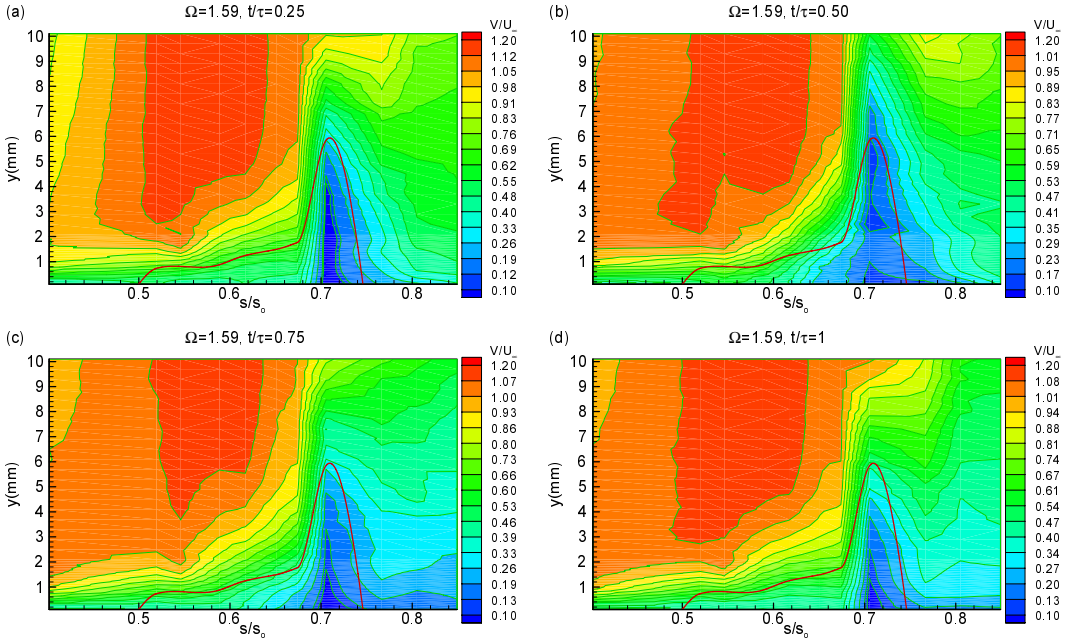

Figure 11.17. Ensemble-averaged velocity contours along the suction surface for different s/s_o with time t/τ as parameter for Ω=1.59 (S_R=160 mm), Re=110,000 (time-averaged separation bubble for Ω=1.59 marked red)

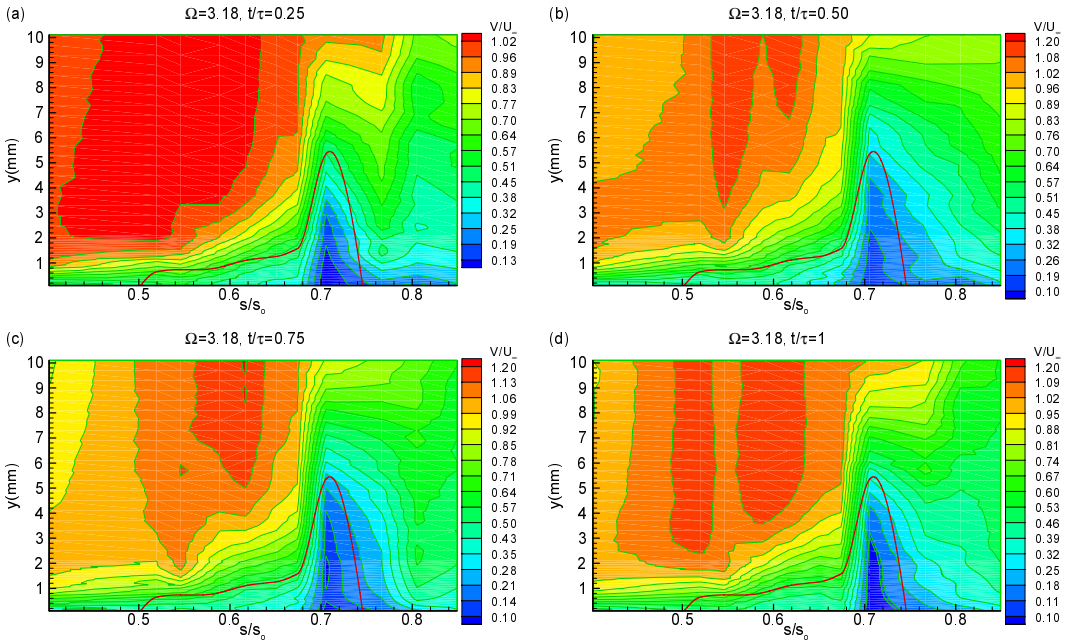

Figure 11.18. Ensemble-averaged velocity contours along the suction surface for different s/s_o with time t/τ as parameter for Ω=3.18 (S_R=80 mm), Re=110,000 (time-averaged separation bubble for Ω=3.18 marked red)

11.9 Contraction, Separation and Regeneration of the Separation Zone

Studying the temporal distribution of the turbulence fluctuations along the longitudinal extension of the separation zone, it becomes clear that, in conjunction with the pressure gradient and periodic wakes, there is another crucial mechanism responsible for the lateral and longitudinal decrease of the separation zone. This mechanism constitutes a combination of the high turbulence fluctuation level and its gradient. It is the temporal gradient of the turbulence fluctuation, or more precisely the fluctuation acceleration $\partial v_{rms}/\partial t$ that provides higher momentum and energy transfer into the boundary layer energizing the separation zone and causing it to partially or entirely disappear. For better understanding this phenomenon, the wake and the fluctuation velocity is presented in Figure 11.19 for the streamwise position s/s_o=0.651. The fluctuation rms velocity is scaled up with the factor of 4 to make it clear and an arbitrary normal position of y=2.85mm is chosen which is sufficiently above the separation zone for a given normal distance.

Figure 11.19 (a) shows two separate regions: (1) a wake vortical core, occupied by vortices that originate from the moving cylindrical rods and generate high turbulence fluctuations, and (2) a wake external region between the adjacent vortical cores with relatively low turbulence activities. The wake configuration is asymmetric as shown in Figure 11.20. As Figure 11.20 shows, the separation zone starts to contract at t/τ=1.25. This point coincides with the streamwise position of the velocity maximum, which exactly corresponds to the position of the fluctuation minimum, as shown in Figure 11.18 (b). At this point, the fluctuation within the vortical core starts to increase while the velocity continuously decreases. This process continues until the end contraction at t/τ=1.41 has been reached. Thereafter, the separation zone is subjected to a process of intensive exchange of momentum and energy that causes the separation to diminish, as shown in Figure 11.20. The process of separation contraction, suppression, and regeneration is summarized in Figure 11.19 (b). It shows more details of separation contraction and suppression. In this context, it is necessary to subdivide the vortical core shown in Figure 11.19 (b) into fourdistinct regions, separated by thick dashed lines, as presented in Figure 11.19 (b). Region (a) is characterized by the initial positive gradient of the fluctuation $\partial v_{rms}/\partial t>0$

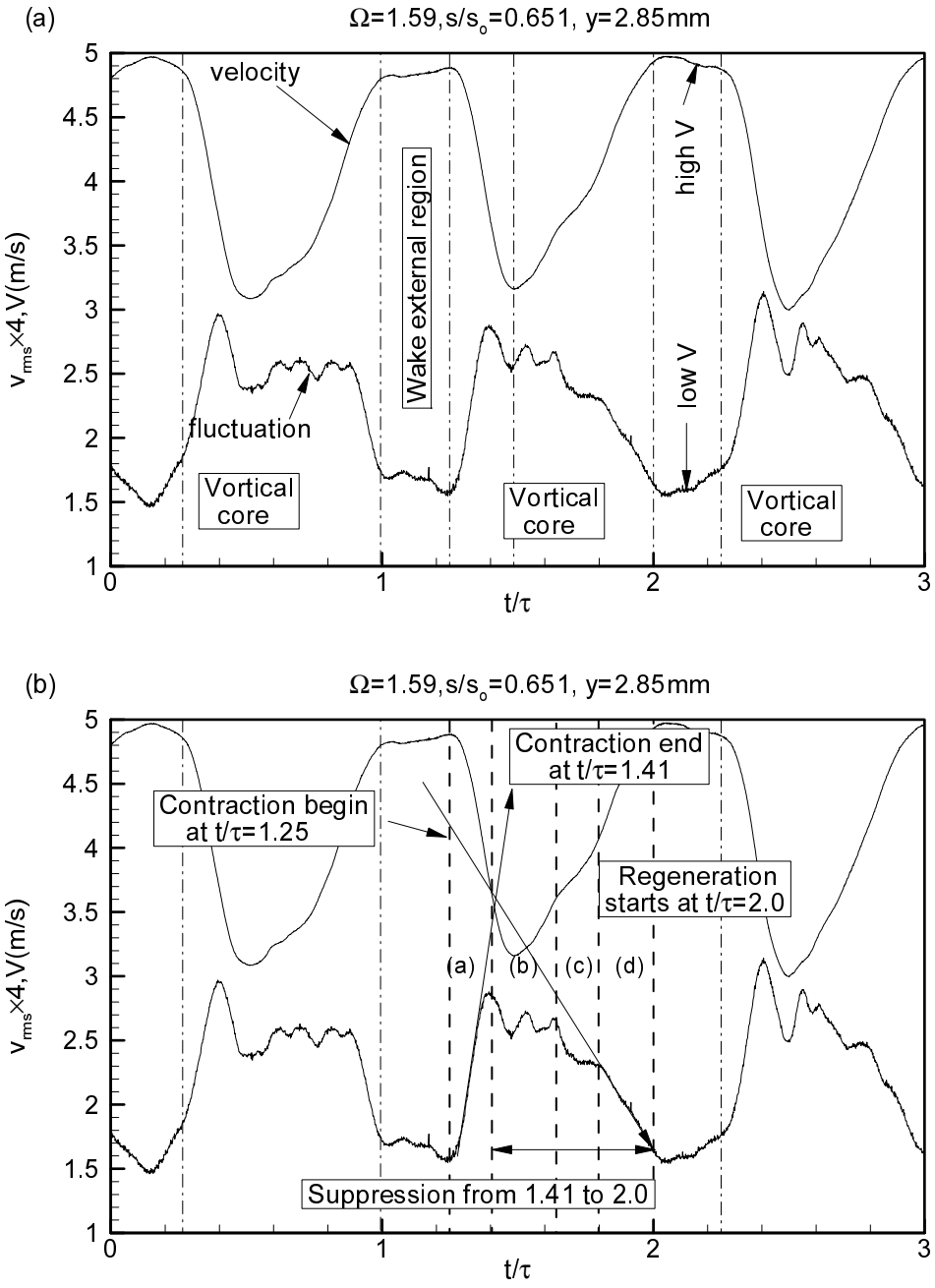

Figure 11.19. Separation, contraction, suppression and regeneration at Re=110,000

marked with an upward arrow. Region (b) represents the substantial part of the vortical core with an intense turbulence activity. Region (c) serves as a transition between region (b) and the relatively calm region (d) characterized by $\partial v_{rms}/\partial t<0$.

For an initial fluctuation gradient $\partial v_{rms}/\partial t>0$, the separation zone begins to contract at $t/\tau=1.25$. This initial gradient is crucial for initiating the contraction process. Once the maximum fluctuation velocity with the temporal gradient $\partial v_{rms}/\partial t=0$ at $t/\tau=1.41$ is reached (region a), the process of energizing the separation zone, thereby preventing its regeneration (region b). Passing the transition region (c), the process of suppression continues until the end of the vortical region at $t/\tau=2.0$ is reached. At this point the external wake region with its low turbulence content arrives causing a regeneration of the separation zone, thus reversing the entire suppression process.

While the existence of higher turbulence fluctuations expressed in terms of higher turbulence intensity is well known for influencing the flow separation, its gradient is crucial in suppressing or preventing the onset and the extension of the separation zone. The fluctuation gradient is an inherent feature of the incoming periodic wake flow and does not exist in a statistically steady flow, that might have high turbulence intensity.

The results clearly indicate that for the particular blade under investigation, one has to do with a massive separation on the suction surface. These observations in comparison with the steady state reference case suggest that, once a massive separation zone is manifested, its size can be significantly reduced by periodic wake impingement, but it cannot be completely removed. The results presented here are valid for blades with a similar pressure distribution discussed earlier. Since the onset and extent of the separation zone is uniquely associated with the pressure gradient, blades can be designed with less local adverse pressure gradient, whose onset can completely be suppressed by impinging wakes.

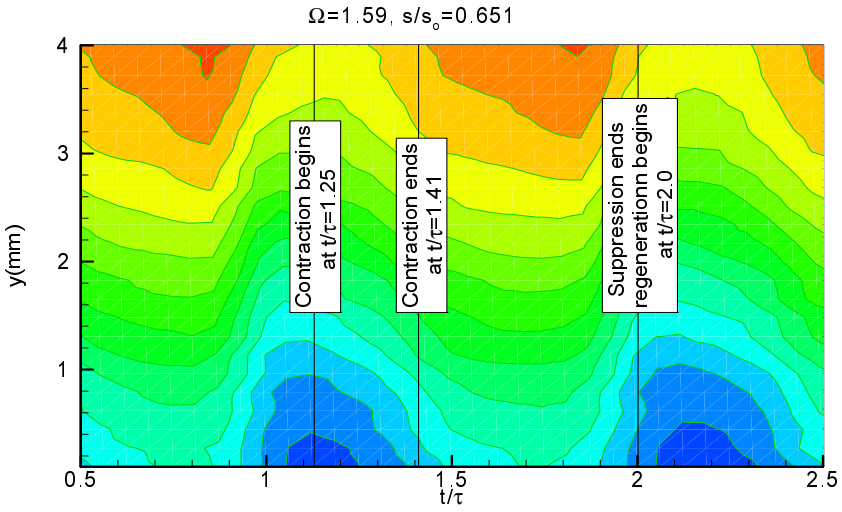

Figure 11.20. Separation zone, definition of contraction begin, contraction end, suppression, and regeneration

11.10 Ensemble-Averaged Fluctuation RMS Velocity Distribution

The temporal-spatial contours of the ensemble-averaged fluctuation rms velocity at three different lateral positions for two reduced frequencies are presented in Figures 11.21(a) to (f). As shown in Figure 11.21, the wakes periodically disturb the boundary layer with high turbulence intensity cores. As Figure 11.21 (a) shows, three wake passings are visible for Ω=1.59 at a normal distance from the wall of y=1.065m. At s/s$_o$=0.52, the visibility of the wake is vanished due to separation. As explained earlier the separation zone starts at s/s$_o$=0.52 and extends up to s/s$_o$=0.746, thus occupying more than 24% of the suction surface and forming a massive separation. It is perfectly matching the result obtained from the Figure 11.1. At s/s$_o$=0.746, the fluctuation rms velocity field in Figure 11.21 (a) shows the stagnant fluid region and the area of the rms maximum, which indicates the development of transition and reattachment. Increasing Ω to 3.18 causes an earlier mixing of the impinging wakes that leads to a complete degeneration of the deterministic periodic flow into a stochastic turbulent flow. For the highest reduced frequency of Ω=3.18, the flow is highly turbulent all along the blade surfaces. As it can be seen from the Figure 11.21 (b),

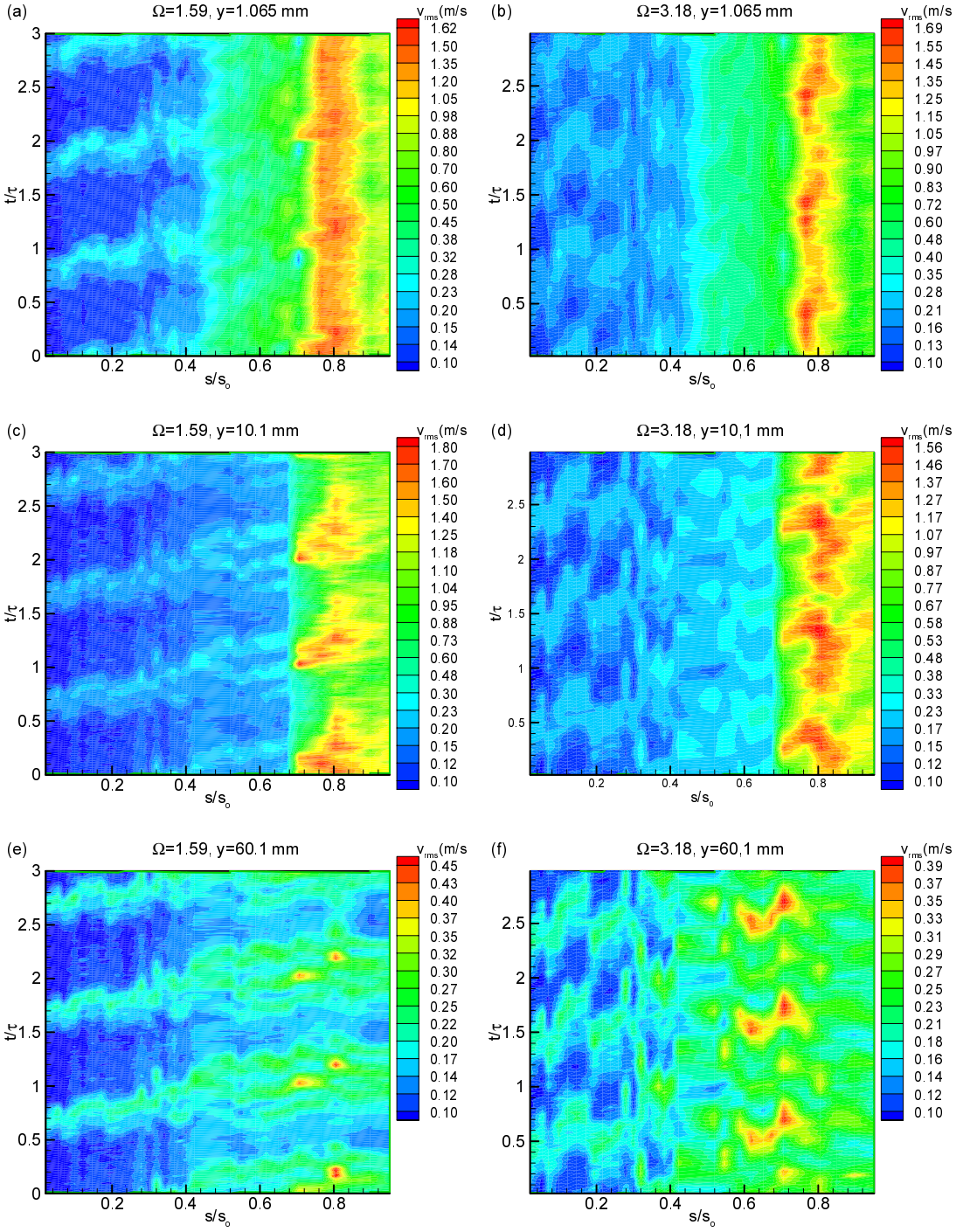

Figure 11.21. Ensemble-averaged rms fluctuation velocity in the temporal-spatial domain at different y positions for Ω=1.59 (S_R=160 mm), and Ω=3.18 (S_R=80 mm)

increasing the reduced frequency has not brought major changes, regarding the structure of the separation zone. The laminar boundary layer and the onset of the separation zone remain the same.

As shown in Figure 11.21 (c) at y=10.1 mm and Ω=1.59, the wakes are visible up to s/s_o=0.676. Up to this particular location, the wake convects above the separation zone, however by moving downstream the same lateral position is within the separation zone. This explains the sharp separation line where the wakes are not visible anymore. This implies that the wakes here, is in the previous figure have not penetrated into the separation zone. As shown in Figure 11.21 (e), farther from the wall at y=60.1 and Ω=1.59, the wake passings are visible, because the wake convects outside the boundary layer and the separation zone.

11.11 Boundary Layer Time-Averaged Integral Quantities

The time-averaged distribution of the boundary layer thickness, displacement thickness, momentum thickness and the shape factor for the suction surface are shown in Figure 11.22. The momentum thickness value for three different reduced frequencies remains the same along the blade and does not demonstrate any unusual behavior within the separation bubble between the separation start point s_s and the re-attachment s_r as shown in Figure 11.22(c). The initial growth of the boundary layer displacement thickness and the shape factor is comparatively small up to the maximum displacement location. As it is seen from the Figures 11.22 (b) and (d), both the boundary layer displacement thickness and the shape factor were decreased in the separation bubble and after the re-attachment, as the reduced wake frequency was increased. This results clearly show the impact of the unsteady wake flow on the boundary layer parameters and hence on the profile loss coefficient and efficiency. The unsteady wake flow causes a reduction of the losses due to the suppressed or reduced separation bubble.

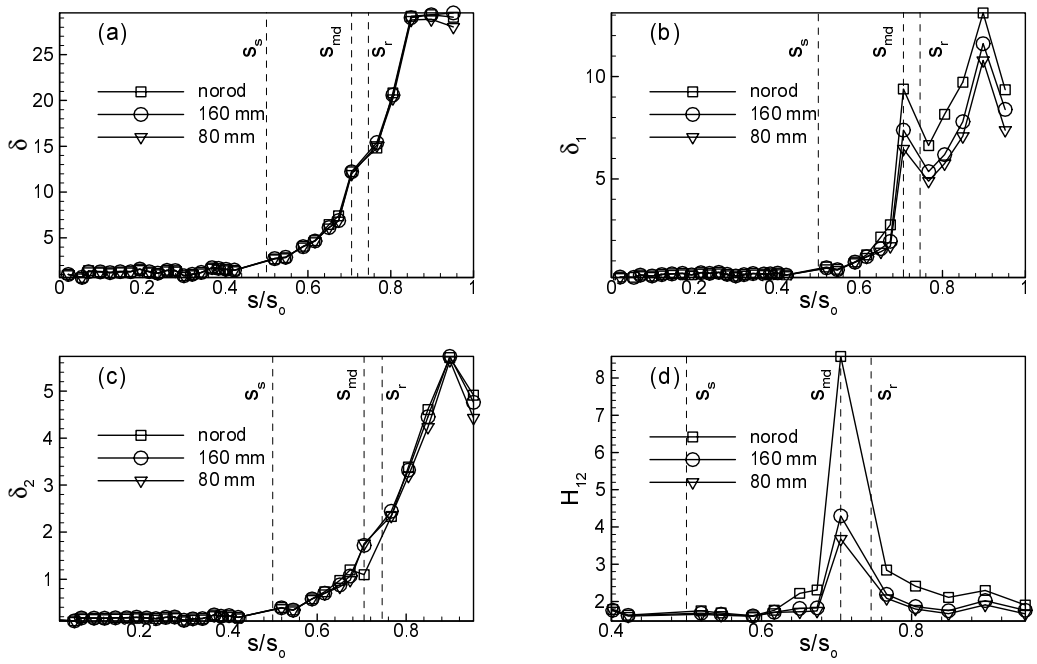

Figure 11.22. Time averaged (a) boundary layer thickness, (b) displacement thickness, (c) momentum thickness and (d) shape factor for three different reduced frequency of Ω=0, 1.59, 3.18 (no rod, 160 mm, 80 mm), Re=110,000, s_s= starting point of separation zone, s_{md}= location of maximum separation bubble height

11.12 Boundary Layer Ensemble Averaged Integral Quantities

The integral parameters, such as the momentum thickness and shape factor, are of particular interest to a turbine designer, since they provide an accurate first estimation of the quality of the designed blade. The ensemble-averaged distributions of the momentum thickness and shape factor for the suction surface are shown in Figure 11.23 (a, b, c, d) for Ω = 1.59 and Ω = 3.18 values discussed earlier. The momentum thickness values are nondimensionalized with respect to the value corresponding to the steady case with Ω = 0. The period τ represents the wake-passing period that is specific to the individual wake generating cluster, which is characterized by the Ω - value under investigation. The periodic behavior of the ensemble-averaged momentum thickness over the entire suction surface as a result of the embedded periodic wake flow, is clearly visible from Figure 11.23. It represents the momentum thickness behavior at different s/s_0 locations upstream, within and

outside the separation bubble. The relative momentum thickness distribution upstream of the separation bubble in Figure 11.23 (a) integrally exhibits a slight increase, whereas inside the zone shown in Figure 11.23 (a), a substantial decrease is apparent. At the immediate vicinity of the separation bubble trailing edge, $s/s_0 = 0.705$ close to re-attachment, Figure 11.23 (b), the momentum thickness experiences a noticeable increase, which by convecting downstream decreases again and approaches the integral values that are close to the steady state case.

The ensemble averaged relative shape factor H_{12} -distributions on the suction surface at the same streamwise locations are plotted in Figure 11.24 (a,b,c,d). Upstream of the separation bubble, Figure 11.24 (a) they experience a similar periodic change with an average slightly close to the steady case. Moving into the separation bubble, Figure 11.24(b), each streamwise location presents its own shape factor that is specific to the velocity distribution we discussed. Similar results are observed when operating at a reduced frequency of Ω=3.18 which is shown in Figure 11.23 and 11.24 (c, d).

The ensemble averaged integral parameters discussed above are essential to calculate the ensemble averaged and time averaged profile loss coefficients at each streamwise position. Furthermore, the integration of the time averaged loss coefficient distribution over the entire blade surface provides the global profile loss coefficient. A simple procedure given in [125] describes how the loss coefficient can be calculated using the integral parameters.

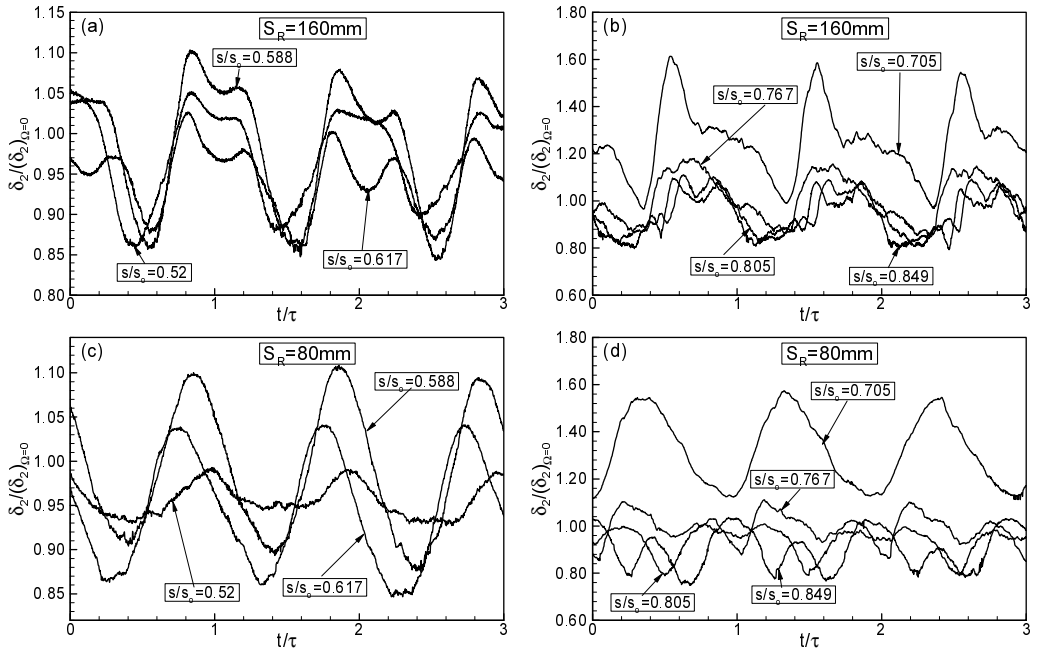

Figure 11.23. Ensemble-averaged relative momentum thickness distribution along the suction surface for different streamwise positions for (a) and (b)at Ω=1.59 (S_R=160 mm), (c) and (d) at Ω=3.18 (S_R=80 mm)

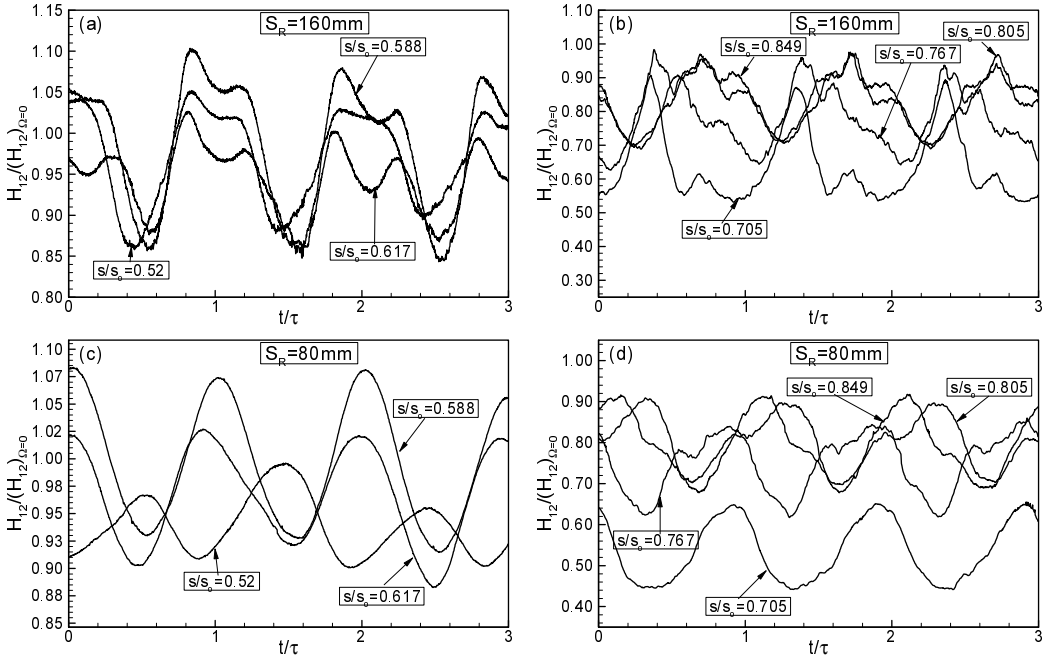

Figure 11.24. Ensemble-averaged relative shape factor distribution along the suction surface for different streamwise positions for (a) and (b)at Ω=1.59 (S_R=160 mm), (c) and (d) at Ω=3.18 (S_R=80 mm)

12. COMBINED EFFECTS OF REYNOLDS NUMBER, TURBULENCE INTENSITY AND UNSTEADY WAKE CONDITIONS ON THE SEPARATION BUBBLE

To investigate the influence of the unsteady wake flow, Reynolds numbers and freestream turbulence intensity levels on the boundary layer development along the suction and pressure surfaces of the LPT blade and, particularly, its impact on the inception and onset of the separation bubble, the detailed surface pressure and boundary layer measurements were performed at a Reynolds number of 110,000 and 150,000. This Reynolds numbers, which pertain to a typical cruise operation, exhibit a representative value within LPT operating range between 75,000 and 400,000 as discussed by Hourmouziadis [122]. For the Reynolds number of 110,000 and 150,000, three different reduced frequencies were examined.

12.1 Surface Pressure Distributions

Detailed pneumatic surface pressure measurements were taken at Re = 110,000, and 150,000. For each Reynolds number three different reduced frequencies, namely $\Omega = 0.0$, 1.59, and 3.18 are applied that correspond to the rod spacings S_R = 80 mm, 160 mm, and ∞ mm. The pressure distributions in Figure 12.1 show the results of the steady case and two unsteady cases. The pressure signals inherently signify the time-averaged pressure because of the internal pneumatic damping effect of the connecting pipes to the transducer. The noticeable deviation in pressure distribution between the steady and unsteady cases, especially on the suction surface, is due to the drag forces caused by the moving rods. The drag forces are imposed on the main stream and cause momentum deficiency that lead to a reduction of the total and static pressure. The time-averaged pressure coefficients along the pressure and suction surfaces are plotted in Figure 12.1. The suction surface (upper portion), exhibits a strong negative pressure gradient. The flow accelerates at a relatively steep rate and reaches its maximum surface velocity that corresponds to the minimum

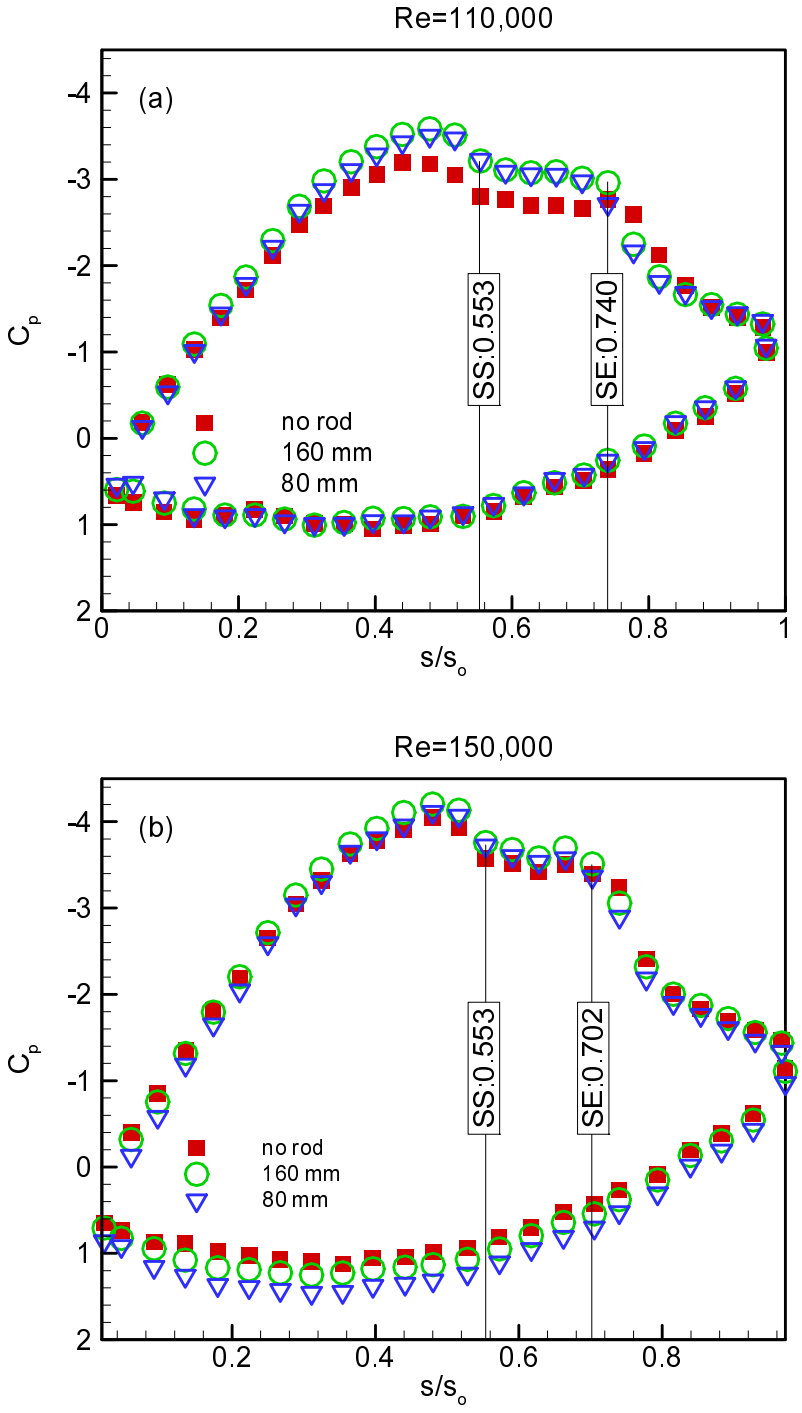

Figure 12.1. Static pressure distributions at two different Re-numbers and reduced frequencies Ω=0, 1.59, 3.18 (no rod, 160 mm, 80 mm), SS=Separation start, SE= Separation end

C_p=-4.0 at s/s_o= 0.42. Passing through the minimum pressure, the fluid particles within the boundary layer encounter, a positive pressure gradient that causes a sharp deceleration until s/s_o= 0.55 has been reached. This point signifies the beginning of the laminar boundary layer separation and the onset of a separation bubble. As seen in the subsequent boundary layer discussion, the separation bubble characterized by a constant C_p- plateau extends up to s/s_o= 0.746, thus occupying more than 19% of the suction surface and constituting a massive separation. Passing the plateau, the flow first experiences a second sharp deceleration indicative of a process of re-attachment followed by a further deceleration at a moderate rate. On the pressure surface, the flow accelerates at a very slow rate, reaches a minimum pressure coefficient at s/s_o= 0.42 and continues to accelerate until the trailing edge has been reached. Unlike the suction surface, the pressure surface boundary layer does not encounter any adverse positive pressure gradient that triggers separation. However, close to the leading edge, a small plateau extending from s/s_o= 0.08 to 0.16 indicates the existence of a small size separation bubble that might be attributed to a minor inlet flow incident angle.

Considering the unsteady case with the reduced frequency Ω = 1.59 corresponding to a rod spacing of S_R=160 mm, Figure 12.1 exhibits a slight difference in the pressure distribution between the steady and unsteady cases. As mentioned above, this deviation is attributed to the momentum deficiency that leads to a reduction of the total and static pressure. For Re=110,000, the wakes have a reducing impact on the streamwise extent of the separation plateau. As seen in Figure 12.1 (a), the trailing edge of the plateau has shifted from s/s_o= 0.74 to s/s_o= 0.702. This shift reduced the streamwise extent of the separation plateau from 19% to 15% of the suction surface length which is in this particular case, 21% of reduction in streamwise extent of the separation. Increasing the reduced frequency to Ω=3.18 by reducing the rod spacing to S_R=80 mm causes a slight shift of the C_p-distribution compared with Ω=1.59 case. One should bear in mind that pneumatically measured surface pressure distribution represents a time integral of the pressure events only.

Increasing the Reynolds number to Re=150,000, has brought major changes in steady state C_p-distribution. The combination of higher Re-number with unsteady wakes reveals

the noticeable deviation on the streamwise extent of the separation plateau. As seen in Figure 12.1 (b), the trailing edge of the plateau has shifted from $s/s_o = 0.74$ to $s/s_o = 0.702$ for Reynolds number of 150,000. The combination of higher Reynolds number with high unsteady wakes introduce fluctuation kinetic energy into the boundary layer which tends to inhibit the separation tendency. C_p-distribution clearly shows that the wake impingement with higher Reynolds number shortens the streamwise extent of the separation zone compared to the steady case. Also, the combination of higher Re-number with unsteady wakes reveals that the noticeable deviation in pressure distribution between the steady and unsteady cases discussed above is diminishing with increasing the Re-number as shown in Figure 12.1(a, b). Two counteracting factors are contributing to this deviation. The first factor is attributed to the momentum deficiency and the associated total pressure losses caused by moving wakes, as discussed above. The second factor pertains to the energizing effect of the impinging wakes on the boundary layer. Although the impinging wakes cause velocity and momentum deficits, their high turbulence intensity vortical cores provide an intensive exchange and transfer of mass, momentum, and energy to the blade surface, thus energizing the low energetic boundary layer. In conjunction with the surface pressure distribution, the kinetic energy of the normal velocity fluctuation component plays a crucial role. In case of a low Re-number flow, the strong damping effect of the wall shear stress has the tendency to reduce the normal contribution of turbulence kinetic energy, thereby diminishing its surface pressure augmenting effect. Increasing the Reynolds number results in a decrease of the damping effect of the wall shear stress, allowing the kinetic energy of the normal velocity fluctuation component to increase the surface pressure, thus offsetting the wake deficit effects on the pressure distribution. This fact is clearly shown in Figure 12.1(a, b), where the pressure distributions of unsteady flow cases at Ω=1.59 and Ω=3.18 systematically approach the steady state cases at Re=150,000.

Detailed information regarding the structure of the separation bubble is delivered by means of a detailed unsteady boundary layer or surface pressure measurement by fast response probes, as will be discussed in the subsequent sections.

12.2 Unsteady Boundary Layer Measurements Results

Figures 12.2(a) to (d) display representative temporal ensemble-averaged velocity distributions inside the separation bubble at s/s_0=0.65 for Re=110,000 for FSTI levels of 1.9%,3%,8%, and 13% at a reduced frequency of Ω=1.59 and a normal distance of y=3.36 mm. Figure 12.2(a) exhibits two distinct regions: (1) a wake vortical core, occupied by vortices that originate from the moving cylindrical rods and generate high turbulence fluctuations, and (2) a wake external region between the adjacent vortical cores with relatively low turbulence activities. As seen in Figure 12.2(a) and (b), increase in turbulence intensity from 1.9% to 3% has reduced the amplitudes of the wake velocity as well as the turbulent fluctuations. Introducing higher FSTI levels of 8% and 13% leads to a complete degeneration of the deterministic periodic wake flow into a stochastic turbulent flow as shown in Figures 12.2(c) and (d). Comparing Figures 12.2(a) and (c) leads to the following conclusion: The periodic unsteady wake flow definitely determines the separation dynamics as extensively discussed in [24] as long as the level of the time averaged turbulence fluctuations is below the maximum level of the wake fluctuation v_{max} shown in Figure 12.2(a). In our case, this apparently takes place at a turbulence level between 3% and 8%. Increasing the inlet turbulence level above v_{max} causes the wake periodicity to totally submerge in turbulence as shown in Figures 12.2(c) and (d). In this case the dynamics of the separation bubble is governed by the flow turbulence that is responsible for complete suppression of the separation bubble. One of the striking features this study reveals is that the separation bubble has not disappeared completely despite the high turbulence intensity and the significant reduction of its size which is reduced to a tiny bubble. At this point the role of the stability of the laminar boundary layer becomes apparent which is determined by the Reynolds number.

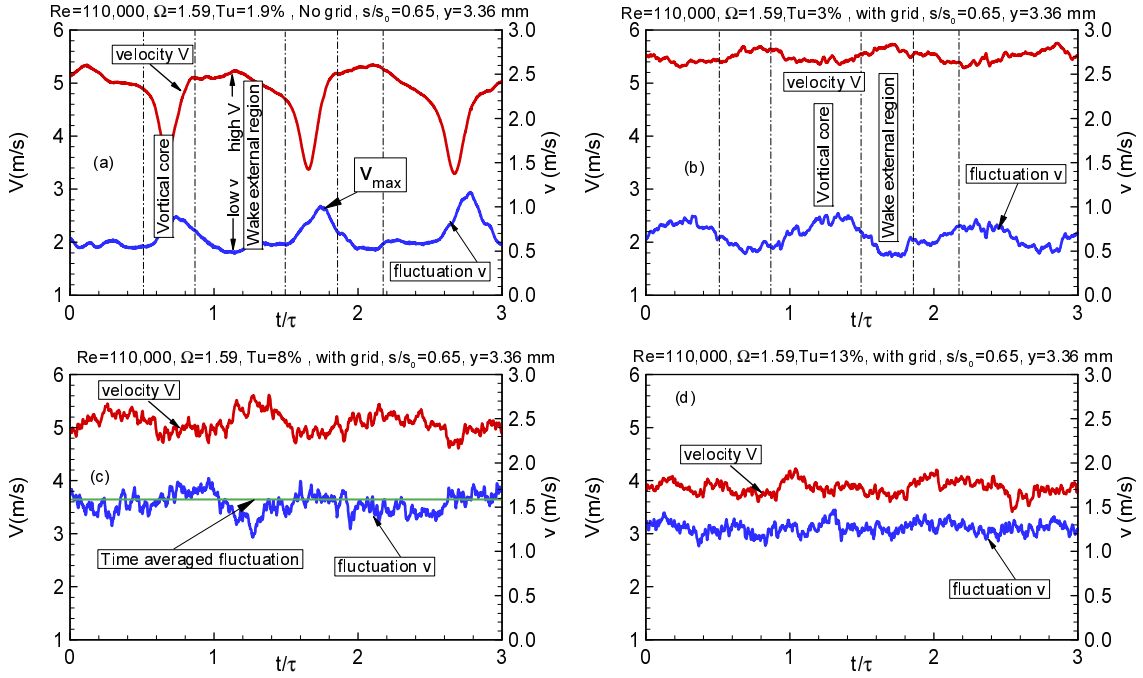

Figure 12.2. Time dependent ensemble averaged velocities and fluctuations for Re= 110,000 at a constant location s/s_0 = 3.36 mm inside the bubble for different inlet turbulence intensities ranging from 1.9% to 13%

12.3 Time Averaged Velocity and Fluctuation Distributions

The effect of wake frequency on time averaged velocity and velocity fluctuation distributions is shown in Figures 12.3(a) to 12.10(b) at 6 representative streamwise locations for Re=110,000 and Re=150,000 with a turbulence intensity level of 1.9%, 3.0%, 8.0% and 13.0%. Figures 12.3(a) to 12.10(b) display the velocity and fluctuation distributions at two streamwise position upstream, two position within and two position downstream of the separation bubble. The diagrams include the steady state data for reference purposes, $\Omega = 0.0$ ($S_R = \infty$), unsteady data for $\Omega = 1.59$ (S_R = 160 mm) and Ω = 3.18 (S_R = 80 mm).

As Figures 12.3(a) to 12.10(b) indicate, in the upstream region of the separation bubble, the flow is fully attached. As seen in Figure 12.3(a), upstream of the separation bubble at s/s_o= 0.49 the velocity distributions inside and the outside the boundary layer experience a slight decrease in magnitude with increasing reduced frequency. However, the

time-averaged velocity distributions seen in Figure 12.4(a) to12.6(a) display no changes with increasing reduced frequency. At the same position, the time averaged velocity fluctuations shown in Figure 12.3(b) exhibit substantial changes within the boundary layer as well as outside it. The introduction of the periodic unsteady wakes with highly turbulent vortical cores and the subsequent mixing, has systematically increased the FSTI level from 1.9% for the steady case to almost 3% for $\Omega = 3.18$ ($S_R = 80$ mm). Comparing the unsteady cases, $\Omega = 1.59$ and 3.18, with the steady reference case $\Omega = 0.0$, indicates that, with increasing Ω, the lateral position of the maximum fluctuation shifts away from the wall. This is due to the periodic disturbance of the stable laminar boundary layer upstream of the separation bubble. However, at the same position, the time-averaged velocity fluctuations shown in Figure 12.4(b) hardly experience any changes with increasing the reduced frequency from $\Omega = 1.59$ to 3.18. Due to the combined effect of the FSTI level of 3% and unsteady wake flow, the lateral positions of the maximum velocity fluctuations remains the same with increasing the reduced frequency.

As seen in Figure 12.3(a), a substantial influence of the wake frequency is observed inside the separation bubble at $s/s_0=0.61$ and $s/s_0=0.73$. Although the impinging wakes are associated with velocity and momentum deficits, their high turbulence intensity vortical cores provide an intensive exchange and transfer of mass, momentum, and energy into the boundary layer, thus energizing the low energetic boundary layer. This kinetic energy of the normal velocity fluctuation component plays a crucial role which tries to reverse the separation tendency. As can be seen from the velocity profiles wake impingement shortens the bubble height and reduces its streamwise extent. Compared to the steady case, however, the onset of the separation bubble has not changed substantially. This shows that, although the impingement of the vortical wake core periodically reduces the separation bubble height, it does not have the sufficient momentum to completely suppress it. Figure 12.4(a) shows, a substantial influence of the combined effect of the higher FSTI level of 3% and unsteady wake flow inside the separation bubble at the same positions. The combination of higher turbulence intensity with unsteady wakes introduce higher fluctuation kinetic energy into the boundary layer than the case without the turbulence grids (FSTI level of 1.9%)

which tends to inhibit the separation tendency and shortens the streamwise extent of the separation bubble. It is observed that starting point of the separation bubble moves further downstream and the re-attachment point occurs earlier. Also, the size of the separation bubble is smaller. Although the combined effect of the turbulence intensity level of 3% and unsteady wake flow periodically reduces the separation bubble height, it does not have the sufficient momentum to completely suppress the bubble.

Introducing the higher FSTI level of 8% subdues the unsteady wake effect to such an extent that the velocity and fluctuation profiles do not reveal any changes with regard to the wake frequency as shown in Figures 12.5(a) and 12.8(b). Increasing the FSTI level to 13% further diminishes the effects of the periodic wakes. As seen in Figure 12.9(a), the separation bubble is almost suppressed for Re=110,000 with the turbulence intensity level of 13%. Hence, the turbulence grid with 13% of turbulence intensity level has not sufficient momentum to completely suppress it. In both turbulence cases of 8% and 13%, the periodic unsteady wakes along with their high turbulence intensity vortical cores seem to be completely submerged in the stochastic high frequency free-stream turbulence generated by grids.

Although Re=150,000 for FSTI level of 1.9% (without grid) shows the similar phenomenon for the velocity and the fluctuation velocity distribution, it is observed that starting point of the separation bubble and the re-attachment point move further downstream. Also, the size of the separation bubble is smaller when compared to that for Re=110,000. However, the combined effect of the higher FSTI level of 3% and unsteady wake flow further shortens the streamwise extent of the separation bubble. It is observed that starting point of the separation bubble moves further downstream and the re-attachment point occurs earlier. Further increasing the FSTI level to 8% and 13% completely suppressed the separation bubble as seen in Figure 12.10(a).

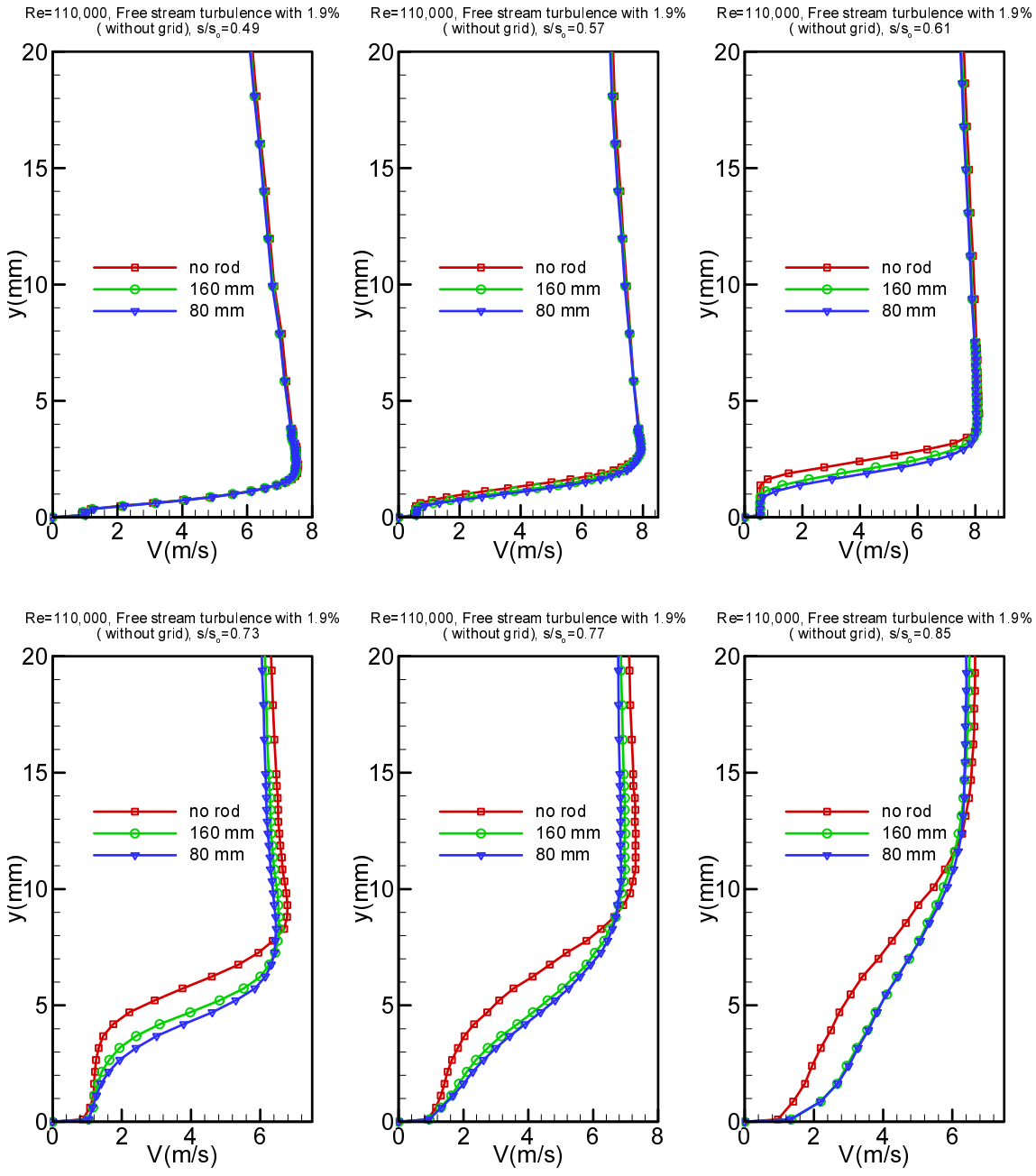

Figure 12.3(a). Distribution of time-averaged velocity along the suction surface for steady case Ω=0 (S_R=∞) and unsteady cases Ω=1.59 (S_R=160 mm) and Ω=3.18 (S_R=80 mm) at Re=110,000 and free-stream turbulence intensity of 1.9% (without grid)

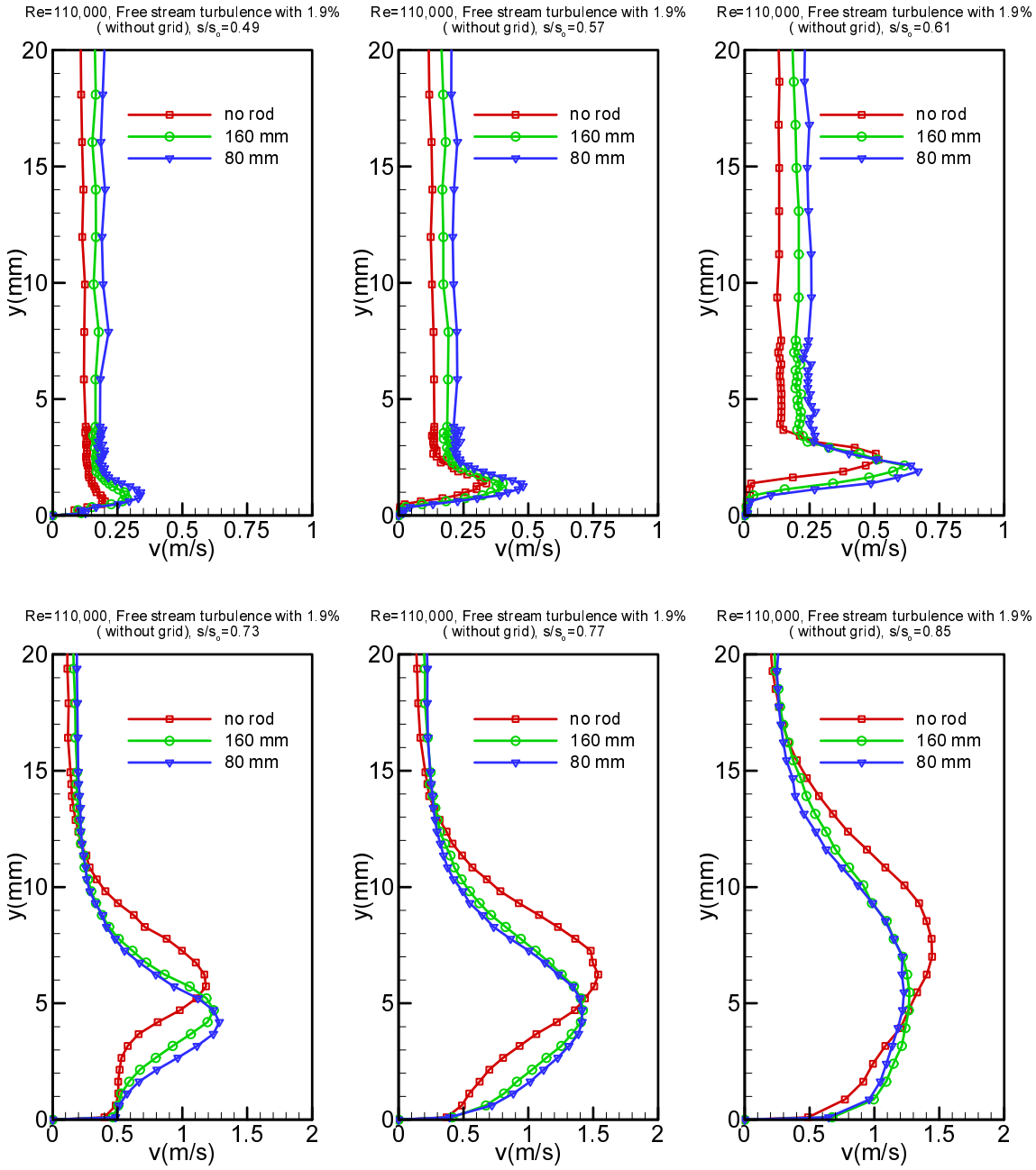

Figure 12.3(b). Distribution of time-averaged fluctuation rms velocity along the suction surface for steady case Ω=0 (S_R=∞) and unsteady cases Ω=1.59 (S_R=160 mm) and Ω=3.18 (S_R=80 mm) at Re=110,000 and free-stream turbulence intensity of 1.9% (without grid)

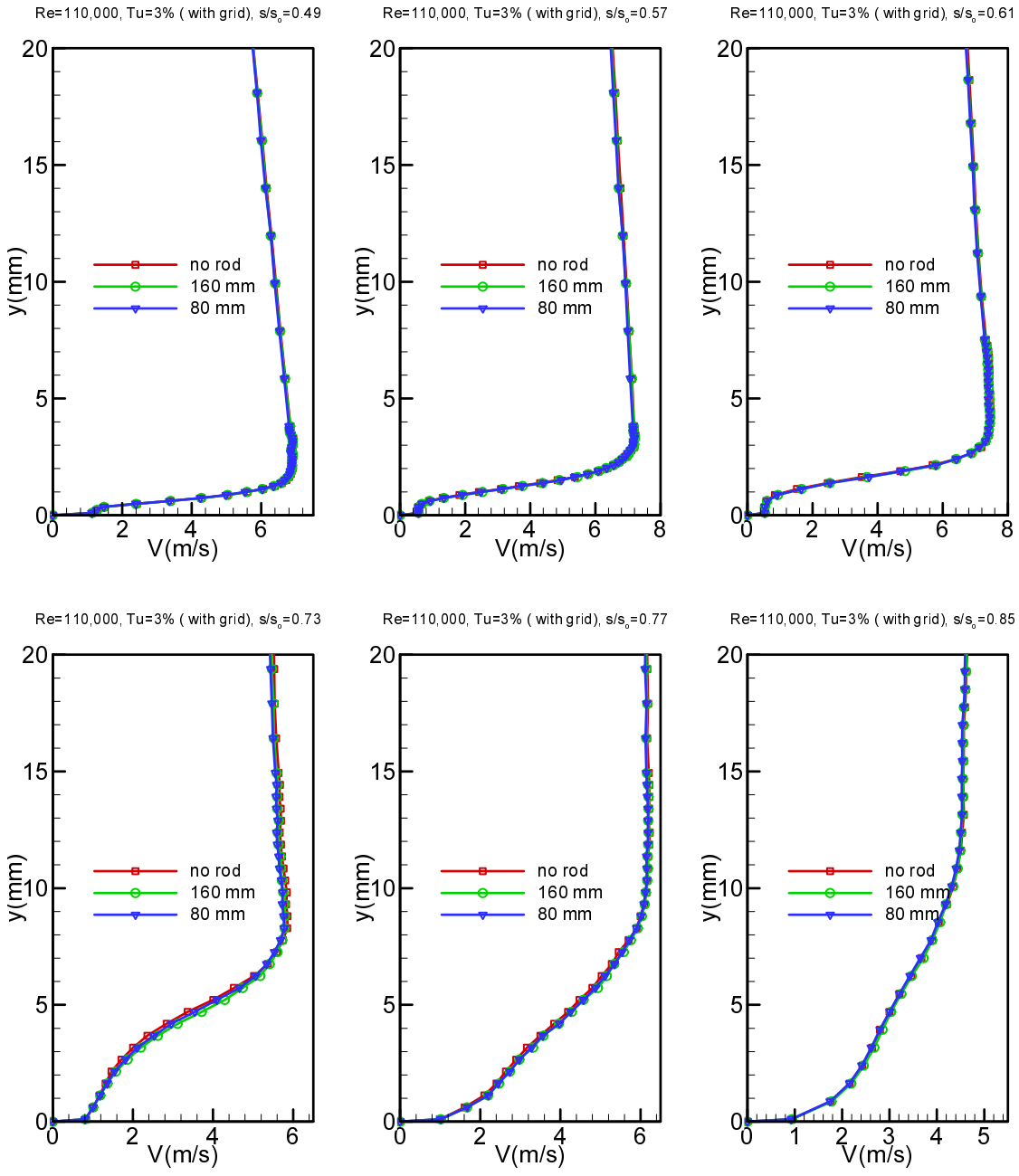

Figure 12.4(a). Distribution of time-averaged velocity along the suction surface for steady case Ω=0 (S_R=∞) and unsteady cases Ω=1.59 (S_R=160 mm) and Ω=3.18 (S_R=80 mm) at Re=110,000 and Tu=3% with grid TG1

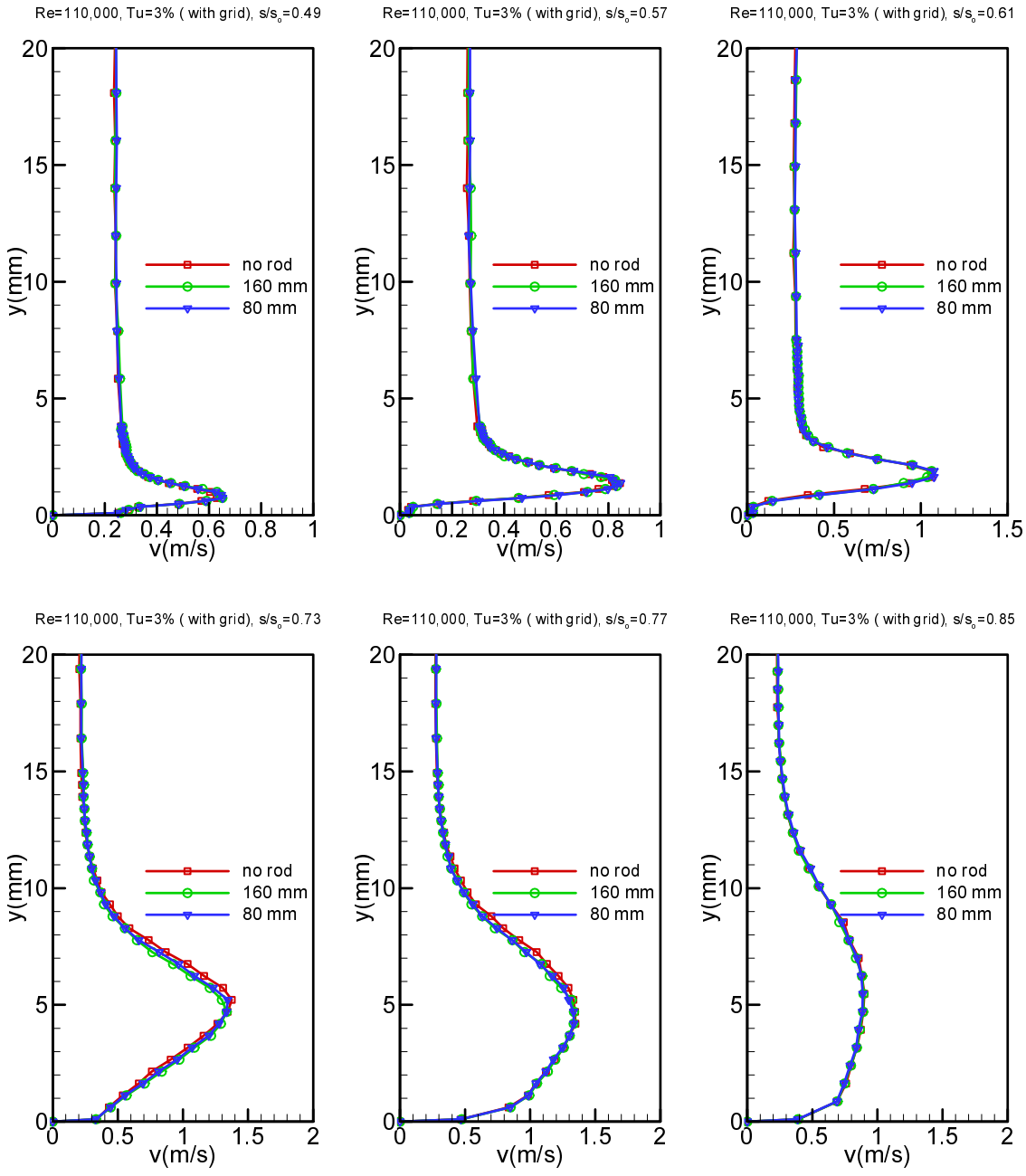

Figure 12.4(b). Distribution of time-averaged fluctuation rms velocity along the suction surface for steady case Ω=0 (S_R=∞) and unsteady cases Ω=1.59 (S_R=160 mm) and Ω=3.18 (S_R=80 mm) at Re=110,000 and Tu=3% with grid TG1

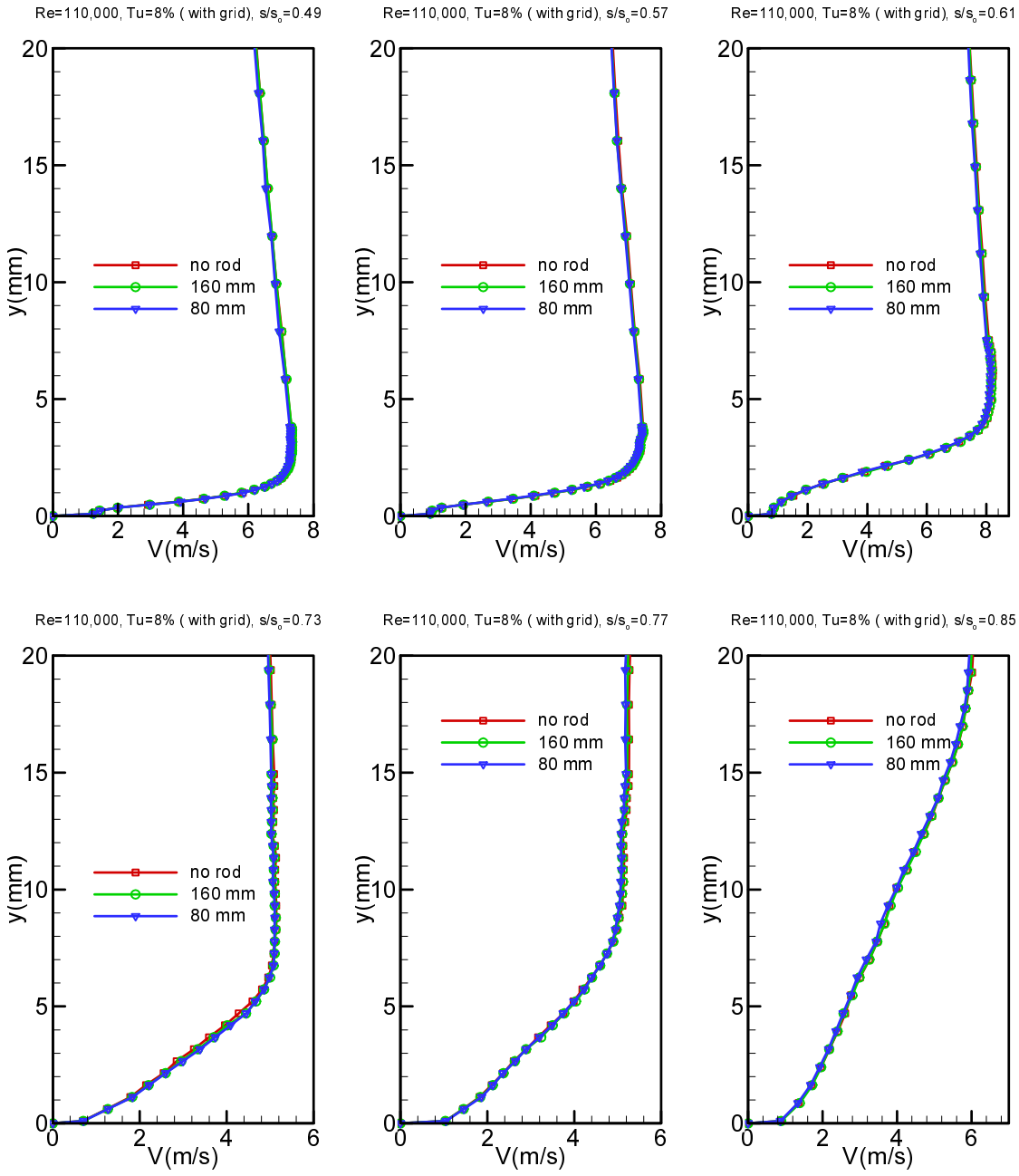

Figure 12.5(a). Distribution of time-averaged velocity along the suction surface for steady case Ω=0 (S_R=∞) and unsteady cases Ω=1.59 (S_R=160 mm) and Ω=3.18 (S_R=80 mm) at Re=110,000 and Tu=8% with grid TG2

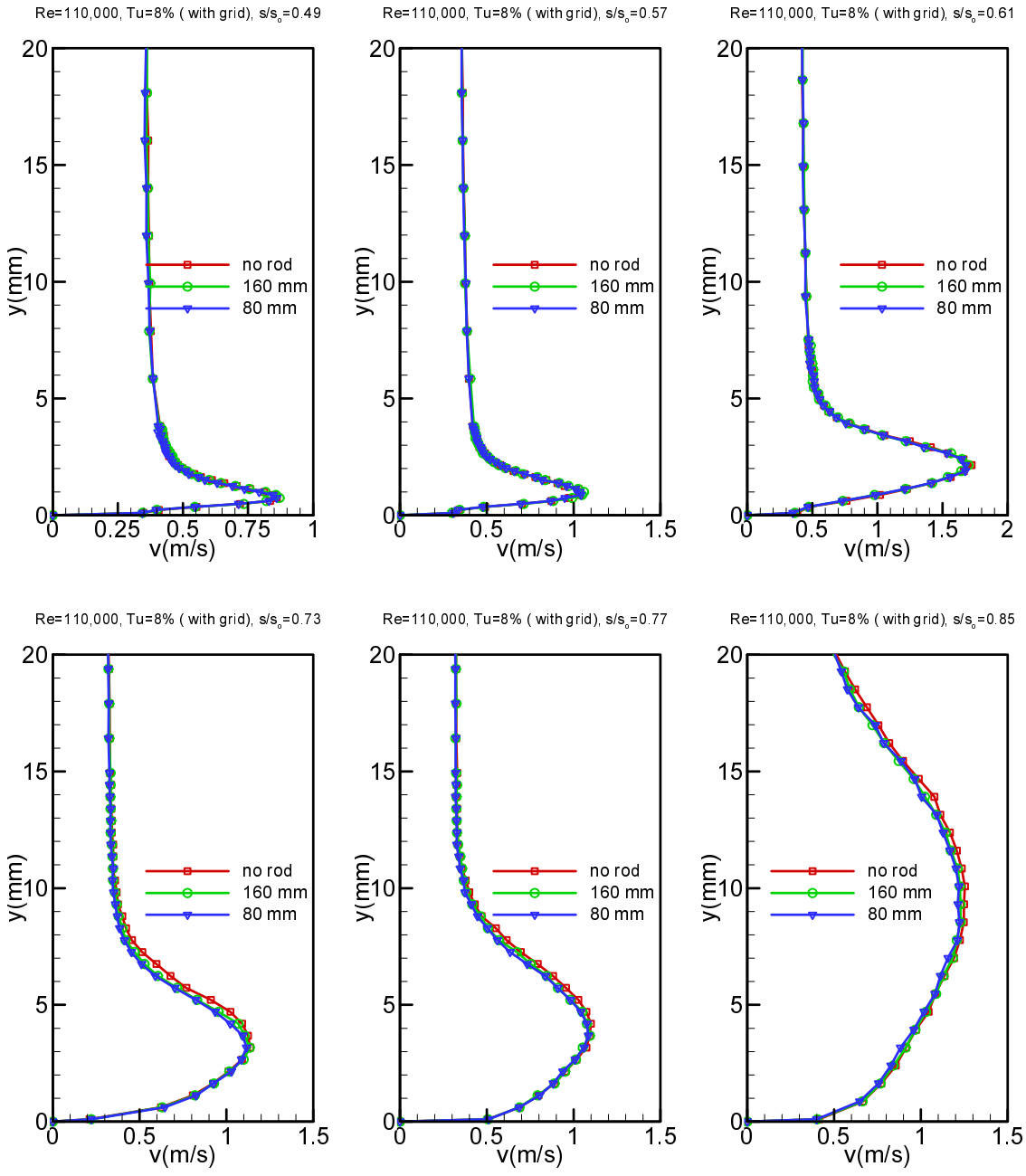

Figure 12.5(b). Distribution of time-averaged fluctuation rms velocity along the suction surface for steady case Ω=0 (S_R=∞) and unsteady cases Ω=1.59 (S_R=160 mm) and Ω=3.18 (S_R=80 mm) at Re=110,000 and Tu=8% with grid TG2

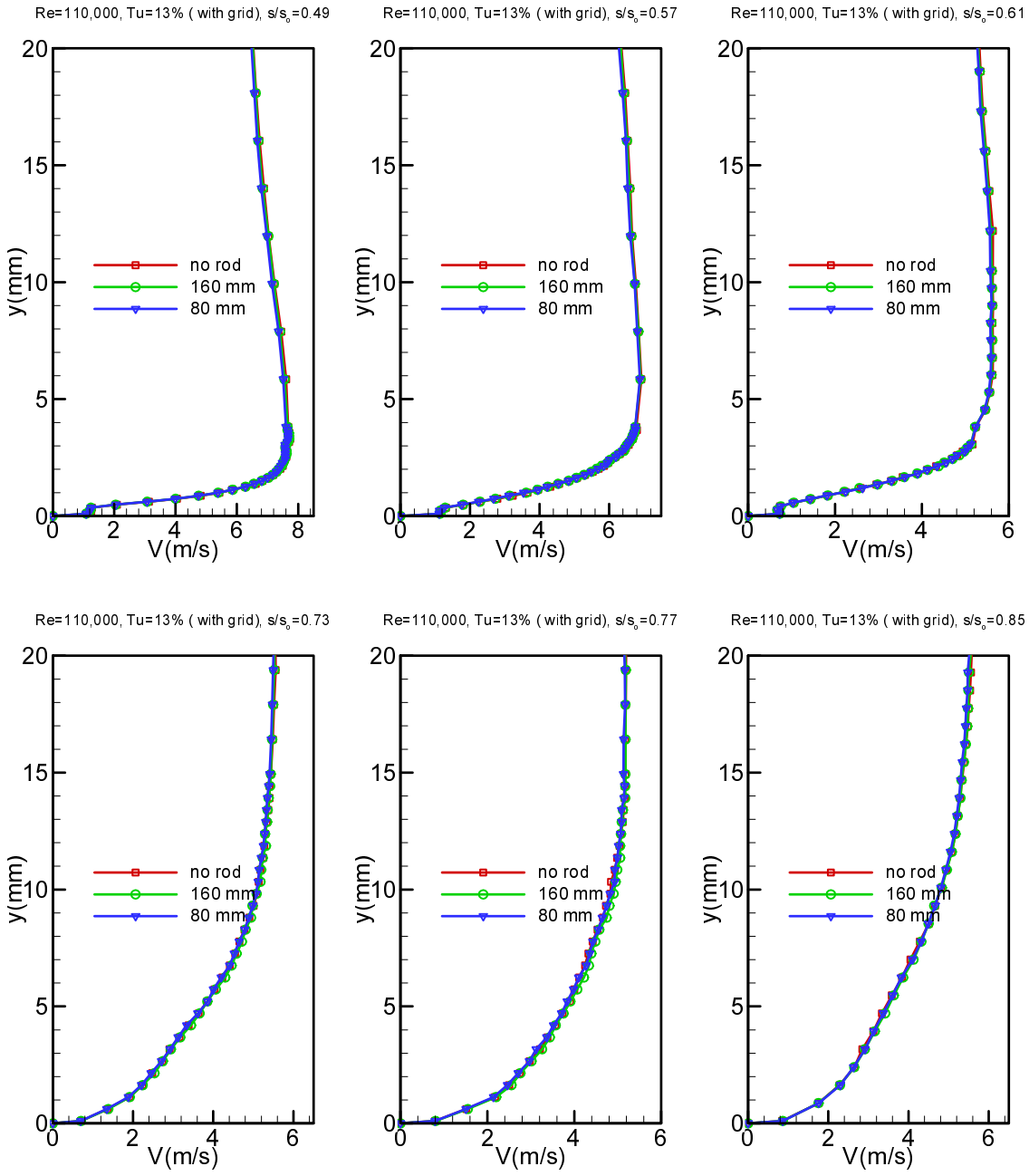

Figure 12.6(a). Distribution of time-averaged velocity along the suction surface for steady case Ω=0 (S_R=∞) and unsteady cases Ω=1.59 (S_R=160 mm) and Ω=3.18 (S_R=80 mm) at Re=110,000 and Tu=13% with grid TG3

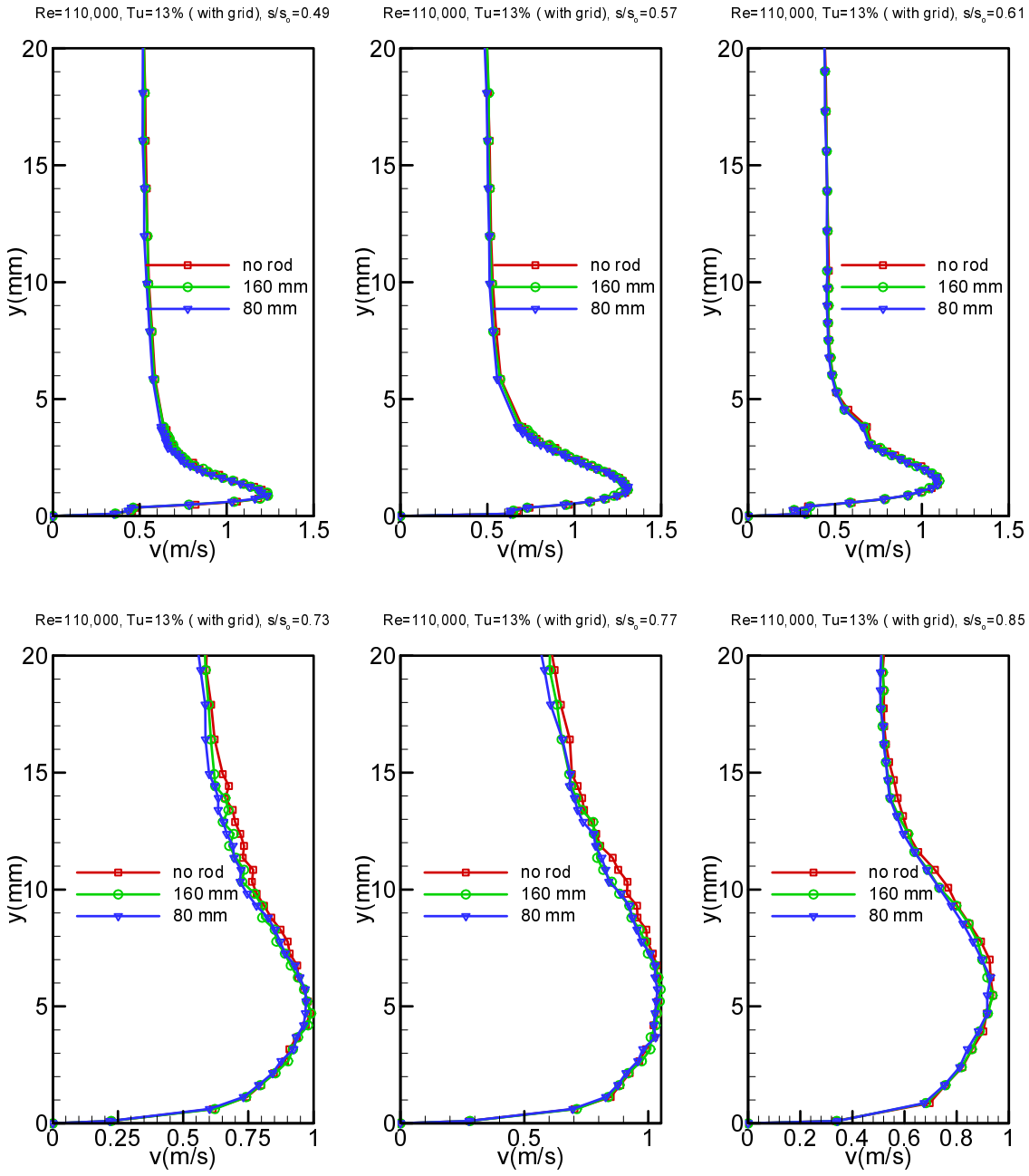

Figure 12.6(b). Distribution of time-averaged fluctuation rms velocity along the suction surface for steady case Ω=0 (S_R=∞) and unsteady cases Ω=1.59 (S_R=160 mm) and Ω=3.18 (S_R=80 mm) at Re=110,000 and Tu=13% with grid TG3

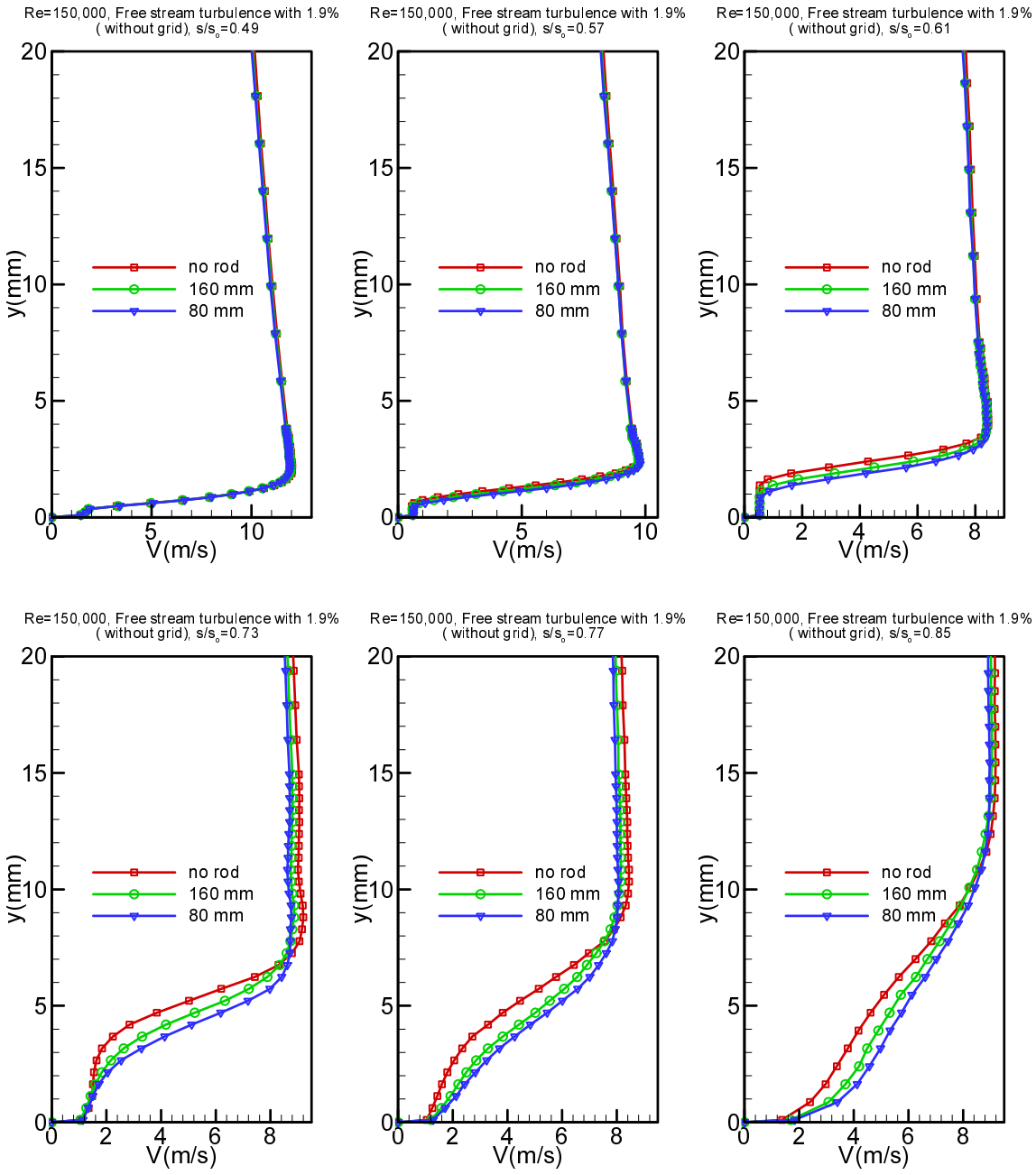

Figure 12.7(a). Distribution of time-averaged velocity along the suction surface for steady case Ω=0 (S_R=∞) and unsteady cases Ω=1.59 (S_R=160 mm) and Ω=3.18 (S_R=80 mm) at Re=150,000 and free-stream turbulence intensity of 1.9% (without grid)

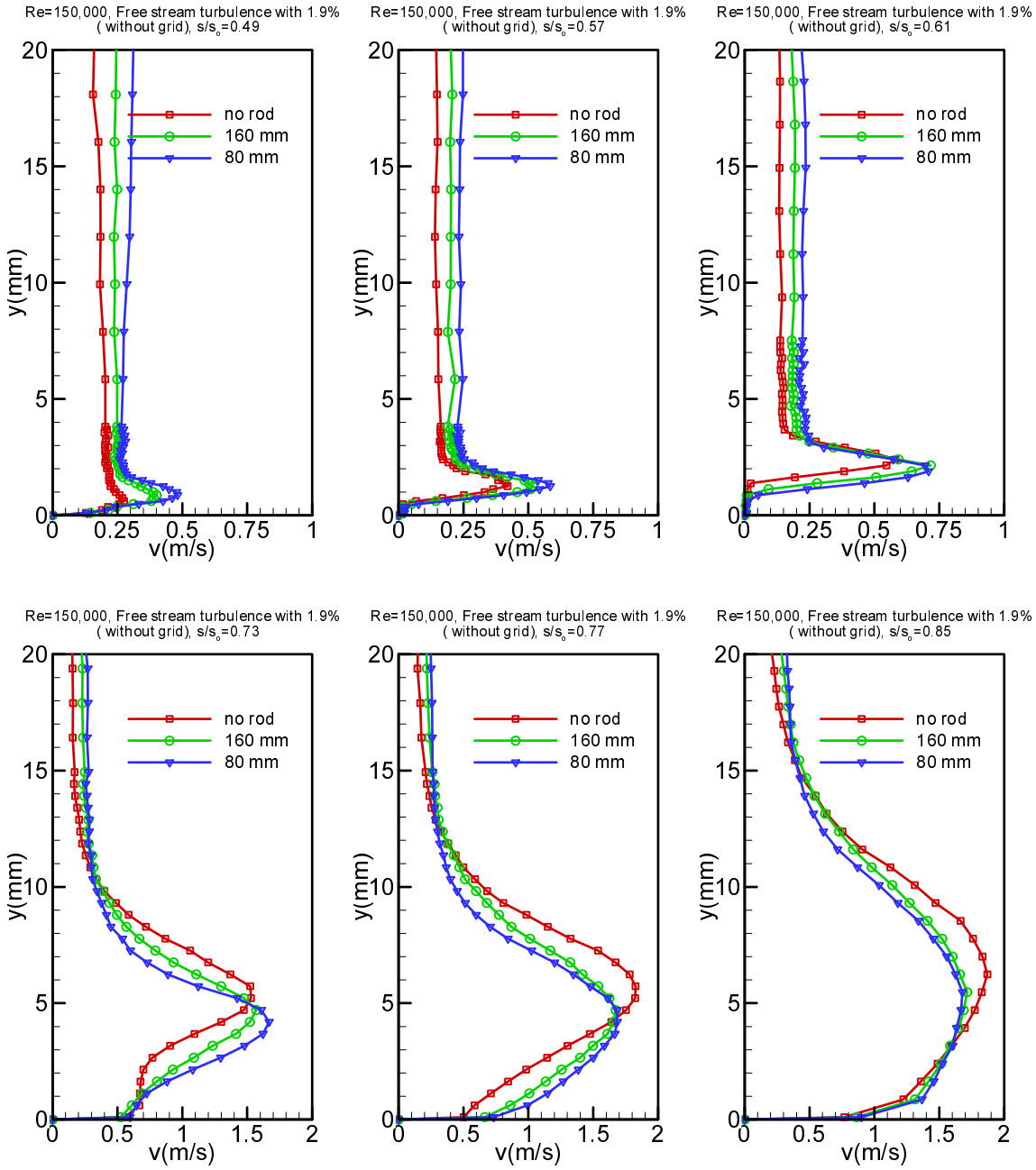

Figure 12.7(b). Distribution of time-averaged fluctuation rms velocity along the suction surface for steady case Ω=0 (S_R=∞) and unsteady cases Ω=1.59 (S_R=160 mm) and Ω=3.18 (S_R=80 mm) at Re=150,000 and free-stream turbulence intensity of 1.9% (without grid)

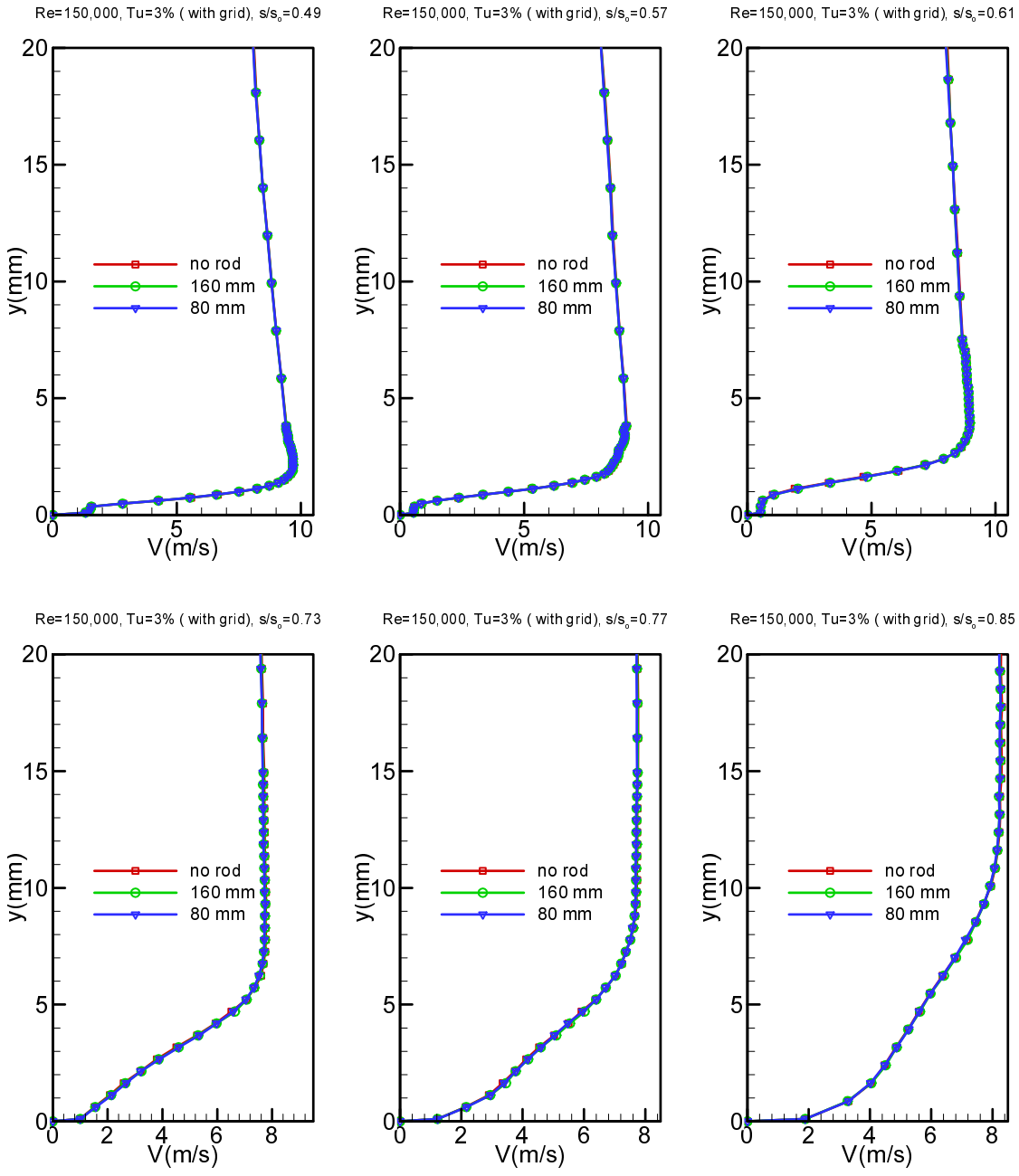

Figure12.8(a). Distribution of time-averaged velocity along the suction surface for steady case Ω=0 (S_R=∞) and unsteady cases Ω=1.59 (S_R=160 mm) and Ω=3.18 (S_R=80 mm) at Re=150,000 and Tu=3% with grid TG1

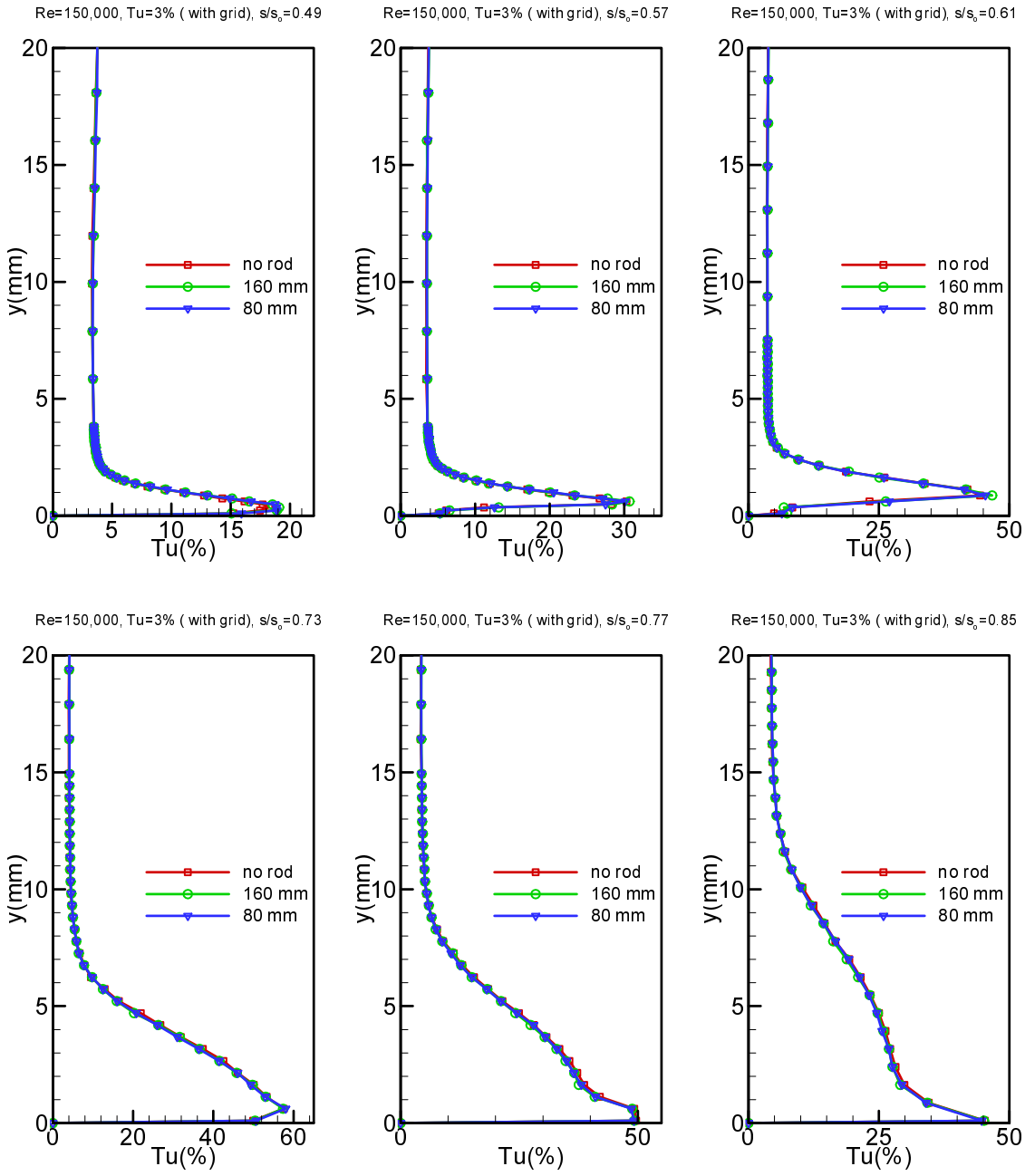

Figure 12.8(b). Distribution of time-averaged fluctuation rms velocity along the suction surface for steady case Ω=0 (S_R=∞) and unsteady cases Ω=1.59 (S_R=160 mm) and Ω=3.18 (S_R=80 mm) at Re=510,000 and Tu=3% with grid TG1

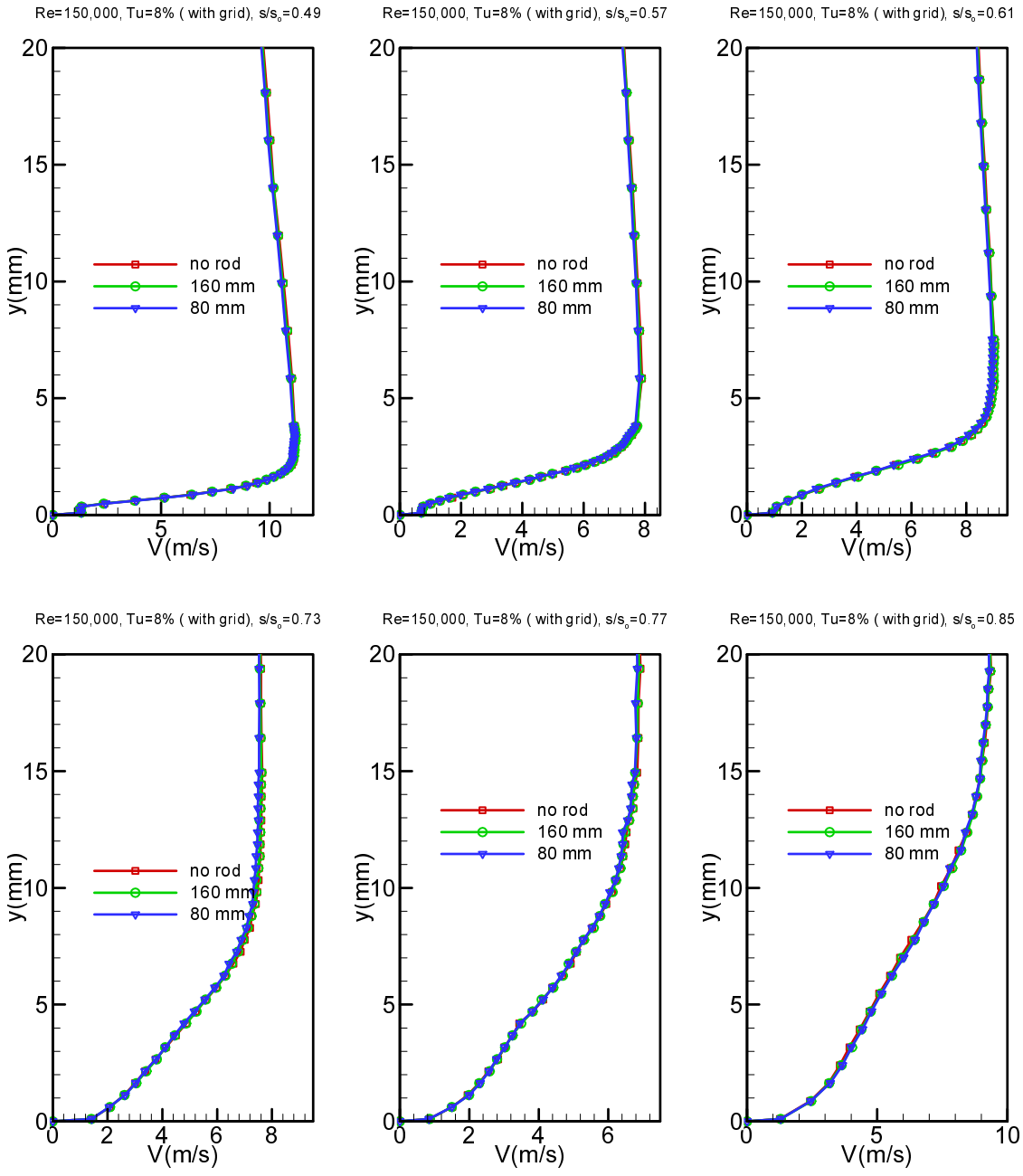

Figure 12.9(a). Distribution of time-averaged velocity along the suction surface for steady case Ω=0 (S_R=∞) and unsteady cases Ω=1.59 (S_R=160 mm) and Ω=3.18 (S_R=80 mm) at Re=150,000 and Tu=8% with grid TG2

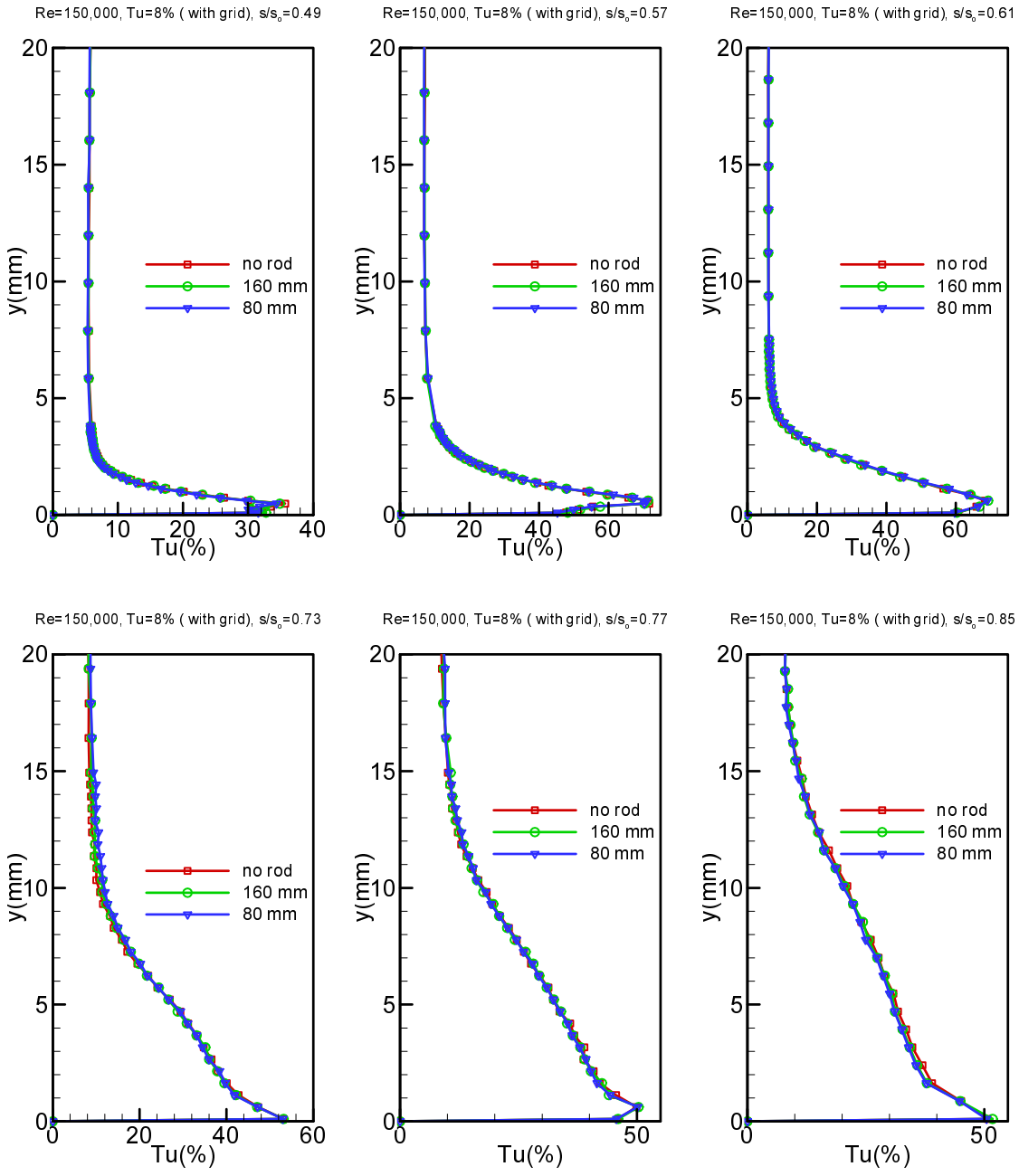

Figure 12.9(b). Distribution of time-averaged fluctuation rms velocity along the suction surface for steady case Ω=0 (S_R=∞) and unsteady cases Ω=1.59 (S_R=160 mm) and Ω=3.18 (S_R=80 mm) at Re=150,000 and Tu=8% with grid TG2

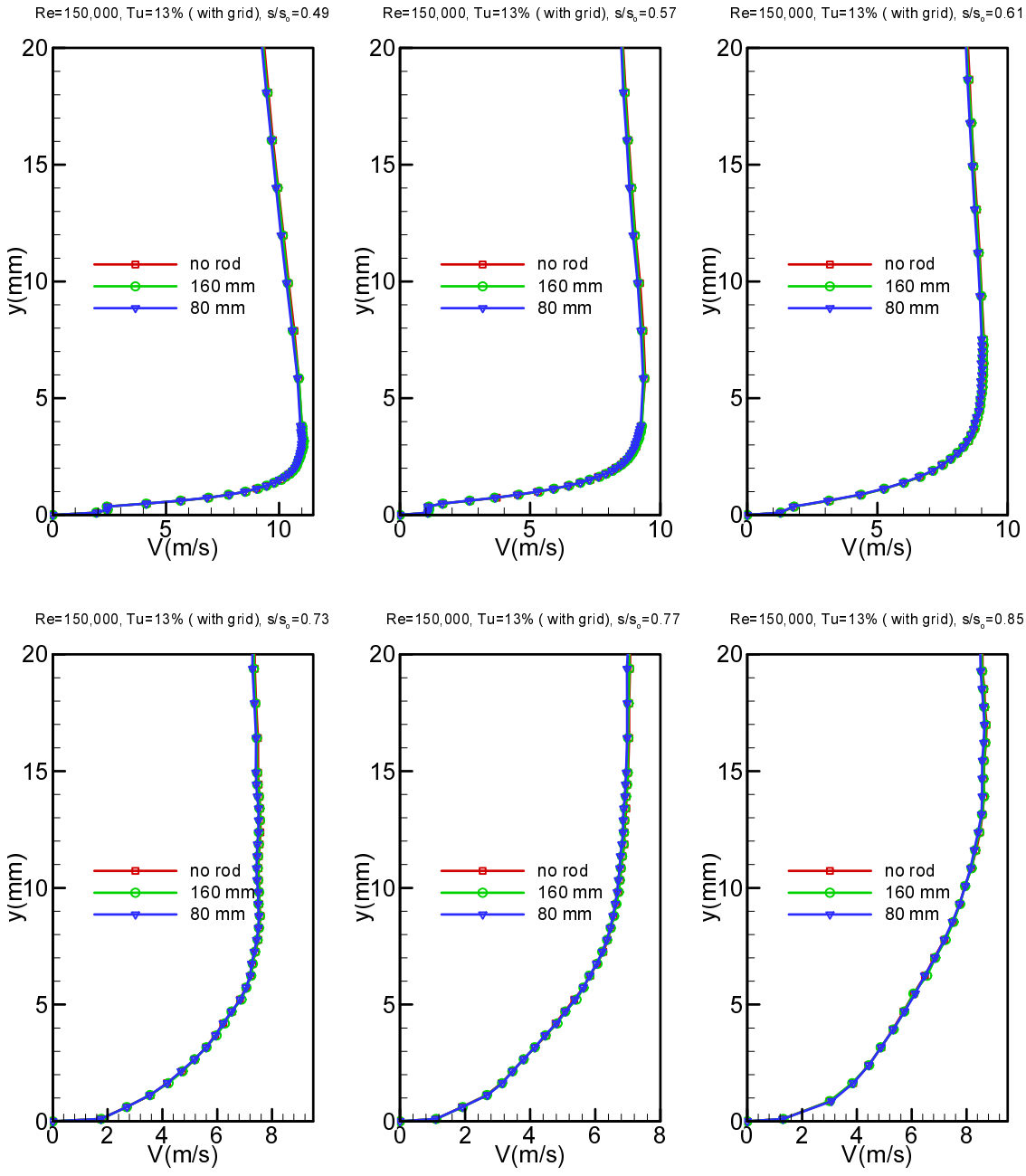

Figure 12.10(a). Distribution of time-averaged velocity along the suction surface for steady case Ω=0 (S_R=∞) and unsteady cases Ω=1.59 (S_R=160 mm) and Ω=3.18 (S_R=80 mm) at Re=150,000 and Tu=13% with grid TG3

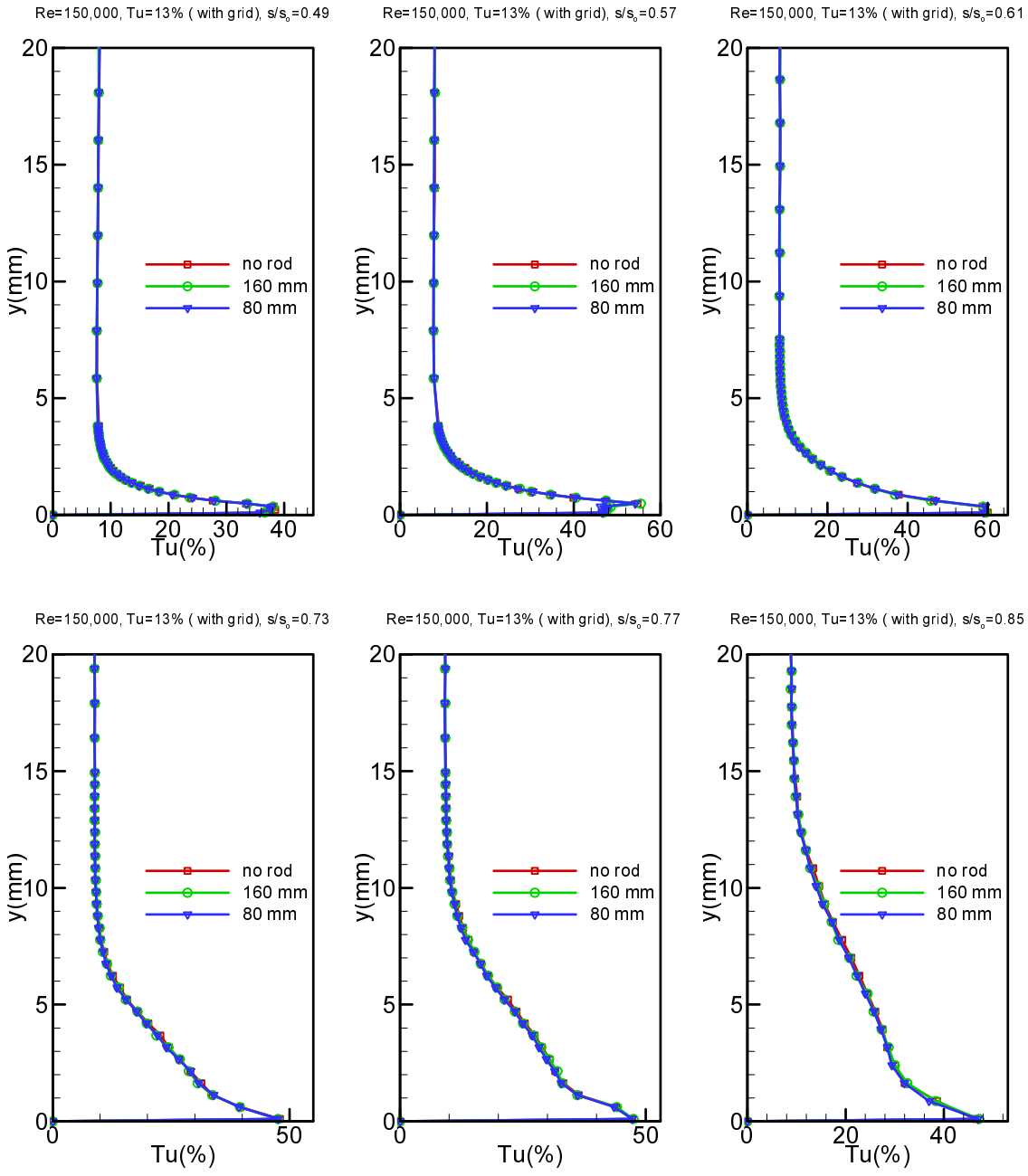

Figure 12.10(b). Distribution of time-averaged fluctuation rms velocity along the suction surface for steady case Ω=0 (S_R=∞) and unsteady cases Ω=1.59 (S_R=160 mm) and Ω=3.18 (S_R=80 mm) at Re=150,000 and Tu=13% with grid TG3

12.4 Temporal Behavior of the Separation Zone Under Unsteady Wake Flow

Velocity distributions on the suction surface with time as the parameter are plotted in Figure 12.11 to 12.26 for the Reynolds numbers of 110,000 and 150,000 with 1.9 percent (free-stream turbulence intensity) and 3,8 and 13 percent (using passive grids) turbulence intensity. Experimental investigations were performed for three different values of $\Omega = 0.0$, 1.59, and 3.18. The nondimensional time (t/τ) values are chosen so that they represent the temporal states within one full period of wake passing. For Re = 110,000 Figures 12.11(a) to 12.11(d) show the velocity distributions inside and outside the boundary layer at fixed s/s_o- locations experience moderate to pronounced changes. Figure 12.11(a) represents the instantaneous velocity distribution upstream of the separation zone followed by Figures. 12.11(b,c,d) which represent the velocity distributions inside the separation zone. In discussing the following results, we simultaneously refer to the wake distribution as well as the turbulence fluctuation results.

Figure 12.11(a) exhibits the velocity distribution on the suction surface at $s/s_o = 0.49$. At this streamwise position, the laminar boundary layer is subjected to a strong negative pressure gradient. The boundary layer distributions at different (t/τ) experience changes in magnitude that reflect the corresponding changes of the impinging periodic wake velocity. It is worth noting, that despite the injection of turbulence kinetic energy by the impinging wakes, no local instantaneous boundary layer transition occurs. This is because of the strong negative pressure gradient that prevents the boundary layer from becoming instantaneously transitional.

As a representative case, we discuss the results plotted in Figure 12.11(d) at $s/s_o = 0.73$. During the time interval from t/τ close to 0.5 (1.5, 2.5, etc.) to about $t/\tau = 0.75$ (1.75, 2.75 etc.), the separation zone is exposed to the wake external flow with relatively lower turbulence level. This flow does not have the capability to suppress the separation zone. Thus the separation region is clearly shown by the velocity distributions at $t/\tau = 0.5$ and $t/\tau = 0.75$. As the wake passes over the blade at $s/s_o = 0.73$ introducing high turbulence kinetic energy into the boundary layer, the boundary layer is energized causing the separation zone to partially reduce or disappear. This leads to an instantaneous re-attachment. This time

interval corresponds to the case where the flow is completely under the influence of wake and correspondingly the reattached velocity distribution assumes a turbulent profile characterized by the curves at $t/\tau = 1.0$, $t/\tau = 0.05$, and $t/\tau = 0.25$ shown in Figure 12.11(d). To emphasize this statement, the steady state velocity distribution at the same streamwise position is also plotted in Figure 12.11(d) using full circles. It shows clearly the separated nature of the boundary layer which coincides with the instantaneous velocity profile at $t/\tau = 0.5$. Intermediate times reflect the gradual change between the separation and re-attachment as the flow is undergoing the influence of the oncoming wake.

Figure 12.15 (a) to (d) show that the velocity distributions outside the boundary layer at fixed s/s_o-locations experience noticeable changes at $\Omega = 3.18$. Increasing the wake passing frequency causes the wake turbulence kinetic energy to increase resulting in a stronger suppression compared with the $\Omega = 1.59$ case.

For turbulence intensity levels of 3,8, and 13 percent, Figures 12.12-12.14and 12.16-12.18 display velocity distributions on the suction surface with time as the parameter at the same streamwise locations as discussed above. As it is seen in Figure 12.12 and 11.16, the velocity distributions still show slight changes at $\Omega = 1.59$ and 3.18. However, at the same positions, the velocity distributions shown in Figures 12.13, 12.14 and 12.17, 12.18 experience a hardly noticeable any changes with increasing the reduced frequency. This is due to the introduction of the passive grids with high turbulence intensity levels and the subsequent mixing, has systematically increased the steady case free stream turbulence level from1.9% to up to 13%, which is higher than the highly turbulent vortical core of $\Omega = 3.18$ (S_R = 80 mm) without any grid.

As it is seen in Figure 12.19 to 12.26, further increasing the Reynolds number and the FSTI level causes starting point of the separation bubble and the re-attachment point move further downstream. Compared with Re=110,000, a stronger suppression of the separation zone is noticed at Re=150,000. It is also observed that increasing the Reynolds number reduces the size of the separation bubble.

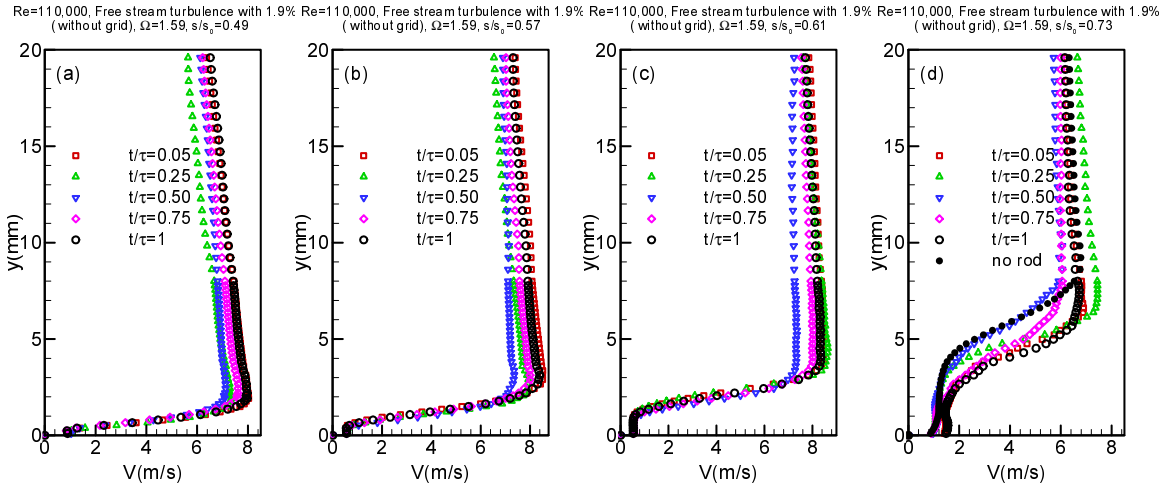

Figure 12.11. Distribution of the ensemble-averaged velocity development along the suction surface for different s/s_o with time t/τ as parameter for Ω=1.59 (S_R=160 mm) at Re=110,000 and free-stream turbulence of 1.9% (without grid)

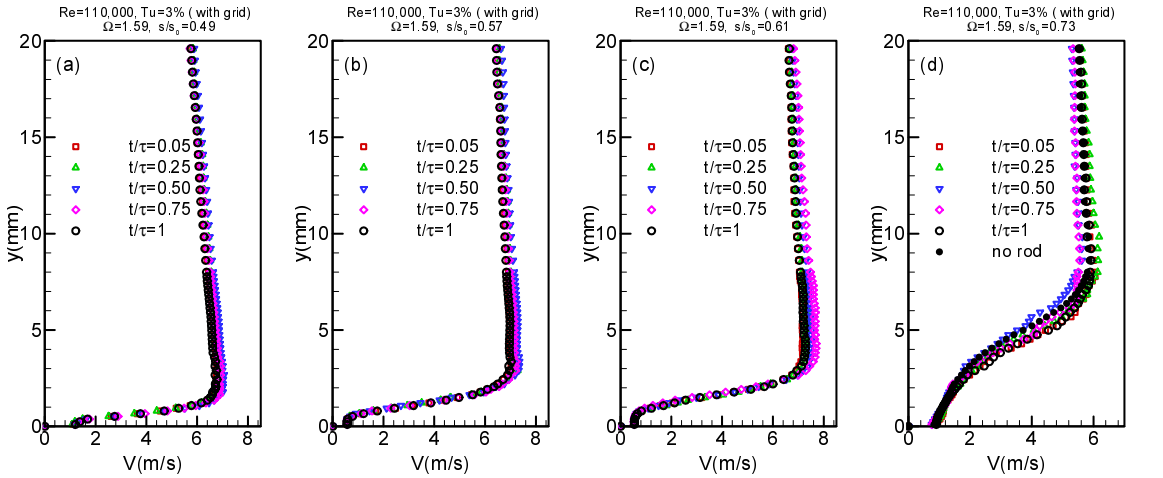

Figure 12.12. Distribution of the ensemble-averaged velocity development along the suction surface for different s/s_o with time t/τ as parameter for Ω=1.59 (S_R=160 mm) at Re=110,000 and Tu=3% with grid TG1

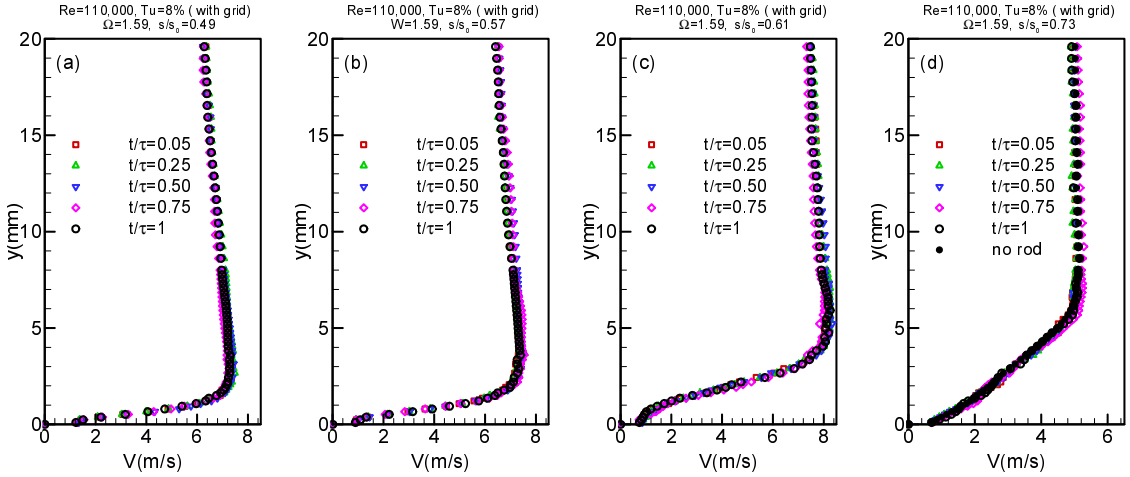

Figure 12.13. Distribution of the ensemble-averaged velocity development along the suction surface for different s/s_o with time t/τ as parameter for Ω=1.59 (S_R=160 mm) at Re=110,000 and Tu=8% with grid TG2

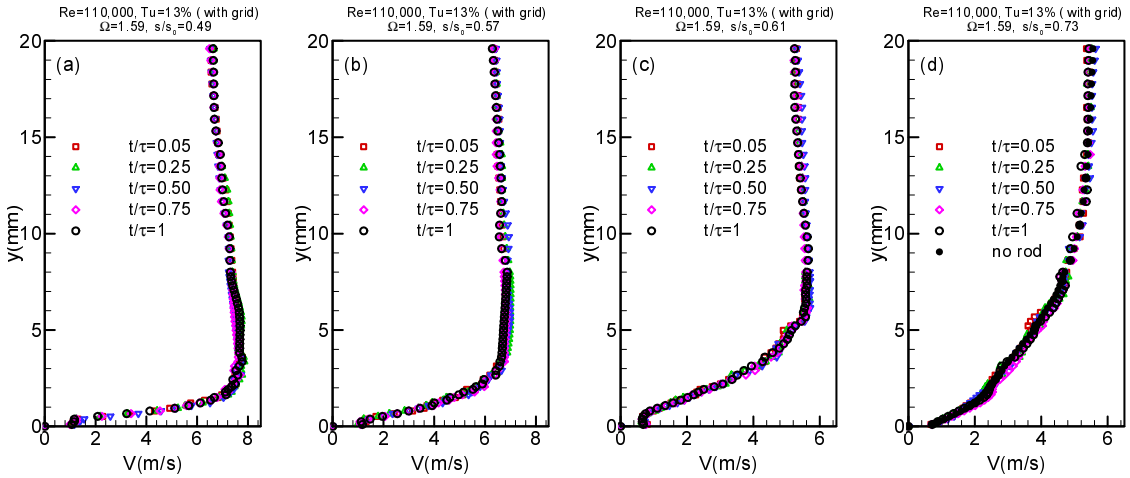

Figure 12.14. Distribution of the ensemble-averaged velocity development along the suction surface for different s/s_o with time t/τ as parameter for Ω=1.59 (S_R=160 mm) at Re=110,000 and Tu=13% with grid TG3

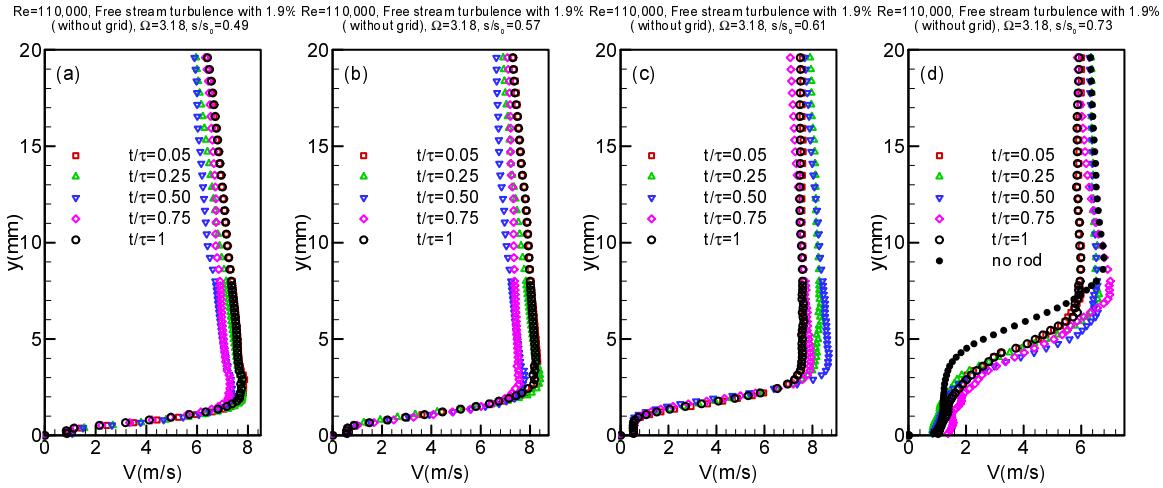

Figure 12.15. Distribution of the ensemble-averaged velocity development along the suction surface for different s/s_o with time t/τ as parameter for Ω=3.18 (S_R=80 mm) at Re=110,000 and free-stream turbulence of 1.9% (without grid)

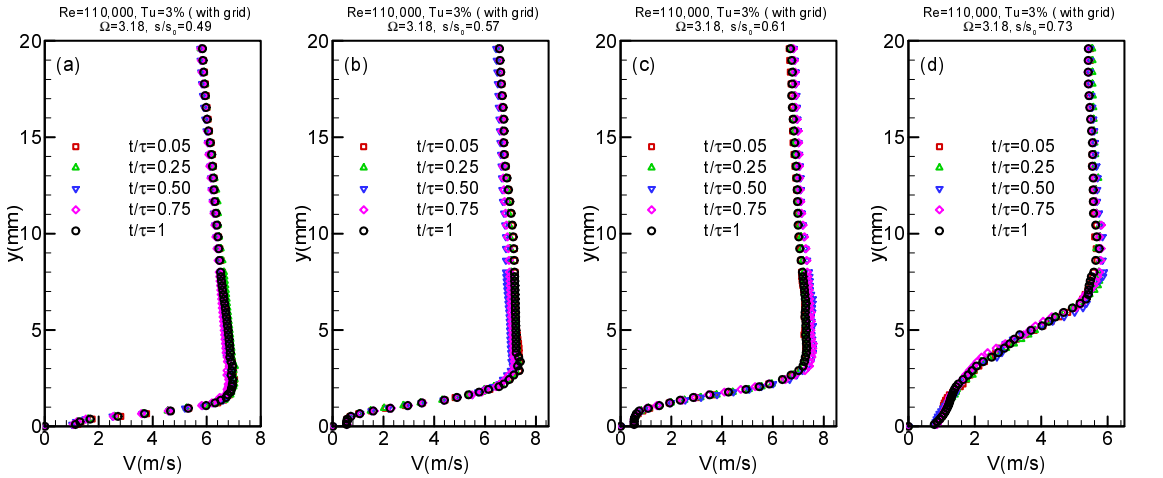

Figure 12.16. Distribution of the ensemble-averaged velocity development along the suction surface for different s/s_o with time t/τ as parameter for Ω=3.18 (S_R=80 mm) at Re=110,000 and Tu=3% with grid TG1

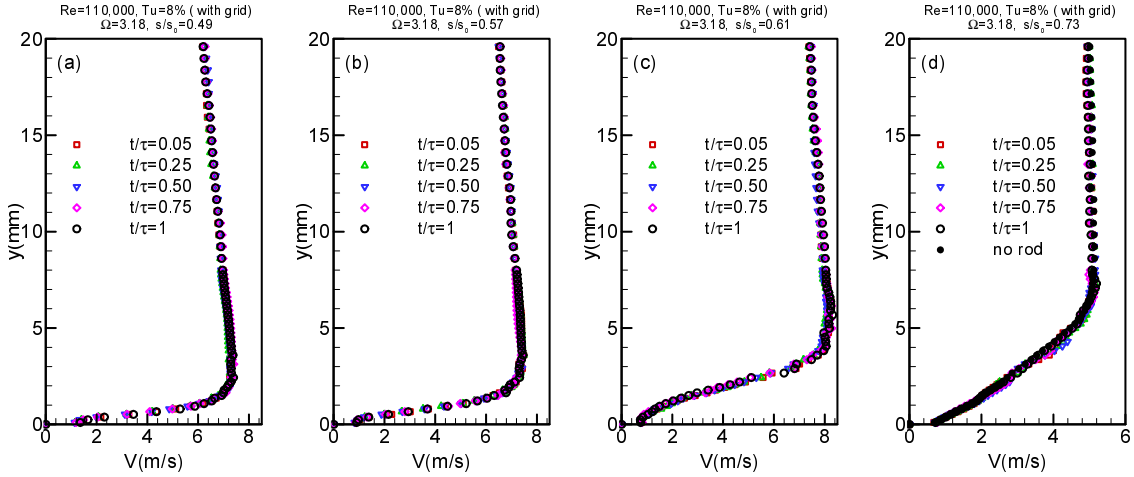

Figure 12.17. Distribution of the ensemble-averaged velocity development along the suction surface for different s/s_o with time t/τ as parameter for Ω=3.18 (S_R=80 mm) at Re=110,000 and Tu=8% with grid TG2

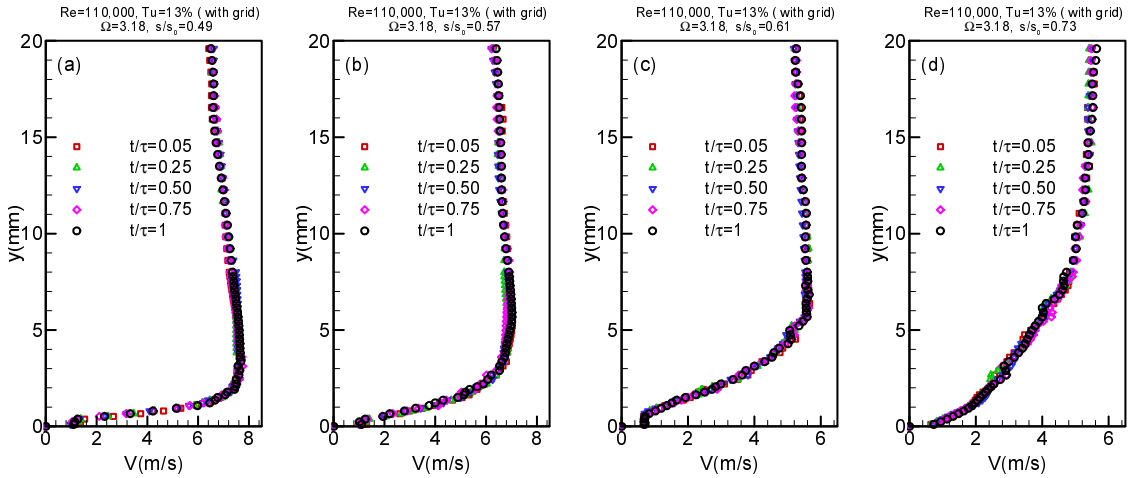

Figure 12.18. Distribution of the ensemble-averaged velocity development along the suction surface for different s/s_o with time t/τ as parameter for Ω=3.18 (S_R=80 mm) at Re=110,000 and Tu=13% with grid TG3

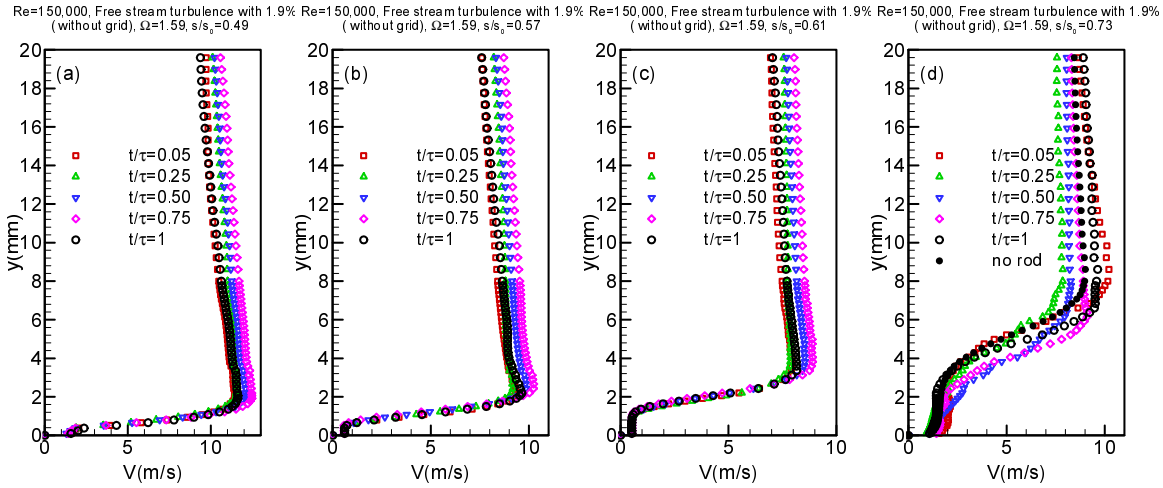

Figure 12.19. Distribution of the ensemble-averaged velocity development along the suction surface for different s/s_o with time t/τ as parameter for Ω=1.59 (S_R=160 mm) at Re=150,000 and free-stream turbulence of 1.9% (without grid)

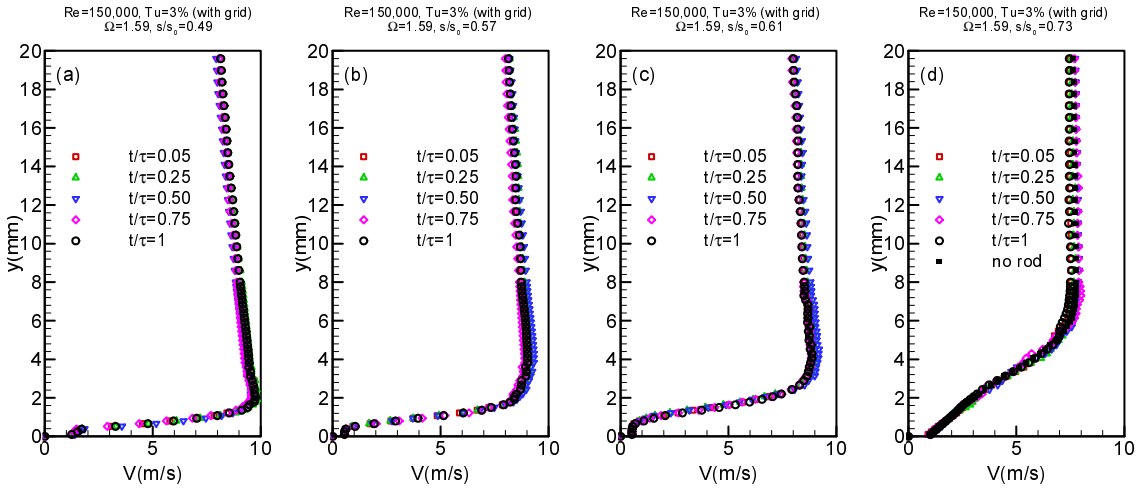

Figure 12.20. Distribution of the ensemble-averaged velocity development along the suction surface for different s/s_o with time t/τ as parameter for Ω=1.59 (S_R=160 mm) at Re=150,000 and Tu=3% with grid TG1

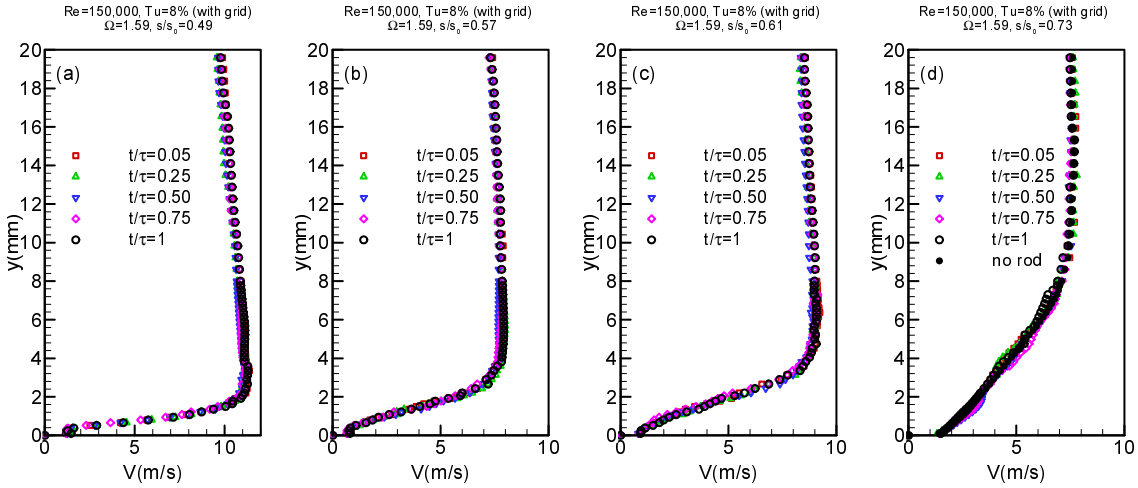

Figure 12.21. Distribution of the ensemble-averaged velocity development along the suction surface for different s/s_o with time t/τ as parameter for Ω=1.59 (S_R=160 mm) at Re=150,000 and Tu=8% with grid TG2

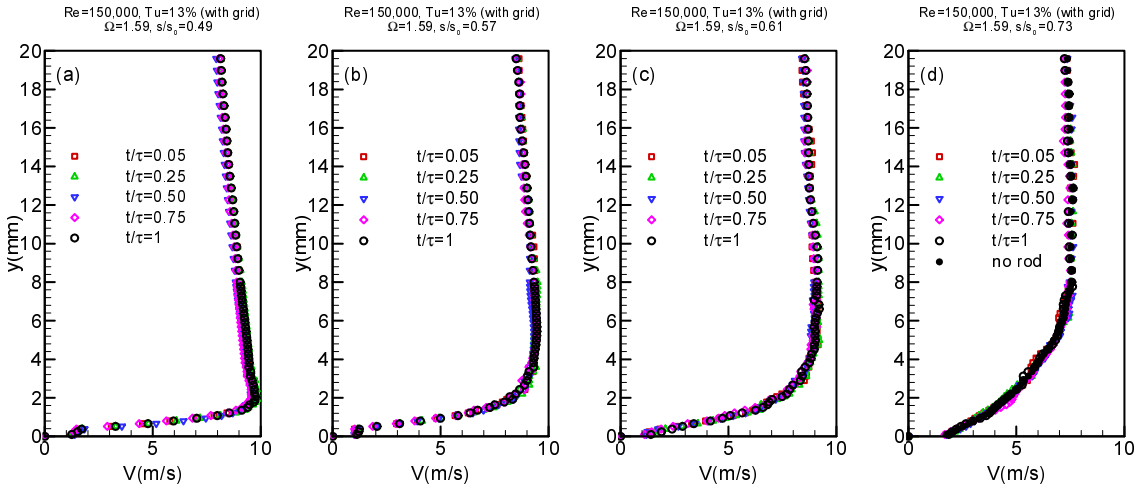

Figure 12.22. Distribution of the ensemble-averaged velocity development along the suction surface for different s/s_o with time t/τ as parameter for Ω=1.59 (S_R=160 mm) at Re=150,000 and Tu=13% with grid TG3

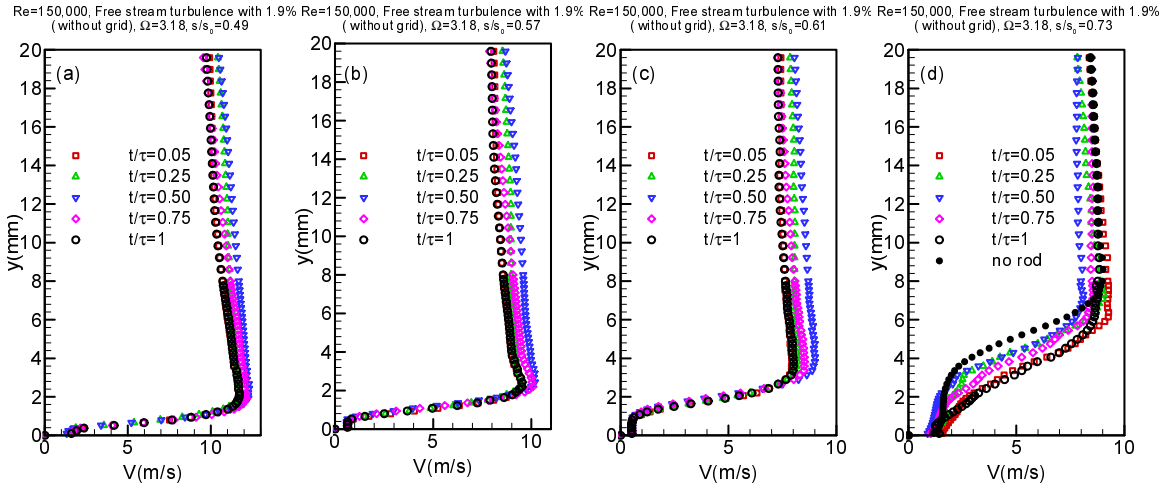

Figure 12.23. Distribution of the ensemble-averaged velocity development along the suction surface for different s/s_o with time t/τ as parameter for Ω=3.18 (S_R=80 mm) at Re=150,000 and free-stream turbulence of 1.9% (without grid)

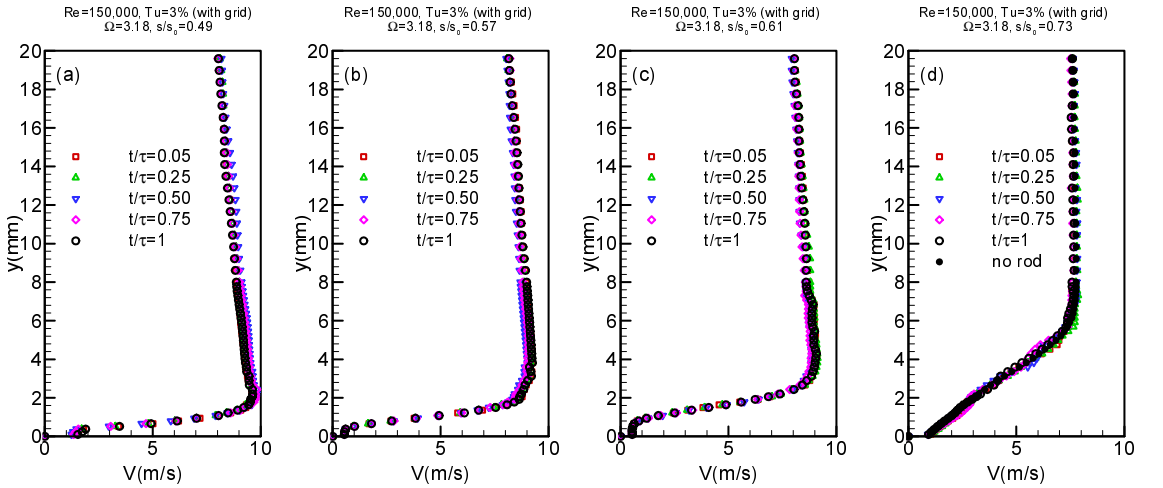

Figure 12.24. Distribution of the ensemble-averaged velocity development along the suction surface for different s/s_o with time t/τ as parameter for Ω=3.18 (S_R=80 mm) at Re=150,000 and Tu=3% with grid TG1

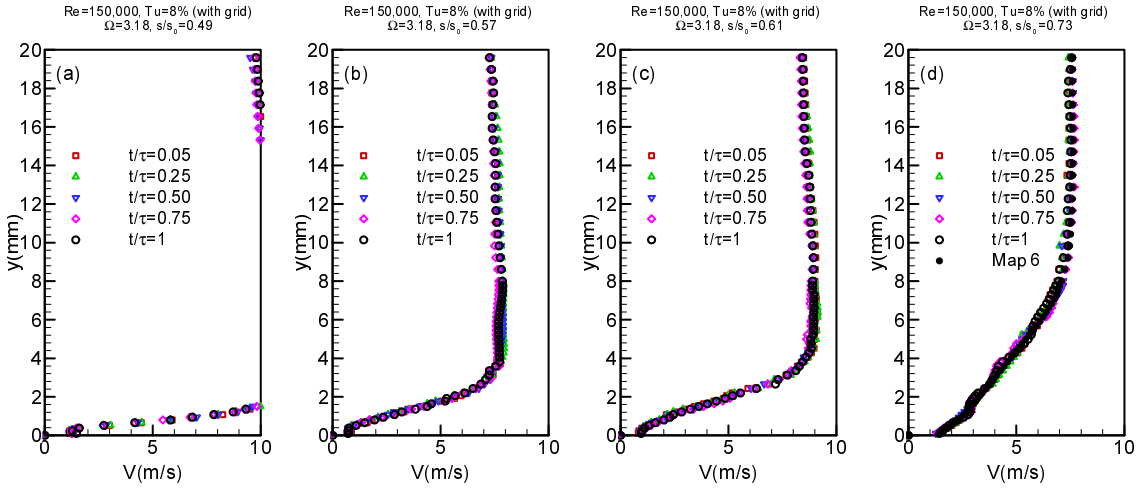

Figure 12.25. Distribution of the ensemble-averaged velocity development along the suction surface for different s/s_o with time t/τ as parameter for Ω=3.18 (S_R=80 mm) at Re=150,000 and Tu=8% with grid TG2

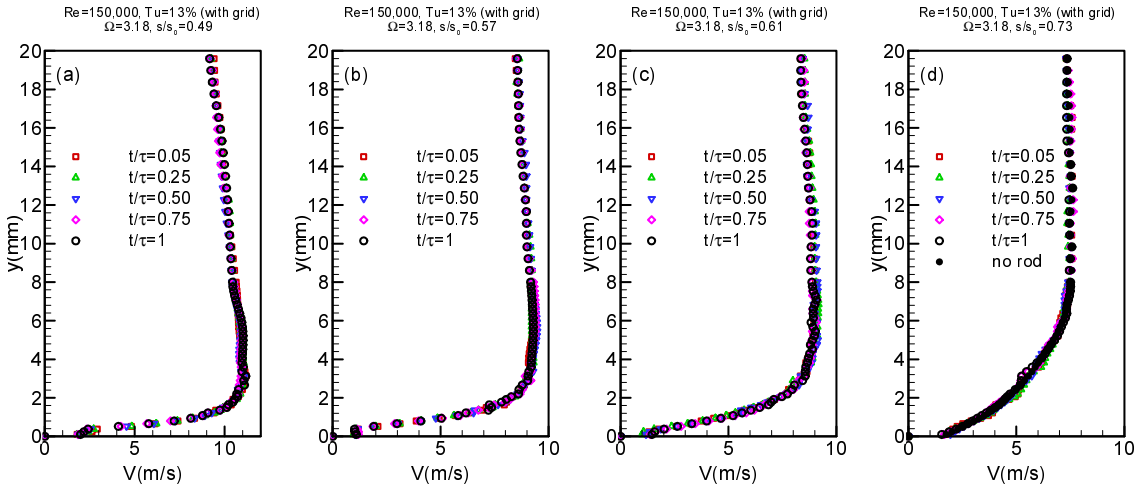

Figure 12.26. Distribution of the ensemble-averaged velocity development along the suction surface for different s/s_o with time t/τ as parameter for Ω=3.18 (S_R=80 mm) at Re=150,000 and Tu=13% with grid TG3

12.5 Behavior of Separation Bubble Under Periodic Wake Flow Condition

The combined effects of the periodic unsteady wakes and high turbulent intensity on the onset and extent of the separation bubble are shown in Figures 12.27 to 12.42 for the Reynolds number of 110,000 and 150,000 with FSTIs of 1.9%, 3.0%, 8.0% and 13.0% for two different frequencies, namely Ω=1.59 (S_R=160 mm) and Ω=3.18 (S_R=80 mm). These figures display the full extent of the separation bubble and its behavior under a periodic wake flow impingement at different t/τ. The value of t/τ corresponds to the point in the cycle at which the data acquisition system is triggered. During a rod passing period, the wake flow and the separation bubble undergo a sequence of flow states which are not noticeably different when the unsteady data are time-averaged.

Variation of FSTI at Ω=1.59: Figure 12.27 (a) exhibits the separation bubble in its full size at t/τ=0.25. At this instant of time, the incoming wakes have not reached the separation bubble. At t/τ=0.5, the wake with its highly turbulent vortical core passes over the blade and generates high turbulence kinetic energy. At this point, the wake turbulence penetrates into the bubble causing a strong mass, momentum and energy exchange between the wake flow and the fluid contained within the bubble. This exchange causes a dynamic suppression and a subsequent contraction of the bubble. As the wake travels over the bubble, the size of the bubble continues to contract at t/τ= 0.75 and reaches its minimum size at, t/τ= 1.0. At t/τ=1, the full effect of the wake on the boundary layer can be seen before another wake appears and the bubble moves back to the original position.

Increasing the turbulence level to 3% by attaching the turbulence grid TG1(detail specifications are listed in Table 4.1) and keeping the same reduced frequency of Ω = 1.59, has reduced the lateral extent of the bubble by about 50%, as can be seen in Figure 12.28 Furthermore, the instance of the wake traveling over the separation bubble, which is clearly visible in Figure 12.27, has diminished almost entirely. Further increasing the turbulence intensity to 8% and 13% respectively, has caused the bubble height to further reduce as shown in Figures 12.29 and 12.30. Although the higher turbulence level has, to a great extent, suppressed the separation bubble as Figures 12.29 and 12.30 clearly show, it was not able to completely eliminate it. There is still a small core of separation bubble remaining.

Its existence is attributed to the stability of the separation bubble at the present Re-number level of 110,000.

Variation of FSTI at Ω= 3.18: Figures 12.31 through 12.34 reflect the dynamic behavior of the separation bubble at the same turbulence levels as above, but at a higher reduced frequency of Ω = 3.18. Similar to the previous case, the case with the cascade FSTI level of 1.9% exhibits the reference configuration for Ω = 3.18 (S_R = 80 mm), where the bubble undergoes periodic contraction and expansion. The temporal sequence of events is identical, with the previous case making a detailed discussion unnecessary. In contrast to the events described in Figure 12.27, the increased wake frequency in the reference configuration, Figure 12.31, is associated with higher mixing and, thus, higher turbulence intensity that causes a more pronounced contraction and expansion of the bubble.

Increasing the turbulence level to 3% has slightly reduced the lateral extent of the bubble as can be seen in Figure 12.32. The instance of the wake traveling over the separation bubble proceeds in an analogous way (discussed in Figure 12.27). Further increasing the turbulence intensity to 8% and 13% respectively, has caused the bubble height to further reduce as shown in Figures 12.33 and 12.34. Although the higher turbulence level has to a great extent, suppressed the separation bubble as Figures 12.33 and 12.34 clearly show, it was not able to completely eliminate it. There is still a small core of separation bubble remaining. Its existence is attributed to the stability of the separation bubble at the present Re-number level of 110,000.

As shown in Figures 12.35 to 12.42, similar results are observed when operating at a Reynolds number of 150,000 with FSTIs of 1.9%, 3.0%, 8.0% and 13.0%. It is observed that increasing Reynolds number to 150,000 moves the separation bubble further downstream. However, doubling the reduced frequency to Ω=3.18, increasing the FSTI level to 13% and the Reynolds number to 150,000 is associated with the higher turbulence intensity that leads to a complete suppression of the separation bubble as shown in Figure 12.42.

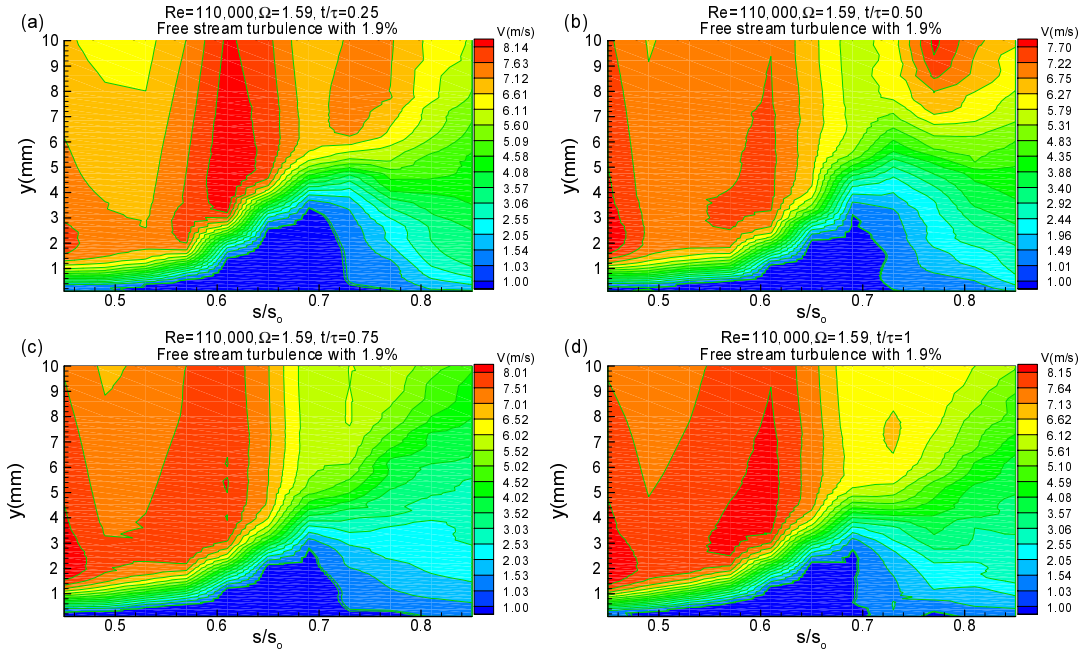

Figure 12.27. Ensemble-averaged velocity contours along the suction surface for different s/s_0 with time t/τ as parameter for Ω=1.59 (S_R=160 mm) at Re=110,000 and free-stream turbulence of 1.9% (without grid)

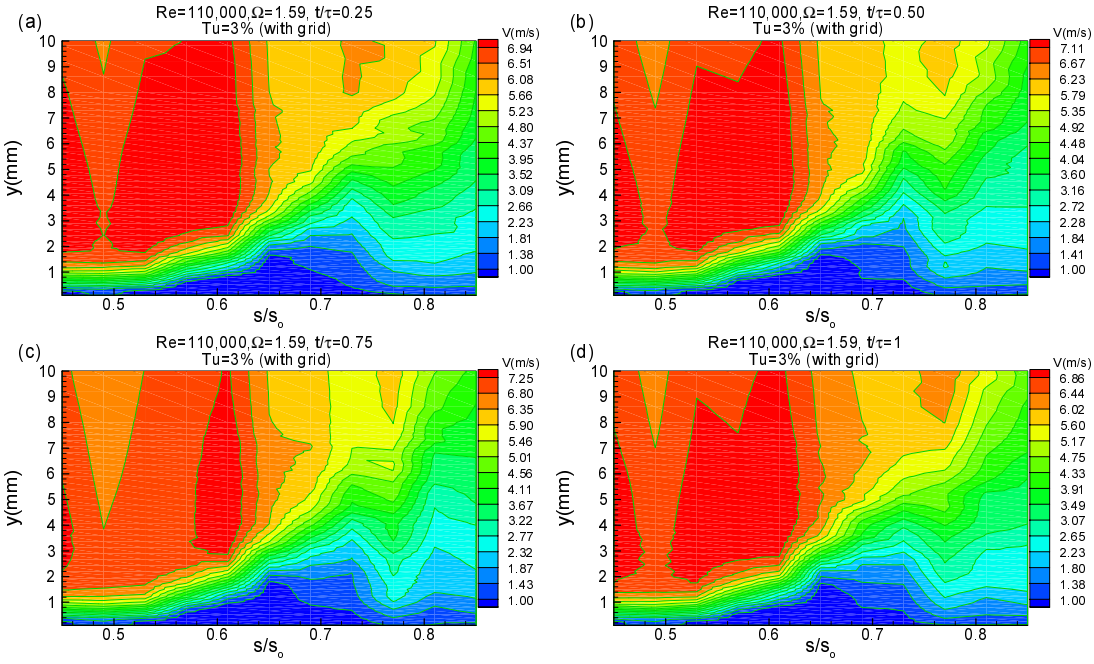

Figure 12.28. Ensemble-averaged velocity contours along the suction surface for different s/s_0 with time t/τ as parameter for Ω=1.59 (S_R=160 mm) at Re=110,000 and Tu=3% with grid TG1

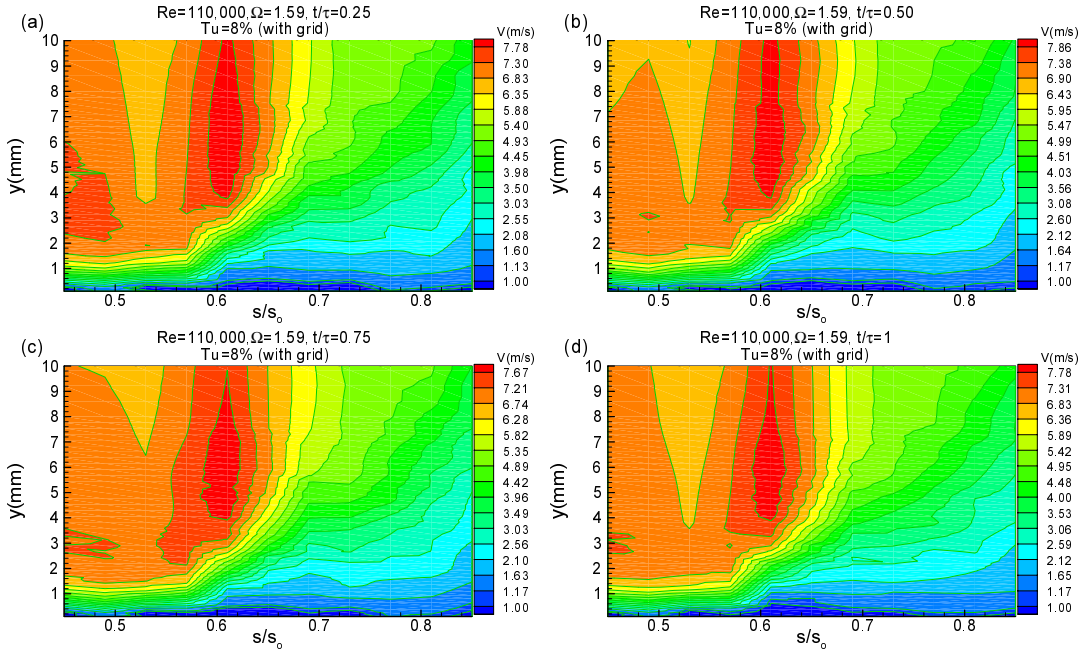

Figure 12.29. Ensemble-averaged velocity contours along the suction surface for different s/s_0 with time t/τ as parameter for Ω=1.59 (S_R=160 mm) at Re=110,000 and Tu=8% with grid TG2

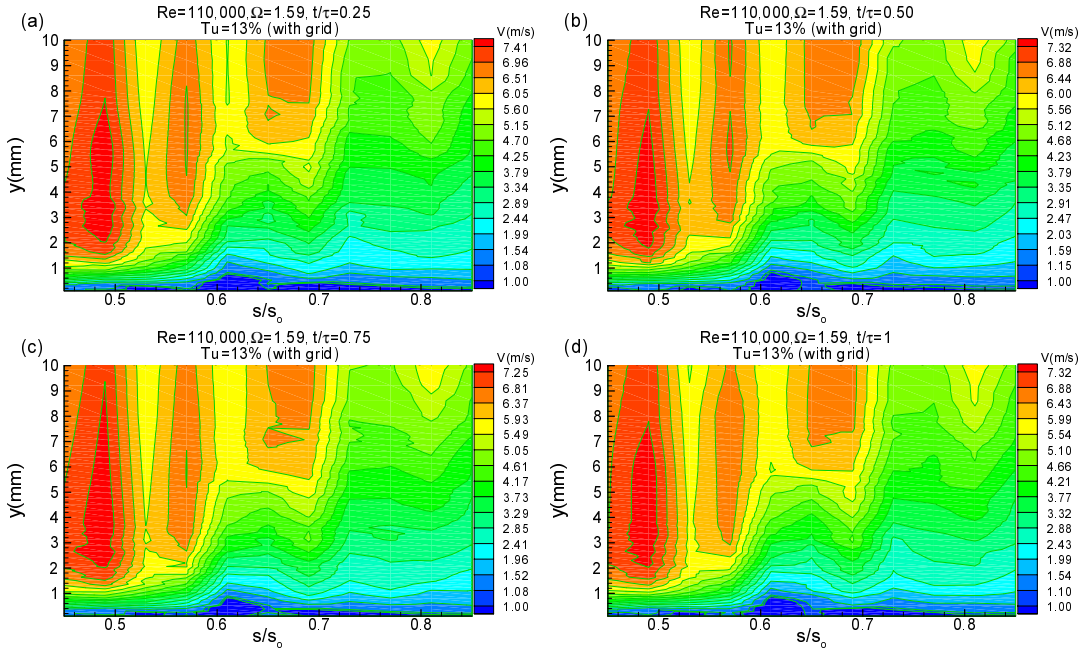

Figure 12.30. Ensemble-averaged velocity contours along the suction surface for different s/s_0 with time t/τ as parameter for Ω=1.59 (S_R=160 mm) at Re=110,000 and Tu=13% with grid TG3

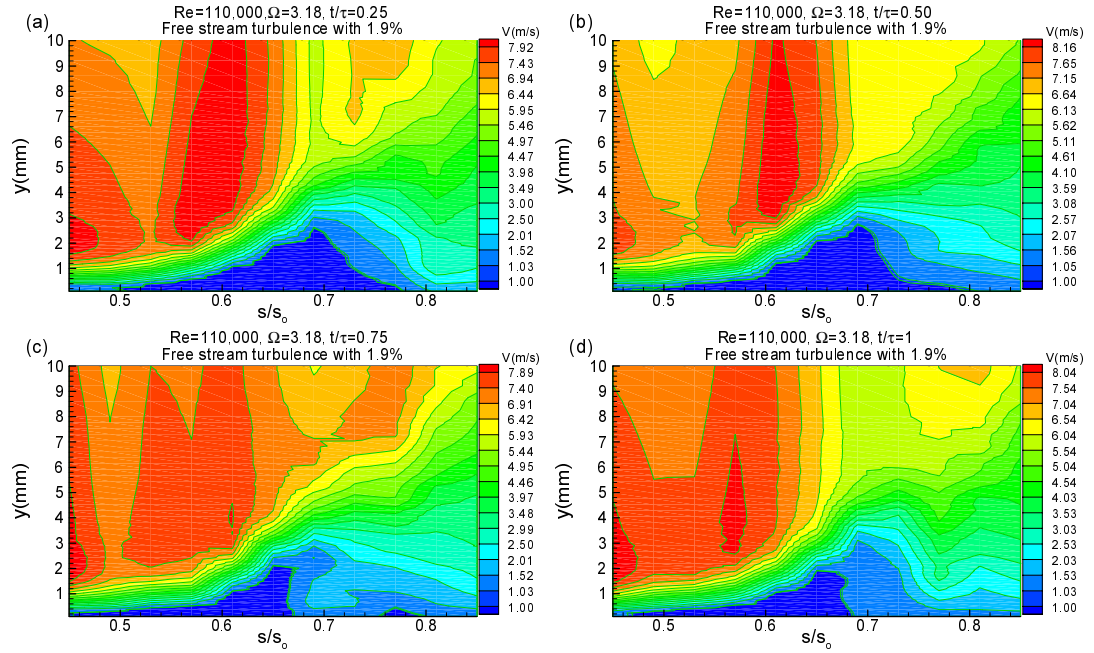

Figure 12.31. Ensemble-averaged velocity contours along the suction surface for different s/s_0 with time t/τ as parameter for Ω=3.18 (S_R=80 mm) at Re=110,000 and free-stream turbulence of 1.9% (without grid)

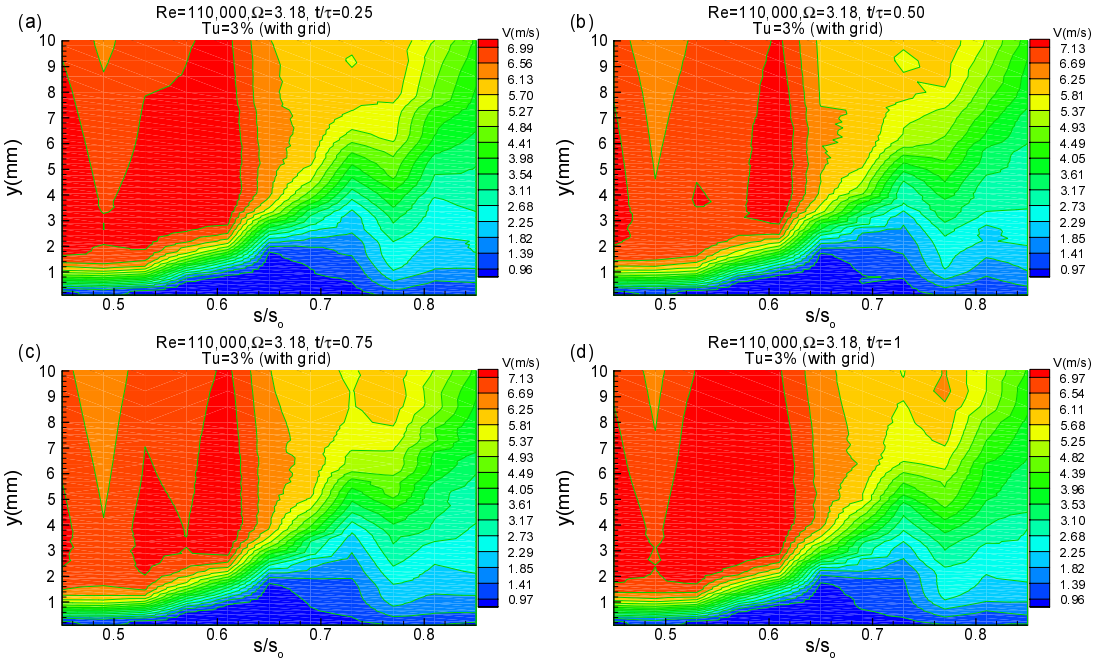

Figure 12.32. Ensemble-averaged velocity contours along the suction surface for different s/s_0 with time t/τ as parameter for Ω=3.18 (S_R=80 mm) at Re=110,000 and Tu=3% with grid TG1

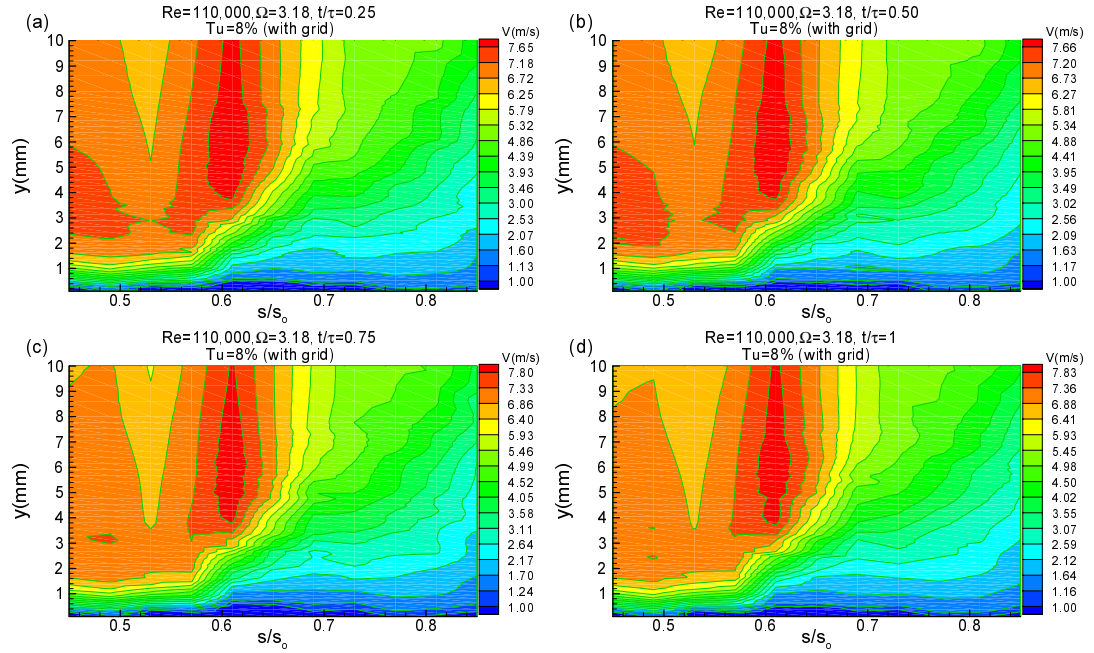

Figure 12.33. Ensemble-averaged velocity contours along the suction surface for different s/s_0 with time t/τ as parameter for Ω=3.18 (S_R=80 mm) at Re=110,000 and Tu=8% with grid TG2

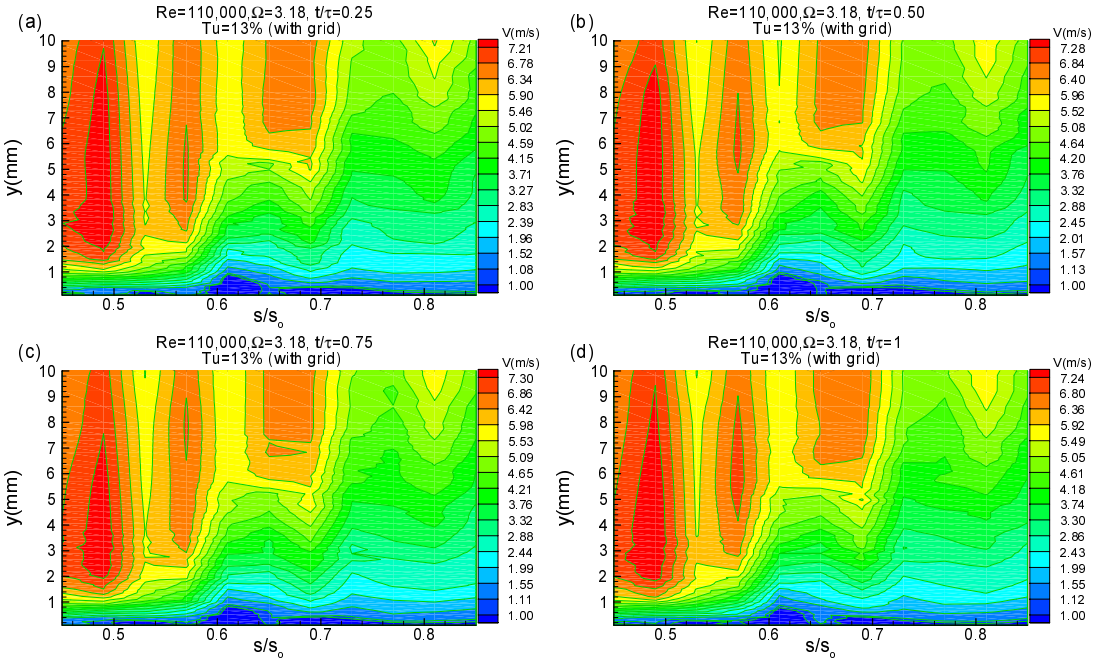

Figure 12.34. Ensemble-averaged velocity contours along the suction surface for different s/s_0 with time t/τ as parameter for Ω=3.18 (S_R=80 mm) at Re=110,000 and Tu=13% with grid TG3

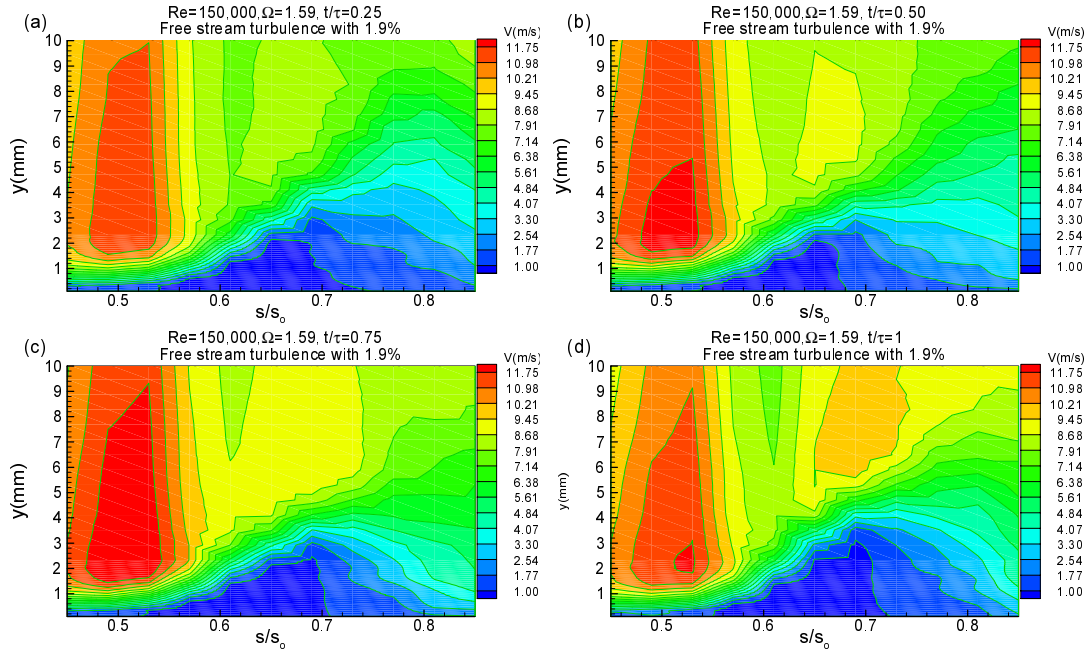

Figure 12.35. Ensemble-averaged velocity contours along the suction surface for different s/s_0 with time t/τ as parameter for Ω=1.59 (S_R=160 mm) at Re=150,000 and free-stream turbulence of 1.9% (without grid)

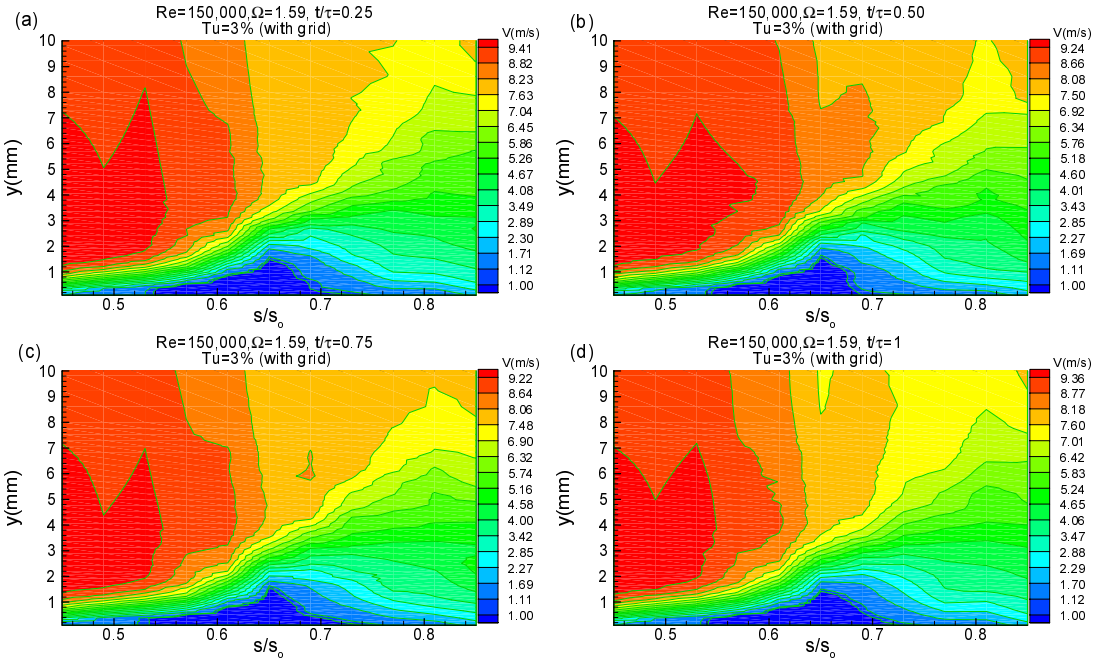

Figure 12.36. Ensemble-averaged velocity contours along the suction surface for different s/s_0 with time t/τ as parameter for Ω=1.59 (S_R=160 mm) at Re=150,000 and Tu=3% with grid TG1

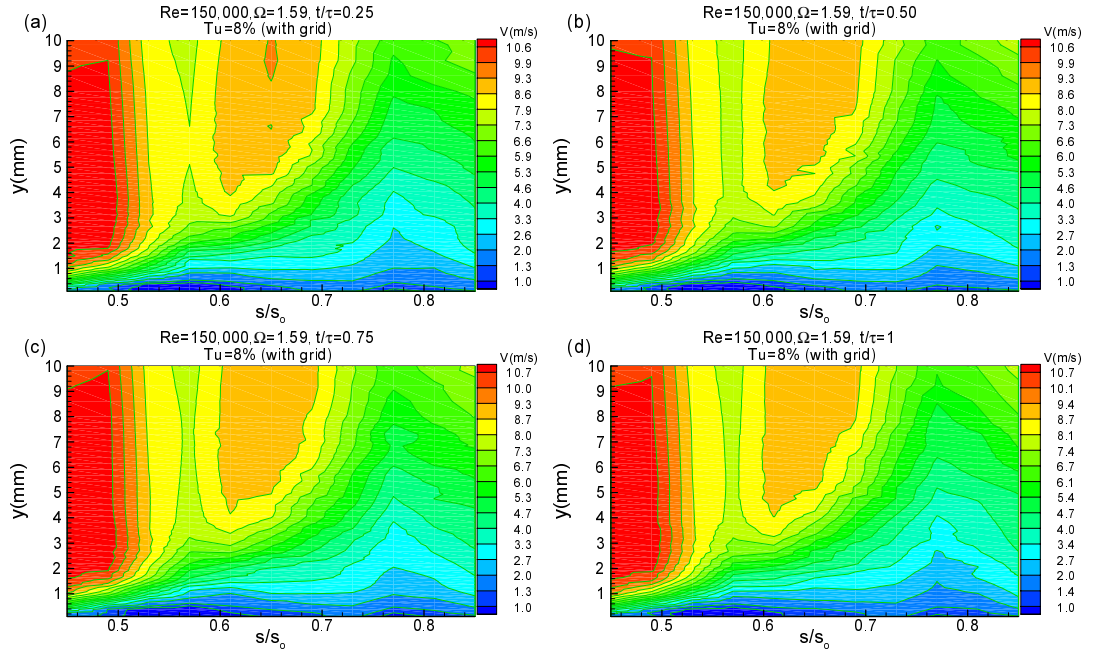

Figure 12.37. Ensemble-averaged velocity contours along the suction surface for different s/s_0 with time t/τ as parameter for Ω=1.59 (S_R=160 mm) at Re=150,000 and Tu=8% with grid TG2

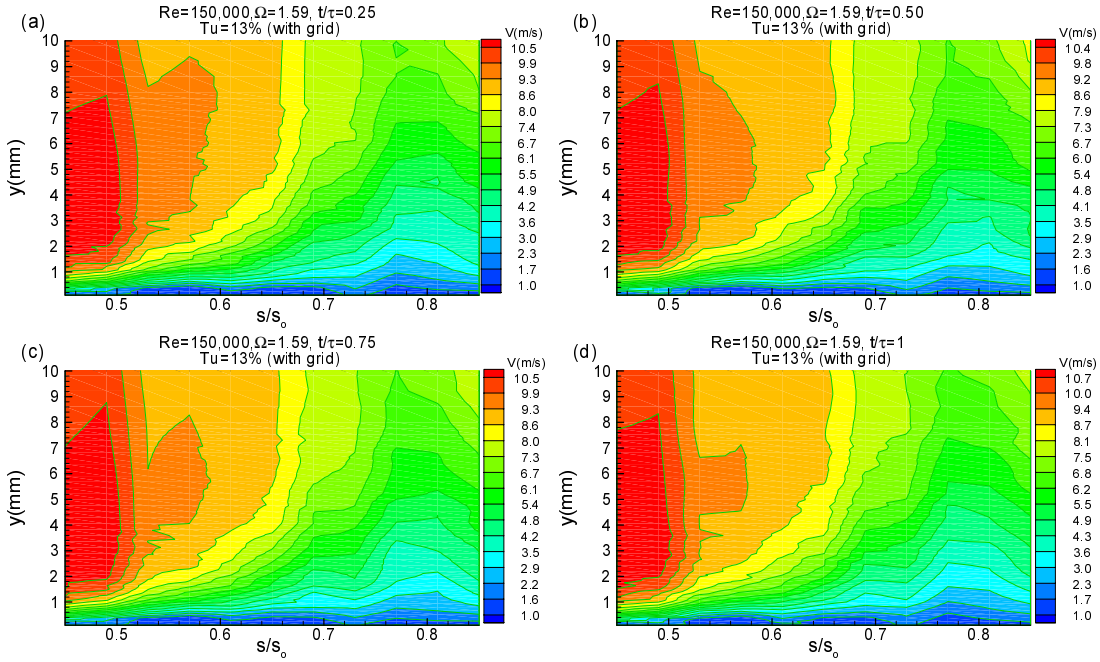

Figure 12.38. Ensemble-averaged velocity contours along the suction surface for different s/s_0 with time t/τ as parameter for Ω=1.59 (S_R=160 mm) at Re=150,000 and Tu=13% with grid TG3

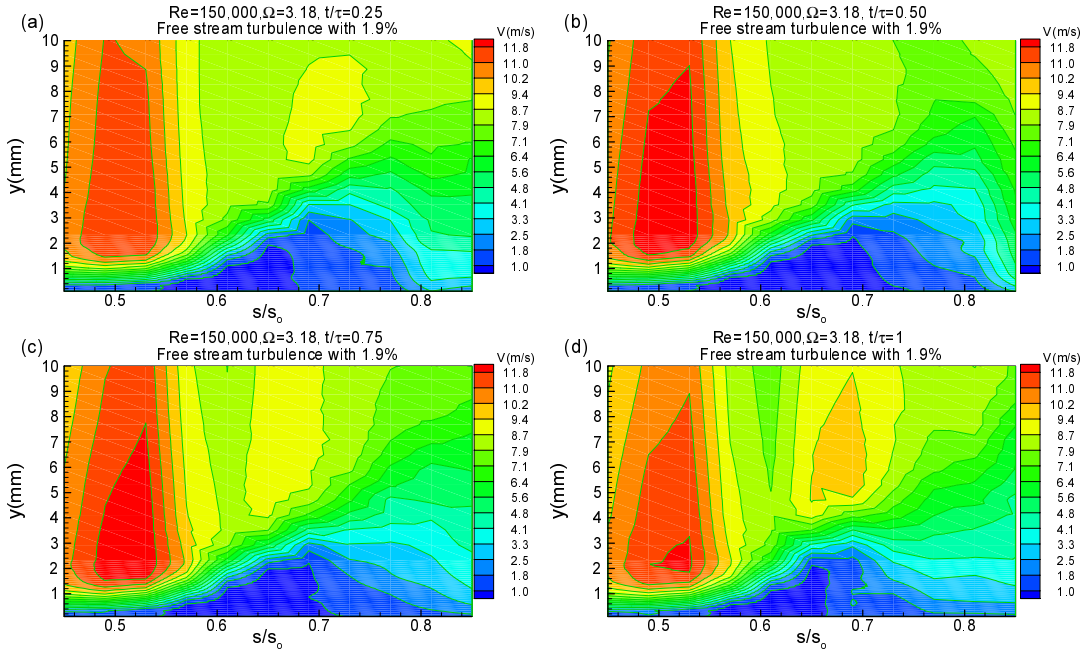

Figure 12.39. Ensemble-averaged velocity contours along the suction surface for different s/s_0 with time t/τ as parameter for Ω=3.18 (S_R=80 mm) at Re=150,000 and free-stream turbulence of 1.9% (without grid)

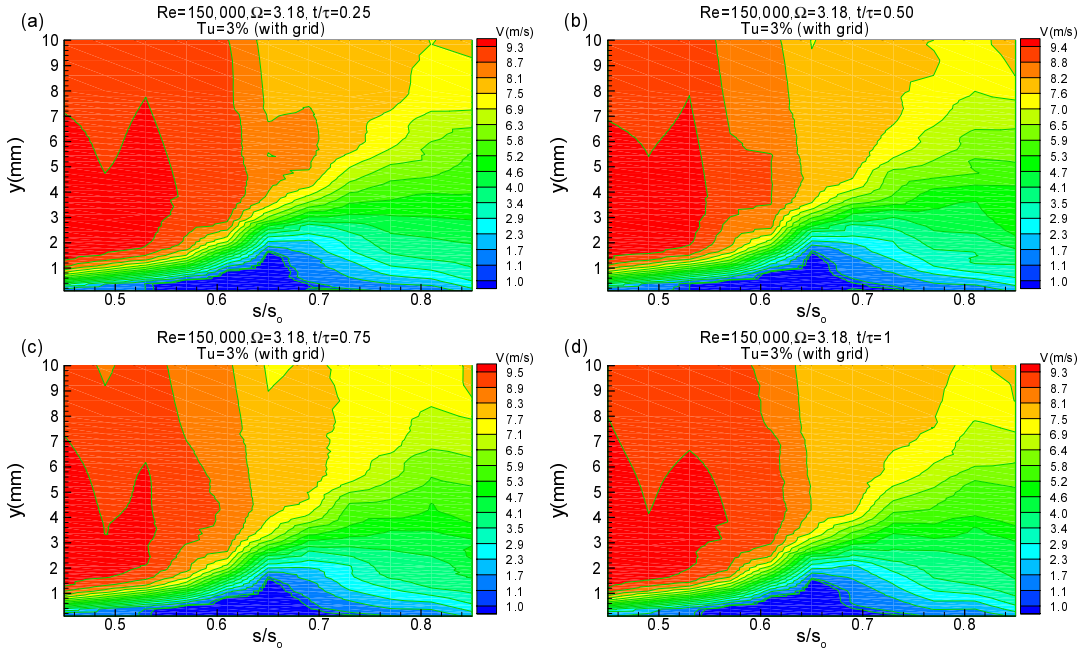

Figure 12.40. Ensemble-averaged velocity contours along the suction surface for different s/s_0 with time t/τ as parameter for Ω=3.18 (S_R=80 mm) at Re=150,000 and Tu=3% with grid TG1

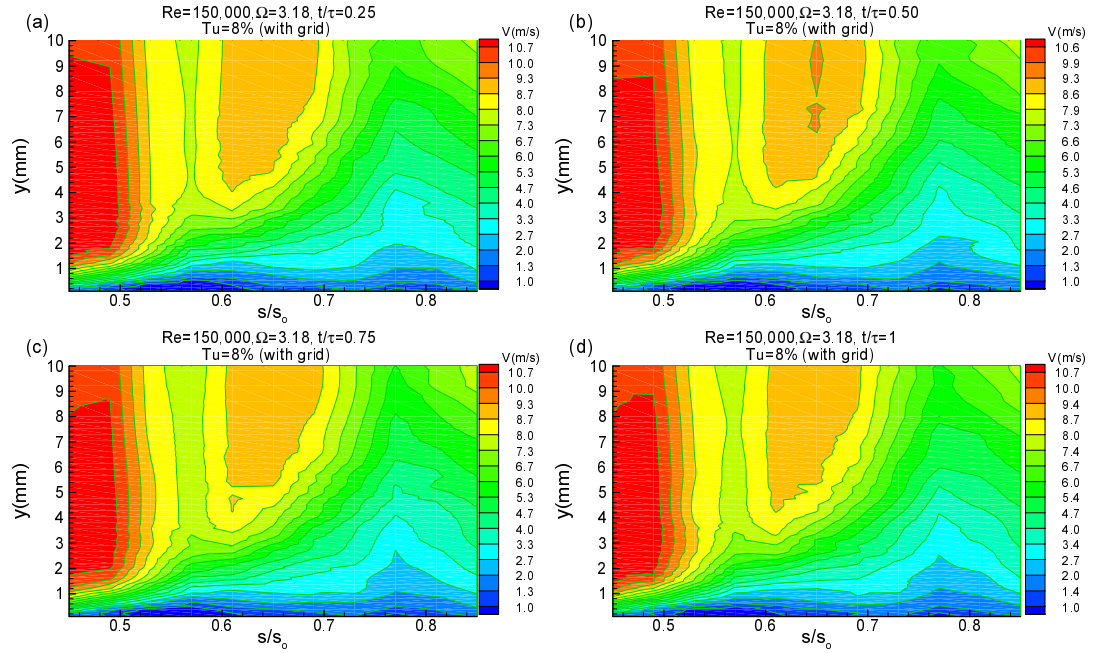

Figure 12.41. Ensemble-averaged velocity contours along the suction surface for different s/s_0 with time t/τ as parameter for Ω=3.18 (S_R=80 mm) at Re=150,000 and Tu=8% with grid TG2

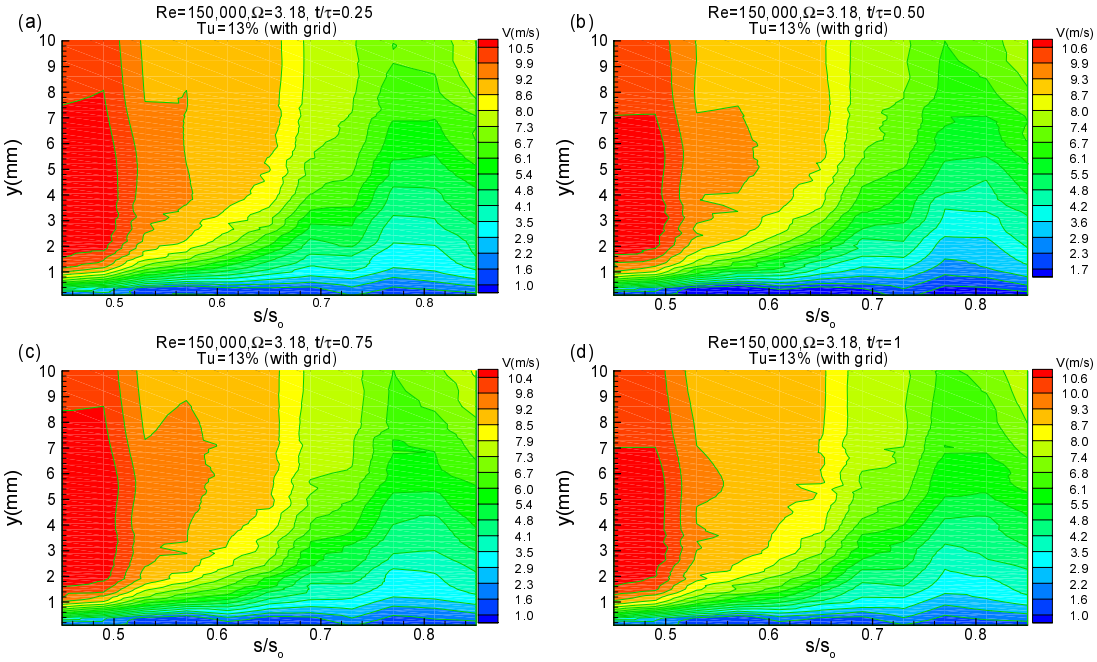

Figure 12.42. Ensemble-averaged velocity contours along the suction surface for different s/s_0 with time t/τ as parameter for Ω=3.18 (S_R=80 mm) at Re=150,000 and Tu=13% with grid TG3

12.6 Time Averaged, Ensemble Averaged Boundary Layer Integral Quantities

The integral parameters, such as the momentum deficiency thickness δ_2 and shape factor H_{12}, are of particular interest to turbine designers, since they provide an accurate first estimation of the quality of the designed blade. While the distribution of momentum deficiency thickness δ_2 provides an insight into the loss behavior of the blade, the distribution of the shape factor H_{12} furnishes sufficiently accurate information about the flow separation behavior.

12.6.1 Time Averaged δ_2-Distribution

For the reference case of FSTI = 1.9%, Figure 12.43(a) , upstream of the separation start the δ_2-values for three different reduced frequencies experience only minor changes. Passing the separation start, major systematic changes are observed with $\Omega = 0$ (no rod) being the largest and $\Omega = 3.18$ the smallest. Thus, increasing the reduced frequency causes a reduction of δ_2 as seen in Figure 12.43(a). Combination of higher FSTI levels with unsteady wakes reveals that the noticeable deviation in δ_2 distribution between the steady and unsteady cases discussed above is diminishing with increasing the turbulence intensity level as shown in Figures. 12.43(b,c,and d). The physical explanation of this phenomenon supported by the experimental results is this: The presence of the unsteady wakes decreases the boundary layer momentum thickness and thus the profile losses as long as the level of the time averaged turbulence fluctuations is below the maximum level of the wake fluctuation v_{max} (shown in Figure 12.2(a)). However the decreasing effect diminishes integrally, whenever the FSTI-level approaches values that cause the wake fluctuation partially or totally submerge into the freestream turbulence as shown in Figures 12.43 (b,c and d).

12.6.2 Time Averaged H_{12}-Distribution

For FSTI = 1.9%, upstream of the separation bubble, the shape factor for three different reduced frequencies experiences only minor changes as shown in Figure 12.44(a). However, approaching the separation bubble, the shape factor systematically increases at

a relatively steep rate, with Ω = 0 as the highest followed by Ω = 1.59 and Ω = 3.18. It reaches a maximum value of about $H_{12} \approx 6.1$ at s/s_o=0.65. Passing the separation bubble, the shape factor sharply decreases approaching a level that is typical of an attached turbulent boundary layer flow. As in δ_2-case, for FSTI= 1.9, major systematic changes are observed with increasing the reduced frequency. However, the combination of higher turbulent intensity level with unsteady wake flow results in significant decrease of the shape factor.

As seen in Figures 12.45 and 12.46, similar time-averaged δ_2 and H_{12} distributions are observed when operating at a Reynolds number of 150,000 with FSTIs of 1.9%, 3.0%, 8.0% and 13.0%.

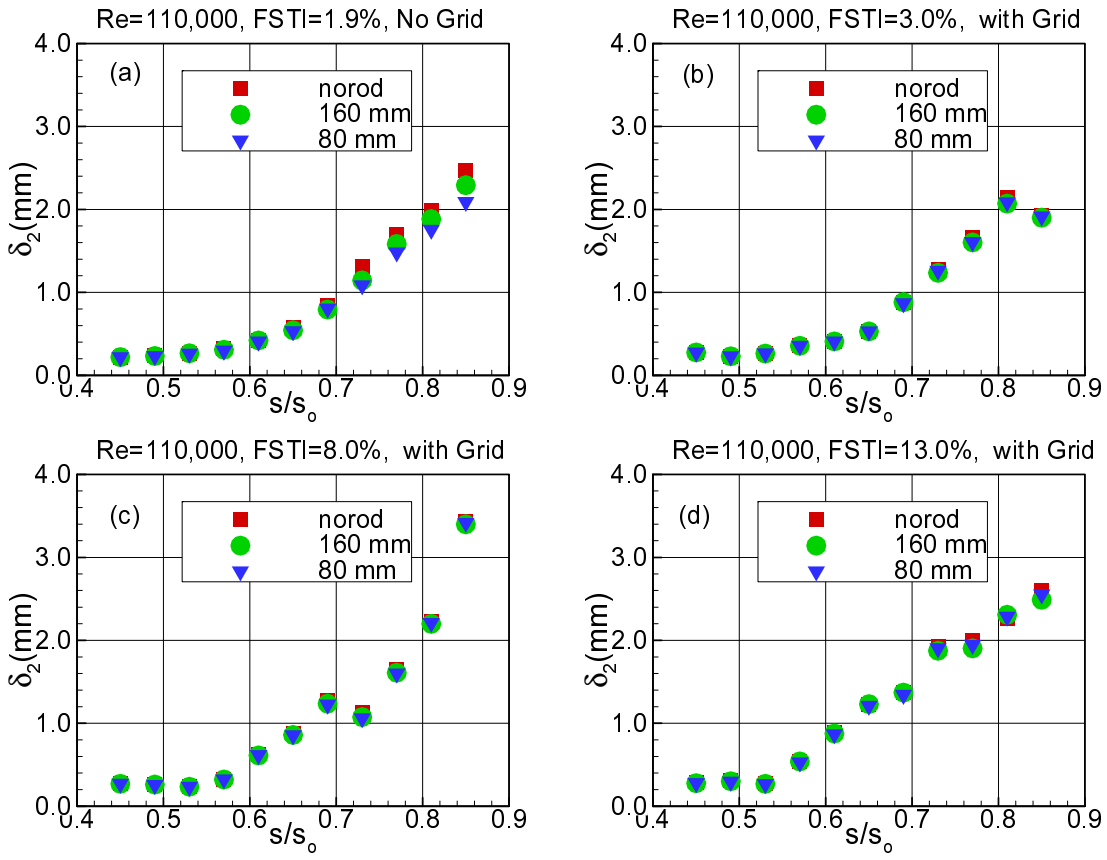

Figure 12.43. Time-averaged momentum thickness for (a) Tu=1.9% (without grid), (b) Tu=3% (with grid TG1), (c) Tu=8% (with grid TG2), (d) Tu=13% (with grid TG3) for three different reduced frequency of Ω=0, 1.59, 3.18 (no rod, 160 mm, 80 mm) at Re=110,000

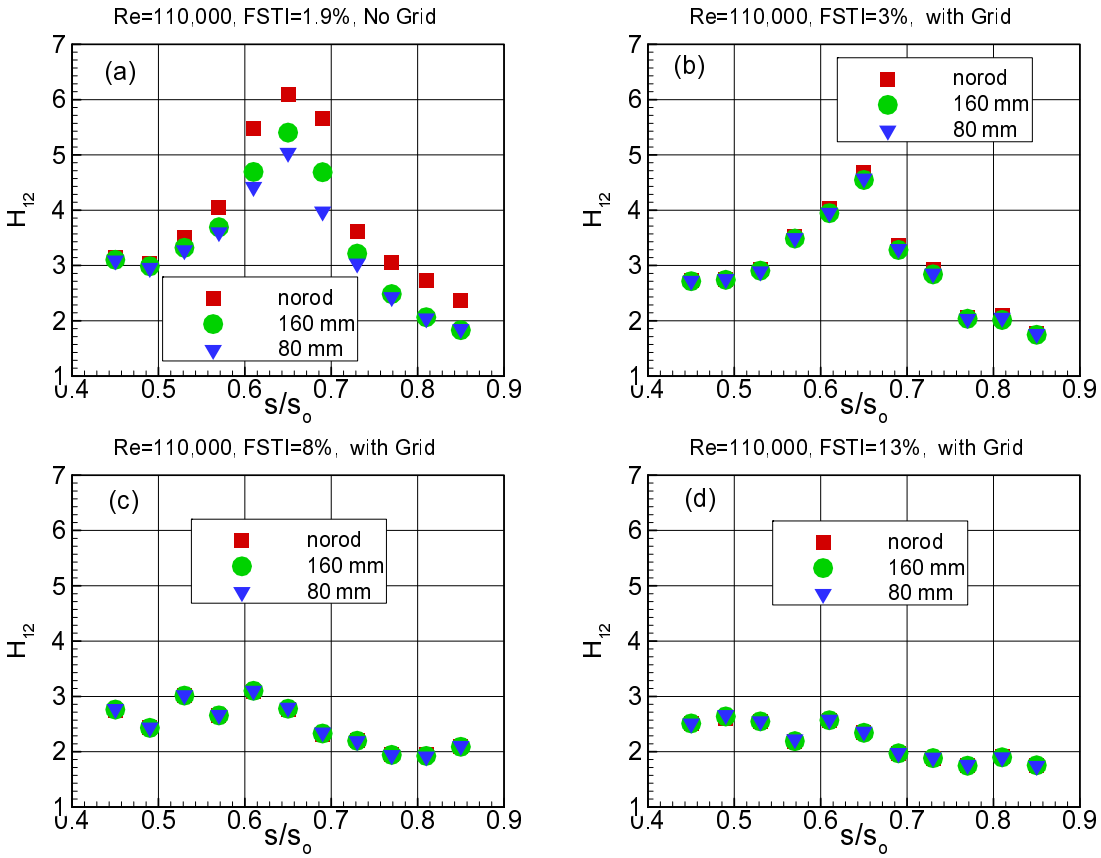

Figure 12.44. Time-averaged shape factor for (a) Tu=1.9% (without grid), (b) Tu=3% (with grid TG1), (c) Tu=8% (with grid TG2), (d) Tu=13% (with grid TG3) for three different reduced frequency of Ω=0, 1.59, 3.18 (no rod, 160 mm, 80 mm) at Re=110,000

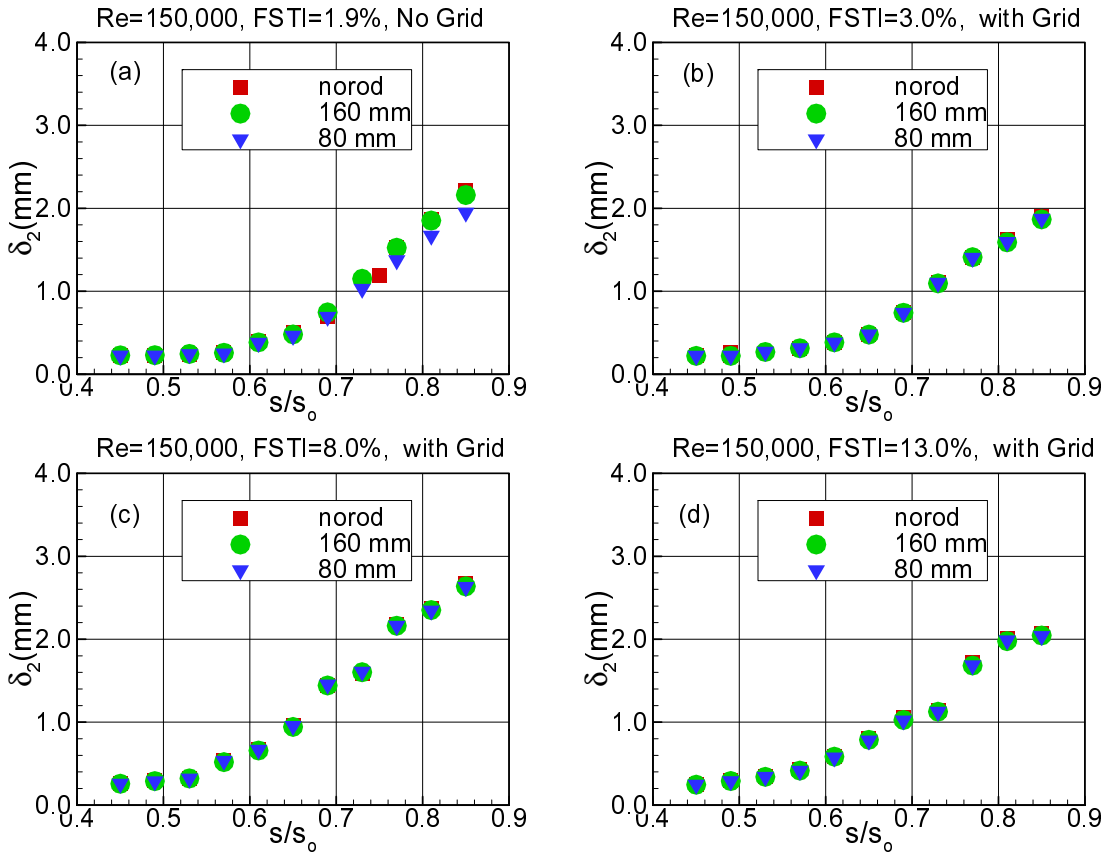

Figure 12.45. Time-averaged momentum thickness for (a) Tu=1.9% (without grid), (b) Tu=3% (with grid TG1), (c) Tu=8% (with grid TG2), (d) Tu=13% (with grid TG3) for three different reduced frequency of Ω=0, 1.59, 3.18 (no rod, 160 mm, 80 mm) at Re=150,000

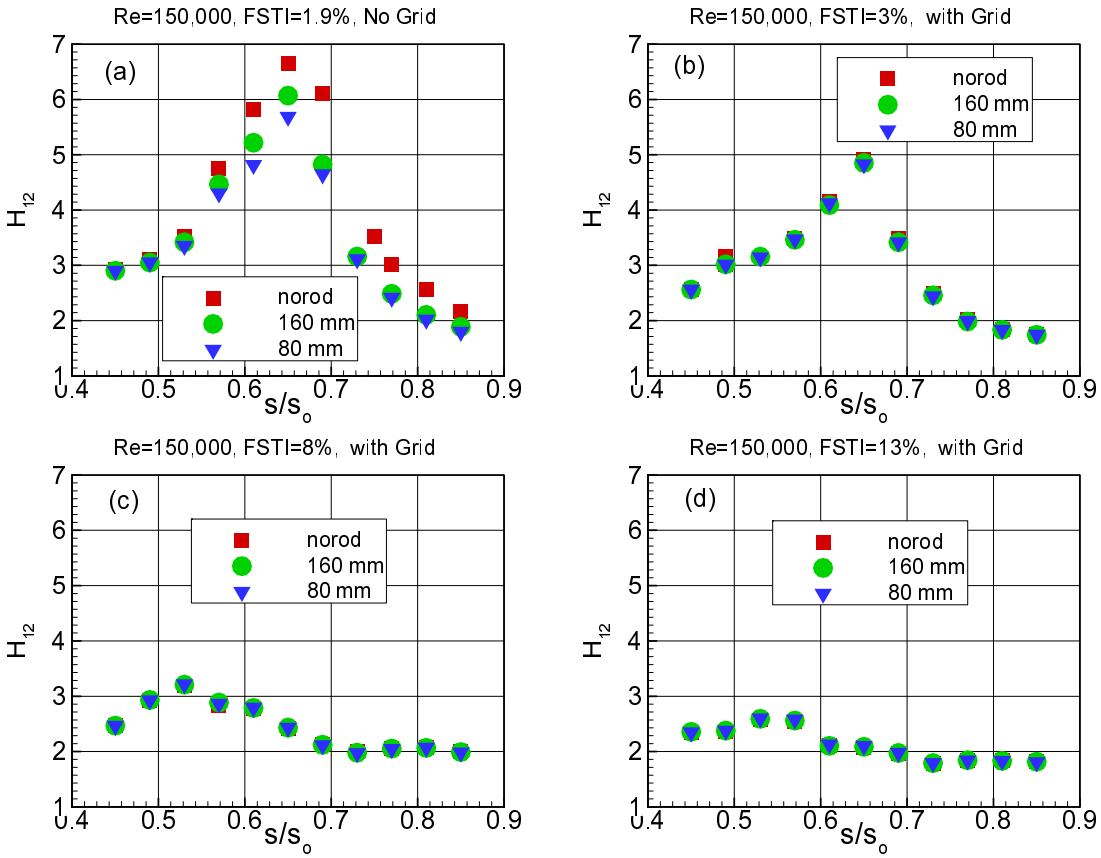

Figure 12.46. Time-averaged shape factor for (a) Tu=1.9% (without grid), (b) Tu=3% (with grid TG1), (c) Tu=8% (with grid TG2), (d) Tu=13% (with grid TG3) for three different reduced frequency of Ω=0, 1.59, 3.18 (no rod, 160 mm, 80 mm) at Re=150,000

12.7 Ensemble Averaged δ_2- Distribution

Ensemble-averaged distributions of the momentum deficiency thickness δ_2 at s/s_0 = 0.61, 0.65, and 0.73 within the separation bubble are shown in Figures 12.47 to 12.50 at Reynolds numbers of 110,000 and 150,000 for Ω = 1.59 and Ω = 3.18 values. The thickness values are nondimensionalized with the value of the steady case at Ω = 0. The period τ represents the wake-passing period that is specific to the individual wake generating cluster, which is characterized by the Ω - value under investigation. The periodic behavior of the ensemble-averaged momentum thickness over the separation bubble as a result of the embedded periodic wake flow, is clearly visible from Figures 12.47(a) and 12.48(a). To avoid repetition, as a representative, the δ_2 -distribution at s/s_0 = 0.65 location in Figure 12.47(a) is generically discussed. For each wake passing period, the periodic δ_2 - distribution reveals of one distinct maximum and one minimum with several peaks and valleys in between. The ensemble averaged δ_2 has a maximum, when the wake flow associated with a pronounced velocity deficit impinges on the separation bubble. This occurs at $t/\tau \approx 0.6$, 1.6, and 2.6. These exactly correspond to the instants at which the ensemble averaged velocity distributions have their minimum as shown in Figure 12.2(a). Likewise, the distinct minimum δ_2 values periodically encountered at $t/\tau \approx 0.4$, 1.4, and 2.4 correspond to the instants at which the wake external core flow impinges on the bubble. The δ_2 -distribution for Ω = 3.18 is presented in Figure 12.48(a) with are similar to the one presented above, repeating the discussion unnecessary.

Increasing the FSTI-level does not affect the periodicity of δ_2-distributions as shown in Figure 12.47(b, c and d) indicates. However, the pronounced phase difference diminishes

Similar results are observed when operating at a reduced frequency of Ω=3.18 which is shown in Figure 12.48(a-d). However, the combination of higher turbulence intensity levels with unsteady wakes reveals that the noticeable deviation in momentum thickness distribution between the steady and unsteady cases discussed above is diminishing with increasing the turbulence intensity level as shown in Figure 12.48(a-d).

Similar ensemble-averaged δ_2 distributions is observed when operating at a Reynolds number of 150,000 with FSTIs of 1.9%, 3.0%, 8.0% and 13.0% as shown in Figures 12.49 and 12.50.

The ensemble averaged integral parameter discussed above is essential to calculate the ensemble averaged and time averaged profile loss coefficients at each streamwise position. Furthermore, the integration of the time averaged loss coefficient distribution over the entire blade surface provides the global profile loss coefficient. A simple procedure given in [124] describes how the loss coefficient can be calculated using the integral parameters.

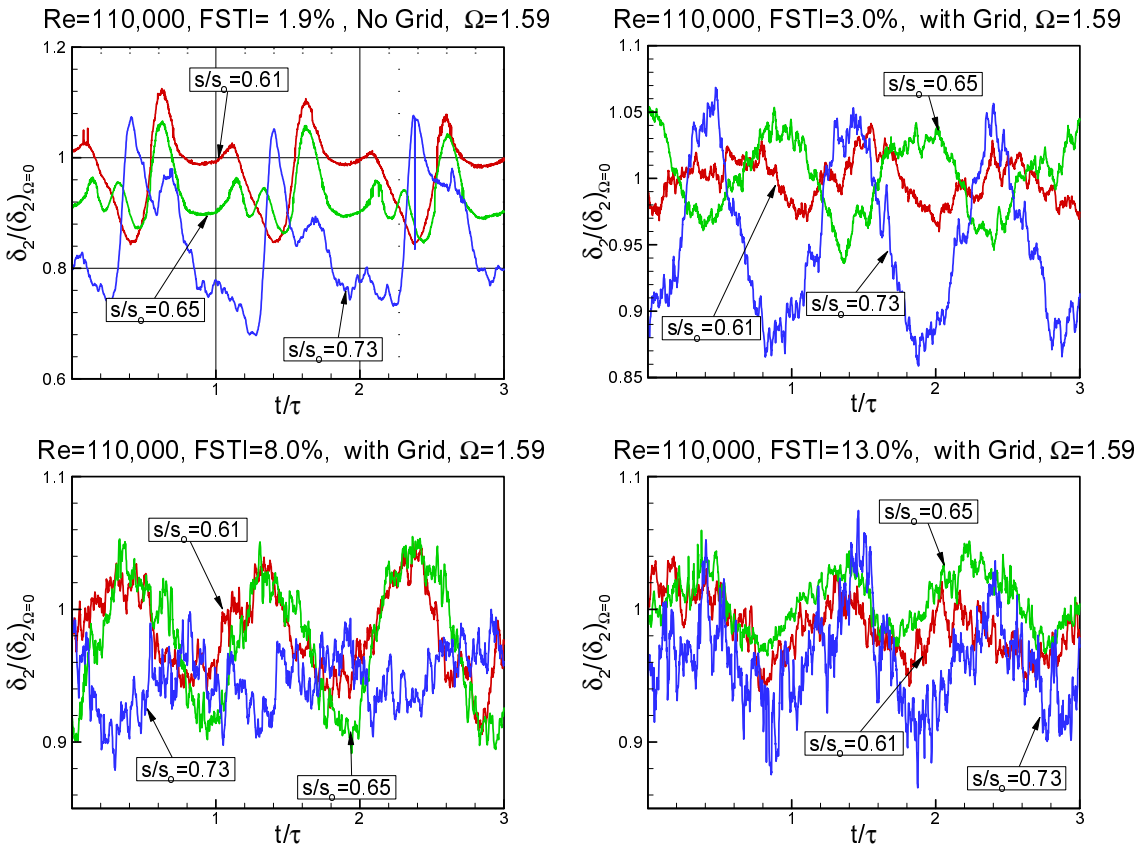

Figure 12.47. Ensemble-averaged relative momentum thickness distribution along the suction surface for different streamwise positions for (a) Tu=1.9% (without grid), (b) Tu=3% (with grid TG1), (c) Tu=8% (with grid TG2), (d) Tu=13% (with grid TG3) for Ω= 1.59(160 mm) at Re=110,000

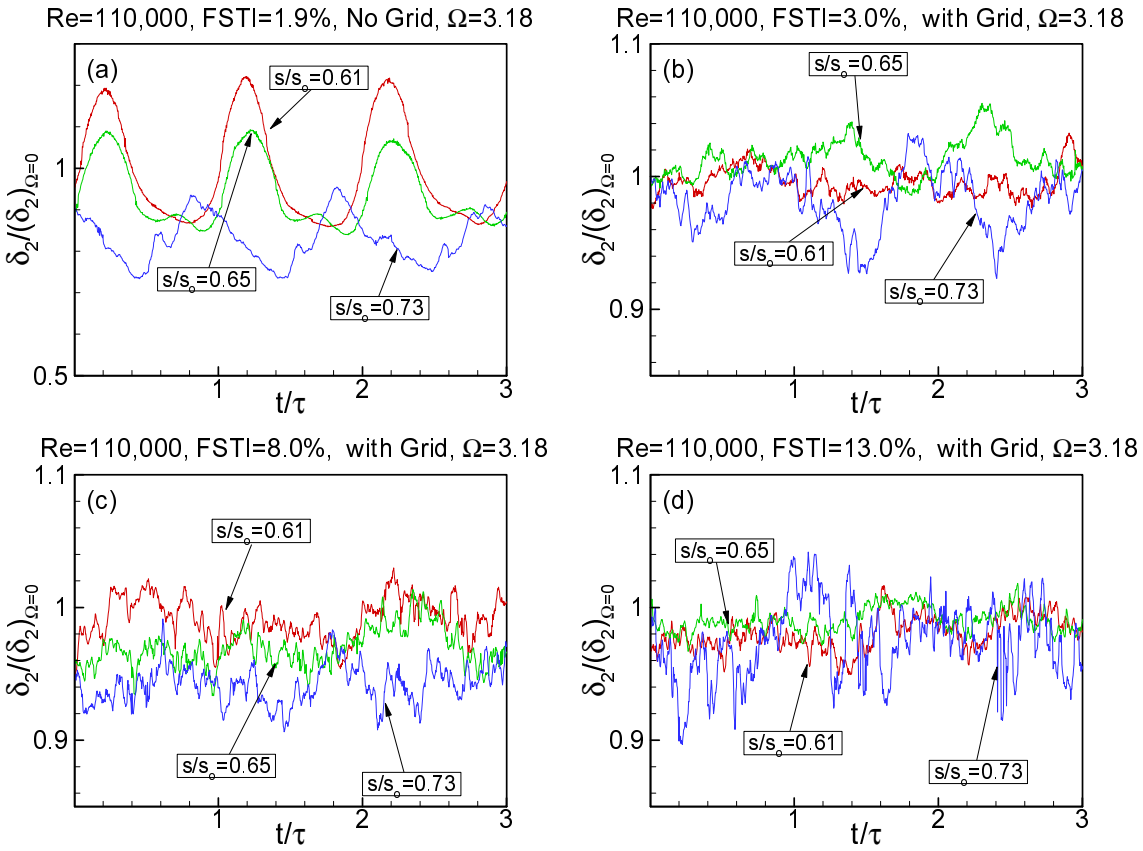

Figure 12.48. Ensemble-averaged relative momentum thickness distribution along the suction surface for different streamwise positions for (a) Tu=1.9% (without grid), (b) Tu=3% (with grid TG1), (c) Tu=8% (with grid TG2), (d) Tu=13% (with grid TG3) for Ω= 3.18(80 mm) at Re=110,000

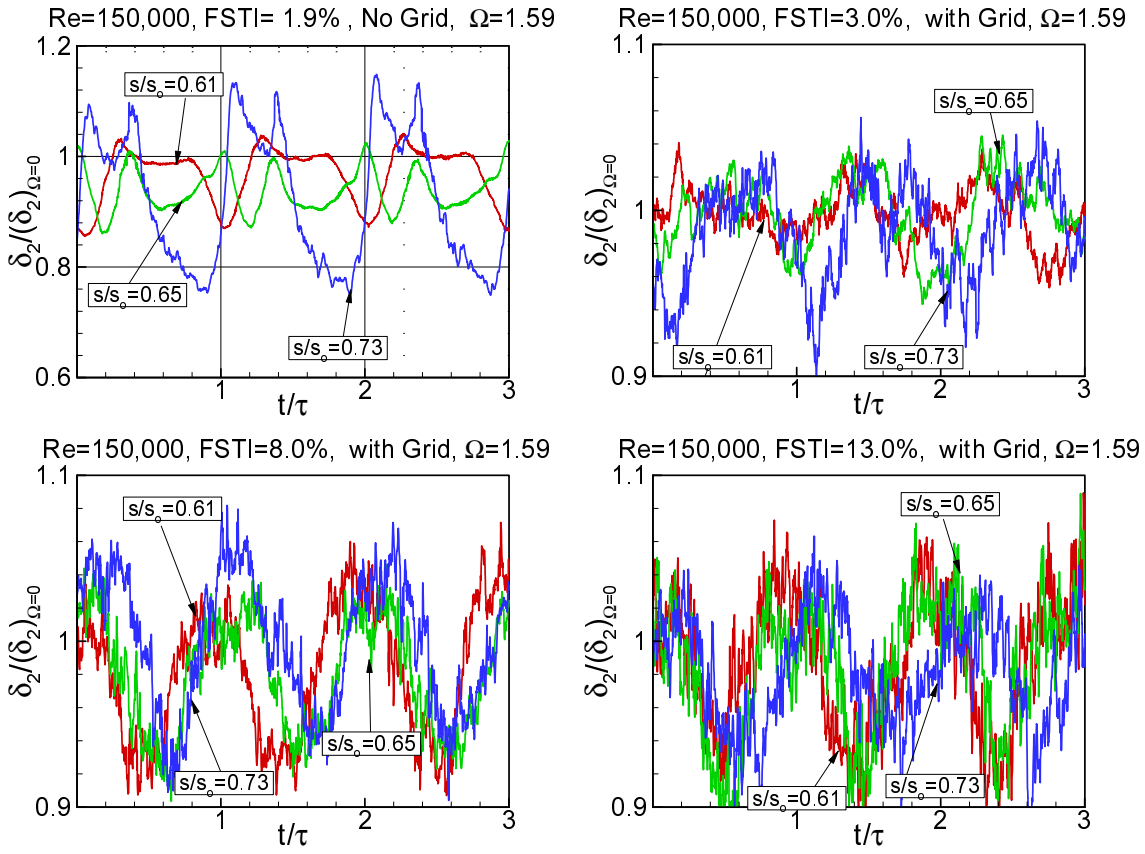

Figure 12.49. Ensemble-averaged relative momentum thickness distribution along the suction surface for different streamwise positions for (a) Tu=1.9% (without grid), (b) Tu=3% (with grid TG1), (c) Tu=8% (with grid TG2), (d) Tu=13% (with grid TG3) for Ω= 1.59(160 mm) at Re=150,000

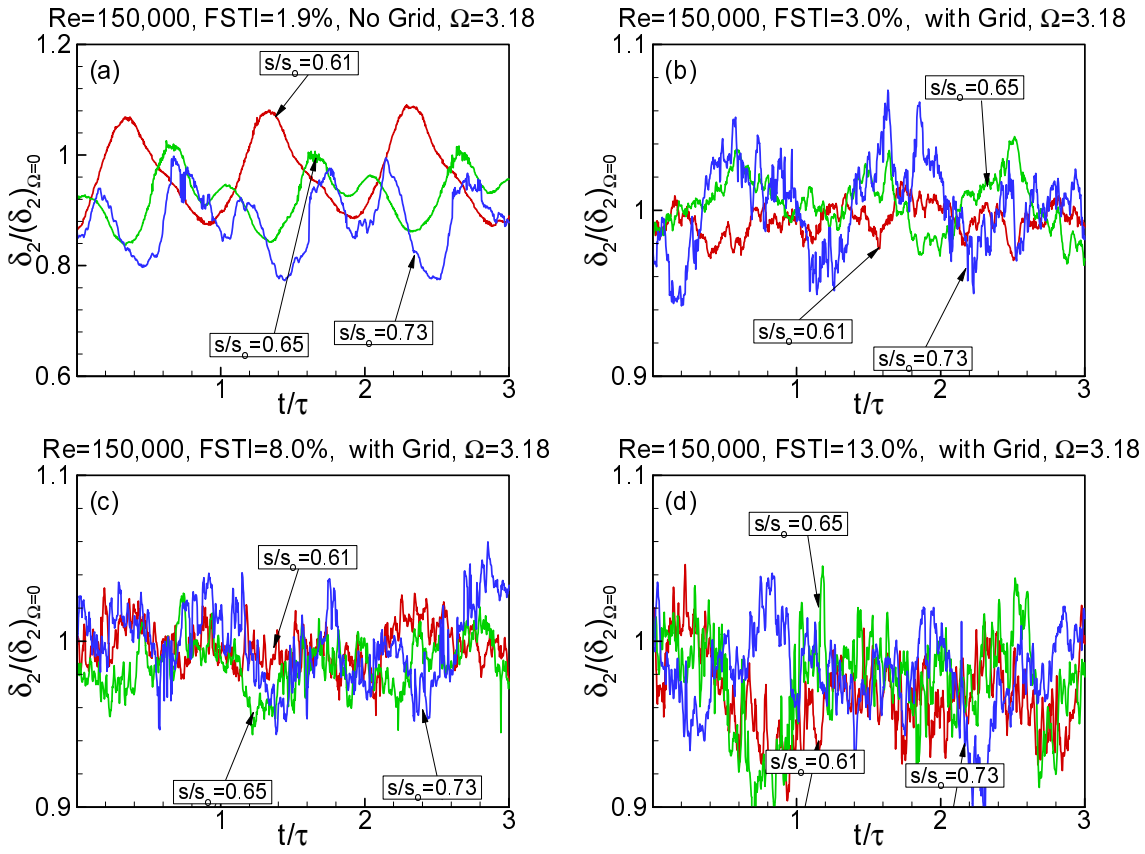

Figure 12.50. Ensemble-averaged relative momentum thickness distribution along the suction surface for different streamwise positions for (a) Tu=1.9% (without grid), (b) Tu=3% (with grid TG1), (c) Tu=8% (with grid TG2), (d) Tu=13% (with grid TG3) for Ω= 3.18(80 mm) at Re=150,000

13. INTERMITTENCY ANALYSIS

In this section, the aerodynamic experimental data collected from the cascade test facility described in Section 4 are analyzed to explain the transition process under unsteady wake flow conditions along the separation bubble. The instantaneous velocities collected inside the boundary layer are processed and the intermittency factor is quantified throughout the blade surface boundary layer. The discriminatory function consisting of 0's and 1's (representing the laminar and turbulent states of the boundary layer) is both time-averaged and ensemble-averaged and expressions are developed for later use in the CFD codes. The following sections explain the processing of velocity signals and their analysis.

13.1 Theoretical Background

The theoretical background for intermittency analysis was developed by number of researchers (Townsend [126], Kaplan and Laufer [127], Kovasznay et al. [70], Antonia and Bradshaw [69]) and extensively reviewed by Hedley and Keffer [68]. The following discussion gives a brief review of their theory and its application to the analysis of the unsteady flow data in this current research.

The flow variables in a turbulent motion are statistically random variables. The behavior of these variables in an intermittent region of the flow can be assumed to represent two mutually exclusive populations associated with turbulent and non-turbulent fluid (Hedley and Keffer [68]). Considering a flow variable, Q(t), which can represent quantities as widely different as a velocity component or the width of a turbulent burst, the continuous measurement of Q(t) can be regarded as one realization from an infinite ensemble. Only, one single realization need be considered for evaluation of temporal averages. If Q(t) is the fluctuating quantity, (e.g. a velocity component at a given point), then the conventional time average is given by:

$$\overline{Q} = \lim_{t \to \infty} \frac{1}{t} \int_{t_1}^{t_1 + t_o} Q(t)\,dt \tag{13.1}$$

To identify the turbulence, so that it is unity inside the turbulent motion and zero otherwise, an intermittency function can be defined so that:

$$I(x,y,z,t)=\begin{cases}1 & for \quad turbulent \quad flow\\ 0 & for \quad non-turbulent \quad flow\end{cases} \tag{13.2}$$

and the time-average of I(x,y,z,t) is the intermittency factor, γ, which gives the fraction of the time that the probe spends in turbulent flow:

$$\gamma=\overline{I}=\lim_{t_o\to\infty}\frac{1}{t_o}\int_{t_o}^{t_1+t_o}I(t)dt \tag{13.3}$$

which is the turbulence fraction or intermittency factor.

Expected values in turbulent and non-turbulent regions can be calculated by carrying out the appropriate conditional averages following the method of Kovasznay et al. [70] and are shown as follows. In turbulent zone:

$$\overline{Q_t}=\sum_{i=1}^{N}\frac{I(t_i)Q(t_i)}{N\overline{I}} \tag{13.4}$$

and in the non-turbulent zone:

$$\overline{Q_l}=\sum_{i=1}^{N}\frac{[1-I(t_i)]Q(t_i)}{N[1-\overline{I}]} \tag{13.5}$$

The constraint on these conditional averages is simply:

$$\overline{Q}=\overline{I}\,\overline{Q_t}+[1-\overline{I}]\overline{Q_l} \tag{13.6}$$

13.2 Turbulent/Non-Turbulent Decisions

13.2.1 Processing of the Signal

Distinct features of turbulent fluid are its rotational nature and the dissipation of mechanical energy through heat through cascade of eddies of diminishing size. Spectral analysis is required for detecting energy cascade and this can not be used as an instantaneous decision for the presence of turbulence. Rotational nature or vortical fluctuations could be

used for instantaneous decisions but their measurement requires a complex probe. Alternatively, it is possible to use a simple probe such as a hot-wire measuring velocity fluctuation, to identify the fine-scale structure in the turbulent fluid. This velocity fluctuation is not unique to the turbulent flow and can not be used for making instantaneous decisions for or against the presence of turbulence. The velocity signal needs to be sensitized to increase its discriminatory capabilities. The commonly used method of sensitizing is to differentiate the signal. This sensitizing of the detector function will have some zeros inside the fully turbulent fluid. These legitimate zeros effect the decision process for the presence of turbulence or non-turbulence. The process of eliminating these zeros is to integrate the signal over a short duration of time T_s, which produces a criterion function S(t). After short term integration, a threshold level C is applied to the criterion function to distinguish between the true turbulence and the signal noise. Applying the threshold level results in an indicator function consisting of zeros and 1's satisfying:

$$I(t) = \begin{cases} 1 & when \quad S(t) \geq C \\ 0 & when \quad S(t) < C \end{cases} \tag{13.7}$$

The resulting random square, I(t), wave along with the original signal is used to condition the appropriate averages using the equations above.

13.2.2 The Detector Function

The choice of the detector function is based on the probability density distribution of the characteristic fluctuation component. Table 13.1 gives some of the examples of detector functions used by previous researchers. Some of these researchers measured the probability density functions and found that the variable (velocity signal) tends to distribute normally about zero. The distribution of the variable deviates from its normal with the order of its derivative. Qualitative probability distributions in turbulent and non-turbulent fluids are shown in Figure 13.1 (Chakka [128]). In non-turbulent fluid, the fluctuations in the signal are narrow and of small amplitude whereas within the turbulent fluid, broader fluctuations can be seen. By sensitizing the signal, the overlap between the turbulent and non-turbulent

probability density functions can be separated thereby increasing it's discriminatory capabilities. A qualitative result of this sensitizing is shown in Figure 13.1. In the non-turbulent zone, the probability of the detector function taking values significantly greater than zero is reduced, whereas in the turbulent zone, the probability density function has a wider distribution.

Table 13.1. Turbulence detector functions

Townsend (1949)	$\|u\|$, $\|\partial u/\partial t\|$
Corrsin & Kistler (1955)	$\|u\|$, $\|\partial u/\partial t\|$
Fiedler & Head (1966)	$\|\partial u/\partial t\|$
Kaplan & Laufer (1970)	$(\partial u/\partial t - \langle \partial u/\partial t \rangle)^2$
Kovasznay et al. (1970)	$\|\partial^2 u/\partial y\, \partial t\|$
Antonia & Bradshaw (1971)	$(\partial u/\partial t)^2$
Antonia (1972)	$(\partial uv/\partial t)^2$
Thomas (1973)	$\|\partial u/\partial t\|$ filtered
Bradshaw & Murlis (1973)	$\|\partial uv/\partial t\|$ or $\|\partial^2 uv/\partial t^2\|$
Schobeiri et al. (1995)	$(\partial^2 u/\partial t^2)^2$

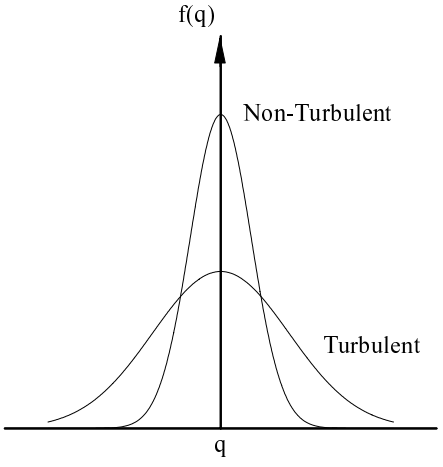

Figure 13.1. Hypothetical probability density distributions inside the turbulent and non-turbulent zones of a fluid [128]

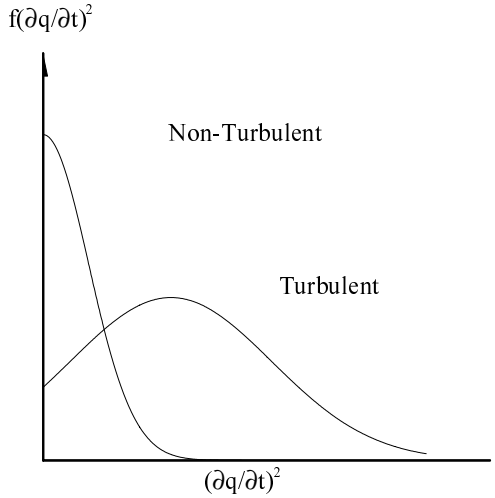

Figure 13.2. Effect of sensitizing (derivatives) on the probability density distributions [128]

13.2.3 The Smoothing Period

Though sensitized detector function separates the probability distributions between the turbulent and non-turbulent zones of the fluid, there is still some overlap between the two near the origin, see Figure 13.2 above. The discrimination between the two zones of the flow will be ideal when the overlap between the two distributions is minimal or zero. This can be achieved by smoothing the signal over a short duration of time thereby eliminating the zeros in the detector function. Hedley and Keffer [68] suggests that the optimum smoothing period is equal to the Kolmogorov length scale divided by the convective velocity. But, in practical analysis the smoothing period is much higher due to the resolution of the probe and the sampling time.

13.3 Experimental Analysis

Following the probabilistic analysis reviewed in the previous section, the velocity signals from the hot-wire probe are analyzed for intermittency distribution during the boundary layer transition. Instantaneous velocities are used to identify this intermittency distribution. The instantaneous velocity is sensitized to increase its discriminatory capabilities between turbulent and non-turbulent parts of the signal. For this purpose, the second derivative of the velocity signal is used and squared for further analysis, and is called the detector function, S(t).

$$S(t) = u\frac{\partial u}{\partial t} \tag{13.8}$$

This detector is chosen to be the most optimum for the unsteady flows under consideration. Figures 13.3 and 13.4 show the probability distributions from the experimental data. A threshold level C is then applied to this detector function to distinguish between the true turbulence and the signal *noise*.

$$I(t) = \begin{cases} 1 & when \quad S(t) \geq C \\ 0 & when \quad S(t) < C \end{cases} \tag{13.9}$$

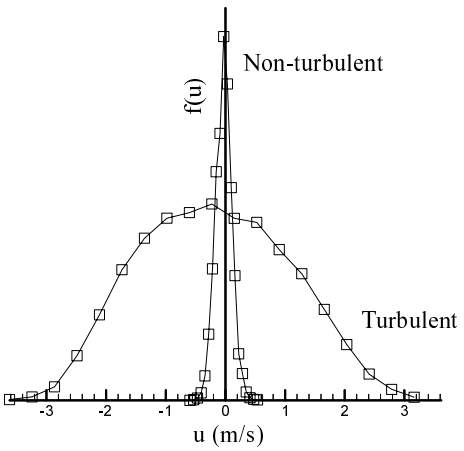

Figure 13.3. Probability density distributions of the instantaneous velocity signals in the non-turbulent and turbulent zones of the fluid [128]

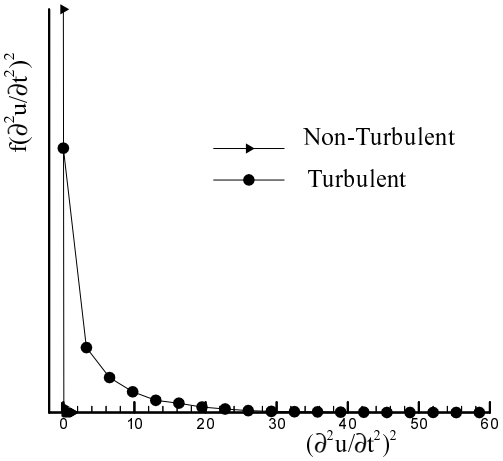

Figure 13.4. Effect of sensitizing the velocity signal [128]

After applying the threshold level to the detector function S(t), the result is a random square wave with 0's representing the laminar case and 1's representing the turbulent behavior of the boundary layer. In steady or no-rod case, this square wave is time-averaged giving the time-averaged intermittency. The time-averaged intermittency for steady case is calculated from the expression:

$$\overline{\gamma} = \int_{t=0}^{T} I(t)dt \tag{13.10}$$

In unsteady flow conditions, the square wave I(t), is ensemble averaged to get the ensemble averaged intermittency as follows

$$< \gamma_i(t_i) >= \frac{1}{n}\sum_{j=1}^{n} I_{ij}(t_i) \tag{13.11}$$

where n is the number of revolutions of the wake generator for which the data are collected. Figure 13.5 show the processing of instantaneous velocities.

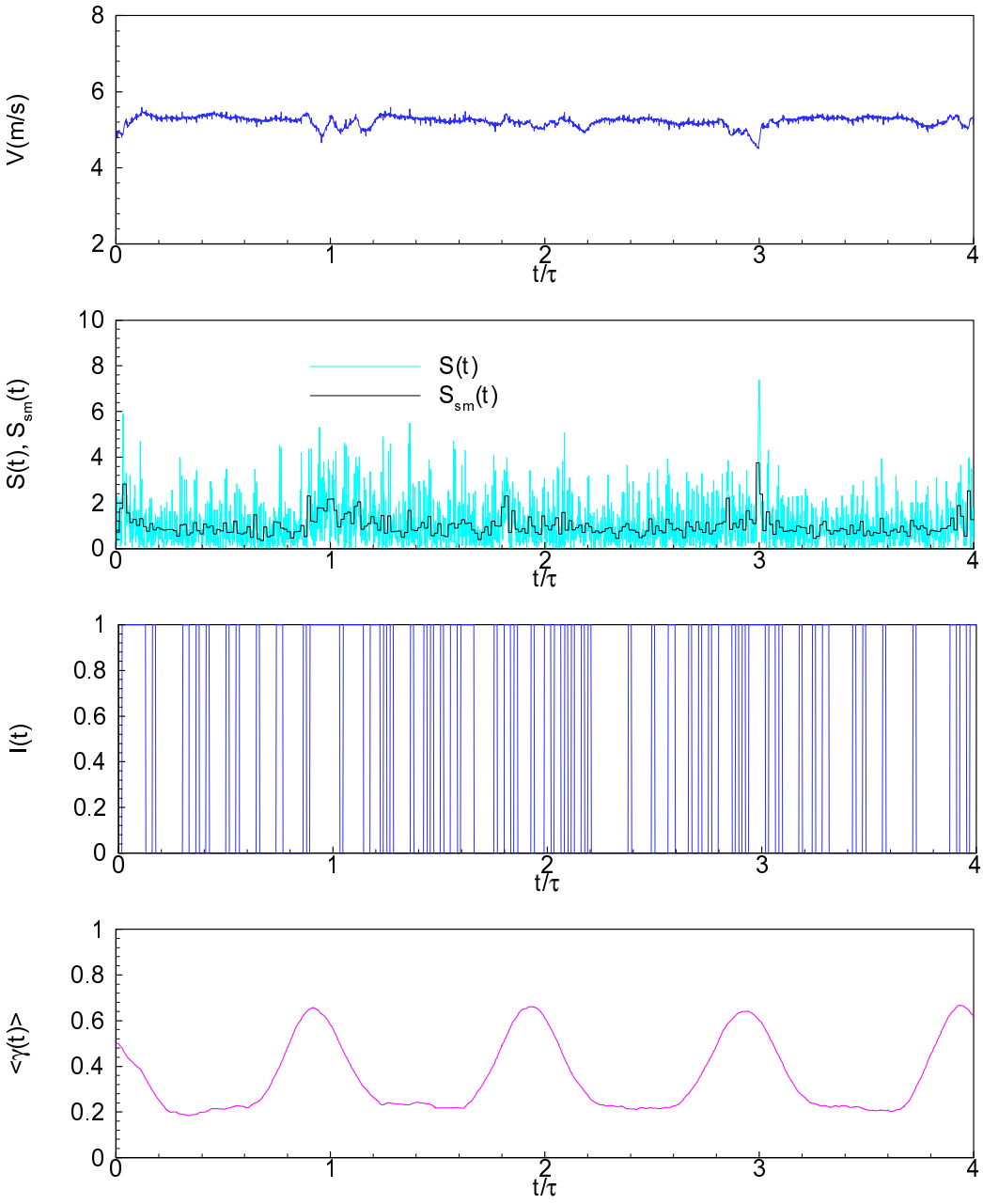

Figure 13.5. Calculation of ensemble-averaged intermittency function from instantaneous velocities for Ω=1.725 at y=0.720 mm

13.4 Ensemble-Averaged Intermittency Distribution

Figure 13.6 presents the temporal-spatial contours of the ensemble-averaged intermittency distribution at three different lateral positions above the blade suction surface, y=1.341 mm, 1.755mm, and 6.10 mm for two reduced frequencies, Ω = 1.59 and Ω=3.18. For better comparison of the effects of the impinging wake frequency, Figure 13.6 exhibits only the first three wakes. In these figures, the wakes with the highly vortical cores display intermittency values close to unity indicating the turbulent character of the boundary layer at the particular instant of time of wake impingement on the surface. Intermittency is approximately equal to zero outside the wake region near the leading edge showing the non-turbulent behavior of the flow.

The wakes represented by narrow green strips pass through the turbine blade channel and periodically switch the boundary layer from laminar to turbulent and vice versa. Upstream of the separation bubble a pre-transitional strip with an ensemble averaged intermittency of $\gamma(t) \approx 0.5$ starting at $s/s_o \approx 0.43$ and ending at $s/s_o \approx 0.52$ separates the attached boundary layer from the bubble leading edge. At s/so≈0.52, the visibility of the wake is vanished due to the interaction with the separation bubble. As figure 5 shows, the separation bubble starts at $s/s_o \approx 0.52$ and extends up to $s/s_o \approx 0.75$, thus occupying more than 24% of the suction surface and forming a massive separation zone. At $s/s_o \approx 0.75$, the intermittency field in Figure 6(a) displays an abrupt change in intermittency level which indicates the start of a re-attachment process. Once the wake passes over the separation zone, its signature re- appears again as spots with higher intermittency level (red) associated with becalmed zones (blue). Increasing Ω to 3.18, Figure 13.6(b) causes an earlier mixing of the impinging wakes which results in widening the areas occupied by the wake vortical core, thus reducing the wake external region. Figure 13.6(b) suggests that further increase of Ω may lead to a complete degeneration of the deterministic periodic wake flow into a stochastic turbulence. Figures 13.6(c) to 13.6(f) display the intermittency distributions at higher normal position from the blade surface. They are quite identical with Figures 13.6(a) and Figure 13.6(b) discussed above.

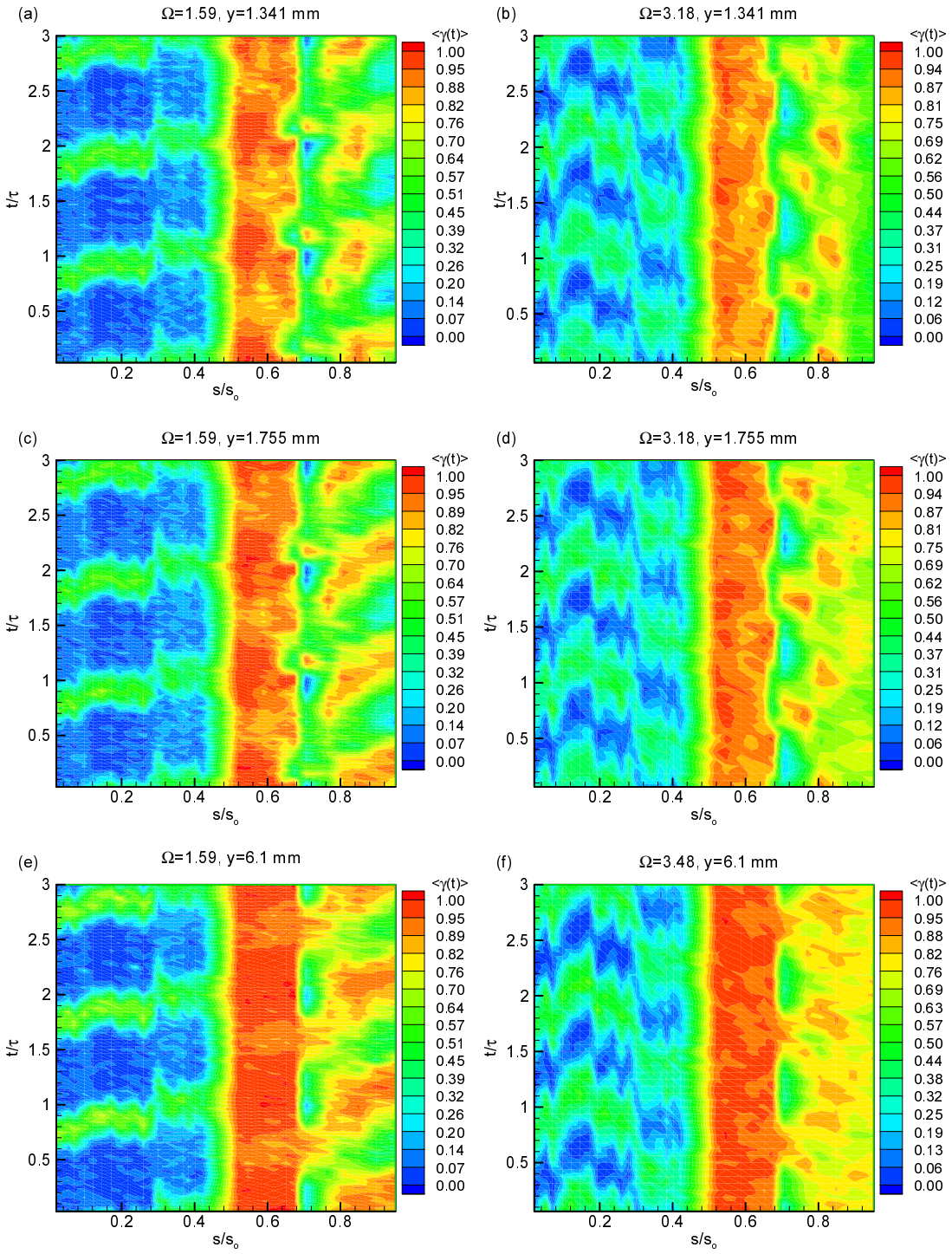

Figure 13.6. Ensemble-averaged intermittency factor in the temporal-spatial domain at different y positions for Ω=1.59 (S_R=160 mm), and Ω=3.18 (S_R=80 mm)

The intermittency distributions in Figure 6 clearly show the unsteady nature of the boundary layer transition. In this form, however, they cannot quantitatively describe the complex unsteady transition, separation and re-attachment process. To establish the basic relations essential for a quantitative description of the unsteady boundary layer transition, we resort to the fundamental study by Schobeiri and his co-workers [4] that deals with the physics of steady and unsteady wake development in a curved environment. The studies clearly show that the turbulence structure of the steady and unsteady wake flow is determined by the wake defect, which is a Gaussian function. Following the above study, we define a dimensionless parameter:

$$\zeta = \frac{tU_w}{b} = \frac{tS_R}{\tau b} = \frac{\xi_2}{b} \; with \quad b = \frac{1}{\sqrt{\pi}} \int_{-\infty}^{+\infty} \Gamma d\xi_2 \tag{13.12}$$

Equation (12.12) relates the wake passing time t with the wake passing velocity in the lateral direction U_w, and the intermittency width b. The latter is directly related to the wake width introduced by Schobeiri and his co-workers [13] and [31]. In an analogous way to find the defect function, we define the relative intermittency, Γ, as:

$$\Gamma = \frac{<\gamma_i(t_i)> - <\gamma_i(t_i)>_{\min}}{<\gamma_i(t_i)>_{\max} - <\gamma_i(t_i)>_{\min}} \tag{13.13}$$

In the above equation, $<\gamma_i(t_i)>$ is the time dependent ensemble-averaged intermittency function, which determines the transitional nature of an unsteady boundary layer. The intermittency $<\gamma_i(t_i)_{max}>$ exhibits the maximum intermittency value inside the wake vortical core. Finally, $<\gamma_i(t_i)_{min}>$ represents the minimum ensemble-averaged intermittency values outside the wake vortical core. Figure 13.7 exhibits the maximum and minimum ensemble-averaged intermittency inside and outside the wake vortical core.

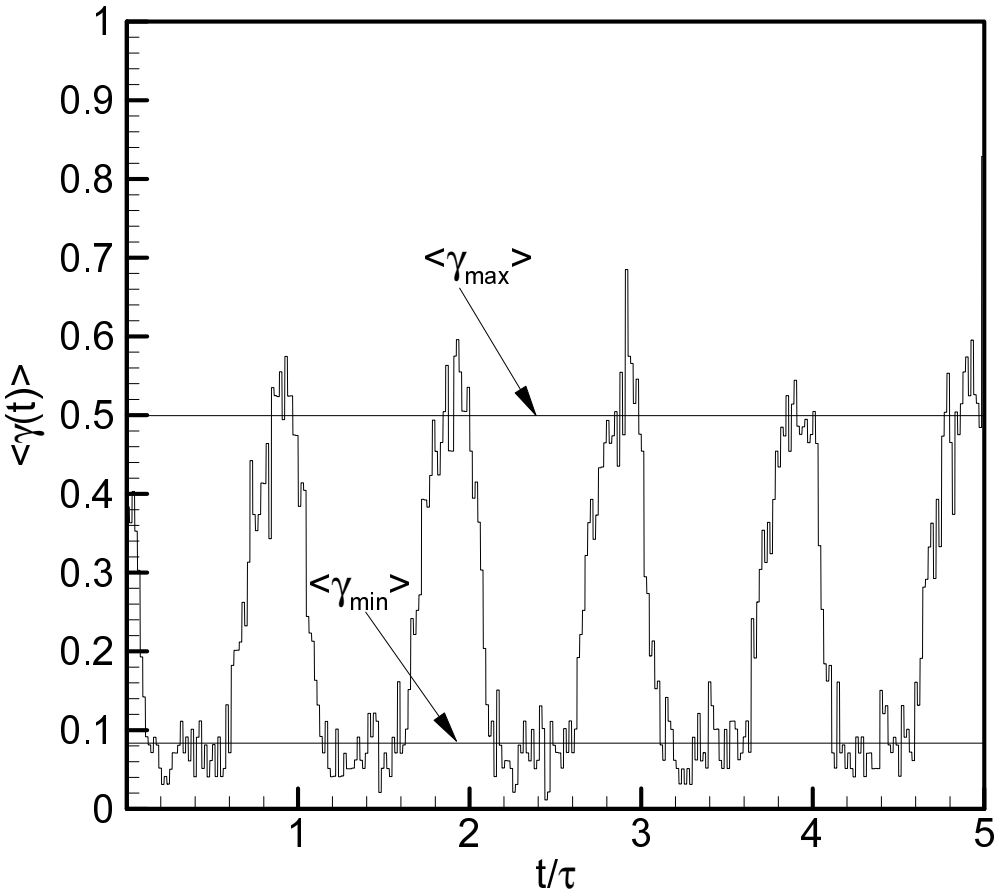

Figure 13.7. Maximum and minimum intermittencies at y=0.1 mm and s/s_o=0.383

A representative relative intermittency function, Γ, is shown in Figure 13.8 (a,b,c,d) for a frequency value of Ω=1.59 at a lateral distances from the blade surface of y =0.858, 0.996, 5.3, and 9.3 mm, with the dimensionless longitudinal distance s/s_o as a parameter. The above distances are representative for intermittency distributions inside, within and outside the separation bubble over the entire suction surface. The symbols represent the experimental data. As seen, for the reduced frequency of Ω=1.59, the measured relative intermittency functions follow very closely a Gaussian distribution, given by:

$$\Gamma = e^{-\zeta^2} \tag{13.14}$$

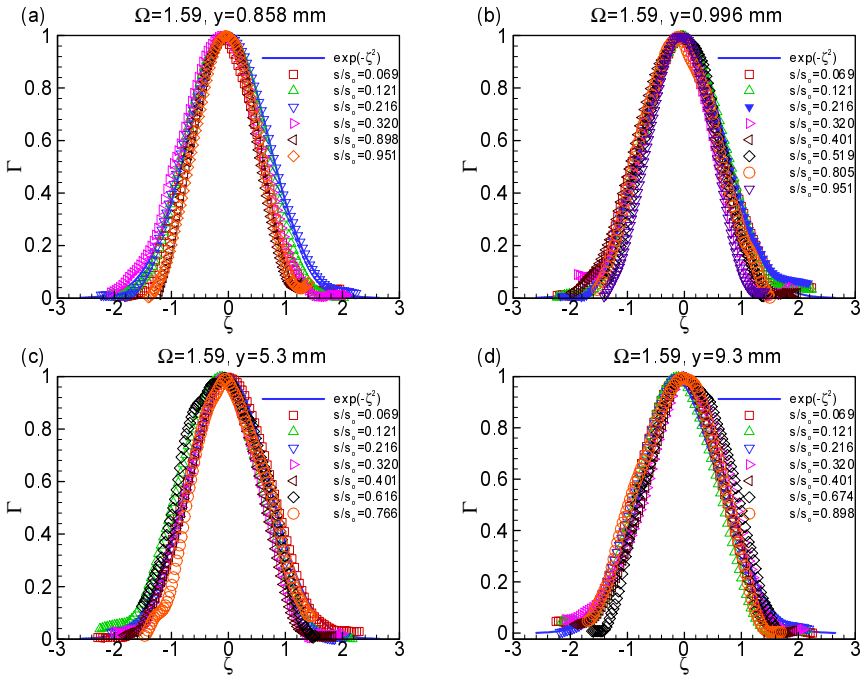

Figure 13.8. Relative intermittency as a function of s/s_o for unsteady frequency of Ω=1.59 (S_R=160 mm) at (a) y=0.858 mm, (b) y=0.996 mm, (c) y=5.3 mm, and (d) y=9.3 mm at Re=110,000

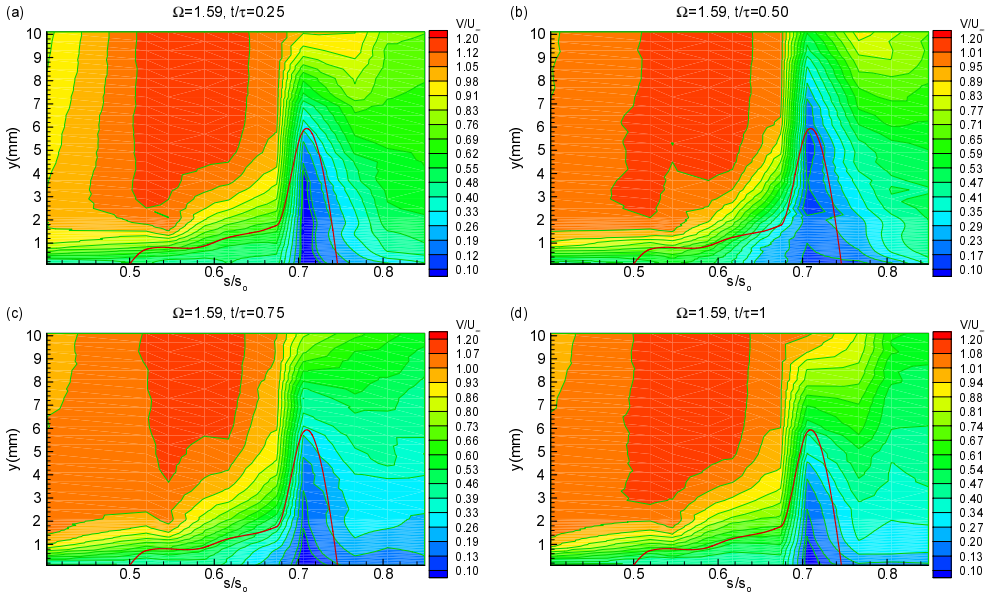

Figure 13.9. Ensemble-averaged velocity contours along the suction surface for different s/s_o with time t/τ as parameter for Ω=1.59 (S_R=160 mm), Re=110,000 (time-averaged separation bubble for Ω=1.59 marked red)

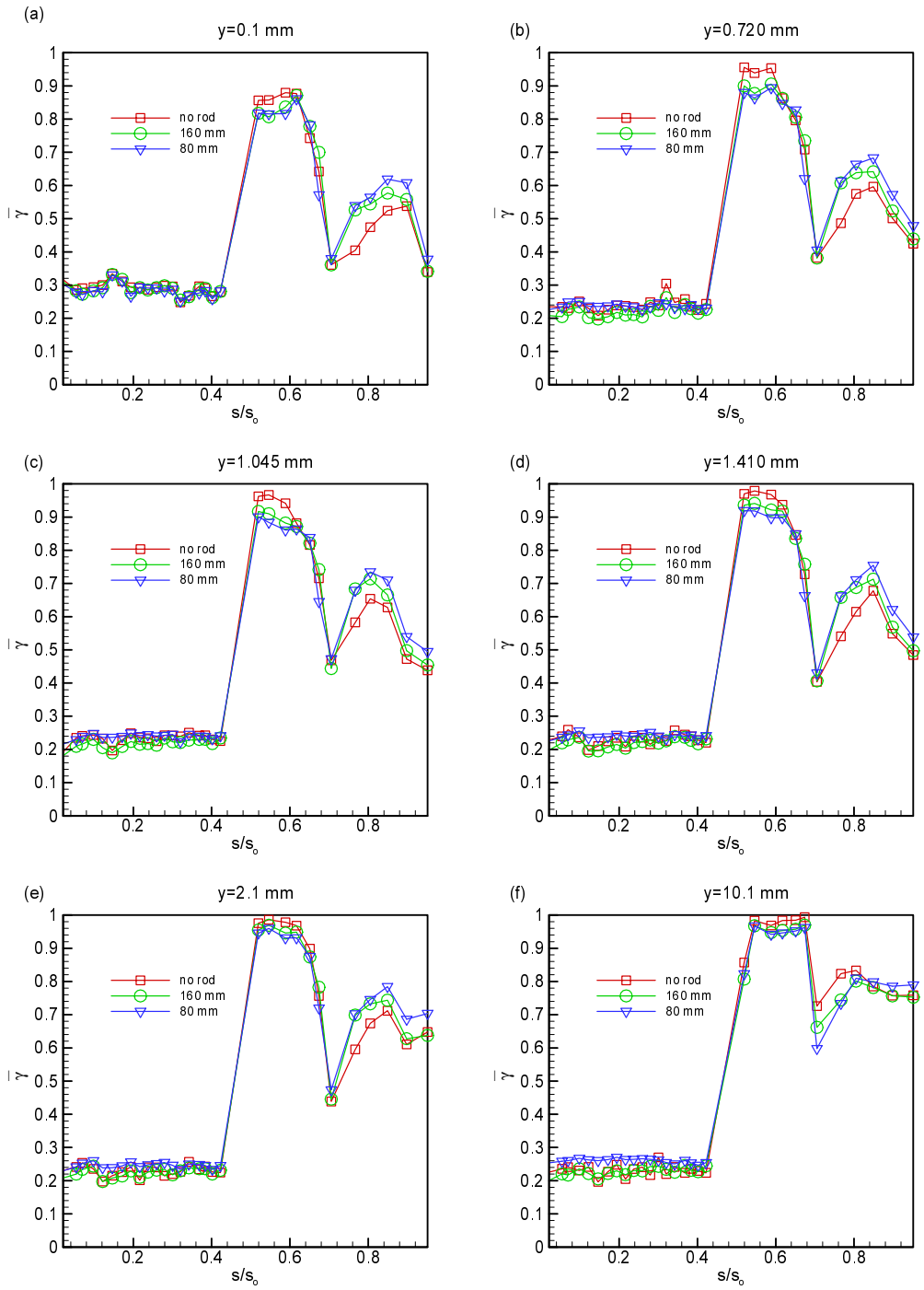

Figure 13.10. Time-averaged intermittency as a function of s/s_o at different lateral positions for steady case Ω=0 (S_R=∞) and unsteady cases Ω=1.59 (S_R=160 mm) and Ω=3.18 (S_R=80 mm) at Re=110,000

with ζ as the non-dimensionalized lateral length scale defined in Eq. (13.12). The slight deviation within and after the separation zone is due to a difficulty associated with capturing the maximum and minimum intermittencies. Using Eq. (13.14) as a generally valid intermittency relationship for unsteady wake flows, the intermittency function $<\gamma_i(t_i)>$ is completely determined if additional information about the intermittency functions $<\gamma_i(t_i)_{max}>$ and $<\gamma_i(t_i)_{min}>$ are available.

The change of the intermittency state is reflected in Figure 13.9, which was extensively discussed in [27]. Figure 13.10 shows the time-averaged intermittency distribution for one steady or no rod case and two unsteady cases on the suction surface, as a function of s/s_o at different normal positions from the blade. Upstream of the leading edge of the separation bubble, the time averaged intermittency is determined by the laminar nature of the boundary layer, which exerts a strong damping effect on the impinging wake fluctuations as extensively discussed in [27]. Approaching the bubble leading edge a steep increase in intermittency indicate a strong turbulent fluctuation within the separation bubble. This exactly corresponds to the findings plotted in Figure 13.5. Close to the wall (y = 0. 1, 0. 720) the intermittency peak is embedded in the separation bubble as shown in Figure 13.10. Moving toward shear layer causes an increases the value of the peak intermittency. At $s/s_o = 0.705$, where the separation bubble height reaches its maximum, the intermittency approaches its minimum and increases again to reach the second maximum.

The distribution of $<\gamma_i(t_i)_{max}>$ and $<\gamma_i(t_i)_{min}>$ in the streamwise direction are plotted in Figure 13.11 for Ω values of 1.59 and 3.18 on the suction surface. The distribution of $<\gamma_i(t_i)_{max}>$ corresponds to the condition when the wake with its high turbulence intensity core impinges on the plate surface. Once the wake has passed over the surface, the same streamwise location is exposed to a low turbulence intensity flow regime with an intermittency state of $<\gamma_i(t_i)_{min}>$, where no wake is present. Figure 13.11 displays the striking features of $<\gamma(t)>_{max}$ and $<\gamma(t)>_{min}$. While for zero and moderate pressure gradients, the minimum intermittency $<\gamma_i(t_i)>_{min}$ distribution reveals a certain similarity to the one described by the Emmons-Narasimha transition model [67], the present LPT-flow case with a strong negative pressure gradient associated with separation, $<\gamma_i(t_i)>_{min}$ exhibits a

remarkably different course that occurs systematically and reproducibly for all Ω-cases at all y-positions over the blade surface. Upstream of the separation bubble, the course of $<\gamma(t)>_{min}$ with the value close to zero indicates a stable *non-turbulent* character of the boundary layer. A sharp increase in intermittency indicates the separation begin shortly before the pressure minimum (Figure 11.1) has been reached. It is followed by a high intermittency region that covers the separation plateau (Figure 11.1) and a steep decrease that is indicative of re-attachment. The streamwise location of the intermittency minimum at $s/s_o \approx 0.7$ coincides with the end of the separation plateau. The following increase in intermittency is due to the steep positive pressure gradient that follows the constant pressure plateau. On the other hand, $<\gamma_i(t_i)>_{max}$ reveals a fundamentally different behavior. As Figure 13.11 shows, the wake flow with an intermittency of $<\gamma_i(t_i)>_{max} \approx 0.8\text{-}0.9$ impinges on the blade surface. By convecting downstream, because of an extremely thin boundary layer, the wake turbulent fluctuations do not undergo a strong damping by the wall shear stress forces and, as was observed in zero and moderate pressure gradient cases reported in [13] and [31].

Utilizing $<\gamma(t)>_{max}$ and $<\gamma(t)>_{min}$ the relative intermittency Γ is found to be described by a Gaussian distribution. This observation is in accord with the findings reported in [13], [31], and very recently in [129] confirming the universal character of Γ. Considering the intermittency results of the current investigations and those reported above, it can be concluded that, in general, $<\gamma_i(t_i)>_{max}$ and $<\gamma_i(t_i)>_{min}$ not only are functions of reduced frequency, but they are also strongly influenced by the pressure gradient, turbulence intensity, Re- and possibly Mach number and surface roughness. This implies that neither $<\gamma_i(t_i)>_{min}$ nor $<\gamma_i(t_i)>_{max}$ have universal character.

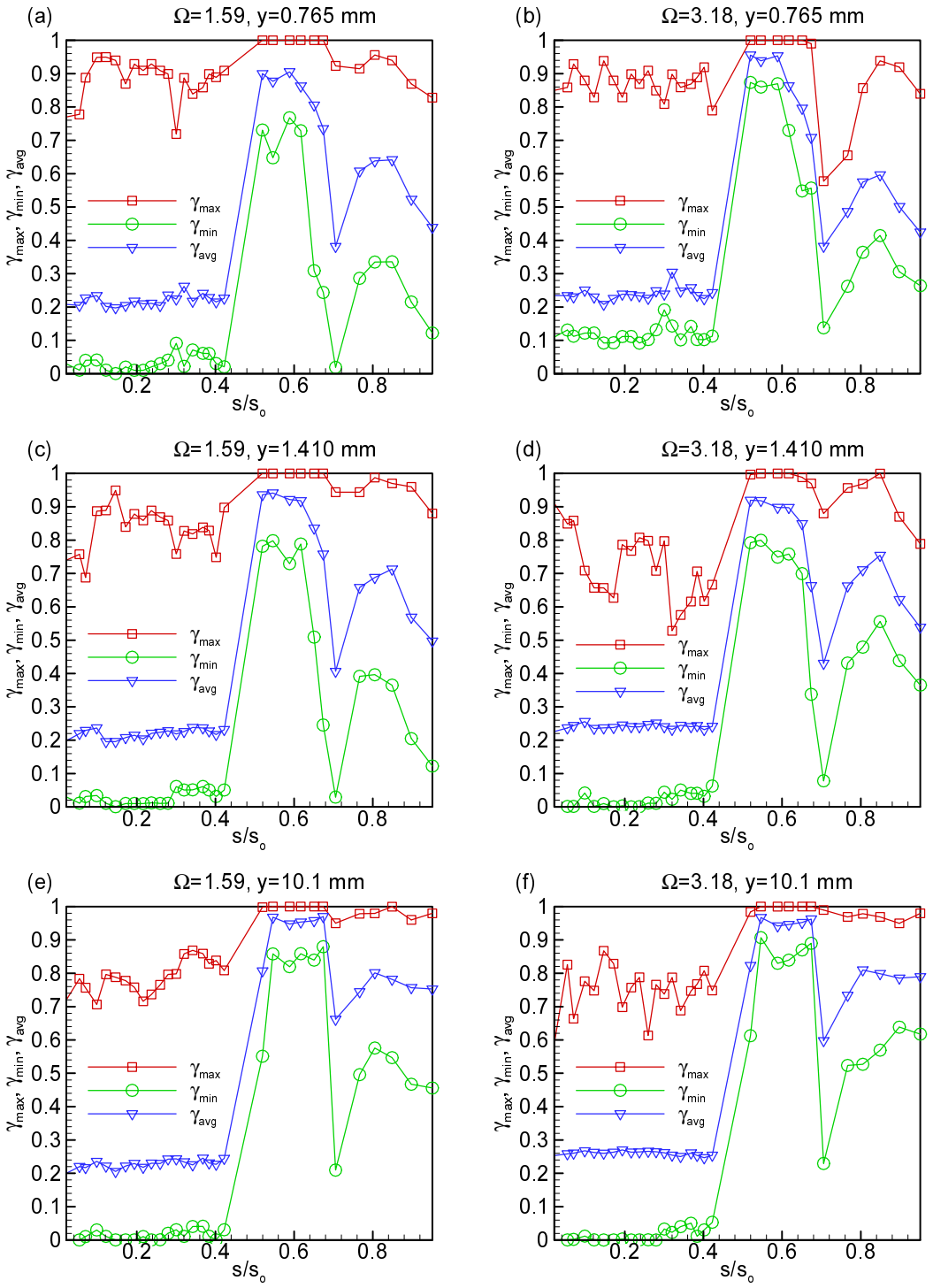

Figure 13.11. Maximum, minimum and time-averaged intermittency as a function of s/s_o at different lateral positions for steady case Ω=0 (S_R=∞) and unsteady cases Ω=1.59 (S_R=160 mm) and Ω=3.18 (S_R=80 mm) at Re=110,000

14. HEAT TRANSFER MEASUREMENTS

In this section, heat transfer experimental data collected from liquid crystal and temperature sensitive paint (TSP) are presented. Liquid crystal technique (LCT) has been used successfully in external aerodynamics to measure the surface temperature of high pressure turbine blades. In recent years, efforts have been made to apply temperature sensitive paint (TSP) technique to turbomachinery components. This study attempts to provide a detailed insight into the heat transfer behavior of a separation zone that is generated as a result of boundary layer development along the suction surface of a highly loaded low pressure turbine (LPT) blade. Particular attention is paid to the application of TSP to a turbine cascade by comparing the results with LCT. Also, the paper experimentally investigates the individual and combined effects of periodic unsteady wake flows and freestream turbulence intensity (Tu) on heat transfer of the separation zone. Heat transfer experiments were carried out at Reynolds number of 110,000, 150,000, and 250,00. For the above Re-numbers, the experimental matrix includes Tus of 1.9%, 3.0%, 8.0%,13.0% and three different unsteady wake frequencies with the steady inlet flow as the reference configuration. Detailed heat transfer measurements are performed with particular attention paid to the heat transfer behavior of the separation zone at different Tus at steady and periodic unsteady flow conditions. The objectives of this study are (a) to quantify the effect of Tu on the aero-thermal behavior of the separation bubble at steady inlet flow condition, (b) to investigate the combined effects of Tu and the unsteady wake flow on the aero-thermal behavior of the separation bubble, and (c) to provide a complete set of heat transfer and aerodynamic data for numerical simulation that incorporates Navier-Stokes and energy equations.

14.1 Heat Transfer Experiments

As indicated previously in Section 5.1.2 and 5.2.3, steady liquid crystal technique and temperature sensitive paint (TSP) technique are used for heat transfer coefficient measurements. This techniques have the advantage of not affecting the turbulence structure

at the surface, as thermocouples or surface mounted hot wire/film probes do. However, their slow response do not allow extracting valuable unsteady information. As a result, in unsteady cases, only time-averaged response can be acquired. The heat transfer coefficients calculated from the experimental data forms a complete set of information along with the aerodynamic data for model development.

14.2 Data Reduction for Heat Transfer Measurements

For the heat transfer measurements a specially designed heat transfer blades are used. Both blades consist of a polyurethane core, two copper connection pieces and are covered with an adhesive sheet, an inconel 600 foil and is described in detailed in Section 5.1.2. The Inconel foil is covered with a self adhesive liquid crystal sheet and temperature sensitive paint and that are used to measure the surface temperature. The heat transfer coefficient on the turbine blade is calculated based on the convective transport of the energy (Hippensteele [130]). The energy losses from the blades are subtracted from the energy input thereby giving the convecting portion of the energy. From this, the heat transfer coefficient on the blade surface is calculated by the expression:

$$h = \frac{Q''_{conv}}{(T - T_{\infty})} \tag{14.1}$$

where T is the temperature from the liquid crystal and TSP, T_{∞} is the free-stream air temperature. Q''_{conv} is the convective portion of the energy equation per unit area and is defined by

$$Q''_{conv} = Q''_{foil} - Q''_{rad} - Q''_{cond} \tag{14.2}$$

where Q''_{foil} is the heat flux of the Inconel foil and Q''_{rad} is the radiation heat flux emitting from the surface of the liquid crystals. These two quantities are given by:

$$Q''_{foil} = \frac{VI}{A_{foil}} \tag{14.3}$$

and

$$Q''_{rad} = \varepsilon\sigma(T^4 - T_\infty^4) \tag{14.4}$$

where R is the resistance of the turbine blade and I is the current passing through it. A_{foil} is the total surface area of the Inconel 600 foil. For the radiation term, ϵ is the emissivity of the liquid crystals and has a value of 0.85 and σ is the Stefan-Boltzmann constant. The conduction losses were calculated and found to be less than 1% of the total power input (Wright [12]) and therefore were neglected.

Detailed surface temperature measurements were taken with TSP on the suction surface. For the validity of the test results, temperature distributions from TSP are compared with thermocouple readings obtained from 6 streamwise locations parallel to the cascade front. As shown in Figure 14.1, TSP results are consistent with thermocouple readings. The heat transfer coefficient distribution on suction and pressure surfaces of the turbine blade is explained in the following sections.

14.3 Local Heat Transfer Coefficient Distribution on Turbine Blade

As in aerodynamic section discussed previously, the steady state case serves as the reference configuration. The matrix for heat transfer experiments includes (a) Reynolds number variation Re = 110,00, 150,000, and 250,00, (b) Free-stream turbulence variation of Tu = 1.9%, 3.0%, 8.0% and 13.0%, and (c) Reduced frequency variation of Ω = 0.0 ($S_R = \infty$), Ω = 1.59 (S_R =160 mm) and Ω =3.18 (S_R = 89 mm). In presenting the heat transfer results, we prefer to use the plain heat transfer coefficient rather than the Nusselt number, which uses thermal conductivity and a constant characteristic length such as the blade chord to form the Nusselt number.

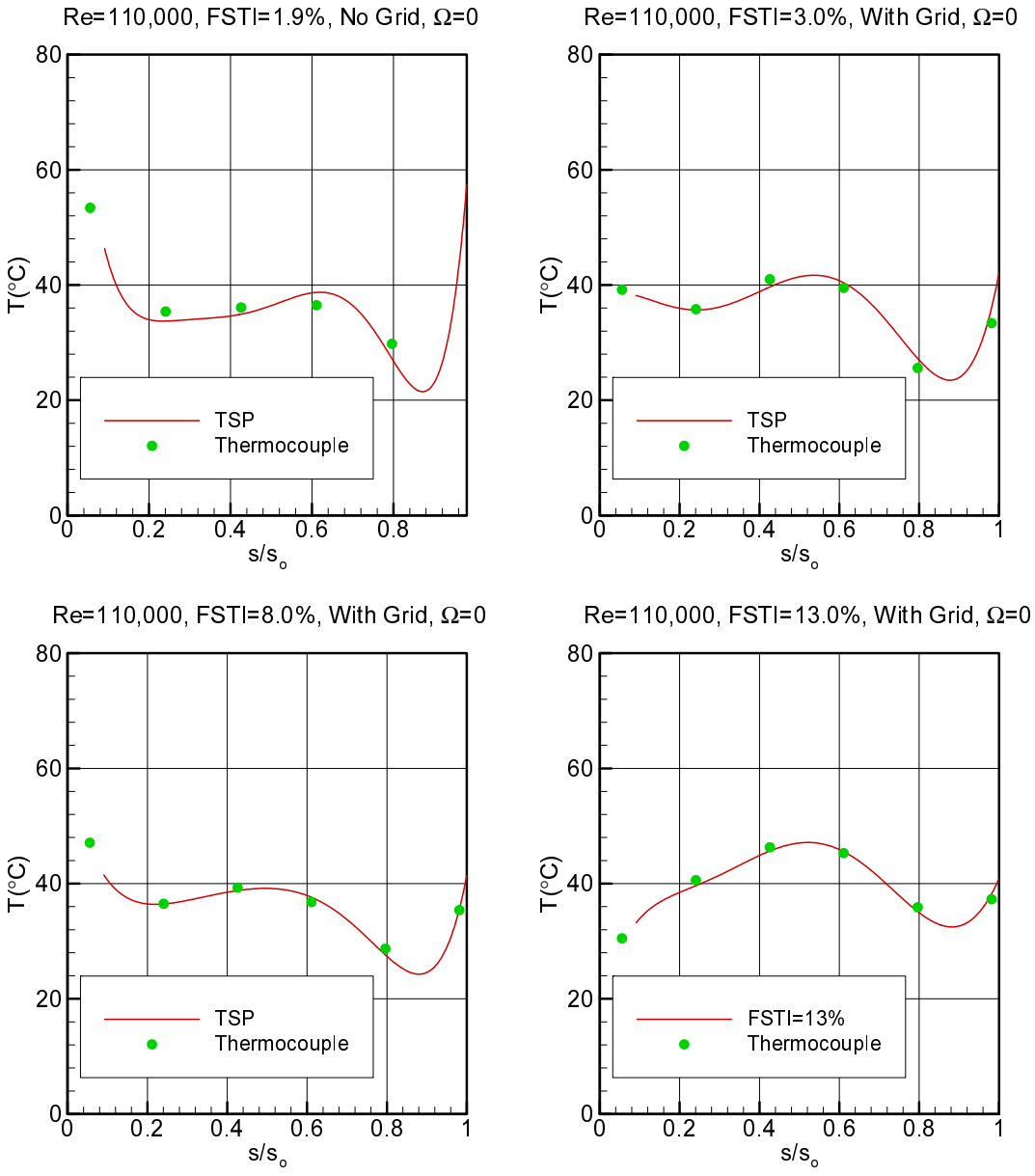

Figure 14.1. Comparison of temperature sensitive paint (TSP) results with thermocouple results for (a) FSTI=1.9% (No Grid), (b) FSTI=3.0% (with grid TG1), (c) FSTI=8.0% (with grid TG2), (b) FSTI=13.0% (with grid TG3) for Ω=0 at Re=110,000

Each figure includes the pressure as well as the suction surface heat transfer coefficient *h* (HTC) as a function of dimensionless surface length s/s_0 for liquid crystal measurements. However, for temperature sensitive paint (TSP) measurements each figure includes only the suction surface heat transfer coefficient *h* (HTC) as a function of dimensionless surface length s/s_0. To be consistent, both liquid crystal and temperature sensitive paint (TSP) results are going to be presented consecutively. While the boundary layer behavior (according to the equation of motion) is completely decoupled from thermal boundary layer behavior, the latter is through the equation of energy directly coupled with the boundary layer aerodynamics. Thus, a detailed description of heat transfer behavior is directly coupled with the aerodynamic results.

14.4 Generic Interpretation of Separation Bubble HTC-Results

To present a generic interpretation of heat transfer results within the separation bubble, we consider Figure 14.2 (details are reported in [131], which includes the pressure distribution (a), the velocity contour (b), the fluctuation contour (c) and a representative HTC-distribution for steady state case (d). Figure 14.2 (a,b,c and d) delivers a coherent picture of separation bubble static, pressure, velocity and turbulence distribution and heat transfer behavior. Figure 14.2 (a) depicts four distinct intervals that mark different events along the suction surface. An initially strong negative pressure gradient starting from the leading edge preserves the stable laminar boundary layer until the pressure minimum at $s/s_0 = 0.494$ has been reached. The laminar boundary layer characterized by the lack of significant lateral turbulence fluctuations[1] is not capable of transferring mass, momentum and energy to the blade surface resulting in an steep drop of HTC from leading edge to $s/s_0 = 0.494$, where the pressure gradient changes the sign, Figure 14.2 (a,b,c, and d). The HTC drops further at a larger slope and assumes a minimum at the start of the separation bubble

[1]Strictly speaking, there is no laminar flow within a turbine component. Comprehensive hot wire measurements by many researchers have repeatedly shown that there are always random fluctuations associated with the velocity distribution. In turbine flow environment the term “non-turbulent” may suitably replace the term “laminar”.

s/s_0 = 0.583. Passing through the pressure minimum, the initially stable laminar (non-turbulent) boundary layer encountersa change in pressure gradient from negative to positive causing it to become unstable and to separate at s/s_0 = 0.583. This point marks the leading edge of the separation bubble, Figure 14.2 (a,b,c,d). From this point on, the turbulence activities outside the bubble continuously increase causing the heat transfer coefficient to raise.

Further increase of HTC beyond s/s_0 = 0.583 occurs at a steep rate until the separation trailing edge at s/s_0 = 0.825 has been reached. The steep increase of HTC within the separation bubble is due to an increased longitudinal and lateral turbulence fluctuations caused by the flow circulation within the bubble. As shown in Figure 14.1(c), the extent of low turbulence envelope is much smaller than the bubble size itself, Figure 14.1(b). This, in accord with the results plotted in Figures 14.2(a) and 14.2(b), implies that the turbulence activity within the bubble is non-uniform and can be subdivided into two distinct zones, Z 1 with lower fluctuation activities that occupies the bubble form the leading edge up to the location, where the bubble lateral extent reaches its maximum height, s/s_0 = 0.695 and Z2 the higher fluctuation zone beyond the maximum height, Figure 14.2(c). It is worth noting that the lateral fluctuation component within the boundary layer cannot be measured using the hot wire techniques. Measuring the lateral component requires a cross-wire, whose dimension is, dependent upon the streamwise location under investigation, can be much larger than the boundary layer. However, extensive experimental and theoretical investigations in [122] shows a pattern similarity between the longitudinal and the lateral turbulence components and a direct correlation between them derived on inductive basis. Thus, the longitudinal turbulence rms shown in Figures 14.2(b) and 14.2(c) are parts of the Reynolds stress tensor that includes the lateral component, which is primarily responsible for lateral exchange of mass, momentum and energy to the blade surface determining the HTC-distribution.

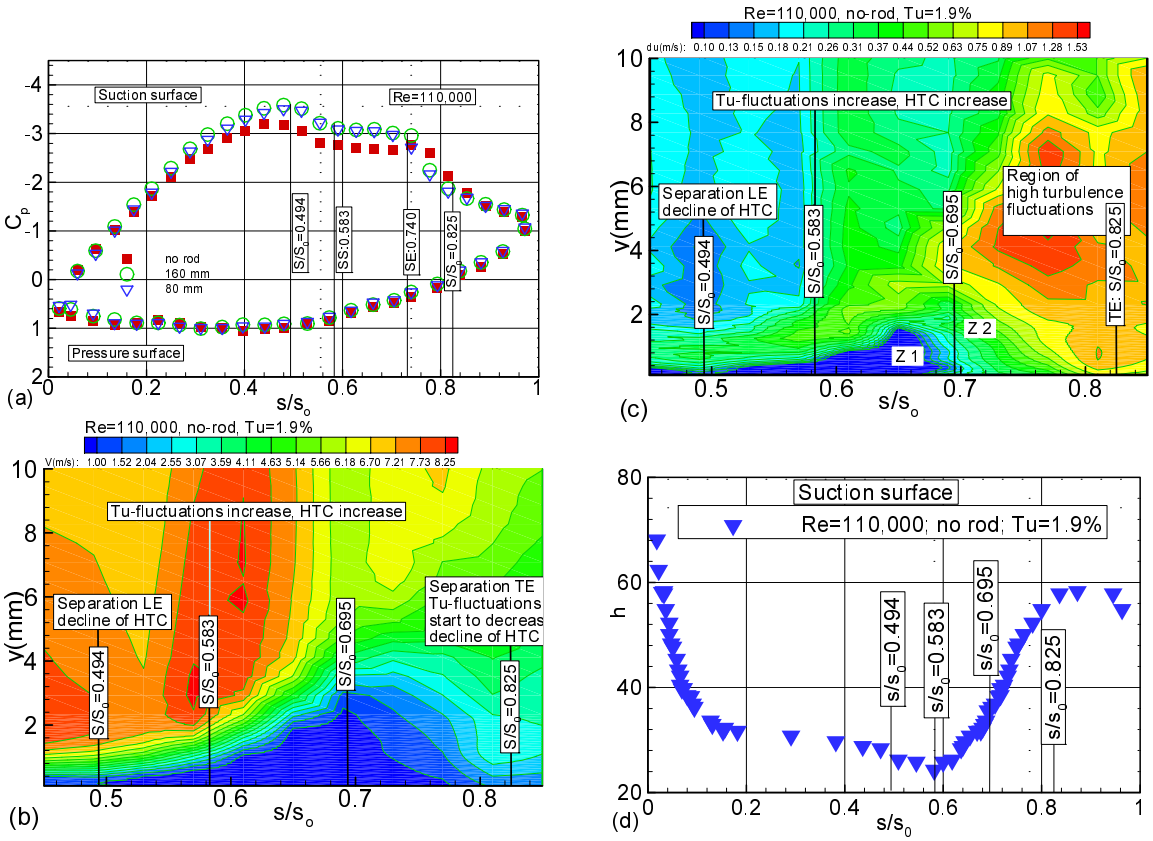

Figure 14.2. Composite picture of interaction between pressure gradient, velocity, turbulence fluctuation and heat transfer

14.5 Steady Inlet Flow Condition, Variation of Re-Number at Constant Tu_{in}

Starting with steady state at Tu = 1.9, Figures 14.3 (LCT) and 14.4 (TSP), the heat transfer coefficient is plotted along the blade surface, where the Reynold number assumes values of Re = 100,00, 150,00, and 250,000.Figure 14.3 (a to d) depicts the HTC along the suction ($s/s_0 > 0$) and pressure surface ($s/s_0 < 0$). However Figure 14.4 (a to d) depicts only HTC along the suction ($s/s_0 > 0$). The steady state case, Figures 13.3(a) and 13.4 (a) show a systematic increase of HTC by increasing the Reynolds number. On the suction side, the position s/s_0 = 0.494 for all three Re-numbers indicates the location of the minimum pressure and s/s_0 = 0.583 the start of the separation bubble. The course of HTC follows the generic discussion presented above making additional discussion unnecessary.

On the pressure surface, $s/s_0 < 0$, Figure 14.3(a) reveals a qualitatively different picture. At Re= 110,000 and for Tu =1.9% the heat transfer coefficient first drops sharply

due to the governing laminar (non-turbulent) boundary layer and reaches a minimum at s/s_0 = 0.143 that signifies the start of the transition region. During the transition process characterized by intermittent changes of flow pattern from laminar to turbulent and vice versa, the random fluctuations in longitudinal as well as lateral directions continuously increase leading to a lateral exchange of mass, momentum and energy with the boundary layer thus increasing the HTC. For Re =110,000, the *first* transition process seems to complete at s/s_0 = 0.34. By passing the first transition region, a process of *relaxation* takes place, where the growth of turbulence fluctuation first decreases to arrive at a second minimum signifying the begin of the *second transition* process. This indicates the transitional nature of turbine boundary layer flow. Increasing Re-number shifts the first transition start upstream and systematically increases the HTC. Pronounced increase in HTC is observed at higher Reynold number as Figure 14.3 (a) shows, where the position of start and end of the first transition and the start of the second transition are marked.

Applying the turbulence generator screen TG1, Figures 14.3(b) and 14.4(b), has increased the free-stream turbulence intensity to Tu = 3.0%. As a consequence, a pronounced exchange of mass, momentum and energy between the flow and the blade surface has taken place resulting in a substantial increase in HTC. For both the suction and pressure surfaces a systematic enhancement of HTC is shown in Figures 14.3(b) and 14.4(b). While on the suction surface the start of the separation bubble has not noticeably altered, on the pressure surface the transition length has substantially decreased. Here as in Figures 14.3(a) and 14.4(a), a systematic increase of the HTC with increasing the Reynolds number is unmistakably discernible. At all three Reynolds cases with Tu =3.0% the heat transfer coefficient (HTC)first drops sharply due to the governing non-turbulent boundary layer and reaches a minimum at s/s_0 = 0.12 followed by a large transitional zone that extends up to s/s_0 =0.75. It is apparent that the higher turbulence activities caused by a free-stream turbulence of 3% washed out the first transition.

Subsequent installation of the second and third screens TG2 and TG3 has increased the turbulence intensity to 8% and 13% respectively. As shown in Figures 14.3(c) and 14.4(c), the combination of higher Reynolds number and turbulence intensity has

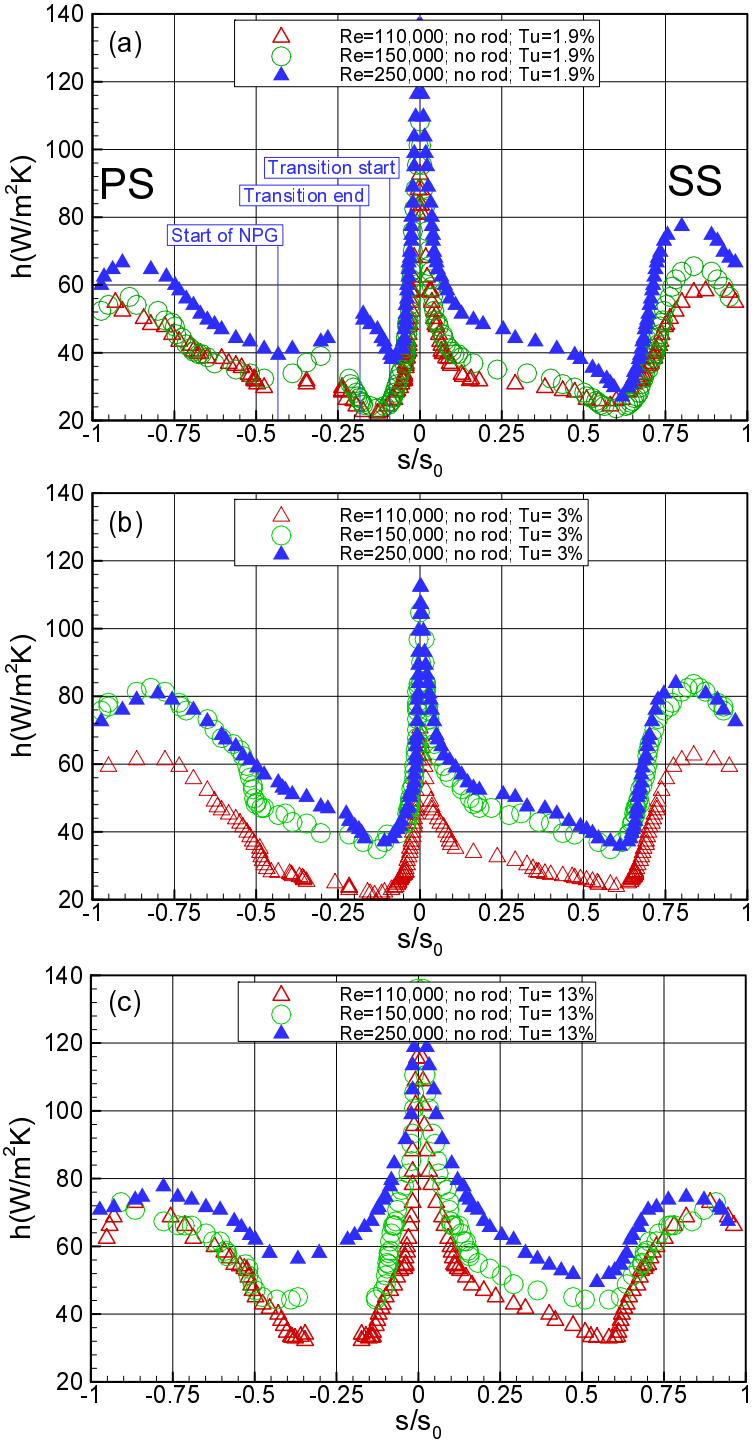

Figure 14.3. Effect of Reynolds number on heat transfer coefficient, (a) Tu = 1.9%, (b) Tu = 3.0%, and (c) Tu = 13% for steady inlet flow condition (using LCT)

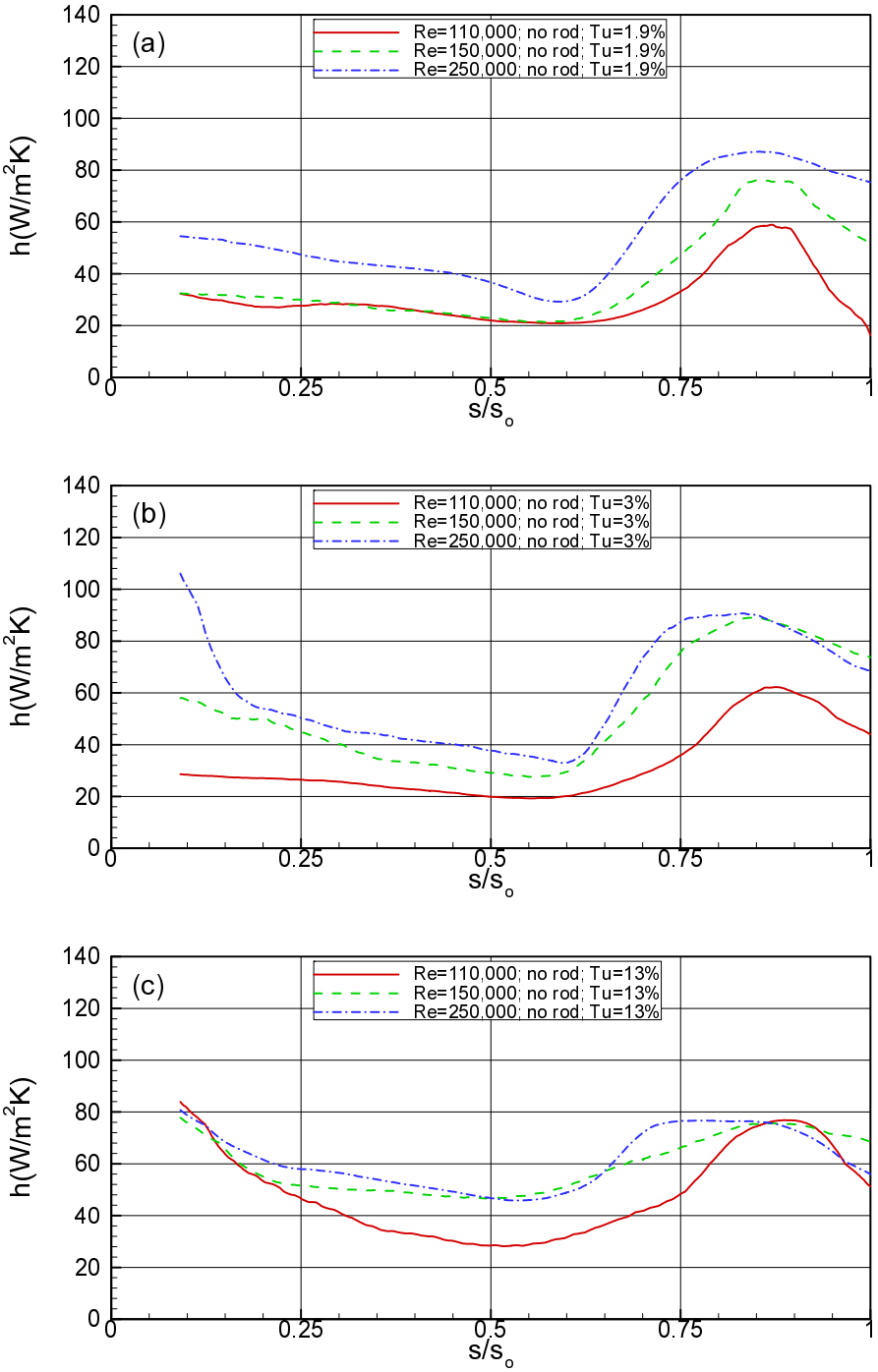

Figure 14.4. Effect of Reynolds number on heat transfer coefficient, (a) Tu = 1.9%, (b) Tu = 3.0%, and (c) Tu = 13% for steady inlet flow condition (using TSP)

substantially increased the HTC. On the pressure surface, Figures 14.3(c) and 14.4(c), the HTC-distributions exhibits for all three Re-numbers a pattern indicative of a systematic increase with higher Re-number is unmistakably recognizable. As shown in Figures 14.3 and 14.4 liquid crystal and temperature sensitive paint results are consistent and showing similar distributions, but there is only 5-10% difference in HTC magnitude.

14.6 Periodic Unsteady Inlet Flow Condition, Variation of Re-Number at Constant Tu_{in}

Periodic unsteady inlet flow conditions for two different reduced frequencies are established by successively attaching rods with spacings, S_R = 160 mm and S_R = 80 mm with the corresponding reduced frequencies of Ω = 1.59 and 3.18, Table 4.1. Keeping the reduced frequency and the turbulence intensity the same, heat transfer measurements were carried out for Re= 110,000, 150,000, and 250,000.

14.6.1 HTC-Results for Ω = 1.59

Figure 14.5(a) and 14.6(a) show the HTC -distribution along the suction ($s/s_0 > 0$) for a reduced frequency Ω = 1.59 (S_R = 160 mm) and Tu = 1.9%, where the Reynold number assumes values of Re = 100,00, 150,00, and 250,000. For Re = 100,00, 150,000 the HTC-distributions does not reveal a substantial increase. This is due to the fact that wakes generated by the translating rods are far apart from each other. Consequently, the turbulence activities of their vortical cores are not mutually interacting and therefore unable to substantially affect the total turbulence picture of the flow leading to almost the same HTC-picture as in Figure 14.3(a) and 14.4(a).

Keeping the reduced frequency Ω = 1.59 (S_R = 160 mm), Figure 14.5(b) and 14.6(b), and increasing the turbulence intensity to Tu = 3% has brought only a minor increase in HTC for the suction surface compared to Figure 14.5(a) and 14.6(a). In both cases, it seems that the wake unsteadiness is about to submerge in the stochastic high frequency free-stream turbulence generated by grids TG1. On the pressure surface, however, major increase in HTC is clearly visible, where the first transition length almost completely disappeared. Similar HTC-results are presented in Figures 14.5 (c, d) and 14.6 (c,d), where systematic

shift of HTC toward higher values are evidenced for all three Reynolds numbers and the remaining turbulence intensities of Tu=8% and 13%.

14.6.2 HTC-Results for $\Omega = 3.18$

Figure 14.7(a to d) presents the HTC on suction and pressure surface at Re = 100,000, 150,000, and 250,000, Tu = 1.9%, 3%, 8%, and 13% for a reduced frequency of $\Omega = 3.18$. However, Figure 14.8(a to d) shows only the HTC -distribution along the suction ($s/s_0 > 0$) at Re = 100,000, 150,000, and 250,000, Tu = 1.9%, 3%, 8%, and 13% for a reduced frequency of $\Omega = 3.18$. The HTC-patterns follow closely those shown in Figures 14.5 and 14.6 with a minor increase in HTC. Increasing the reduced frequency by reducing the rod spacing from 160 mm to 80 mm, two objectives were targeted: (a) doubling the unsteady frequency and (b) reducing the distance between the wake by 50%, thereby causing an active mutual interaction and mixing of the wakes. The compounded effects of (a) and (b) superimpose additional turbulence fluctuations on the free-stream turbulence raising the overall fluctuation level, thus, resulting in an increased HTC. On the suction surface, the HTC-distributions pertaining to Re = 110,000 and 150,000 almost coincide, while the larger Re = 250,000 reveals substantially higher values. This implies that, keeping Ω and Tu constant, a substantial HTC can be achieved by substantially increasing the Re-number. In all three Tu-cases, it seems that the wake unsteadiness has submerged into the stochastic high frequency free-stream turbulence generated by grids TG2 and TG3. On the pressure surface, major increase in HTC is clearly visible, where the transition length almost completely disappears.

14.7 Effect of Unsteady Wake Frequency Ω on Heat Transfer Coefficient

The effect of unsteady wake frequency on HTC are implicitly contained in Figures 14.3 to 14.8. However, from aerodynamics-heat transfer interaction point of view, it is of interest to present it explicitly. Figures 14.9 to 14.12 present the results for Re = 110,000 and 250,000 at constant Tu, where the reduced frequency Ω is varied from $\Omega = 0.0$ ($S_R=\infty$) to $\Omega = 3.18$ (S_R=80 mm). The case with Re=150,000 is very much similar to the case Re=

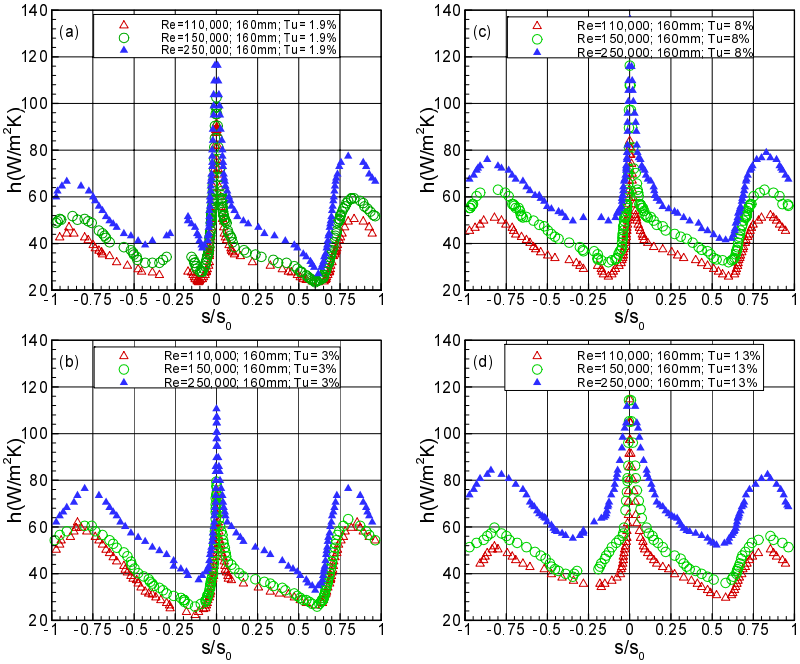

Figure 14.5. Effect of Reynolds number on heat transfer coefficient, (a) Tu=1.9%, (b) Tu=3.0%, (c) Tu=8%, and (d) Tu=13% for unsteady inlet flow condition with Ω = 1.59 (S_R =160 mm),(using LCT)

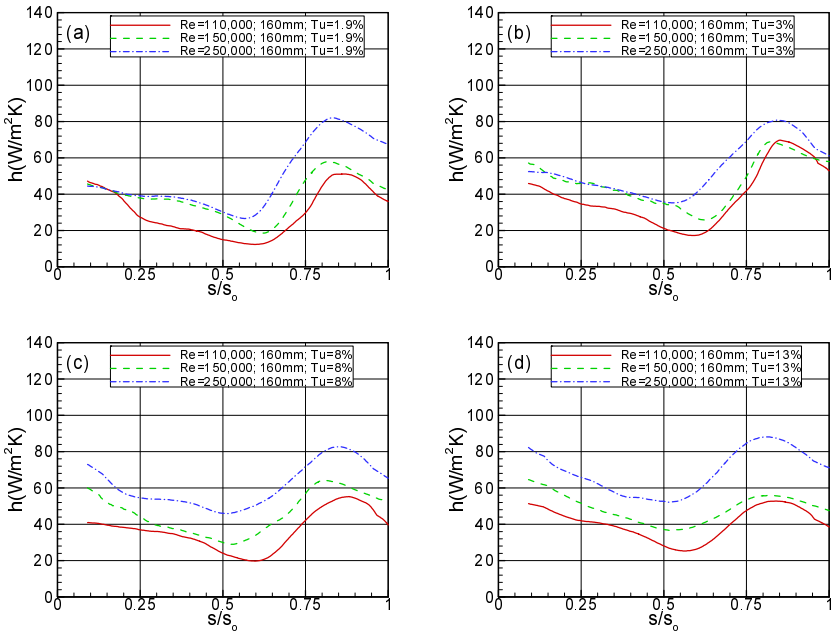

Figure 14.6. Effect of Reynolds number on heat transfer coefficient, (a) Tu=1.9%, (b) Tu=3.0%, (c) Tu=8%, and (d) Tu=13% for unsteady inlet flow condition with Ω = 1.59 (S_R =160 mm),(using TSP)

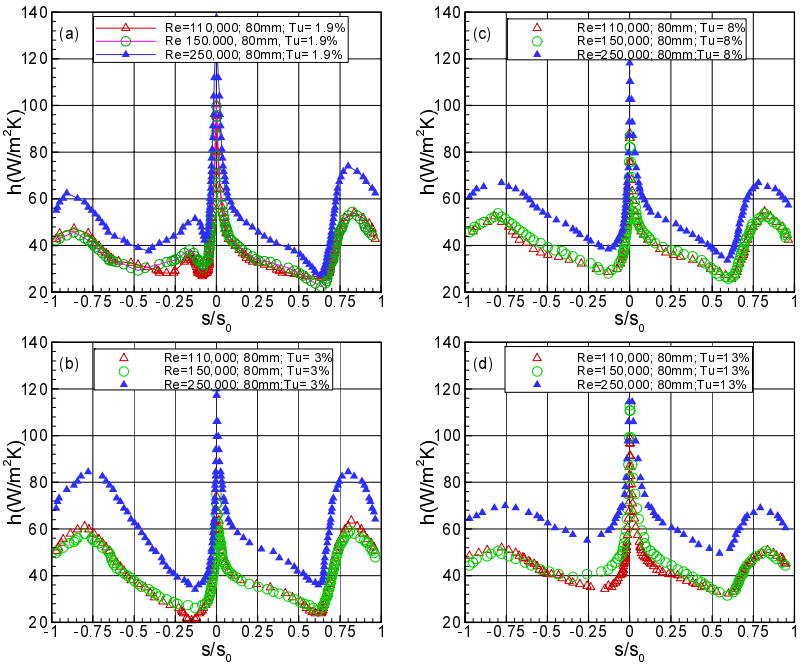

Figure 14.7. Effect of Reynolds number on heat transfer coefficient, (a) Tu=1.9%, (b) Tu=3.0%, (c) Tu=8%, and (d) Tu=13% for unsteady inlet flow condition with Ω = 3.18 (S_R =80.0 mm),(using LCT)

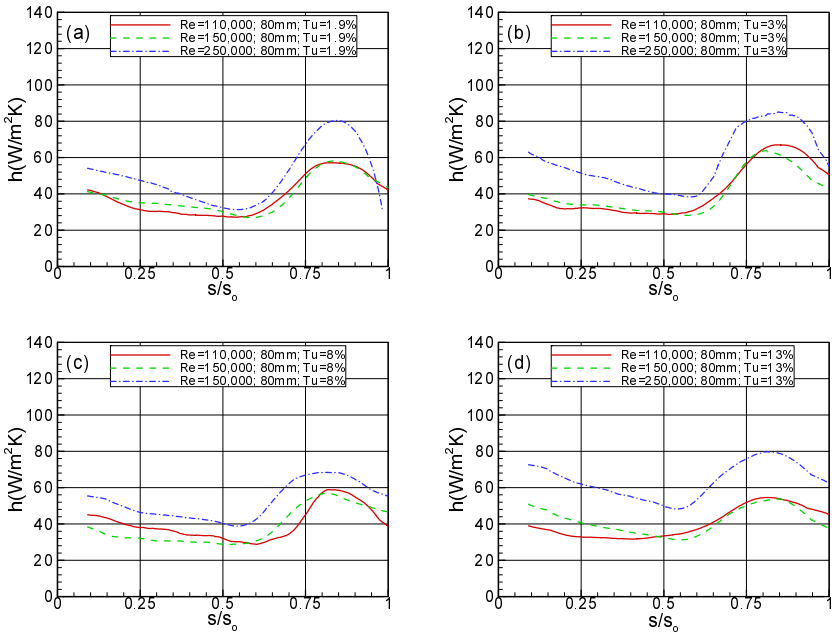

Figure 14.8. Effect of Reynolds number on heat transfer coefficient, (a) Tu=1.9%, (b) Tu=3.0%, (c) Tu=8%, and (d) Tu=13% for unsteady inlet flow condition with Ω = 3.18 (S_R =80.0 mm),(using TSP)

110,000, makes its presentation unnecessary. Figures 14.9(a) and 14.10(a) present the HTC-distribution for Re = 110,000 and Tu = 1.9% with the reduced frequency as a parameter. On the suction surface only a marginal changes in HTC are depicted. On the pressure surface, however, noticeable changes are observed within the transitional region, where the transition star moves t upstream. Increasing the turbulence intensity to TU=3%, Figures 14.9(b) and 14.10(b), initiate the process of submerging the wake into the free-stream turbulence. Little changes are observed on the suction surface, on the pressure surface, however, the first transition region is washed out due to the combined effects of turbulence intensity and unsteadiness, which is in accord with the results presented in Figures 14.3(b) and 14.4(b). A seemingly different HTC- pattern emerges, when the turbulence intensity is increased. As shown in Figures 14.9(c, d) and 14.10(c, d) with Tu = 8% and 13%, respectively, the HTC-distributions for both unsteady cases with Ω = 1.59 and 3.18 are almost identical, the steady state case (no rod), however, shows towards the second half of the blade increasingly higher HTC-values. This, at first glance appears to be incompatible with the widespread notion that the unsteady wakes generally contribute to intensifying the turbulence activities, thus increasing the HTC. However, expediting the turbulence fluctuations for steady and unsteady cases shows that the calming effect discussed in aerodynamics section is responsible for calming the turbulence activities, thus reducing the HTC. Similar HTC-distribution pattern is revealed for Re=250,000 shown in Figures 14.11(a, b, c, and d) and 14.12(a, b, c, and d).

14.8 Comparison of TSP with Thermocouples and LCT

To determine the distribution of temperature and local heat transfer coefficient on a heated surface exposed to cooling air, thermocouples, temperature sensitive paint (TSP) and thermochromic liquid crystals were used. Figures 14.13(a) and 14.13(b) show the temperature and HTC -distribution along the suction ($s/s_0 > 0$) for a reduced frequency Ω = 3.18 (S_R = 80 mm) and Tu = 1.9%, where the Reynold number assumes value of Re = 250,000. For the validity of the test results, temperature distributions from TSP are compared with thermocouple readings obtained from 6 streamwise locations along the

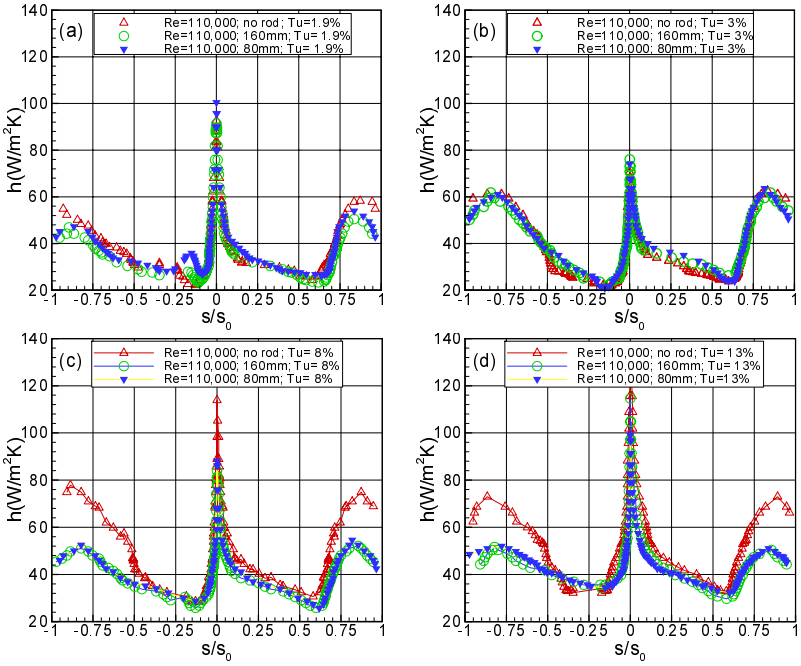

Figure 14.9. Effect of unsteady wake frequency on heat transfer coefficient, (a) Tu=1.9%, (b) Tu=3.0%, (c) Tu=8%, and (d) Tu=13% for Ω = 0.0, 1.59, and 3.18 for Re= 110,000(using LCT)

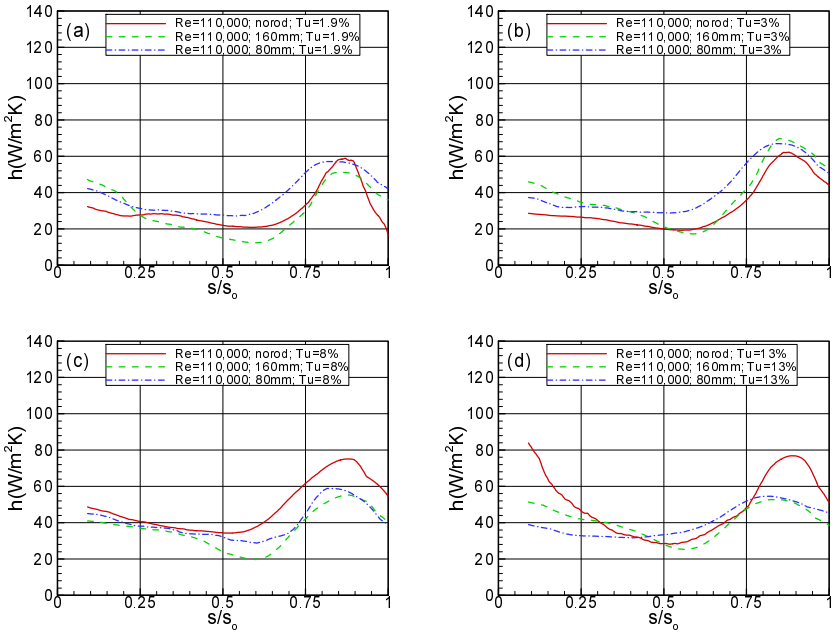

Figure 14.10. Effect of unsteady wake frequency on heat transfer coefficient, (a) Tu=1.9%, (b) Tu=3.0%, (c) Tu=8%, and (d) Tu=13% for Ω = 0.0, 1.59, and 3.18 for Re= 110,000(using TSP)

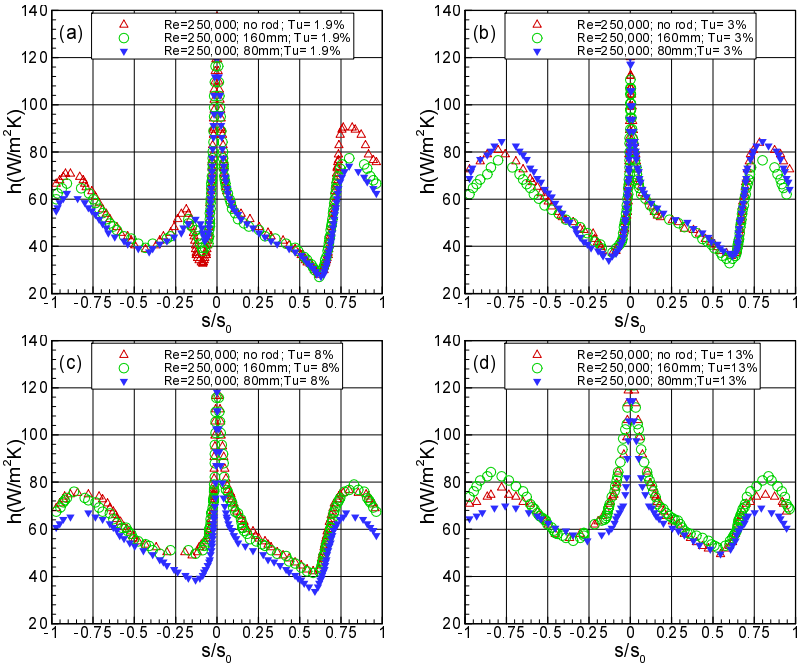

Figure 14.11. Effect of unsteady wake frequency on heat transfer coefficient, (a) Tu=1.9%, (b) Tu=3.0%, (c) Tu=8%, and (d) Tu=13% for Ω = 0.0, 1.59, and 3.18 for Re= 250,000(using LCT)

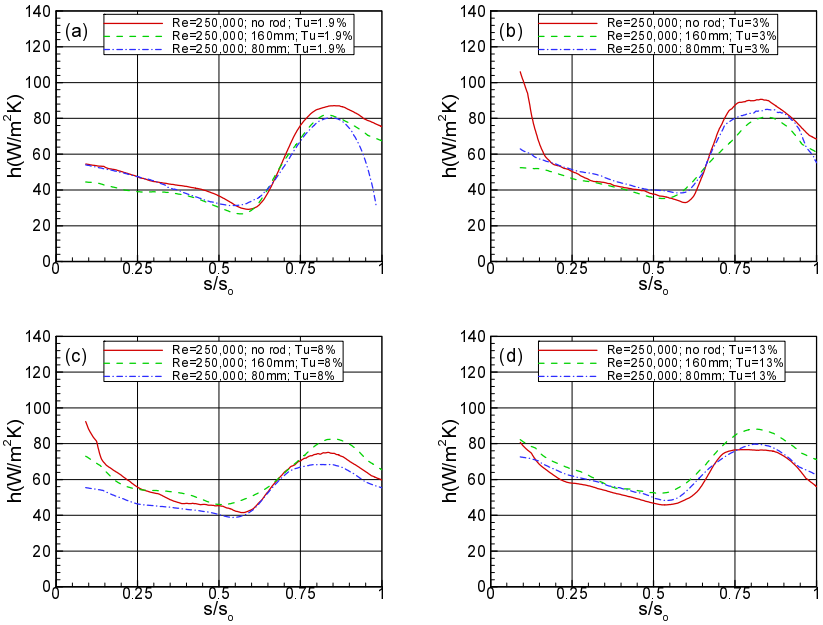

Figure 14.12. Effect of unsteady wake frequency on heat transfer coefficient, (a) Tu=1.9%, (b) Tu=3.0%, (c) Tu=8%, and (d) Tu=13% for Ω = 0.0, 1.59, and 3.18 for Re = 250,000, (using TSP)

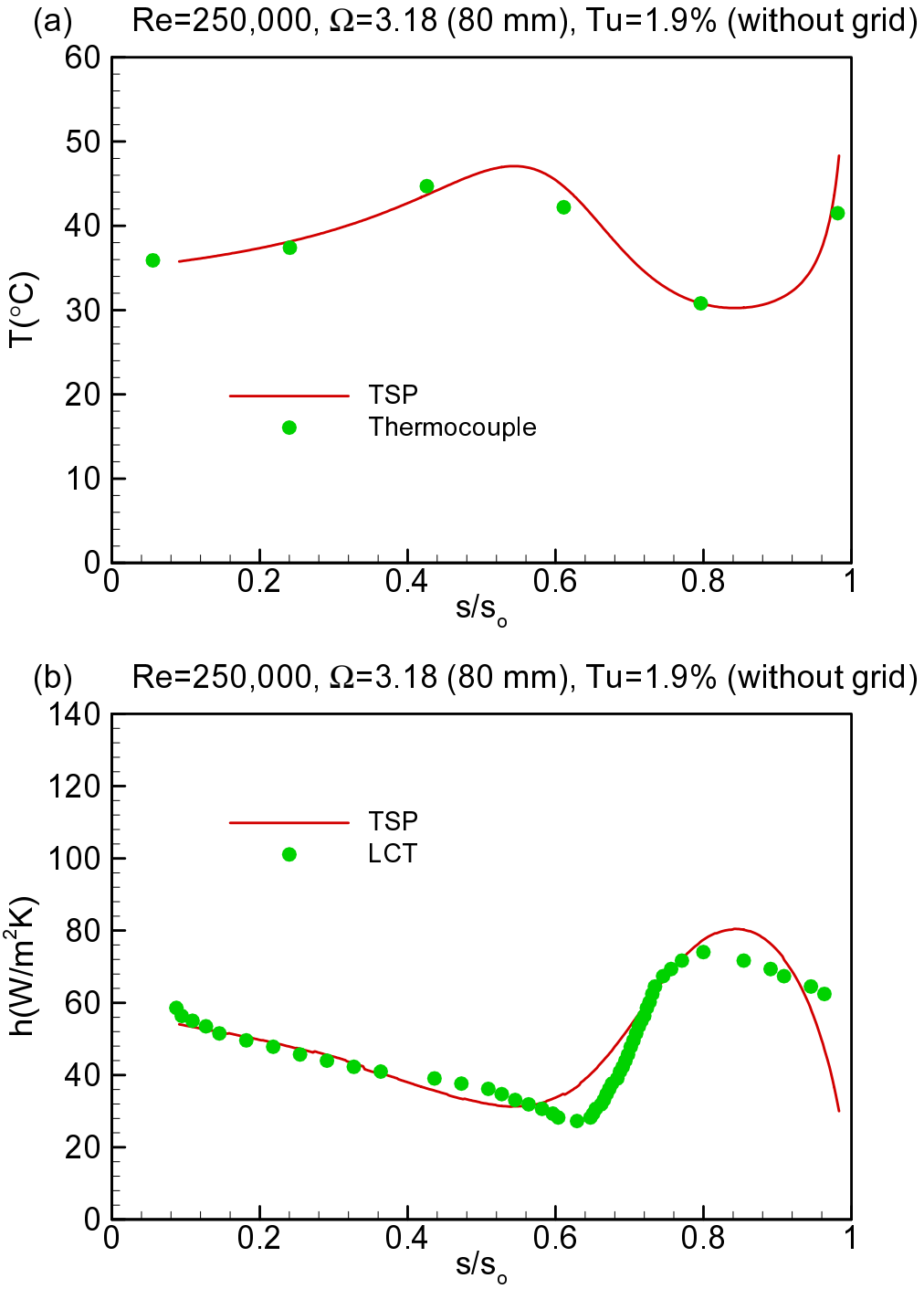

Figure 14.13. Comparison of (a) temperature sensitive paint (TSP) results with thermocouple results, (b) temperature sensitive paint (TSP) results with liquid crystal results for Ω=3.18 at Re=250,000

blade. As shown in Figure 14.13 (a), TSP results are consistent with thermocouple readings. Thermocouples provides low-resolution compared to TSP for temperature measurements. Steady liquid crystal technique and temperature sensitive paint (TSP) techniques have the advantage of not affecting the turbulence structure at the surface, as thermocouples or surface mounted hot wire/film probes do. However, their slow response do not allow extracting valuable unsteady information. As a result, in unsteady cases, only time-averaged response can be acquired. As shown in Figures 14.13 (b) liquid crystal and temperature sensitive paint results are consistent and showing similar distributions, with only 5-10% difference in HTC magnitude. Yellow band tracking liquid crystal measurement technique offer the opportunity for precise temperature and local heat transfer measurements with low spatial resolutions. TSP measurements compare to thermocouple and liquid crystal measurements have a better spatial resolution and decreased data acquisition time with precise temperature and local heat transfer measurements.

15. CONCLUSIONS

A detailed aerodynamic and heat transfer experimental study on the behavior of the separation bubble along the suction surface of a highly loaded LPT blade under combined effects of periodic unsteady wake flows and free-stream turbulence intensity was presented. Varying the turbulence intensity levels, one steady and two different unsteady inlet wake flow conditions with the corresponding passing frequencies, the wake velocity and the turbulence intensities were investigated by utilizing a large-scale, subsonic research facility. Periodic unsteady wake flow was established by translational motion of two parallel moving timing belts on which cylindrical rods are attached. While for the aerodynamic study a representative Reynolds number of Re = 110,000 was applied, for heat transfer investigations the Reynold number was varied as Re = 110,000, 150,000, and 250,000. In both aerodynamics and heat transfer investigations turbulence intensities of Tu = 1.9%, 3.0%, 8.0% , 13% and unsteady parameters of Ω = 0.0, 1.59, and 3.18 were applied.

15.1 Aerodynamics

1. Slight changes of the pressure distribution occurred, while operating at the unsteady flow conditions. Increasing the Reynolds number from Re = 110,000 to Re=150,000, has not brought major changes in steady state C_p-distribution. However, the combination of higher Reynolds number with higher unsteady wake frequency introduced higher fluctuation kinetic energy into the boundary layer which tends to reverse the separation tendency. C_p-distribution clearly shows that the wake impingement with higher Reynolds number shortens the streamwise extent of the separation zone compared to the steady case.
2. Detailed unsteady boundary layer measurement identified the onset and extent of the separation bubble as well as its behavior under the unsteady wake flow. Passing the wake flow with its highly turbulent vortical core over the separation region, caused a periodic contraction and expansion of the separation bubble and a reduction of the separation bubble height. Increasing the passing frequency associated with a higher turbulence intensity further reduced the separation bubble height. It was observed that,

by increasing the Reynolds number to 150,000, the leading edge and trailing edge of the separation bubble and thus the re-attachment point moved further downstream to s/s_o= 0.56 and s/s_o= 0.788 respectively. Also, the size of the separation bubble was further reduced.

3. Detailed unsteady boundary layer measurement identified the onset and extent of the separation zone as well as its behavior under unsteady wake flow. Passing the wake flow with its highly turbulent vortical core over the separation region caused a periodic contraction and expansion of the separation zone. It was proposed that, in conjunction with the pressure gradient and periodic wakes, the temporal gradient of the turbulence fluctuation, or more precisely the fluctuation acceleration $\partial v_{rms}/\partial t$ provides higher momentum and energy transfer into the boundary layer energizing the separation zone and causing it to partially or entirely disappear. We found that for $\partial v_{rms}/\partial t>0$, the separation zone starts to contract whereas for $\partial v_{rms}/\partial t<0$ it gradually assumes the shape before the contraction. The existence of higher turbulence fluctuations expressed in terms of higher turbulence intensity is well known for influencing the flow separation; its gradient is of crucial importance in suppressing or preventing the onset and the extent of the separation zone. The fluctuation gradient is an inherent feature of the incoming periodic wake flow and does not exist in a statistically steady flow that might have high turbulence intensity.
4. Detailed unsteady boundary layer measurement identified the onset and extent of the separation bubble as well as its behavior under the individual and combined effects of unsteady wake flow and high turbulence intensity. It was found that the periodic unsteady wake flow definitely determines the separation dynamics as long as the level of the time averaged turbulence fluctuations is bellow the maximum level of the wake fluctuation v_{max}. Increasing the inlet turbulence level above v_{max} caused the wake periodicity totally submerge in turbulence. In this case the separation dynamics of the bubble is governed by the flow turbulence that is responsible for partial or total suppression of the separation bubble.

5. The time-averaged integral quantities showed the impact of the unsteady wake flow and the turbulence on the boundary layer parameters and hence, on the profile loss coefficient and efficiency. One of the striking features this study reveals is that the separation bubble has not disappeared completely despite the high turbulence intensity and the significant reduction of its size which is reduced to a tiny bubble.

15.2 Heat Transfer

While the boundary layer behavior (according to the equation of motion) is completely decoupled from thermal boundary layer behavior, the latter is through the equation of energy directly coupled with the boundary layer aerodynamics. Considering the aerodynamic results, following conclusions are drawn:

1. Individual and combined effect of Re at constant Tu, steady inlet flow: Keeping the turbulence intensity constant, the HTC increased systematically on both surfaces. At lower turbulence intensity, Tu=1.9%, the Reynolds number increase caused the transition start to shift upstream. Systematically increasing Tu caused the transition region to partially or totally disappear.
2. Individual and combined effects of Re at constant Tu, periodic unsteady inlet flow: Keeping the turbulence intensity constant as above and utilizing a constant reduced frequency of $\Omega = 1.59$, the HTC increased systematically on both surfaces. At lower turbulence intensity, Tu=1.9%, the Reynolds number increase caused the transition start to shift upstream. The increase of HTC is predominantly accomplished by higher Re-number. Systematically increasing Tu caused the transition region to partially or totally disappear. Here, as in the above steady case, the wake effect on time averaged HTC is noticeable as long as the unsteady wake are not completely submerged in the stochastic free-stream turbulence. Increasing the reduced frequency to $\Omega = 3.18$, reduced the transition region and pushed the transition start further upstream.
3 Individual and combined effects of reduced frequency Ω at constant Re and constant Tu: Keeping the Reynolds number and turbulence intensity constant, the variation of reduced frequency at low Re-number and turbulence intensity did not have a

substantial effect on time averaged HTC on the suction surface. On the pressure surface, however, the transition length was reduced and its start moved further upstream. Keeping the same low Re= 110,00 and increasing the turbulence intensity to Tu = 3.0, the wake turbulence started to submerge into the free-stream turbulence leading to an increased HTC-distribution on the suction side with the largest difference of about 30% in the non-turbulent region, $s/s_0 \approx 0.4$. On the pressure surface, the unsteady effect was most visible in the transitional region. A seemingly different HTC- pattern emerged, when the turbulence intensity was increased to Tu = 8% and 13%, respectively. While the HTC-distributions for both unsteady cases with $\Omega = 1.59$ and 3.18 were almost identical, the steady state case (no rod), showed towards the second half of the blade increasingly higher HTC-values. This, at first glance appears to be incompatible with the widespread notion that the unsteady wakes generally contribute to intensifying the turbulence activities, thus increasing the HTC. However, expediting the turbulence fluctuations for steady and unsteady cases shows that the calming effect discussed in aerodynamics section is responsible for calming the turbulence activities, thus reducing the HTC. Similar HTC-distribution pattern was revealed for Re=250,000.

15.3 Intermittency Analysis

1. Intermittency analysis of the current boundary layer experimental data with the flow separation determined the minimum, maximum, and the relative intermittency functions, $<\gamma_{min}>$,–$<\gamma_{max}>$ and Γ. The minimum intermittency function, $<\gamma_{min}>$, represented the boundary layer behavior when it is exposed to the wake external region (region between the turbulent wake strips). On the other hand, $<\gamma_{max}>$ describes the state of the boundary layer when it is subjected to the wake vortical core with its high turbulence level.
2. The relative intermittency factor followed a Gaussian distribution confirming the universal character of the relative intermittency function. In contrast to the relative intermittency function Γ, the minimum as well as the maximum intermittency do not

suggest to have a universal character. Several parameters, such as free-stream turbulence intensity, reduced frequency, surface roughness, Re-number, and pressure gradient are instrumental in affecting the pattern of these two intermittencies. Future studies need to incorporate these parameters.

REFERENCES

[1] Arndt, N., 1993, “Blade Row Interaction in a Multistage Low Pressure Turbine,” ASME Journal of Turbomachinery, **115**, pp. 137-146.

[2] Mayle, R. E., 1991, “The Role of Laminar-Turbulent Transition in Gas Turbine Engines,” ASME Journal of Turbomachinery, **113**, pp.509-537.

[3] Schobeiri, M. T., and Radke, R. E., 1994, "Effects of Periodic Unsteady Wake Flow and Pressure Gradient on Boundary Layer Transition along the Concave Surface of a Curved Plate," ASME Paper 94-GT-327.

[4] Schobeiri, M. T., John, J., and Pappu, K., 1996, “Development of Two-Dimensional Wakes Within Curved Channels, Theoretical Framework and Experimental Investigation,” ASME Journal of Turbomachinery, **118**, pp. 506-518.

[5] Pfeil, H., and Pache, W., 1977, “Messungen von Strömungsgrenzschichten unter Turbo-maschinenbedingungen,“ Zeitschrift fur Flugwissenschaften und Weltraumforschung 1, **4**, pp. 267-278.

[6] Pfeil, H., and Herbst R., 1979 "Transition Procedure of Instationary Boundary Layers," ASME Paper No. 79-GT-128.

[7] Pfeil, H., Herbst, and R., Schröder, T., 1983, "Investigation of the Laminar Turbulent Transition of Boundary Layers Disturbed by Wakes," ASME Journal of Engineering for Power, **105**, pp. 130-137.

[8] Orth, U., 1993, “Unsteady Boundary Layer Transition in Flow Periodically Disturbed by Wakes,” ASME Journal of Turbomachinery, **115**, pp. 707-713.

[9] Dullenkopf, K., Schulz, A., and Wittig, S., 1991, “The Effect of Incident Wake Conditions on the Mean Heat Transfer of an Airfoil,” ASME Journal of Turbomachinery, **113**, pp. 412-418.

[10] Liu, X., and Rodi, W., 1991, "Experiments on Transitional Boundary Layers with Wake-Induced Unsteadiness," Journal of Fluid Mechanics, **231**, pp. 229-256.

[11] Schobeiri, M. T., Read, K., and Lewalle, J., 2003, “Effect of Unsteady Wake Passing Frequency on Boundary Layer Transition, Experimental Investigation and Wavelet Analysis,” ASME Journal of Fluids Engineering, **125**, pp. 251-266.

[12] Wright, L., and Schobeiri, M. T., 1999, "The Effect of Periodic Unsteady Flow on Boundary Layer and Heat Transfer on a Curved Surface," ASME Journal of Heat Transfer, **120**, pp. 22-33.

[13] Chakka, P., and Schobeiri, M. T., 1999, "Modeling of Unsteady Boundary Layer Transition on a Curved Plate under Periodic Unsteady Flow Condition: Aerodynamic and Heat Transfer Investigations," ASME Journal of Turbomachinery, **121**, pp. 88-97.

[14] Halstead, D. E., Wisler, D. C., Okiishi, T. H., Walker, G. J., Hodson, H. P., and Shin, H. W., 1997, " Boundary Layer Development in Axial Compressors and Turbines: Part 3 of 4 LP Turbines, " ASME Journal of Turbomachinery, **119**, pp. 225-237.

[15] Lou, W., and Hourmouziadis, J., 2000, "Separation Bubbles under Steady and Periodic Unsteady Main Flow Conditions,"ASME Paper 2000-GT-270.

[16] Kaszeta, R., Simon T. W, and Ashpis, D. E., 2001, "Experimental Investigation of Transition to Turbulence as Affected by Passing Wakes ," ASME Paper, 2001-GT-0195.

[17] Volino, R. J., and Hultgren L. S., 2001, "Measurements in Separated and Transitional Boundary Layers under Low-Pressure Turbine Airfoil Conditions," ASME Journal of Turbomachinery, **123**, pp. 189-197.

[18] Brunner, S., Fottner, L., and Schiffer, H-P., 2000, "Comparison of Two Highly Loaded Turbine Cascade under the Influence of Wake-Induced Transition," ASME 2000-GT-268.

[19] Cardamone, P., Stadtmüller P., Fottner, and L, Schiffer, H-P., 2000, "Numerical Investigation of the Wake-Boundary Layer Interaction on a Highly Loaded LP Turbine Cascade Blade," ASME 2002-GT-30367.

[20] Schröder, Th., 1989, "Measurements with Hot-Film Probes and Surface Mounted Hot Film Gages in a Multi-Stage Low Pressure Turbine," European Propulsion Forum, Bath, UK.

[21] Haueisen V., Hennecke D. K., and Schröder, T., 1997, "Measurements with Surface Mounted Hot Film Sensors on Boundary Layer Transition in Wake Disturbed Flow," AGARD-CP-598.

[22] Shyne, R. J., Sohn K. H., and De Witt, K. J., 2000, " Experimental Investigation of Boundary Layer Behavior in a Simulated Low Pressure Turbine," ASME Journal of Fluids Engineering, **122**, pp. 84-89.

[23] Van Treuren, K., Simon T., Koller M. V., Byerley A. R., Baughn J. W., and Rivir, R., 2002, " Measurements in a Turbine Cascade Flow under Ultra Low Reynolds Number Conditions," ASME Journal of Turbomachinery, **124**, pp. 100-106.

[24] Schobeiri, M. T., Öztürk, B., and Ashpis, D., 2005," On the Physics of the Flow Separation Along a Low Pressure Turbine Blade under Unsteady Flow Conditions," ASME Journal of Fluid Engineering, **127**, pp. 503-513.

[25] Schobeiri, M. T., and Öztürk, B., 2004, " Experimental Study of the Effect of the Periodic Unsteady Wake Flow on Boundary Layer Development, Separation, and Re-attachment Along the Surface of a Low Pressure Turbine Blade," ASME Journal of Turbomachinery, **126**, pp. 663-676.

[26] Öztürk, B., Schobeiri, M. T., and Ashpis, D., 2005, "Effect of Reynolds Number and Periodic Unsteady Wake Flow Condition on Boundary Layer Development, Separation, and Re-attachment along the Suction Surface of a Low Pressure Turbine Blade," ASME Paper GT2005-68600.

[27] Öztürk, B., Schobeiri, M. T., and Ashpis, D., 2005, "Intermittent Behavior of the Separated Boundary Layer along the Suction Surface of a Low Pressure Turbine Blade under Periodic Unsteady Flow Conditions,"ASME Paper GT2005-68603.

[28] Schobeiri, M. T., Pappu, K., and Wright, L., 1995, "Experimental Study of the Unsteady Boundary Layer Behavior on a Turbine Cascade," ASME 95-GT-435.

[29] Schobeiri, M. T., John, J., and Pappu, K., 1997, "Experimental Study on the Effect of Unsteadiness on Boundary Layer Development on a Linear Turbine Cascade," Journal of Experiments in Fluids, **23**, pp. 303-316.

[30] Schobeiri, M. T., and Wright, L., 2003, "Advances in Unsteady Boundary Layer Transition Research," Part I and II: International Journal of Rotating Machinery, **9,** pp, 1-22.

[31] Schobeiri, M. T., and Chakka, P., 2002, "Prediction of Turbine Blade Heat Transfer and Aerodynamics Using Unsteady Boundary Layer Transition Model," International Journal of Heat and Mass Transfer, **45**, pp. 815-829.

[32] Öztürk, B., and Schobeiri M. T., 2006, "Effect of Turbulence Intensity and Periodic Unsteady Wake Flow Condition on Boundary Layer Development, Separation, and Re-attachment over the Separation Bubble along the Suction Surface of a Low Pressure Turbine Blade,"ASME Paper GT2006-91293.

[33] Coton, T., and Arts, T., 2004, "Investigation of a High Lift LP Turbine Blade Submitted to Passing Wakes Part 1: Profile Loss and Heat Transfer," ASME GT2004-53768.

[34] Coton, T., Arts, and T., 2004, "Investigation of a High Lift LP Turbine Blade Submitted to Passing Wakes Part 2: Boundary Layer Transition," ASME GT2004-53768.

[35] Opoka, M. M., Thomas, R. L., and Hodson, H.P., 2006, "Boundary Layer Transition on the High Lift T106A LP Turbine Blade with an Oscillating Downstream Pressure Field,"ASME Paper GT2006-91038.

[36] Rivir, R. B., Sondergaard, R., Bons, J. P., and Lake, J. P., 2000, "Passive and Active Control of Separation in Gas Turbines", AIAA 2000-2235.

[37] Bons, J. P., Sondergaard, R., and Rivir, R. B, 1999, " Control of Low Pressure Turbine Separation Using Vortex Generator Jets," AIAA Paper No. 99-0367.

[38] Lin, J. C., 1999, " Control of Turbulent Boundary Layer Separation Using Micro-Vortex Generators," AIAA Paper No. 99-3404.

[39] Bons, J. P., Sondergaard, R., and Rivir, R. B, 2001 "Turbine Separation Control Using Pulsed Vortex Generator Jets," ASME Journal of Turbomachinery, **123**, pp.198-206.

[40] Sondergaard, R., Bons, J. P., Sucher, M., and Rivir, R. B., 2002, "Reducing Low-Pressure Turbine Stage Blade Count Using Vortex Generator Jet Separation Control", ASME GT-2002-30602.

[41] Bons, J., Hansen, L. C. Clark, J., Koch, P., and Sondergaard, R., 2005, "Designing Low-Pressure Turbine Blades with Integrated Flow Control," ASME GT2005-68962.

[42] Volino, R. J., 2003, "Separation Control on Low-Pressure Turbine Airfoils Using Synthetic Vortex Generator Jets," ASME Paper GT-2003-38729.

[43] McAuliffe, B. R., and Sjolander, S. A., 2004, "Active Flow Control Using Steady Blowing for a Low-Pressure Turbine Cascade," ASME GT-2004-53646.

[44] Huang, J., Corke, T., and Thomas, F., 2003, "Plasma Actuators for Separation Control on Low Pressure Turbine Blades," AIAA Paper 2003-1027.

[45] Hultgren, L. S., and Ashpis, D. E., 2003, "Demonstration of Separation Delay with Glow Discharge Plasma Actuators," AIAA Paper 2003-1025.

[46] Bons, J. P., Reimann, and D., Bloxham, M., 2006, "Separated Flow Transition on an LP Turbine Blade with Pulsed Flow Control,"ASME Paper GT2006-90754.

[47] Lake, J. P., King, P. I., and Rivir, R. B., 2000, "Low Reynolds Number Loss Reduction on Turbine Blades with Dimples and V-Grooves," AIAA Paper No. 00-0738.

[48] Volino, R. J., 2003, " Passive Flow Control on Low-Pressure Turbine Airfoils," ASME Paper GT-2003-38728,.

[49] Bohl, D.G., and Volino, R. J., 2005, "Experiments with Three Dimensional Passive Flow Control Devices on Low-Pressure Turbine Airfoils," ASME GT-2005-68969.

[50] Zhang, X., F., and Hodson, H., 2004," The Combined Effects of Surface Trips and Unsteady Wakes on the Boundary Layer Development of an Ultra-High-Lift LP Turbine Blade, ASME GT-2004-53081.

[51] Zhang, X. F., Vera, M., Hodson, H. and Harvey, N., 2005, " Separation and Transition Control on an Aft-loaded Ultra-High-Lift LP Turbine Blade at Low Reynolds Numbers Low-Speed Investigation," ASME GT-2005-68892.

[52] Van Treuren, K.W., Simon, T., Von Koller, M., Byerley, A.R., Baughn, J.W., and Rivir, R., 2002, "Measurements in a Turbine Cascade Flow under Ultra Low Reynolds Number Conditions," ASME Journal of Turbomachinery, **124,** pp. 100-106.

[53] Murawski, C.G., and Vafai, K., 1999, "Effect of Variable Axial Chord on a Low-Pressure Turbine Blade," Journal of Propulsion and Power, **15**, pp. 667-674.

[54] Byerley, A.R., Störmer, O, Baughn, J.W., Simon, T.W., VanTreuren, K.W., and List, J., 2002, "Using Gurney Flaps to Control Laminar Separation on Linear Cascade Blades," ASME Journal of Turbomachinery, **125**, pp. 114-120.

[55] Sieverding, C.H., Bagnera, C., Boege, A.C., Antòn, J.A.C., and Luère, V., 2004, "Investigation of the Effectiveness of Various Types of Boundary Layer Transition Elements of Low Reynolds Number Turbine Bladings," ASME Paper GT2004-54103.

[56] Vera, M., Hodson, H.P., and Vazquez, R., 2004, "The Effects of a Trip Wire and Unsteadiness on a High Speed Highly Loaded Low-Pressure Turbine Blade," ASME Paper GT2004-53822.

[57] Abu-Ghannam, B. J., and Shaw, R., 1980, "Natural Transition of Boundary Layers-The Effects of Turbulence, Pressure Gradient and Flow History," Journal of Mech. Eng. Sci., **22**, pp. 213-228.

[58] Gostelow, J. P., and Blunden, A. R., 1989, "Investigations of Boundary Layer Transition in an Adverse Pressure Gradient," ASME Journal of Turbomachinery, **111**, pp. 366-375.

[59] Dullenkopf, K., and Mayle, R. E., 1994, "An Account for Free-Stream Turbulence Length Scale on Laminar Heat Transfer," ASME Paper No. 94-GT-174.

[60] Pache, W., 1976, "Zur Frage der Entwicklung von Strömungsgrenzsschichten bei instationärer Zuströmung in Turbomachinen," Dissertation D-17, Technische Hochschule, Darmstadt, Germany.

[61] Schobeiri, M. T., 1979, "Theoretische und experimentelle Untersuchungen laminarer und turbulenter Strömungen in Diffsoren," Dissertation D-17, Technische Hochschule, Darmstadt, Germany.

[62] Herbst, R., 1980, "Entwicklung von Strömungsgrenz- schichten bei instationärer Zuströmung in Turbomaschinen," Dissertation D-17, Technische Hochschule, Darmstadt, Germany.

[63] Walker, G. J., 1989, "Modeling of Transitional Flow in Laminar Separation Bubbles," 9th Int. Symp. Air Breathing Engines, pp. 539-548, Athens.

[64] Paxson, D. E., and Mayle, R. E., 1991, "Laminar Boundary Layer Interaction with an Unsteady Passing Wake," Journal of Turbomachinery, **113**, pp. 419-427.

[65] Dullenkopf, K., and Mayle, R. E., 1994, "An Account for Free-Stream Turbulence Length Scale on Laminar Heat Transfer," ASME Paper No. 94-GT-174.

[66] Emmons, H. W., 1951, "The Laminar-Turbulent Transition in Boundary Layer-Part I," Journal of the Aeronautical Sciences, **18**, pp. 490-498

[67] Dhawan, S., and Narasimha, R., 1958, "Some Properties of Boundary Layer Flow During the Transition from Laminar to Turbulent Motion," Journal of Fluid Mechanics, **3**, pp. 418-436.

[68] Hedley, B. T., and Keffer F. J., 1974, "Turbulent/Non-Turbulent Decisions in an Intermittent Flow," Journal of Fluid Mechanics, **64**, pp. 625-644.

[69] Antonia, R. A., and Bradshaw, P., 1971, "Conditional Sampling of Turbulent Shear Flows," Imp. College Aero. Rep. No. 71-04, London.

[70] Kovasznay, L.S.G., Kibens, V., and Blackwelder, R. F., 1970, "Large scale motion in the Intermittent Region of a Turbulent Boundary Layer," Journal of Fluid Mechanics, **41**, pp. 283.

[71] Bradshaw, P., and Murlis, J., 1973, "On the Measurement of Intermittency in Turbulent Flows," Imp. College Aero. Tech. Note, No. 73-108, London.

[72] Launder, B. E., and Spalding, D.B., 1972, Mathematical Models of Turbulence, Academic Press, New York.

[73] Crawford, M. E., and Kays, W. M., 1976, "STAN5 (TEXSTAN version)-A Program for Numerical Computation of Two Dimensional Internal and External Boundary Layer Flow," NASA CR-2742.

[74] Schmidt, R. C., and Patankar, S. V., 1991, "Simulating Boundary Layer Transition with Low-Reynolds-Number k-ϵ Turbulence Models: Part I-An Evaluation of Prediction Characteristics; Part II-An Approach to Improving the Predictions,"ASME Journal of Turbomachinery, **113**, pp. 10-26.

[75] Wolf, W., Homeyer, Lars., and Fottner, L., 2001, " Experimental Investigation of Heat Transfer in Separated Flow onA Highly Loaded LP-Turbine Cascade, " Proceedings of the RTO/AVT Symposium and Specialists Meeting Heat Transfer and Cooling in Propulsion and Power Systems, Loen, Norway.

[76] Brear, M. J., Hodson H. P. and Harvey, N., W. 2001, "Pressure Surface Separations in Low Pressure Turbines, Part 1 of 2. Midspan Behavior," ASME GT2001-0437.

[77] Deinert, M., and Hourmouziadis, J., 2004, "Film Cooling in Unsteady Flow with Separation Bubble,"ASME-GT2004 - 53075.

[78] Butler, R. J., Byerley, A. R., Treuren, K. V., and Baughn, J. W., 2001, "The Effect of Turbulence Intensity and Length Scale on Low-Pressure Turbine Blade Aerodynamics," International Journal of Heat and Fluid Flow, **22**,pp. 123-133.

[79] Choi, J., Teng, S., Han, J. C., and Ladeinde, F., 2004, "Effect of Free-Stream Turbulence on Turbine Blade Heat Transfer and Pressure Coefficients in Low

Reynolds Number Flows," International Journal of Heat and Fluid Flow, **47**,pp. 3441-3452.

[80] Private communication with Professor J. C. Han, Gas Turbine Heat Transfer Laboratory, Texas A&M University.

[81] Private communication with Dr. A. Ameri, NASA Glen Research Center, Cleveland OH.

[82] Han, J.-C., Zhang, L., and Ou, S., 1993, "Influence of Unsteady Wake on Heat Transfer Coefficient from a Gas Turbine Blade," ASME Journal of Heat Transfer, **115**, pp. 904-911.

[83] Dunn, M. G., 1986, "Heat Flux Measurements for the Rotor of a Full-Stage Turbine: Part I-Time Averaged Results," ASME Journal of Turbomachinery, **108**, pp. 90-97.

[84] Doorly, D. J., 1988, "Modeling of Unsteady Flow in a Turbine Rotor Passage," ASME Journal of Turbomachinery, **110**, pp. 27-37.

[85] Doorly, D. J., Oldfield, M.L.G, and Scrivener, C. T. J., 1985, "Wake-Passing in a Turbine Rotor Cascade," AGARD-CP-**390**, pp. 1-18.

[86] Abhari, R. S., Guenette, G. R., Epstein, A.H., and Giles, M. B., 1992, "Comparison of Time-Resolved Measurements and Numerical Calculations," ASME Journal of Turbomachinery, **114**, pp. 818-827.

[87] Mayle, R. E., and Dullenkopf, K., 1989, "A Theory for Wake-Induced Transition," ASME 89-GT-57, presented at the International Gas Turbine and Aero-Engine Congress and Exposition, Toronto, Canada, June 4-8, 1989.

[88] Brown, A., Burton, and R. C., 1978, "The Effects of Free-Stream Turbulence Intensity and Velocity Distribution on Heat Transfer to Curved Surfaces,"ASME Journal of Engineering for Power, **100**, pp. 159-168.

[89] Brown, A., and Martin, B. W, 1979, "Heat Transfer to Turbine Blade, with Special Reference to the Effects of Mainstream Turbulence," ASME Paper 79-GT-26.

[90] Brown, A., and Martin, B. W, 1982, "Flow Transition Phenomena and Heat Transfer over the Pressure Surfaces of Gas Turbine Blades," ASME Journal of Engineering for Power, **104**, pp. 360-367.

[91] Blair, M.F., 1982, "Influence of Free-Stream Turbulence on Boundary Layer Transition in Favorable Pressure Gradients," ASME Journal of Engineering for Power, **104**, pp. 743-750.

[92] Blair, M.F., 1982, "Influence of Free-Stream Turbulence on Turbulent Boundary Layer Heat Transfer and Mean Profile Development, Part 1 – Experimental Data, ASME Journal of Heat Transfer, **105**, pp. 33-40.

[93] Blair, M.F., 1982, "Influence of Free-Stream Turbulence on Turbulent Boundary Layer Heat Transfer and Mean Profile Development, Part 2 – Analysis of Results, ASME Journal of Heat Transfer, **105**, pp. 41-47.

[94] Simonich, J. C., and Bradshaw, P., 1978, "Effect of Free-Stream Turbulence on Heat Transfer through a Turbulent Boundary Layer," ASME Journal of Heat Transfer, **100**, pp. 671-677.

[95] Hancock, P.E., and Bradshaw, P., 1983, "Effect of Free-Stream Turbulence on Turbulent Boundary Layer," ASME Journal of Fluid Engineering, **105**,pp. 284-289.

[96] Wang, T., Simon, T. W., and Buddhavarapu, J., 1985, "Heat Transfer and Fluid Mechanics Measurements in Transitional Boundary Layer Flows," ASME Journal of Engineering for Power, **107**, pp. 1007-1015.

[97] Wang, T., and Simon, T. W., 1987, " Heat Transfer and Fluid Mechanics Measurements in Transitional Boundary Layer on Convex-Curved Surfaces," ASME Journal of Turbomachinery, **109**, pp. 443-451.

[98] Kestoras, M. D., and Simon, T. W., 1993, " Combined Effets of Concave Curvature and High Free-Stream Turbulence Intensity of Boundary Layer Heat and Momentum Transport", ASME 97-WA/HT-56.

[99] Zhang, L., and Han, J. C., 1994, " Influence of Mainstream Turbulence on Heat Transfer Coefficients from a Gas Turbine Blade," ASME J. Heat Transfer, **116**, pp. 896-903.

[100] Zhang, L., and Han, J. C., 1995, "Combined Effect of Free-Stream Turbulence and Unsteady Wake on Heat Transfer Coefficients from a Gas Turbine Blade," ASME Journal of Heat Transfer, **117**, pp. 407-412.

[101] Dullenkopf, K., and Mayle, R. E., 1995, "The Effects of Incident Turbulence and Moving Wakes on Laminar Heat Transfer in Gas Turbines," ASME 94-GT-174.

[102] Liu, T., Campbell, B. T., Burns, S. P., and Sullivan, J. P, 1997,"Temperature and Pressure Sensitive Luminescent Paints in Aerodynamics", Applied Mechanics Reviews, **50**, pp.227-246.

[103] Navarra, K, Rabe, D., Fonov, S., Goss, L., and Hah, C., 2001, "The Application of Pressure and Temperature Sensitive Paints to an Advanced Compressor", Journal of Turbomachinery, **123**, pp. 823-829.

[104] Lachendro, N., Crafton, J., Guille, M., and Sullivan, J. P, 1998, "In Flight Pressure Measurements of a Transonic Wing Using A Pressure Sensitive Paint Based Laser Scanning System", PSP Workshop, Seattle Washington.

[105] Pappu, K. R., 1997, "Theoretical and Experimental Study on Periodic Unsteady Wake Development, Unsteady Boundary Layer Development, and Trailing Edge Ejection Mixing Loss Optimization in a Linear Turbine Cascade," Ph.D., Texas A&M University, Texas, USA.

[106] John, J., and Schobeiri, M. T., 1993, "A Simple and Accurate Method for Calibrating X-Probes," ASME Journal of Fluids Engineering, **115**, pp.148-152.

[107] Hinze, J. O., 1959, Turbulence, 2nd edition McGraw-Hill, New York.

[108] Champagne, F. H., Sleicher, C. A., and Wehrmann, O. H., 1996, "Turbulence Measurements with Inclined Hot-Wires, Part 1: Heat Transfer Experiments with Inclined Hot-Wire," Journal of Fluid Mechanics, **28**, pp. 153-175.

[109] Schröder, T., 1985, " Entwicklung des Instationären Nachlaufs hinter quer zur Strömungsrichtung between Zylindern und dessen Einfluß auf das Umschlagverhalten von ebenen Grenzschichten stromabwärts angeordneter Versuchskörper," Dissertation D-17, Technische Hochschule, Darmstadt, Germany.

[110] Fonov, V. S., 2003, "Development and Analysis of Data Processing Methods Applied to Luminescent Coating Systems in Aerodynamics," Ph.D., Heriot-Watt University, Edinburgh, Scotland.

[111] Liu, T., Guille, M., and Sullivan, J.P., 2001, "Accuracy of Pressure Sensitive Paint", AIAA Journal, **39**, pp. 103-112.

[112] Gouin, S., and Gouterman, M., 2000, "Ideality of Pressure-Sensitive Paint. I. Platinum Tetra(pentafluorophenyl) Porphine in Fluoroacrylic Polymer", Journal of Applied Polymer Science, **77**, pp. 2795–2804.

[113] Kegalj, M., 2005, "Effect of Periodic Unsteady Inlet Flow Condition and Freestream Turbulence on Heat Transfer along the Suction and Pressure Surface of a Low Pressure Turbine Blade," Diplomarbeit Technische Universität, Darmstadt, Germany.

[114] Schobeiri, M.T., 2003, "Turbomachinery Flow Physics and Dynamic Performance," published by Springer-Verlag, Berlin.

[115] Bellhouse, B.J., and Schultz, D.L., 1966, " Determination of Mean and Dynamic Skin Friction, Separation and Transition in Low-Speed Flow with a Thin-Film Heated Element ", Journal of Fluid Mechanics, **24**, pp 379-400.

[116] Schröder, T., 1991, "Investigations of Blade Row Interaction and Boundary Layer Transition Phenomena in a Multistage Areo Engine Low-Pressure Turbine by Measurements with Hot-Film Probes and Surface Mounted Hot-Film Gauges," Von Karman Institute for Fluid Mechanics, Lecture Series.

[117] Haueisen, V., 1996, "Untersuchungen des Grenzschichtumschlags am Kreiszylinder bei unterschiedlichen stationären und instationären Zuströmbedingungen", Dissertation, Technische Universität Darmstadt, Germany.

[118] Tiedemann, M., 1998, " Investigation of the Unsteady Rotor Boundary Layer Transition in a Transonic High Pressure Turbine Stage", Dissertation, Technische Universität Darmstadt, Germany.

[119] Kline, S. J., and McKlintock, F. A., 1953, "Describing Uncertainties in Single-Sample Experiments," Mechanical Engineering, **75**, pp. 3-8.

[120] Yavuzkurt, S., 1984, "A Guide to Uncertainty Analysis of Hot-Wire Data," ASME Journal of Fluids Engineering, **106**, pp. 181-186.

[121] Coleman, H.W., and Steele, W.G., 1989, "Experimentation and Uncertainty Analysis for Engineers", John Wiley & Sons, New York.

[122] Hourmouziadis, J., 1989, "Blading Design for Axial Turbomachines," AGARD Lecture Series LS-167.

[123] Eifler, J., 1975, "Zur Frage der freien turbulenten Strömungen, insbesondere hinter ruhenden und bewegten Zylindern," Dissertation D-17, Technische Hochschule Darmstadt, Germany.

[124] Hourmouziadis, J., Buckl, F., and Bergmann, P., 1987, "The Development of the Profile Boundary Layer in a Turbine Environment," ASME Journal of Turbomachinery, **109**, pp.286-295.

[125] Schobeiri, M. T., 2001, "Experimental Determination of LPT-Profile Losses at Low Reynolds Numbers," Progress Report No 12, NASA GRC.

[126] Townsend, A.A., 1966, "The Mechanism of Entrainment in Free Turbulent Flows", J. Fluid Mech., **26**, pp. 689-715.

[127] Kaplan, R. E., Laufer, J., 1968, "The Intermittently Turbulent Region of the Boundary Layer", Rep. USC AE 110. University of Southern Calififornia, Los Angeles.

[128] Chakka, P., 1998, "Unsteady Wake Effects on Boundary Layer Transition and Heat Transfer Characteristics of Curved Plate and Turbine Blade," Ph.D., Texas A&M University, Texas, USA.

[129] Schobeiri, M. T., 2005, " Intermittency Based Unsteady Boundary Layer Transition Modeling, Implementation into Navier-Stokes Equations," ASME Paper, GT2005-68375.

[130] Hippensteele, S. A., Russell, L. M., and Stepka, S., 1983, "Evaluation of a Method for Heat Transfer Measurements and Thermal Visualization Using a Composite of a Heater Element and Liquid Crystals," ASME Journal of Heat Transfer, **105**, pp. 184-189.

[131] Schobeiri, M. T., Öztürk, B., Müller, M., Kegalje, and M., Bensing, D., 2006, "On the Physics of Heat Transfer and Aerodynamic Behavior of Separated Flow along a Highly Loaded Low Pressure Turbine Blade under Periodic Unsteady Wake Flow and Varying of Turbulence Intensity , Part I: Aerodynamics and Part II: Heat Transfer," submitted to ASME Journal of Turbomachinery.

APPENDIX A

A.1 Data Reduction Programs

1. Data reduction program for obtaining time-averaged parameter for steady measurement

```
*-----------------------------------------------------------------------------------------------------
-
*   ENSEMBLE- This program calculates the time averaged velocity,
*                    turbulence intensity, and fluctuation rms velocity
*                    for single wire probes and applies ANGLE CORRECTION
*   FILES: filp         : data file containing the the information on
*         (input)          the number of data points and the names of
*                          document file, data file and output file.
*                          .dat -data files      (input)
*                          .doc -document filles.(input)
*                           ...a.out - output files.  (output)
*   CTA.CAL           : velocity calibration file  (input)
*   Signal connection:
*   Ch1 : Trigger                  Ch3: Differential pressure transducer
*  Ch2 : Thermocouple          Ch4: Hot wire
*-----------------------------------------------------------------------------------------------------
-
      program ENSEMBLE
      parameter (max=2000000)
      integer nsamp,sampfreq,i,nb,j
      integer theta,theta1
      real tsens,fcorr,vcorr,vcorr1
      real hwvel(4),sum,v
      real gamma,tcal
      real trig,temp,pres,hw,kin_visc
      real ctc(5),acal(3),t(2)
      real u(max),du(max),tur1(max),Re_ex(max)
      real dt(max),dx(max)
      character*115 fil
      character*115 inputfile
c     open the file containing velocity calibration constants for hot wire
      open(unit=8,file='cta.cal')
      read(8,*)(ctc(i), i=5,1,-1)
      write(*,*) ctc(5),ctc(4),ctc(3),ctc(2),ctc(1)
      close(8)
      open the file containing angle calibration coefficients
      open(unit=9,file='angcal.cof')
      read(9,*)(acal(i), i=1,3)
      close(unit=9)
```

```
c     open the master file
      open(unit=10,file='BUSPROAC.PAR')
      read(10,*) tsens
      read(10,*) theta
      read(10,*) tcal
      close(10)
      open(unit=13,file='caltherm.cof')
      read(13,*)(t(i), i=1,2)
      write(*,*) t(2),t(1)
      close(unit=13)
      open(unit=7,file='master.fil')
      read(7,*)nfile
      vcorr=acal(1)+(acal(2)*theta)+(acal(3)*theta*theta)
      vcorr1=acal(1)+(acal(2)*theta1)+(acal(3)*theta1*theta1)
      fcorr=vcorr/vcorr1
      write(*,*)'V_correction factor is,',fcorr
      nsamp=20000
      sampfreq=20000
      do j=1,nfile
         read(7,200)inputfile
         do i=1,max
            u(i)=0.0
         enddo
         open(unit=11,file=inputfile,status='old')
         sum=0.0
         do 510 i=1,nsamp
               read(11,*)temp,hw
                  temp=t(2)*temp+t(1)
               hw=hw*sqrt((tsens-tcal)/abs(tsens -temp))
                  hw=hw*(hw*(hw*(hw*ctc(5)+ctc(4))+
     $            ctc(3))+ctc(2))+ctc(1)
                  hw=hw*fcorr
                  hw=hw/vcorr
c     Calculate the sum for the ensemble average of the U velocity
                  u(i)=hw+u(i)
                  sum=sum+u(i)
510      continue
         close(11)
         v=sum/nsamp
         do i=1,nsamp
            u(i)=u(i)
         enddo
c     Calculate the ensemble RMS and turbulence calculation
```

```
      do i=1,max
         du(i)=0.0
      enddo
      open(unit=11,file=inputfile,status='old')
      do 600 i=1,nsamp
            read(11,*)temp,hw
               temp=t(2)*temp+t(1)
            hw=hw*sqrt((tsens-tcal)/abs(tsens -temp))
               hw=hw*(hw*(hw*(hw*ctc(5)+ctc(4))+
     $         ctc(3))+ctc(2))+ctc(1)
               hw=hw*fcorr
               hwvel=hw/vcorr
               du(i)=(hw-v)**2
600   continue
      close(11)
      delt=20.0/float(nsamp)
      d=0.2715
      do i=1,nsamp
         du(i)=sqrt(du(i))
         tur1(i)=du(i)*100./u(i)
         dt(i)=(i)*delt*1000
      enddo
      ip=index(inputfile,'.')
      fil=inputfile(:(ip-1))//'.out'
c     Write to the output file
      open(unit=12,file=fil,status='new')
      write(12,74)
      do i=1,nsamp
         write(12,75)dt(i),u(i),du(i),tur1(i)
      enddo
      close(12)
   enddo
c  Formats
5  format(a26,f9.3)
74 format('   dt[ms]    u[m/s]    du[m/s]   Tu[%]')
75 format(4(1x,f16.10))
200format(a115)
   stop
   end
```

2. Data reduction program for obtaining ensemble-averaged parameter for unsteady measurement

```
*-----------------------------------------------------------------------------------------------------
-
*   ENSEMBLE- This program calculates the ensemble averaged velocity,
*                    turbulence intensity, and fluctuation rms velocity
*                    for single wire probes and applies ANGLE CORRECTION
*   FILES: filp         : data file containing the the information on
*         (input)          the number of data points and the names of
*                          document file, data file and output file.
*                          .dat -data files      (input)
*                          .doc -document filles.(input)
*                           ...a.out - output files.  (output)
*   CTA.CAL          : velocity calibration file              (input)
*  Signal connection:
*  Ch1 : Trigger                 Ch3: Differential pressure transducer
*  Ch2 : Thermocouple         Ch4: Hot wire
*-----------------------------------------------------------------------------------------------------
-
      program ENSEMBLE
      parameter (max=2500000)
      integer sampfreq,nsamp,i,nb,j
      integer nsamperevol,nrev
      integer ntext(6)
      real rps,rpm,vcorr,vcorr1,fcorr
      real hwvel(4)
      real gamma,tsens,tcal
      real trig,temp,pres,hw,hwfil
      real ctc(5),acal(3),t(2)
      real u(max),du(max),tur(max),ufil(max),dufil(max)
      real dt(max),dx(max),turfil(max)
      character*50 fil
      character*50 inputfile
c     open the file containing velocity calibration constants for hot wire
      open(unit=8,file='cta.cal')
      read(8,*)(ctc(i), i=5,1,-1)
      write(*,*) ctc(5),ctc(4),ctc(3),ctc(2),ctc(1)
      close(8)
c     open the file containing angle calibration coefficients
      open(unit=9,file='angcal.cof')
      read(9,*)(acal(i), i=1,3)
      close(unit=9)
```

```
c    open the master file
     open(unit=10,file='BUSPROAC.PAR')
     read(10,*) tsens
     read(10,*) theta
     read(10,*) tcal
     close(10)
     open(unit=13,file='caltherm.cof')
     read(13,*)(t(i), i=1,2)
     write(*,*) t(2),t(1)
     close(unit=13)
     open(unit=7,file='master.fil')
     read(7,*)nfile

     vcorr=acal(1)+(acal(2)*theta)+(acal(3)*theta*theta)
     vcorr1=1.6372625
     fcorr=vcorr/vcorr1
     write(*,*)'V_correction factor is = ',fcorr
c    write(*,*)acal(3),acal(2), acal(1)
     sampfreq=20000
     rps=1
     nrev=100
     nsamperevol=float(sampfreq)/rps
     nsamp=int(float(nrev)*nsamperevol)
     rpm=rps*60
     do j=1,nfile
        read(7,200)inputfile
        do i=1,max
           ufil(i)=0.0
           u(i)=0.0
        enddo
        open(unit=11,file=inputfile,status='old')
        do 800 nb = 1,nrev
                do 510 i=1,nsamperevol
c                     read(11,*)temp,pres,hwfil,hw
                   read(11,*)trig,temp,pres,hwfil,hw
                      temp=t(2)*temp+t(1)
                   hwfil=hwfil*sqrt((tsens-tcal)/(tsens -temp))
                      hwfil=hwfil*(hwfil*(hwfil*(hwfil*ctc(5)+ctc(4))+
    $                 ctc(3))+ctc(2))+ctc(1)
                   hw=hw*sqrt((tsens-tcal)/(tsens -temp))
                      hw=hw*(hw*(hw*(hw*ctc(5)+ctc(4))+
    $                 ctc(3))+ctc(2))+ctc(1)
                   hw=hw/fcorr
```

```
c                         hw=hw/vcorr
*    Calculate the sum for the ensemble average of the U velocity
                          ufil(i)=ufil(i)+hwfil
                        u(i)=u(i)+hw
510               continue
800     continue
        close(11)
        do i=1,nsamperevol
         ufil(i)=ufil(i)/nrev
           u(i)=u(i)/nrev
        enddo
c    Calculate the ensemble RMS and turbulence calculation
        do i=1,max
           du(i)=0.0
           dufil(i)=0.0
        enddo
        open(unit=11,file=inputfile,status='old')
        do 900 nb=1,nrev
        do 600 i=1,nsamperevol
              read(11,*)temp,pres,hwfil,hw
              read(11,*)trig,temp,pres,hwfil,hw
                 temp=t(2)*temp+t(1)
              hwfil=hwfil*sqrt((tsens-tcal)/(tsens -temp))
                 hwfil=hwfil*(hwfil*(hwfil*(hwfil*ctc(5)+ctc(4))+
    $            ctc(3))+ctc(2))+ctc(1)
              hw=hw*sqrt((tsens-tcal)/(tsens -temp))
                 hw=hw*(hw*(hw*(hw*ctc(5)+ctc(4))+
    $            ctc(3))+ctc(2))+ctc(1)
                 hw=hw/fcorr
c                hw=hw/vcorr
                 dufil(i)=(hwfil-ufil(i))**2+dufil(i)
                 du(i)=(hw-u(i))**2+du(i)
600     continue
900     continue
        close(11)
        delt=1.0/float(sampfreq)
        vbelt = 5.0*rpm/60.0
        delx = vbelt*delt
        do i=1,nsamperevol
         dufil(i)=sqrt(dufil(i)/nrev)
           turfil(i)=dufil(i)*100./ufil(i)
           du(i)=sqrt(du(i)/nrev)
           tur(i)=du(i)*100./u(i)
```

```
            dt(i)=(i-1)*delt*1000
            dx(i)=(i-1)*delx*1000
         enddo
         ip=index(inputfile,'.')
         fil=inputfile(:(ip-1))//'.out'
c    Write to the output file
         open(unit=12,file=fil,status='new')
         write(12,74)
         write(12,76)
         do i=1,nsamperevol
            write(12,75)dt(i),dx(i),ufil(i),dufil(i),turfil(i),u(i),du(i),
     &       tur(i)
c           write(12,75)dt(i),ufil(i),dufil(i),turfil(i),u(i),du(i),tur(i)
         enddo
         close(12)
      enddo
c    Formats
5    format(a26,f9.6)
74   format('VARIABLES="dt(msec)", "dx(mm)", "ufil(m/s)", "dufil(m/s)",
     & "Tufil(%)", "u(m/s)", "du(m/s)", "Tu(%)"')
76   format('ZONE I=20000, F=POINT')
75   format(8(1x,f15.10)
200    format(a50)
      stop
      end
```

3. Data reduction program for separating the data into three segments and each corresponding to one wake passing frequency

```
*-------------------------------------------------------------------------------
*     SEP_DATA - This program reads the data and separates
*                        data into three separate segments, each corresponding
*                     to one wake passing frequency
*     Files - Reads in LIMIT.TXT which specifies the starting and ending
*              length for each wake passing frequency.
*     Variables
*     nsamp=number of samples
*     s1=starting point  (steady)
*     s2=starting point for the  wake passing frequency zone (160 mm)
*     s3=starting point for the wake passing frequency zone (80 mm)
*     e1=end point for the steady zone
*     e2=end point for the  wake frequency zone (160 mm)
*     e3=end point for the  wake frequency zone (80 mm)
```

```
*-------------------------------------------------------------------------------------

      program sep_data
      implicit none
      integer max,ncount,nst,ip
      parameter(max=60000)
      integer nsamp,i,sampfreq,nfile,j
      real s1,s2,s3,s4,e1,e2,e3,e4
      real dt(max),dx(max),u(max),du(max),tur(max)
      real ufil(max),dufil(max),turfil(max)
      real dtm,delt
      character*135 label
      character*60 fil1,fil2,fil3
      character*60 inputfile
      open(unit=1,file='limit.txt',status='old')
      read(1,*)nsamp
      read(1,*)sampfreq    !Hz
      read(1,*)s1,e1
      read(1,*)s2,e2
      read(1,*)s3,e3
c     read(1,*)s4,e4
      close(1)
      open(unit=7,file='master1.fil')
      read(7,*)nfile
      do j=1,nfile
         read(7,'(a)')inputfile
         delt=1./float(sampfreq)
         ncount = 1
         ip=index(inputfile,'.')
         fil1=inputfile(:(ip-1))//'a.out'
         fil2=inputfile(:(ip-1))//'b.out'
         fil3=inputfile(:(ip-1))//'c.out'
         open(unit=2,file=inputfile,status='old')
         open(unit=3,file=fil1)
         open(unit=4,file=fil2)
         open(unit=5,file=fil3)
         read(2,'(a)')label
         read(2,'(a)')label
         do i=1,nsamp
            read(2,24)dt(i),dx(i),ufil(i),dufil(i),turfil(i),u(i),du(i),tur(i)
c     selecting the first wake passing frequency zone (steady)
            if((dx(i).ge.s1).and.(dx(i).le.e1)) then
               if(ncount.eq.1) then
```

```
                nst = i
                ncount = 2
                endif
            dtm = (i-nst)*delt*1000+75
            write(3,24)dtm,dx(i),ufil(i),dufil(i),turfil(i),u(i),du(i),tur(i)
            endif
c   selecting the second wake passing frequency zone (160 mm)
            if((dx(i).ge.s2).and.(dx(i).le.e2)) then
                if(ncount.eq.2) then
                nst = i
                ncount = 3
                endif
            dtm = (i-nst)*delt*1000+400
            write(4,24)dtm,dx(i),ufil(i),dufil(i),turfil(i),u(i),du(i),tur(i)
            endif
c   selecting the third wake passing frequency zone (80 mm)
            if((dx(i).ge.s3).and.(dx(i).le.e3)) then
                if(ncount.eq.3) then
                nst = i
                ncount = 4
                endif
            dtm = (i-nst)*delt*1000+700
c         dtm = (i-nst)*delt*1000+700
            write(5,24)dtm,dx(i),ufil(i),dufil(i),turfil(i),u(i),du(i),tur(i)
            endif
        end do
        close(2)
        close(3)
        close(4)
        close(5)
    enddo
24  format(8(1x,f15.10))
    end
```

4. Data reduction program for obtaining time-averaged quantities

```
    program average
    implicit none
    character*85 outfile
    character*65 inputfile
    real dt,dx,u,du,Tu,m_dt,m_dx,m_u
    real m_du,m_Tu
```

```
      integer i,j,k,nfile,counter
      open(1,file='media2.inf ',status='old')
      read(1,*)nfile
      read(1,'(a)')outfile
      open(3,file=outfile,status='unknown')
      do i=1,nfile
         m_u=0.0
         m_du=0.0
         m_Tu=0.0
         read(1,'(a)')inputfile
         open(2,file=inputfile,status='old')
         read(2,*)
         counter=0
         do while (.not.eof(2))
            read(2,*)dt,u,du,Tu
          counter=counter+1
          m_u=u+m_u
          m_du=du+m_du
          m_Tu=Tu+m_Tu
         end do
         m_u=m_u/float(counter)
         m_du=m_du/float(counter)
         m_Tu=m_Tu/float(counter)
         write(3,100)m_u,m_du,m_Tu
         close(2)
      enddo
100format(3(1x,f18.10))
      end
```

5. Data reduction program for obtaining time-averaged boundary layer parameters

```
------------------------------------------------------------------------------------------------------
--
c     This program generates the ensemble averaged boundary layer parameters,
c     delta,delta1,delta2,delta3,H12,H23, etc. as a function of time (t/T : 0-3)
------------------------------------------------------------------------------------------------------
--
      program ENSBL2
      implicit none
      integer i,j,n,k,counter
      integer npol,start,ns,ks
```

```
      character*65 inputfile,fo1
      real y,srod,ycoord,itime
      real dt,dx,ufil,dufil,tufil,t,tau,u1,du,tu
      real a,g,u,f1,f2,f3
      real yintpol,uintpol,upot,ypot
      real break0,cscoef0,break1,cscoef1
      real break2,cscoef2,break3,cscoef3
      real low,high,ue,delta,delta1,delta2,delta3
      real H12,H23,xt
      real*8 acoeff(20),var(20),coeff(20)
      real csitg,csval
      real Udelta,S1,y1,y2,Udelta1
      dimension dt(100),ufil(100),dufil(100)
      dimension tufil(100)
      dimension u1(100),du(100),tu(100)
      dimension ypot(50),upot(50)
      dimension a(100),g(100),y(100),u(100),f1(100),f2(100),f3(100)
      dimension yintpol(500),uintpol(500)
      dimension break0(100),cscoef0(4,100),break1(100),cscoef1(4,100)
      dimension break2(100),cscoef2(4,100),break3(100),cscoef3(4,100)
c     csakm    Gives spline coefficients of the data points
c     csitg    Uses the spline coefficients to calculate the integral
c     iwkin    Assigns larger workspace for the program
c     csval    Gives the interpolated values using the spline coeffs
c     lsfit    Fits the potential flow with a first order polynomial
      external csakm,csitg,iwkin,csval,lsfit
      call iwkin(43338)
      write(*,*)'Enter the approximate BL thickness in mm. '
      read(*,*)ycoord
      ycoord=ycoord/1000.
      open(unit=2,file='master.fil',status='old')
      read(2,25) fo1
      read(2,25) inputfile
25    format(a65)
      close(unit=2)
c     Input of the data
      open(unit=8,file=inputfile,status='old')
      read(8,*)
      read(8,*)
      i=0
      do while(.not.eof(8))
         i=i+1
         read(8,*) a(i),ufil(i),dufil(i),tufil(i),u1(i),du(i),tu(i)
```

```
      a(i)=a(i)/1000.0
      g(i)=u1(i)
    enddo
    close(unit=8)
    open(unit=14,file=fo1,status='new')
    write(14,74)
c   Calculation of the potential flow fit
c   Initializing the parameters
    n=i-1
    start=0
    i=1
    do while(a(i).le.ycoord)
      if(a(i).lt.ycoord) then
      start=i+1
      elseif(a(i).eq.ycoord) then
      start=i
      endif
       i=i+1
    enddo
c   Assigning the data to fit for potential flow
    do i=start,n
      ypot(i-start+1)=a(i)
      upot(i-start+1)=g(i)
    enddo
c   Fitting the potential flow
    npol=1
    ns=n-start+1
    call LSFIT(ns,ypot,upot,npol,acoeff,var,coeff,ks)
c   Calculating Ue and u(i) where u-inviscid=a(i)*coeff(2)+coeff(1)
c    f1(i)   function to be integrated for displacement thickness
c    f2(i)   function to be integrated for momentum thickness
c    f3(i)   function to be integrated for energy thickness
    Ue=coeff(1)
    do i=1,n
      y(i)=a(i)
      u(i)=g(i) - (a(i)*coeff(2)+coeff(1)) + Ue
      f1(i)=1-u(i)/Ue
      f2(i)=u(i)/Ue*(1.0-u(i)/Ue)
      f3(i)=u(i)/Ue*(1.0-u(i)*u(i)/Ue/Ue)
    enddo
c   Calculation of the boundary layer thickness, delta using the
c   calculated velocity "u".
c   The boundary layer thickness is located using interpolated values
```

```
c    of the calculated velocity "u".
     xt=0.0
     call csakm(n,y,u,break0,cscoef0)
     do i=1,500
        xt=xt+y(n)/500
        yintpol(i)=xt
        uintpol(i)=csval(xt,n-1,break0,cscoef0)
     enddo
     i=1
     do while((abs(Ue-uintpol(i)).ge.0.01*Ue).and.(i.le.500))
        i=i+1
     enddo
     k=i-1
     delta=yintpol(k)
c    Limits of integration
     low=0.0
     high=delta
     call csakm(n,y,f1,break1,cscoef1)
     delta1=csitg(low,high,n-1,break1,cscoef1)
     call csakm(n,y,f2,break2,cscoef2)
     delta2=csitg(low,high,n-1,break2,cscoef2)
     call csakm(n,y,f3,break3,cscoef3)
     delta3=csitg(low,high,n-1,break3,cscoef3)
     H12=delta1/delta2
     H23=delta2/delta3
     delta=delta*1000.
     delta1=delta1*1000.
     delta2=delta2*1000.
     delta3=delta3*1000.
**************************************************************************
c    S1 is the slope of the potential core of u vs y
c    write(*,*)coeff(1),coeff(2),coeff(3),Ue
     S1=coeff(2)
c    Find delta and Udel at y/delta=1.0
c    Up(i)=S1*a(i)+Ue
     do i=1,n
        y1=a(i)*1000.0
        y2=a(i+1)*1000.0
        if((y1.lt.delta).and.(y2.gt.delta))then
c        Udelta1=S1*delta/1000+Ue
        Udelta=(delta-y1)*(g(i+1)-g(i))/(y2-y1)+g(i)
        endif
        enddo
```

```
c    write(*,*)Udelta,Udelta1
c    Output data to the file "bounlay.par" to be read by the program law of the wall
     write(14,34)delta/1000,delta1/1000,delta2/1000,delta3/1000,Udelta, S1,Ue
34   format(7(1x,f15.10))
74   format('      delta         delta1         delta2          delt
    &a3        Udelta             S1          Ue')
     stop
     end
     SUBROUTINE LSFIT(N,X,Y,NPOL,A,VAR,Coeff,KS)
C  NOTE: This file contains LSFIT, LSGET, and SIMQ
C  LSFIT IS A LEAST-SQUARES POLYNOMIAL FIT OF Y VS. X.  THE
POLYNOMIAL
C  IS OF ORDER NPOL.
C  N=NUMBER OF DATA POINTS
C  X=INDEPENDENT VARIABLE
C  Y=DEPENDENT VARIABLE
C  NPOL=ORDER OF POLYNOMIAL TO BE FIT
C  A IS THE COEFFICIENT MATRIX WHICH MUST BE DIMENSIONED TO AT
LEAST
C  (NPOL+1)*(NPOL+1) IN THE CALLING PROGRAM
C  VAR IS A DUMMY ARRAY WHICH MUST BE DIMENSIONED TO AT LEAST
C  NPOL+NPOL+1 IN THE CALLING PROGRAM.
C  Coeff=ANSWER VECTOR, I.E. THE COEFFICIENTS OF THE POLYNOMIAL.
Coeff
C  MUST BE DIMENSIONED TO AT LEAST NPOL+NPOL+1 IN THE CALLING
 PROGRAM
     IMPLICIT REAL*8 (A-H,O-Z)
     REAL*8 A(1),Coeff(1),VAR(1)
     REAL*4 X(1),Y(1)
     NPOLP1=NPOL+1
     NPOL2=NPOL+NPOL
     DO 60 I=0,NPOL2
              IP=I+1
              XAV=0.d0
              XYAV=0.d0
              DO 50 J=1,N
                       XINC=1.d0
                       if(i.ne.0) then
                       DO 40 K=1,I
                                XINC=XINC*X(J)
40                     CONTINUE
                       end if
                       XAV=XAV+XINC
```

```
                XYAV=XYAV+XINC*Y(J)
50          CONTINUE
            VAR(IP)=XAV/N
            Coeff(IP)=XYAV/N
60  CONTINUE
    ICOUNT=0
    DO 80 I=1,NPOLP1
            DO 70 J=1,NPOLP1
                ICOUNT=ICOUNT+1
                INDEX=I+J-1
                A(ICOUNT)=VAR(INDEX)
70          CONTINUE
80  CONTINUE
    CALL SIMQ(A,Coeff,NPOLP1,KS)
    RETURN
    END
C-------------------------------------------------------------------------------------------------------
--
    SUBROUTINE LSGET(NPOL,Coeff,XINPUT,YOUT)
C   LSGET IS THE LEAST-SQUARES 'GET' SUBROUTINE TO BE USED IN
C   CONJUNCTION WITH LSFIT.
C   NPOL = ORDER OF POLYNOMIAL
C   XINPUT = X POINT WHERE Y IS WANTED
C   YOUT = FITTED VALUE OF THE POLYNOMIAL AT X
    REAL*8 Coeff(1)
    REAL*4  XINPUT,YOUT
    NPOLP1=NPOL+1
    YOUT=0.
    XINC=1.
    DO 10 I=1,NPOLP1
            IF (I.GT.1) XINC=XINC*XINPUT
            YOUT=YOUT+XINC*Coeff(I)
10  CONTINUE
    RETURN
    END
C-------------------------------------------------------------------------------------------------------
C   SUBROUTINE SIMQ
C   PURPOSE
C   OBTAIN SOLUTION OF A SET OF SIMULTANEOUS LINEAR EQUATIONS,
C   AX=B
C   USAGE
C   CALL SIMQ(A,B,N,KS)
C   DESCRIPTION OF PARAMETERS
```

```
C   A - MATRIX OF COEFFICIENTS STORED COLUMNWISE.  THESE ARE
C   DESTROYED IN THE COMPUTATION.  THE SIZE OF MATRIX A IS
C   N BY N.
C   B - VECTOR OF ORIGINAL CONSTANTS (LENGTH N). THESE ARE
C   REPLACED BY FINAL SOLUTION VALUES, VECTOR X.
C   N - NUMBER OF EQUATIONS AND VARIABLES. N MUST BE .GT. ONE.
C   KS - OUTPUT DIGIT
C   0 FOR A NORMAL SOLUTION
C   1 FOR A SINGULAR SET OF EQUATIONS
C   REMARKS
C   MATRIX A MUST BE GENERAL.
C   IF MATRIX IS SINGULAR , SOLUTION VALUES ARE MEANINGLESS.
C   AN ALTERNATIVE SOLUTION MAY BE OBTAINED BY USING MATRIX
C   INVERSION (MINV) AND MATRIX PRODUCT (GMPRD).
C   SUBROUTINES AND FUNCTION SUBPROGRAMS REQUIRED
C   NONE
C   METHOD
C   METHOD OF SOLUTION IS BY ELIMINATION USING LARGEST PIVOTAL
C   DIVISOR. EACH STAGE OF ELIMINATION CONSISTS OF INTERCHANGING
C   ROWS WHEN NECESSARY TO AVOID DIVISION BY ZERO OR SMALL
C   ELEMENTS.
C   THE FORWARD SOLUTION TO OBTAIN VARIABLE N IS DONE IN
C   N STAGES. THE BACK SOLUTION FOR THE OTHER VARIABLES IS
C   CALCULATED BY SUCCESSIVE SUBSTITUTIONS. FINAL SOLUTION
C   VALUES ARE DEVELOPED IN VECTOR B, WITH VARIABLE 1 IN B(1),
C   VARIABLE 2 IN B(2),....., VARIABLE N IN B(N).
C   IF NO PIVOT CAN BE FOUND EXCEEDING A TOLERANCE OF 0.0,
C   THE MATRIX IS CONSIDERED SINGULAR AND KS IS SET TO 1. THIS
C   TOLERANCE CAN BE MODIFIED BY REPLACING THE FIRST STATEMENT.
C-----------------------------------------------------------------------------------------------
-
      SUBROUTINE SIMQ(A,B,N,KS)
      IMPLICIT REAL*8 (A-H,O-Z)
      DIMENSION A(1),B(1)
C   FORWARD SOLUTION
      TOL=0.0d0
      KS=0
      JJ=-N
      DO 65 J=1,N
         JY=J+1
         JJ=JJ+N+1
         BIGA=0
         IT=JJ-J
```

```
      DO 30 I=J,N
C   SEARCH FOR MAXIMUM COEFFICIENT IN COLUMN
            IJ=IT+I
            IF(ABS(BIGA)-ABS(A(IJ))) 20,30,30
 20         BIGA=A(IJ)
            IMAX=I
 30   CONTINUE
C   TEST FOR PIVOT LESS THAN TOLERANCE (SINGULAR MATRIX)
      IF(ABS(BIGA)-TOL) 35,35,40
 35   KS=1
   RETURN
C   INTERCHANGE ROWS IF NECESSARY
 40 I1=J+N*(J-2)
   IT=IMAX-J
   DO 50 K=J,N
   I1=I1+N
   I2=I1+IT
   SAVE=A(I1)
   A(I1)=A(I2)
   A(I2)=SAVE
C   DIVIDE EQUATION BY LEADING COEFFICIENT
 50A(I1)=A(I1)/BIGA
   SAVE=B(IMAX)
   B(IMAX)=B(J)
   B(J)=SAVE/BIGA
C   ELIMINATE NEXT VARIABLE
   IF(J-N) 55,70,55
 55IQS=N*(J-1)
   DO 65 IX=JY,N
   IXJ=IQS+IX
   IT=J-IX
   DO 60 JX=JY,N
   IXJX=N*(JX-1)+IX
   JJX=IXJX+IT
 60A(IXJX)=A(IXJX)-(A(IXJ)*A(JJX))
 65B(IX)=B(IX)-(B(J)*A(IXJ))
C   BACK SOLUTION
 70NY=N-1
   IT=N*N
   DO 80 J=1,NY
   IA=IT-J
   IB=N-J
   IC=N
```

```
      DO 80 K=1,J
      B(IB)=B(IB)-A(IA)*B(IC)
      IA=IA-N
   80 IC=IC-1
      RETURN
      END
```

6. Data reduction program for obtaining equally distributed profile along the y axis by using Akima interpolation

```
      Program int
      implicit none
      integer i,nfils,ip,j,counter,k,nintv,n
      real srod,dt,dx,coord,uintpol
      real ufilintpol,duintpol,tuintpol,dufilintpol,tufilintpol
      real ufil,dufil,tufil,u1,du,tu
      real xt,newcoord
      real break0,cscoef0,xdat,fdat
      real csval
      character*45 inputfile
      character*85 outputfile
      dimension inputfile(50),outputfile(50)
      dimension dx(50,20000)
      dimension dt(50,20000),ufil(50,20000),dufil(50,20000)
      dimension tufil(50,20000),coord(50),xt(50)
      dimension u1(50,20000),du(50,20000),tu(50,20000)
      dimension ufilintpol(50,20000),newcoord(50),xdat(50),fdat(50)
      dimension dufilintpol(50,20000),uintpol(50,20000),duintpol(50,20000),
     &          tuintpol(50,20000),tufilintpol(50,20000)
      dimension break0(50),cscoef0(4,50)
c     csakm    Gives spline coefficients of the data points
c     iwkin    Assigns larger workspace for the program
c     csval    Gives the interpolated values using the spline coefficients
      external csakm,csval
      call iwkin(43338)
      open(unit=2,file='master.fil',status='old')
      read(2,*)nfils
      do i=1,nfils
         read(2,25) inputfile(i)
25       format(a45)
      enddo
      close(2)
```

```
      open(unit=10,file='11_234coord.dat',status='old')
      do i=1,nfils
          read(10,*) coord(i)
      enddo
      close(10)
      do i=1,nfils
          open(unit=8,file=inputfile(i),status='old')
          j=0
         do while(.not.eof(8))
          j=j+1
          read(8,*) dt(i,j),dx(i,j),ufil(i,j),dufil(i,j),
     &                 tufil(i,j),u1(i,j),du(i,j),tu(i,j)
          enddo
          counter=j
      enddo
      close(unit=8)
      n=nfils
      open(unit=20,file='10_56coord.dat',status='old')
      do i=1,nfils
          read(20,*) newcoord(i)
      enddo
      close(20)
      nintv=n-1
c     Interpolation of the filtered velocity
      do j=1,counter
          do i=1,nfils
           fdat(i)=ufil(i,j)
              xdat(i)=coord(i)
          enddo
          call csakm(n,xdat,fdat,break0,cscoef0)
          do i=1,nfils
           xt=newcoord(i)
              ufilintpol(i,j)=csval(xt,nintv,break0,cscoef0)
          enddo
      enddo
c     Interpolation of the filtered rms velocity
      do j=1,counter
          do i=1,nfils
           fdat(i)=dufil(i,j)
              xdat(i)=coord(i)
          enddo
          call csakm(n,xdat,fdat,break0,cscoef0)
          do i=1,nfils
```

```
          xt=newcoord(i)
             dufilintpol(i,j)=csval(xt,nintv,break0,cscoef0)
          enddo
       enddo
c      Interpolation of the filtered turbulence intensity
       do j=1,counter
          do i=1,nfils
           fdat(i)=tufil(i,j)
             xdat(i)=coord(i)
          enddo
          call csakm(n,xdat,fdat,break0,cscoef0)
          do i=1,nfils
           xt=newcoord(i)
             tufilintpol(i,j)=csval(xt,nintv,break0,cscoef0)
          enddo
       enddo
c      Interpolation of the raw velocity
       do j=1,counter
          do i=1,nfils
           fdat(i)=u1(i,j)
             xdat(i)=coord(i)
          enddo
          call csakm(n,xdat,fdat,break0,cscoef0)
          do i=1,nfils
           xt=newcoord(i)
             uintpol(i,j)=csval(xt,nintv,break0,cscoef0)
          enddo
       enddo
c      Interpolation of the raw rms velocity
       do j=1,counter
          do i=1,nfils
           fdat(i)=du(i,j)
             xdat(i)=coord(i)
          enddo
          call csakm(n,xdat,fdat,break0,cscoef0)
          do i=1,nfils
           xt=newcoord(i)
             duintpol(i,j)=csval(xt,nintv,break0,cscoef0)
          enddo
       enddo
c      Interpolation of the raw velocity
       do j=1,counter
          do i=1,nfils
```

```
          fdat(i)=tu(i,j)
             xdat(i)=coord(i)
          enddo
          call csakm(n,xdat,fdat,break0,cscoef0)
          do i=1,nfils
           xt=newcoord(i)
             tuintpol(i,j)=csval(xt,nintv,break0,cscoef0)
          enddo
      enddo
      open(unit=22,file='masterout.fil',status='old')
      do i=1,nfils
          read(22,45) outputfile(i)
45        format(a85)
      enddo
      close(22)
      do i=1,nfils
          open(unit=30,file=outputfile(i),status='new')
          do j=1,counter
             write(30,24) dt(i,j),dx(i,j),ufilintpol(i,j),dufilintpol(i,j),
     &                    tufilintpol(i,j),uintpol(i,j),duintpol(i,j),tuintpol(i,j)
24           format(8(1x,f15.10))
          enddo
      enddo
      end
```

7. Data reduction program for obtaining equally distributed values along y axis for time-averaged values

```
ccccccccccccccccccccccccccccccccccccccccccccccccccccccccccccccccccccccccccccccccccccc
ccThis program generates the interpolated time-averaged values along the boundary
layerc  c
ccccccccccccccccccccccccccccccccccccccccccccccccccccccccccccccccccccccccccccccccccccc
c
      program interpolation
      integer ndata,npoint
      parameter(ndata=50)
      parameter(npoint=28)
      integer i,nintv
      real break(ndata),cscoef(4,ndata),csval,f,xnew(ndata),fdata(npoint),xdata(npoint)
      real uintpol(ndata),tuintpol(ndata)
      real y(npoint),ufil(npoint),tufil(npoint),u1(npoint)
      real du(npoint),tu(npoint),dufil(npoint)
      character*40 inputfile
```

```
      character*30 outputfile
      external csakm,csval
      open(unit=2,file='master.fil',status='old')
      read(2,25) inputfile
      read(2,35) outputfile
25    format(a40)
35    format(a30)
      close(unit=2)
      open(unit=8,file=inputfile,status='old')
      do i=1,npoint
         read(8,*) y(i),u1(i),tu(i)
      enddo
      close(unit=8)
      open(unit=9,file='newpoints.txt',status='old')
      do i=1,ndata
         read(9,*) xnew(i)
      enddo
c     Interpolation of the velocity
      do 10 i=1,npoint
          xdata(i)=y(i)
          fdata(i)=u1(i)
10    continue
      call csakm(ndata,xdata,fdata,break,cscoef)
      nintv=ndata-1
      do 20 i=1, ndata
             x=xnew(i)
          uintpol(i)=csval(x,nintv,break,cscoef)
20    continue
c     Interpolation of the turbulence intensity
      do 30 i=1,npoint
             xdata(i)=y(i)
             fdata(i)=tu(i)
30    continue
      call csakm(ndata,xdata,fdata,break,cscoef)
      nintv=ndata-1
      do 40 i=1, ndata
             x=xnew(i)
          tuintpol(i)=csval(x,nintv,break,cscoef)
40    continue
      open(unit=10,file=outputfile,status='new')
      do i=1, ndata
         write(10,75) xnew(i),uintpol(i),tuintpol(i)
      enddo
```

```
75  format(3(1x,f15.10))
    end
```

8. Data reduction program for obtaining contour plots from time-averaged results

```
c-------------------------------------------------------------------------------
c     Used for data analysis for unsteady boundary layer (UBL-series)
c     development study.
c     This is a processing program that converts s series of ensemble
c     averaged xxxxxxxa,b.OUT files to plots in the distance/time
c     domain.
c-------------------------------------------------------------------------------
      program CONT
      implicit none
      integer nfils,i,j,n
      real ufil,dufil,Tufil
      real dt,dx,u(50),du,Tu(50),y(50)
      real ratio
      character*30 inputfile
      character*35 outfile
      nfils=30
      outfile='D:\results\cfd\contourcfd.out'
      open(3,file=outfile,status='unknown')
      write(3,74)
      write(3,76)
      do i=1,50
         open(unit=11,file='ratio.inf',status='old')
         do j=1,nfils
            open(unit=10,file='contour.fil',status='old')
            read(11,*)ratio
          read(10,'(a)')inputfile
            open(2,file=inputfile,status='old')
            do n=1,50
             read(2,*)y(n),u(n),Tu(n)
          enddo
            write(3,93)ratio,y(i),u(i),Tu(i)
         enddo
         close(10)
         close(11)
      enddo
      close(3)
```

```
93  format(4(1x,f15.10))
74  format('VARIABLES="s/s_o","y(mm)","u(m/s)","Tu(%)"')
76  format('ZONE I=1500, F=POINT')
    stop
    end
```

9. Data reduction program for obtaining contour plots from time-averaged results

```
c-------------------------------------------------------------------------------------
c     Used for data analysis for unsteady boundary layer (UBL-series)
c     development study.
c     This is a processing program that converts s series of ensemble
c     averaged xxxxxxxa,b.OUT files to plots in the distance/time
c     domain.
c-------------------------------------------------------------------------------------
      program CONT
      implicit none
      integer nfils,i,j
      real ufil,dufil,Tufil,m_Tufil,m_dufil,m_ufil
      real dt,dx,u,du,Tu,m_dt,m_dx,m_u
      real ratio,srod,period,wallnormal
      character*75 inputfile,outfile
      write(*,*)'Enter rod spacing in mm.'
      read(*,*) srod
      period=srod/5
      open(unit=10,file='contour.fil',status='old')
      read(10,*)nfils
      read(10,'(a)')outfile
      open(3,file=outfile,status='unknown')
      write(3,74)
      write(3,76)
      open(unit=11,file='ratio.inf',status='old')
c     open(unit=11,file='11_7coord.dat',status='old')
      do i=1,nfils
         read(11,*)ratio
c        read(11,*)wallnormal
         read(10,'(a)')inputfile
         open(2,file=inputfile,status='old')
         do while (.not.eof(2))
            read(2,*)dt,dx,ufil,dufil,Tufil,u,du,Tu
```

```
c         if(dt.ge.400)then
            if(dt.ge.700)then
c           dt=dt-400.0
            dt=dt-700.0
          if(dt/period.gt.3.0)then
          go to 22
            endif
            write(3,93)ratio,dt/period,ufil,dufil,Tufil,u,du,Tu
c           write(3,93)dt/period,wallnormal,ufil,dufil,Tufil,u,du,Tu
          endif
        enddo
22      close(2)
     enddo
     close(3)
93  format(8(1x,f15.10))
74  format('VARIABLES="s/so","t/tau","ufil(m/s)", "dufil(m/s)", "Tufil
   &(%)","u(m/s)","du(m/s)","Tu(%)"')
c74format('VARIABLES="t/tau","y/l","ufil(m/s)", "dufil(m/s)", "Tufil
c &(%)","u(m/s)","du(m/s)","Tu(%)"')
76  format('ZONE I=29791, F=POINT')
     stop
     end
```

10. Data reduction program for image alignment using cross-correlation method

```
clear all
close all
% cross-correlation with automatic reading
% This program creates pictures out of picture fragments. The input file
% must contain the list of pictures to put together, commencing with the
% picture on the right. Also the program works only with horizontal pictures.
% possible changes:
% write-data: if input is 'y' tecplot and matlab files containing the data
%       will be made. if not desired change to any character.
%
% write-picture: if input is 'y' a tif picture will be written. May not
%       work, if values are to small, for example: a value of 0.3
%       transformed into 8 bit data will equal 0, so the whole picture will
%       be black, possibility: multiply, that maximum value of the picture
%       times a factor will equal the maximum in the transformed data, for
%       example: max. picture value=1, max 8-bit data 256, so the factor
%       would be 256 and so on.
```

```
%
% u and
% v: u and v set the averaging constants. Example: u=0.9, v=.1; at the left
%       side of the overlapping the weighting is: 90% left 10% right picture, see
%       figure (4)
%
% f and
% g: f and g set the mask size, which is correlated over the picture. The
%       source for the size is the left picture (the mask size is constant).
%       Example: left picture 100x100, right picture 100x200, f=.1, g=.2. The
%       mask is: right picture 100x(20 to 40), the mask size depends only on the
%       left picture size:(right picture should be the source picture)

%%%%%%%%%%%%%%%%%%%%%%%%%%%%%%%%%%%%%%%%%%%%%%%%%%%%%%%%%%%%%%%%%%%%%%%%%%%%%%%
%%%%%%%%%%%%%%%%%%%%%%%%%%%%%%%%%%%%%%%%%%%%%%%%%%%%%%%%%%%%%%%%%%%%%%%%%%%%%%% Input Filenames
filename=uigetfile('*.txt','Textfile with Filenames'); % get file with filenames in GUI
window
tic % start timer
%%%%%%%%%%%%%%%%%%%%%%%%%%%%%%%%%%%%%%%%%%%%%%%%%%%%%%%%%%%%%%%%%%%%%%%%%%%%%%%
%%%%%%%%%%%%%%%%%%%%%%%%%%%%%%%%%%%%%%%%%%%%%%%%%%%%%%%%%%%%%%%%%%%%%%%%%%%%%%% writing factors
write_data='y'; % write data? 'y' if yes
write_picture='n'; % write picture? 'y' if yes
%%%%%%%%%%%%%%%%%%%%%%%%%%%%%%%%%%%%%%%%%%%%%%%%%%%%%%%%%%%%%%%%%%%%%%%%%%%%%%%
%%%%%%%%%%%%%%%%%%%%%%%%%%%%%%%%%%%%%%%%%%%%%%%%%%%%%%%%%%%%%%%%%%%%%%%%%%%%%%% reading
filenames
fid=fopen(filename); % open file
line=0;
i=0;
%warning off MATLAB:nonIntegerTruncatedInConversionToChar % turning an
unimportant warning message
while line ~= -1; % loop for lines in file. abort when last line was read out
   i=i+1;
   line=fgetl(fid); % read out line and write it in array
   filenames(i,:)=line; % array with filenames
end
filenames=filenames(1:i-1,:); % cutout the last entry (when last line is reached, the
readout is -1)
fclose(fid); % close file
numfiles=size(filenames); % how many files are available
%%%%%%%%%%%%%%%%%%%%%%%%%%%%%%%%%%%%%%%%%%%%%%%%%%%%%%%%%%%%%%%%%%%%%%%%%%%%%%%
%%%%%%%%%%%%%%%%%%%%%%%%%%%%%%%%%%%%%%%%%%%%%%%%%%%%%%%%%%%%%%%%%%%%%%%%%%%%%%% averaging faktors
u=0.9; % averaging constant
v=0.1; % averaging constant
```

```
%%%%%%%%%%%%%%%%%%%%%%%%%%%%%%%%%%%%%
%%%%%%%%%%%%%%%%%%%%%%%%%%%%%%%%%%%%% loop for files
z=2;
name2=filenames(1,:);
I2=load(name2);
while z<numfiles(1)+1;
   name1=filenames(z,:);
   z=z+1;
   I1=load(name1); % read out matrix from file
   %%%%%%%%%%%%%%%%%%%%%%%%%%%%%%%%%%%%%
   %%%%%%%%%%%%%%%%%%%%%%%%%%%%%%%%%%%%% setting the
mask picture
   im1=I1;
   im2=I2;
   sim1=size(im1);
   sim2=size(im2);

   f=0.25*sim1(2); % setting the boundary for the mask picture
   g=0.6*sim1(2); % setting the boundary for the mask picture
   im=im1;
   ma=im2(:,f:g); % mask is part of the right picture
   %%%%%%%%%%%%%%%%%%%%%%%%%%%%%%%%%%%%%
   %%%%%%%%%%%%%%%%%%%%%%%%%%%%%%%%%%%%% Calculation of
the Cross Correlation
   sim=size(im);
   sma=size(ma);
   Nj=sma(2);
   %%%%%%%%%%%%%%%%%%%%%%%%%%%%%%%%%%%%%
   %%%%%%%%%%%%%%%%%%%%%%%%%%%%%%%%%%%%% Loops depend
on picture size m by n
   j=0;
   while j<(sim(2)-((Nj)-1)); % loop for pixel in x direction
      j=j+1;
      imc=im(:,(j:(j+((Nj)-1))));  % Imagepart for comparisson
      r(j)=sum(sum(imc.*ma))./(sqrt(sum(sum(imc.^2))).*sqrt(sum(sum(ma.^2))));
%Corrrelation
   end
   %%%%%%%%%%%%%%%%%%%%%%%%%%%%%%%%%%%%%
   %%%%%%%%%%%%%%%%%%%%%%%%%%%%%%%%%%%%% Connecting
the pictures
    [C1,II1]=max(r);
   [C2,II2]=max(C1);
   aa=II1(II2); % position of the match
```

```
   %%%%%%%%%%%%%%%%%%%%%%%%%%%%%%%%%%%
   %%%%%%%%%%%%%%%%%%%%%%%%%%%%%%%%%%% putting the
picture together
   pic=[im1(:,1:aa-1),im2(:,(f):end)];

    %%%%%%%%%%%%%%%%%%%%%%%%%%%%%%%%%%%
   %%%%%%%%%%%%%%%%%%%%%%%%%%%%%%%%%%% Averaging of
the melted picture
   gg=sim1(2)-aa;
   k=0;
   cal=[];
   x=[1 gg+1];
   y=[u v];
   x1=[1:gg+1]';
   p=polyfit(x,y,1); % calculating the averaging funktion
   y1=polyval(p,x1);
   while k<gg+1;
      cal(:,k+1)=(y1(k+1).*im1(:,aa+k))+((1-y1(k+1)).*im2(:,f+k)); % averaging
      k=k+1;
   end
   picci=[im1(:,1:aa-1),cal,im2(:,f+gg+1:end)]; % putting the averaged picture together
   s_pic=size(pic);
   I2=picci;
end
%%%%%%%%%%%%%%%%%%%%%%%%%%%%%%%%%%%
%%%%%%%%%%%%%%%%%%%%%%%%%%%%%%%%%%% decision if data
files should be written
if write_data=='y';
   %%%%%%%%%%%%%%%%%%%%%%%%%%%%%%%%%%%
   %%%%%%%%%%%%%%%%%%%%%%%%%%%%%%%%%%% writing the
tecplot file
   i=0;
   j=0;
   s=size(picci);
   imax=s(1);
   jmax=s(2);
   fid=fopen([name1(end-5:end-4),'-',name2(end-5:end-4),'.dat'],'w');
   fprintf(fid,'%s\n','variables="I" "J" "Int."');
   str=['zone i=',num2str(imax*jmax),' f=point'];
   fprintf(fid,'%s\n',str);
   while i<imax;
      i=i+1;
      j=0;
```

```
      while j<jmax;
         j=j+1;
         fprintf(fid,'%6.2f %6.2f %6.2f\n',i,j,picci(i,j));
      end

   end
   fclose(fid);
   %%%%%%%%%%%%%%%%%%%%%%%%%%%%%%%%%%
   %%%%%%%%%%%%%%%%%%%%%%%%%%%%%%%%%% writing the
matlab file
   dlmwrite([name1(end-5:end-4),'-',name2(end-5:end-4),'.txt'],picci,'\t'); % writing the
picture matrix
else
   'no data file has been written'
end
%%%%%%%%%%%%%%%%%%%%%%%%%%%%%%%%%%
%%%%%%%%%%%%%%%%%%%%%%%%%%%%%%%%%% write pictures
if write_picture=='y'
   picci8=uint8(picci); % changing the data format from double to 8 bit
   imwrite(picci8,[name1(end-5:end-4),'-',name2(end-5:end-4),'.tif'],'tif') % writing the
picture
else
   'no picture file has been written'
end
%%%%%%%%%%%%%%%%%%%%%%%%%%%%%%%%%%
%%%%%%%%%%%%%%%%%%%%%%%%%%%%%%%%%%
figure(1);
subplot(2,2,3);plot(r);
grid on;
title(['Correlation r over Position,matching Pixel=',num2str(aa)]);
xlabel('Pixel of the left picture []');
ylabel('Correlation r []');
ylim([0 1]);
subplot(2,2,4);contourf(pic);
set(gca,'YDir','reverse');
axis equal;
title('Melted Picture');
xlabel('Pixel []');
ylabel('Pixel []');
ylim([1 s_pic(1)]);
subplot(2,2,1);contourf(im1);
axis equal;
set(gca,'YDir','reverse');
```

```
title('Left Picture');
xlabel('Pixel []');
ylabel('Pixel []');
ylim([1 sim1(1)]);
subplot(2,2,2);contourf(im2);
axis equal;
set(gca,'YDir','reverse');
title('Right Picture');
xlabel('Pixel []');
ylabel('Pixel []');
ylim([1 sim2(1)]);
%%%%%%%%%%%%%%%%%%%%%%%%%%%%%%%%%%%%
%%%%%%%%%%%%%%%%%%%%%%%%%%%%%%%%%%%%
figure(2)
subplot(2,2,1);contourf(im1);
axis equal;
set(gca,'YDir','reverse');
title('Left Picture');
xlabel('Pixel []');
ylabel('Pixel []');
ylim([1 sim1(1)]);

subplot(2,2,2);contourf(im2);
axis equal;
set(gca,'YDir','reverse');
title('Right Picture');
xlabel('Pixel []');
ylabel('Pixel []');
ylim([1 sim2(1)]);

subplot(2,2,3); contourf(pic);
set(gca,'YDir','reverse');
axis equal;
title('Melted Picture');
xlabel('Pixel []');
ylabel('Pixel []');
ylim([1 s_pic(1)]);

subplot(2,2,4); contourf(picci);
set(gca,'YDir','reverse');
axis equal;
title('Melted Picture with averaging');
xlabel('Pixel []');
```

```
ylabel('Pixel []');
ylim([1 s_pic(1)]);

%%%
```

11. Data reduction program for image alignment using the markers

```
clear all
close all
% file averaging
% The setup for this program is"black\point1\pic001.tif". The
% first folder name is set in the array "dire". the second is variable and
% will be read out automatically, the picture name is also variable. All
% picture files must be tif files, or the skript must be changed ( search
% and replace for "tif"). The outputfile will be created in the main folder
% (for example "black\*.txt") and will be a matrix file named -.txt and a
% picture file named *.tif.
% The algorithm is a simple averaging formula.
% An important command for this file is the "eval()" command. It is
% executing the value of an character array, for example character array
% "cara='x=6'" is executed in "eval(cara)". The advantage of this procedure
% is the abicity of automated command forming with variable names.
tic; % start timer
n=0;
%dire=strvcat('set7','set8','set9','set10','set11','set12','set13','set14','set15','set16','set17','set
18','set19'); %directory names
dire=strvcat('windon');
%%%%%%%%%%%%%%%%%%%%%%%%%%%%%%%%%%%%%
black=dlmread('black.txt');     %read textfile with the black picture
angle=dlmread('suction_angles.txt');
crop_x_min=dlmread('suction_crop_x_min.txt');
crop_y_min=dlmread('suction_crop_y_min.txt');
pixelshift=dlmread('suction_pixelshift.txt');
zoom=dlmread('suction_zoom.txt');
pixelshift_total= sum(pixelshift); %sum of all pixelshifts, same for all sets
pixelsize_x= 40; %with in pixels of the cropped picture
pixelsize_y= 30; %hight in pixels of the cropped picture
pixels_combined= pixelshift_total + pixelsize_x; %calculate the with of the combined
picture in pixels based on the pixelwith of the singel pictures and the sum of the
pixelshifts
fa=double(zeros(pixelsize_y,pixels_combined)); %vektor for the counter to average the
picture
IM16_comb=uint16(zeros(pixelsize_y,pixels_combined)); %initalizing the array for the
combined picture
IM16_comb_av=uint16(zeros(pixelsize_y,pixels_combined)); %initalizing the array for
the averaged combined picture
IM_comb=double(zeros(pixelsize_y,pixels_combined)); %initalizing the array for the
combined picture
```

```
IM_comb_sum=double(zeros(pixelsize_y,pixels_combined)); %initalizing the array for
the averaged combined picture
%crop_positions=(zeros(50,2));
while n<1; %loop for different main directories (black,windon,...)
   n=n+1;
   exec=['cd ',dire(n,:),';'];  %change actual directory to windoff etc...
   eval(exec);
%%%%%%%%%%%%%%%%%%%%%%%%%%%%%%%%%%%%%%%%%%%%%%%%%%%%%%%%%%%%%%%%%%%%%%%%%%%%%%%
   root_direct=dir; %array with all objects in main directory
   i=2;
   sroot=size(root_direct);
   while i<sroot(1); % loop for all inner directory's
      i=i+1
      if root_direct(i).isdir==1; % decision if object is a folder
         direcn=root_direct(i).name; % folder name
         exec=['direc=dir(fullfile(direcn,"*.tif"));']; % array with all tif files in the inner
directory
         eval(exec);
         sdirec=size(direc);
         IM=0;
         k=0;
         j=0;
         while j<sdirec(1); % loop for all tif files in actual folder
            j=j+1;
            exec=['filename=[direcn,'\',direc(j).name];']; % create the filename
            eval(exec);
            im=0;
            k=k+1; % counter for number of images
            im=imread(filename,'tif'); % reading the picture from filename
            im=double(im)-32768; % changing the matrix type from 16 bit to float
            IM=IM+im; % sum of the pictures
         end
         a_str=strrep(direcn,'position',''); %extract position number by deleting "position"
in direcn
         a=str2num(a_str); %convert position number into a number
        % Averaging the picture
         IM=IM./k;
         IM16=uint16(IM);
         imwrite(IM16,[dire(n,:),'_mean_bic_',direcn,'.tif'],'tif'); % write the averaged
picture
         dlmwrite([dire(n,:),'_mean_bic_',direcn,'.txt'],IM,'\t'); % write the averaged
matrix
         %Substract the black picture
```

```
        %IM=IM-black;
        %Rotating the averaged picture
        IMrot_bic=imrotate(IM,angle(a),'bicubic'); %rotating picture
        IM16rot_bic=uint16(IMrot_bic-1);
        imwrite(IM16rot_bic,[dire(n,:),'_mean_rot_bic_',direcn,'.tif'],'tif'); % write the
rotated picture
         %Zoom rotated picture
        IMrot_bic_zoom = imresize(IMrot_bic,zoom(a),'bicubic'); %zoom the rotated
picture
        IM16rot_bic_zoom=uint16(IMrot_bic_zoom-1);
        imwrite(IM16rot_bic_zoom,[dire(n,:),'_mean_rot_bic_zoom',direcn,'.tif'],'tif'); %
write the zoomed,rotated picture
        %Crop rotated, zoomed picture
IMrot_bic_zoom_crop=imcrop(IMrot_bic_zoom,[crop_x_min(a),crop_y_min(a),pixelsiz
e_x-1,pixelsize_y-1]); %crop the zoomed, rotated picture
        IM16rot_bic_zoom_crop=uint16(IMrot_bic_zoom_crop-1);
imwrite(IM16rot_bic_zoom_crop,[dire(n,:),'_mean_rot_bic_zoom_crop',direcn,'.tif'],'tif')
; % write the rotated, zoomed, cropped picture

dlmwrite([dire(n,:),'_mean_rot_bic_zoom_crop',direcn,'.txt'],IMrot_bic_zoom_crop,'\t');
% write the rotated, zoomed, cropped matrix
        x=sum(pixelshift(1:a))+1;
        IM16_comb(:,x:x+pixelsize_x-1)=IM16rot_bic_zoom_crop(:,:);
        imwrite(IM16_comb,[dire(n,:),'bic_combined',direcn,'.tif'],'tif'); % write the
combined picture
        IM_comb_sum(:,x:x+pixelsize_x-1)= IM_comb_sum(:,x:x+pixelsize_x-1)+
IMrot_bic_zoom_crop;
        fa(:,x:x+pixelsize_x-1)=fa(:,x:x+pixelsize_x-1)+1;
      else
      end
   end
   IM_comb_av=IM_comb_sum./fa; %averaging the picture
   IM16_comb_av=uint16(IM_comb_av);
   imwrite(IM16_comb_av,[dire(n,:),'bic_combined_averaged',direcn,'.tif'],'tif'); % write
the picture
   dlmwrite([dire(n,:),'bic_combined_averaged',direcn,'.txt'],IM_comb_av,'\t'); % write
the matix
   cd ..;
end
toc; % end timer
```

APPENDIX B

B.1 Uncertainty Analysis for Single Hot-Wire Measurements

Kline-McKlintock Uncertainty Analysis for Single Hot-Wire Probe Calibration

I) Calibration

$Tair := (22.7 + 273.15)K$

$\omega Tair := 0.5K$

Free-stream air temperature

$Pamb := \left(\frac{753.8}{25.4}\right) in\_Hg$

$\omega Pamb := \left(\frac{0.5}{25.4}\right) in\_Hg$

Atmospheric pressure

$R := 287 \frac{joule}{kg \cdot K}$

Gas constant, uncertainty assumed to be zero

$Ea := 0.33$

$\omega Ea := 0.002$

Voltage of Anemometer

$D1 := 38.1mm$

$\omega D1 := 0.5mm$

Outer diameter of calibration nozzle

$D2 := 152.9mm$

$\omega D2 := 0.5mm$

Inner diameter of calibration nozzle

$Ptrans := \left(\frac{0.04}{25.4}\right) in\_Hg$

$\omega Ptrans := 0.6Pa$

Pressure read from pressure transducer

1) Determine uncertainty for air density

$\rho := \frac{Pamb}{R \cdot Tair}$

$\rho = 1.18 \frac{kg}{m^3}$

Note: DrhoDTair=Partial derivative of rho with respect to Tair

$D\rho DTair := \frac{-Pamb}{R \cdot Tair^2}$

$D\rho DTair = -3.989 \times 10^{-3} \frac{kg}{m^3 K}$

$D\rho DPamb := \frac{1}{R \cdot Tair}$

$D\rho DPamb = 1.178 \times 10^{-5} \frac{s^2}{m^2}$

$\omega\rho := \left[(D\rho DTair \cdot \omega Tair)^2 + (D\rho DPamb \cdot \omega Pamb)^2 \right]^{0.5}$

$\omega\rho = 2.143 \times 10^{-3} \frac{kg}{m^3}$

$$\%\rho := \left(\frac{\omega\rho}{\rho}\right)\cdot 100$$

$$\%\rho = 0.182$$

2) Determine uncertainty for velocity

$$V := \left[\frac{(2\cdot Ptrans)}{\rho\cdot\left(1-\frac{D1^4}{D2^4}\right)}\right]^{0.5}$$

$$V = 3.008\frac{m}{s}$$

$$DVDD2 := -2.828427124746190097\left[\frac{Ptrans^{0.5}}{\rho^{0.5}\cdot\left(1-\frac{D1^4}{D2^4}\right)^{1.5}}\right]\cdot\frac{D1^4}{D2^5}$$

$$DVDD2 = -0.152Hz$$

$$DVDD1 := 2.828427124746190097\left[\frac{Ptrans^{0.5}}{\rho^{0.5}\cdot\left(1-\frac{D1^4}{D2^4}\right)^{1.5}}\right]\cdot\frac{D1^3}{D2^4}$$

$$DVDD1 = 0.611Hz$$

$$DVDp := -0.707106781186547524\frac{Ptrans^{0.5}}{\rho^{1.5}\cdot\left(1-\frac{D1^4}{D2^4}\right)^{0.5}}$$

$$DVDp = -1.274\frac{m^4}{kg\,s}$$

$$DVDPtrans := \frac{0.707106781186547524}{\left[\rho^{0.5}\cdot\left(1-\frac{D1^4}{D2^4}\right)^{0.5}\right]\cdot Ptrans^{0.5}}$$

$$DVDPtrans = 0.283\frac{m^2 s}{kg}$$

$$\omega V := \left[(DVDD1\cdot\omega D1)^2 + (DVDD2\cdot\omega D2)^2 + (DVDp\cdot\omega\rho)^2 + (DVDPtrans\cdot\omega Ptrans)^2\right]^{0.5}$$

$$\omega V = 0.17\frac{m}{s}$$

$$\%V := \left(\frac{\omega V}{V}\right)\cdot 100$$

$$\%V = 5.642$$

The percentage of uncertainty for other velocities

$$V := 15\frac{m}{s}$$

$$\%V := 0.284$$

$V := 10\frac{m}{s}$

$\%V := 0.529$

$V := 5\frac{m}{s}$

$\%V := 2.053$

The uncertainty of the curve fit according to S. Yavuzkurt (1984) is 1.2%. Thus, the new velocity uncertainty is given by

$$\%Vn := \left[\left(\omega V \cdot \frac{100}{V}\right)^2 + 1.2^2\right]^{0.5}$$

$\%Vn = 3.6$

The curve fir uncertainty percentage is calculated as follows:

1) The measured velocity is curved fit against anemometry voltage
2) The residuals of the curve fit are calculated
3) The residuals are divided by measured velocity at which they occur
4) The quantity in 3) is squared and summed foe all velocties
5) The sum of the squares is divided by the number of data points and the square root is taken
6) Thr percentage uncertainty in the curve fit is called beta and the equation as given by S. Yavuzkurt is given below

$$beta := \left[\frac{\left[\sum_i \left(\frac{\Delta Ucf}{U}\right)\cdot i\right]}{n}\right]^{0.5}$$

Determine uncertainty of velocity due to error in anemometer voltage

$$Vn1 := \left(1.374268 + 4.3283137Ea + 1.4779551Ea^2 - 0.24928452Ea^3 + 0.1867769Ea^4\right)\frac{m}{s}$$

$$DVn1DEa := 4.3283137 + 2.9559102Ea - 0.74785356Ea^2 + 0.7471076Ea^3$$

$DVn1DEa = 5.249$

$$\omega Vn1 := DVn1DEa\,\omega Ea \cdot \frac{m}{s}$$

$Vn1 = 2.957\frac{m}{s}$

$\omega Vn1 = 0.01\frac{m}{s}$

Total calibration uncertainty for velocity due to velocity reading, curve fit, and voltage error

$$\%Vtotalc := \left[\%Vn^2 + \left(100 \cdot \frac{\omega Vn1}{Vn1}\right)^2\right]^{0.5}$$

$\%Vtotalc = 3.617$

II) Determine uncertainty of the velocity after data reduction

$E := 0.33$

$\omega E := 0.002$

Anemometer voltage

$Tsen := 250$

$\omega Tsen := 0.5$

Temperature of hot-wire sensor (C)

$T := 24$

$\omega T := 1$

Temperature of air during measurements (C)

$Tcal := 22.7$

$\omega Tcal := 1$

Temperature of air during calibration (C)

En is the anemometer voltage that has been corrected for temperature

$$En := E\cdot\left[\frac{(Tsen - T)}{(Tsen - Tcal)}\right]^{0.5}$$

$En = 0.329$

$$DEnDTcal := 0.5\cdot E\cdot\left[\frac{(Tsen - T)^{0.5}}{(Tsen - Tcal)^{1.5}}\right]$$

$DEnDTcal = 7.238\times 10^{-4}$

$$DEnDT := -0.5\cdot\frac{E}{\left[(Tsen - T)^{0.5}\cdot(Tsen - Tcal)^{0.5}\right]}$$

$DEnDT = -7.28\times 10^{-4}$

$$DEnDE := \frac{(Tsen - T)^{0.5}}{(Tsen - Tcal)^{0.5}}$$

$DEnDE = 0.997$

$$\omega En := \left[(DEnDTcal\cdot\omega Tcal)^2 + (DEnDT\cdot\omega T)^2 + (DEnDE\cdot\omega E)^2\right]^{0.5}$$

$\omega En = 2.243\times 10^{-3}$

$$\%En := 100\cdot\frac{\omega En}{En}$$

$\%En = 0.682$

Determine uncertainty of effective velocity due to error in corrected voltage

$$Vn := \left(1.374268 + 4.3283137En + 1.4779551En^2 - 0.24928452En^3 + 0.1867769En^4\right)\frac{m}{s}$$

$Vn = 2.952\frac{m}{s}$

$$DVnDEn := 4.3283137 + 2.9559102En - 0.74785356En^2 + 0.7471076En^3$$

$DVnDEn = 5.247$

$$\omega Vdata := DVnDEn\cdot\omega En\cdot\frac{m}{s}$$

$\omega Vdata = 0.012\frac{m}{s}$

Total velocity uncertainty for calibration and data reduction

$$\%Vtotal := \left[\left(100\cdot\frac{\omega Vdata}{Vn}\right)^2 + \%Vtotalc^2\right]^{0.5}$$

$\%Vtotal = 3.639$

B.2 Uncertainty Analysis for Liquid Crystal Measurements

Heat Transfer Coefficient

In this appendix the calculation of the heat transfer coefficient is reviewed respective of the uncertainty. The Kline-McKlintock method was performed.

Parameters

Parameter	Value	Uncertainty	Description
T_{yb}	44.6 °C	$\omega(T_{yb})$ = 0.5 K	Yellow Band Temperature
T_{air}	Variable	$\omega(T_{air})$ = 0.5 K	Free Stream Air Temperature
U	Variable	$\omega(U)$ = 0.1 %	Voltage
I	Variable	$\omega(I)$ = 0.1 %	Current
W	0.2 m	$\omega(W)$ = 0.0005 m	Width of the Inconel Foil
s_0	0.506 m	$\omega(s_0)$ = 0.0005 m	Arc Length of the Blade
ε	0.85	$\omega(\varepsilon)$ = assumed 0	Emissivity
σ	5.667 10^{-8} W/m^{2}K^4	$\omega(\sigma)$ = assumed 0	Stefan Boltzman Constant

Table B.1. Parameters for uncertainty analysis

Uncertainty for Radiation Losses

For the uncertainty calculation the partial derivatives have to be determined:

$$\frac{\partial \dot{E}_{rad}}{\partial T_{yb}} = 4\varepsilon\sigma T_{yb}^3 \tag{B.1}$$

$$\frac{\partial \dot{E}_{rad}}{\partial T_{air}} = -4\varepsilon\sigma T_{air}^3 \tag{B.2}$$

$$\omega\left(\dot{E}_{rad}\right) = \sqrt{\left(\frac{\partial \dot{E}_{rad}}{\partial T_{yb}} \cdot \omega T_{yb}\right)^2 + \left(\frac{\partial \dot{E}_{rad}}{\partial T_{air}} \cdot \omega T_{air}\right)^2} \tag{B.3}$$

With these equations the deviation for the radiation heat loss is determined:

$$\Delta\left(\dot{E}_{rad}\right) = \frac{\omega\left(\dot{E}_{rad}\right)}{\dot{E}_{rad}}$$

Uncertainty for Input Power

The equation for the power supply is calculated with:

$$P_{el-A} = \frac{U \cdot I}{W \cdot s_0}$$

The partial derivatives are:

$$\frac{\partial P_{el-A}}{\partial s_0} = -\frac{U \cdot I}{W \cdot s_0^2}$$

$$\frac{\partial P_{el-A}}{\partial W} = -\frac{U \cdot I}{W^2 \cdot s_0}$$

$$\frac{\partial P_{el-A}}{\partial I} = \frac{U}{W \cdot s_0}$$

$$\frac{\partial P_{el-A}}{\partial U} = \frac{I}{W \cdot s_0}$$

With these equations the deviation for the power supply is determined:

$$\omega\left(P_{el-A}\right) = \sqrt{\left(\frac{\partial P_{el-A}}{\partial s_0} \cdot \omega\left(s_0\right)\right)^2 + \left(\frac{\partial P_{el-A}}{\partial W} \cdot \omega\left(W\right)\right)^2 + \left(\frac{\partial P_{el-A}}{\partial I} \cdot \omega\left(I\right)\right)^2 + \left(\frac{\partial P_{el-A}}{\partial U} \cdot \omega\left(U\right)\right)^2}$$

$$\Delta\left(P_{el-A}\right) = \frac{\omega\left(P_{el-A}\right)}{P_{el-A}}$$

Uncertainty for Heat Transfer Coefficient

The heat transfer coefficient is calculated with the following equation:

$$h = \frac{P_{el-A} - \dot{E}_{rad}}{T_S - T_{air}}$$

Calculation of the partial derivates:

$$\frac{\partial h}{\partial T_{air}} = -\frac{P_{el-A} - \dot{E}_{rad}}{\left(T_{yb} - T_{air}\right)^2}$$

$$\frac{\partial h}{\partial T_{yb}} = -\frac{P_{el-A} - \dot{E}_{rad}}{\left(T_{yb} - T_{air}\right)^2}$$

$$\frac{\partial h}{\partial \dot{E}_{rad}} = -\frac{1}{T_{yb} - T_{air}}$$

$$\frac{\partial h}{\partial P_{el-A}} = \frac{1}{T_{yb} - T_{air}}$$

The deviation for the heat transfer coefficient is:

$$\omega(h) = \sqrt{\left(\frac{\partial h}{\partial T_{air}} \cdot \omega(T_{air})\right)^2 + \left(\frac{\partial h}{\partial T_{yb}} \cdot \omega(T_{yb})\right)^2 + \left(\frac{\partial h}{\partial \dot{E}_{rad}} \cdot \omega\left(\dot{E}_{rad}\right)\right)^2 + \left(\frac{\partial h}{\partial P_{el-A}} \cdot \omega(P_{el-A})\right)^2}$$

$$\Delta(h) = \frac{\omega(h)}{h}$$

The uncertainty for the heat transfer coefficient is highly dependent on the temperature difference between the yellow band temperature T_{yb} and the free stream air temperature T_{air}.For this reason the measurements were executed during lower outside temperatures

APPENDIX C

C.1 Turbulence Length Scale Calculations

In order to document the turbulent scales, one dimensional power spectra of u' was measured using the single-sensor anemometer probe. The power spectral measurements were collected by sampling 20000 data points at 20 kHz (low-pass filtered at 10 kHz). The power spectral distribution were computed using Matlab, using the script lengthscale.m included at the Appendix-A.

The power spectra are presented in Figure C.1. From these data, the integral length scales of the flow, $\Lambda_{u,x}$, can be calculated. Using relations developed by Hinze [107], the integral length scales can be calculated by extrapolating the PSD values in Figure C.1. to f = 0 and using the following formula:

$$\Lambda_{u,x} = \frac{\bar{u}E_u(f = 0)}{4u'^2_{rms}} \tag{C.1}$$

From these results, integral length scales were calculated for FSTI of 1.9, 3, 8 and 13%. The results are presented in Table C.1.

Table C.1. Turbulence length scale for different FSTI

Turbulence Intensity Level	**Λ(cm)**
Tu_{in} = 1.9%	4.13
Tu_{in} = 3.0%	3.25
Tu_{in} = 8.0%	3.01
Tu_{in} = 13.0%	2.34

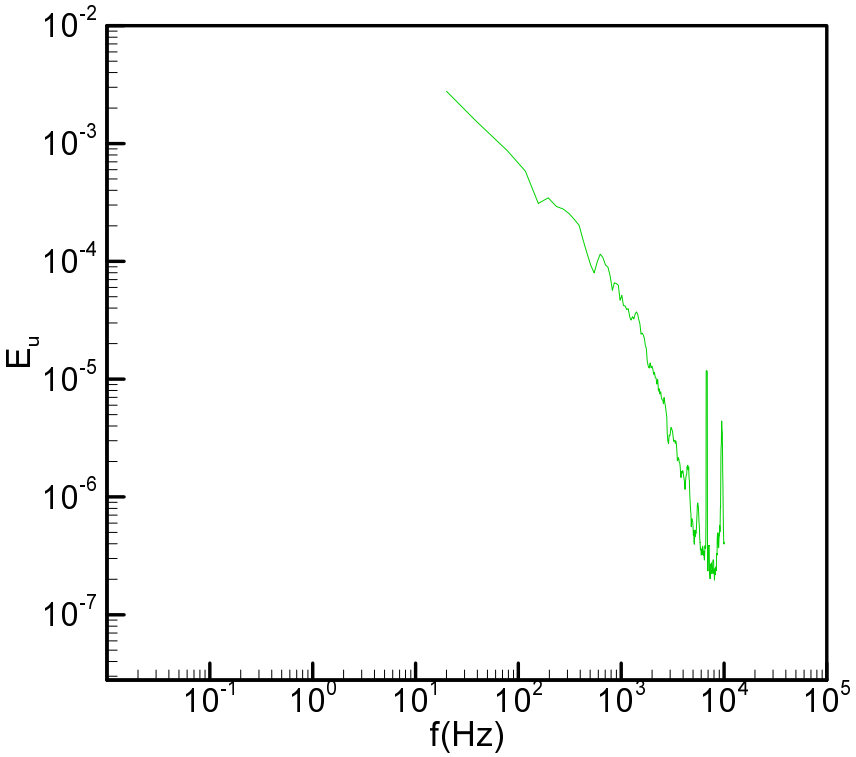

Figure C.1. Power spectral distribution of turbulence in x-directions for FSTI=13%

VITA

Burak Ozturk was born in Bursa, Turkey on January 7, 1977. He attended Galatasaray High School and obtained his Bachelor of Science degree in mechanical engineering at Middle East Technical University in June 2000. He joined the Master of Science program at Texas A&M University at 2000. He worked as a Graduate Research Assistant at the Turbine Performance and Flow Research Laboratory in the Department of Mechanical Engineering under the supervision of Dr. M. T. Schobeiri. He completed his Master of Science Degree in mechanical engineering at Texas A&M University in August 2003. He received his Ph.D. in December 2006. He can be contacted through his advisor Dr. M. T. Schobeiri, Professor of Mechanical Engineering, Texas A&M University, College Station, TX, 77843, USA.